

Wall Jet Boundary Layer Flows Over Smooth and Rough Surfaces

Benjamin Scott Smith

Dissertation submitted to the faculty of the Virginia Polytechnic Institute
and State University in partial fulfillment of the
requirements for the degree of

Doctor of Philosophy
In
Aerospace Engineering

William J. Devenport
Ricardo A. Burdisso
Roger L. Simpson
Wayne L. Neu
Wing F. Ng

April 21, 2008
Blacksburg, Virginia

Keywords: wall jet, rough surface, turbulent boundary layer, surface pressure fluctuations

Copyright © 2008 by Benjamin S. Smith

Wall Jet Boundary Layer Flows Over Smooth and Rough Surfaces

Benjamin Scott Smith

Abstract

The aerodynamic flow and fluctuating surface pressure of a plane, turbulent, two-dimensional wall jet flow into still air over smooth and rough surfaces has been investigated in a recently constructed wall jet wind tunnel testing facility. The facility has been shown to produce a wall jet flow with Reynolds numbers based on the momentum thickness, $Re_\theta = \frac{\theta U_m}{\nu}$, of between 395 and 1100 and nozzle exit Reynolds numbers, $Re_j = \frac{U_m b}{\nu}$, of between 16000 and 45000. The wall jet flow properties (δ , δ^* , θ , $y_{1/2}$, U_m , u^* , etc.) were measured and characterized over a wide range of initial flow conditions and measurement locations relative to the wall jet source. These flow properties were measured for flow over a smooth flow surface and for flow over roughness patches of finite extent. The patches used in the current study varied in length from 305 mm to 914 mm (between 24 and 72 times the nozzle height, b) and were placed so that the leading edge of the patch was fixed at 1257 mm ($x/b = 99$) downstream of the wall jet source. These roughness patches were of a random sand grain roughness type and the roughness grain size was varied throughout this experiment. The tests covered roughness Reynolds numbers (k^+) ranging from less than 2 to over 158 (covering the entire range of rough wall flow regimes from hydrodynamically smooth to fully rough). For the wall jet flows over 305 mm long patches of roughness, the displacement and momentum thicknesses were found to vary noticeably with the roughness grain size, but the maximum velocity, mixing layer length scale, $y_{1/2}$, and the boundary layer thickness were not seen to vary in a consistent, determinable way. Velocity spectra taken at a range of initial flow conditions and at several distinct heights above the flow surface showed a limited scaling dependency on the skin friction velocity near the flow surface.

The spectral density of the surface pressure of the wall jet flow, which is not believed to have been previously investigated for smooth or rough surfaces, showed distinct differences with that seen in a conventional boundary layer flow, especially at low frequencies. This difference is believed to be due to the presence of a mixing layer in the wall jet flow. Both the spectral shape and level were heavily affected by the variation in roughness grain size. This effect was most notable in overlap region of the spectrum. Attempts to scale the wall jet surface pressure spectra using outer and inner variables were successful for the smooth wall flows. The scaling of the rough wall jet flow surface pressure proved to be much more difficult, and conventional scaling techniques used for ordinary turbulent boundary layer surface pressure spectra were not able to account for the changes in roughness present during the current study. An empirical scaling scheme was proposed, but was only marginally effective at scaling the rough wall surface pressure.

Acknowledgements

First of all, I would like to thank the Lord who has been an immeasurable source of strength during my entire educational experience. I have no doubt that many of my accomplishments over the past 10 years of my life have been made possible by His faithfulness, and I am very blessed with the educational opportunities that I have been given.

I must also thank my family whose prayers and support have aided me in this endeavor in ways that cannot be easily put into words. In particular, I would like to thank my father for being a constant source of wisdom and encouragement. I would like to thank my mother who fostered in me, at an early age, a love for learning and who poured so much into my life while I was growing up. I would also like to thank my sister, Leah, for her support during my time here at Virginia Tech. I hope I can encourage her in her educational endeavors as much as she has encouraged me in mine.

I would very much like to thank my advisor Dr. William Devenport for all of his advice and guidance over the past 5 years. I have always been struck by his love and excitement for research, and I know without a doubt that this has influenced me greatly. Dr. Devenport has always helped me to improve my skills and abilities, and I am very grateful. I would also like to thank him for the way in which he interacted with me and the other members of the Advanced Turbulent Flow Research Group after the unthinkable events of April 16, 2007. His concern and care for our research group during that time were greatly appreciated.

For this project I would like to thank the Office of Naval Research, and in particular Dr. Ki-Han Kim, for sponsoring this experimental work through grants N00014-05-1-0516 and N00014-07-1-0458. I would also like to thank my advisory committee members both past and present: Dr. Ricardo Burdisso, Dr. William Mason, Dr. Wayne Neu, Dr. Wing Ng, and Dr. Roger Simpson. I appreciate all of their time and support during my graduate studies greatly.

I owe a huge thank you to the members of the Aerospace and Ocean Engineering machine shop. Bruce Stanger and James Lambert really can make just about anything, and their expertise and advice regarding the fabrication and construction of numerous experimental components has proved to be absolutely priceless. I would also like to extend a sincere thanks to Mark Montgomery, Steve Edwards, and Bill Oetjens who have been a pleasure to work with over the past several years.

I would also like to thank several co-workers who have become close friends. I feel privileged to have worked alongside Dr. Dustin Grissom during the greater part of my graduate studies. He is a man of great intelligence, but more importantly, a man of the finest character, and I truly wish him all the best. I would like to thank Dr. Nanyaporn Intaratep for enforcing the “working environment”. I consider myself fortunate to have gained her friendship. In particular, I would like to thank Dr. Aurelien Borgoltz, and (soon to be) Dr. Joshua Staubs. The three of us went through this process at nearly the same time, and the support and encouragement I have experienced from my association with these two gentlemen is, in large part, responsible for my

current state of sanity. I hope I have been of as much help to them as they have to me. I would like to thank JV Larsen and Beatriz Diaz Acosta for their hospitality and welcoming personalities which made me feel welcome during my early days as a graduate student. I would like to thank the rest of the wonderful people I have had the privilege to work with, namely Nathan Alexander, Erin Crede, Derek Geiger, Dr. Ruolong Ma, Matt Rasnick, and Liz Knize.

Finally, I would like to extend a thank you to several friends outside of my academic circle, namely, Kevin Seaton, James W. Gray III, Steve Bae, Amy French, Shea Sizemore, and Dr. Neil Steiner, with whom I have developed lasting friendships over the course of my studies at Virginia Tech.

Thank you all.

Ben S.

Contents

1	Introduction and Problem Description	1
1.1	Motivation	1
1.2	Wall Jet Physical Description	1
1.3	Review of Previous Work	2
1.3.1	Wall Jet Review	2
1.3.1.1	Wall Jet Experimental Study Overview	2
1.3.1.2	The Beginning	3
1.3.1.3	The Outer Layer	3
1.3.1.4	The Inner Layer	5
1.3.1.5	Wall Jet Parameter Relations	6
1.3.1.6	Combined Inner/Outer Layer Solutions	7
1.3.1.7	Other Skin Friction Correlations	9
1.3.1.8	Effects of Roughness on the Wall Jet Flow	10
1.3.2	Wall Pressure Fluctuations Under Conventional Turbulent Boundary Layers	12
1.3.2.1	Overview	12
1.3.2.2	Smooth Wall Surface Pressure	12
1.3.2.3	Rough Wall Surface Pressure	15
1.4	Objectives and Experimental Approach	16
2	Wall Jet Tunnel and Instrumentation	18
2.1	Virginia Tech Wall Jet Tunnel	18
2.1.1	The Facility Itself	18
2.1.2	Facility Instrumentation and Hardware	25
2.1.3	Data Acquisition System	26

2.2	Aerodynamic Measurement Systems	26
2.2.1	Flattened Pitot Measurement System.....	27
2.2.2	Hotwire Anemometry	28
2.2.3	Hotwire Calibration Methods	30
2.3	Surface Pressure Measurement Systems	31
2.4	Roughness	33
2.5	Testing Facility Basic Acoustic Characteristics.....	35
2.6	Uncertainty Estimates	36
3	Velocity Field of the Wall Jet With and Without Roughness	38
3.1	Smooth Wall Jet	38
3.1.1	Smooth Wall Jet Test Conditions	38
3.1.2	The Nozzle Exit	40
3.1.3	Two Dimensionality of the Flow	44
3.1.4	Overall Wall Jet Characteristics.....	47
3.1.5	Streamwise development of the Wall Jet.....	51
3.1.6	Wall Jet Self Similarity.....	52
3.1.7	Effects of Initial Flow Conditions on the Wall Jet Flow	57
3.1.8	Turbulent Character of the Wall Jet Flow.....	59
3.1.9	Wall Jet Flow in the Inner Region	65
3.1.10	Skin Friction.....	65
3.1.11	Wall Jet Flow in Inner Coordinates	67
3.1.12	Turbulent Character of the Wall Jet in the Inner Region.....	70
3.1.13	Smooth Wall Jet Velocity Spectra	72
3.1.14	Relation of the Smooth Wall Mean Velocity, Turbulence, and Spectral Data.....	79
3.1.15	Smooth Wall Jet Flow Summary	79

3.2	Rough Wall Jet Flow Characteristics	80
3.2.1	Rough Wall Jet Test Conditions	80
3.2.2	Considerations for Abrupt Changes in Surface Condition	82
3.2.3	Effects of Roughness Height on the Wall Jet Flow	86
3.2.4	Effects of Initial Flow Conditions on the Rough Wall Jet Flow.....	88
3.2.5	Turbulent Character of the Rough Wall Jet Flow	91
3.2.6	Rough Wall Jet Outer Flow Parameters.....	95
3.2.6.1	Effects of Roughness Variation for 305 mm Patch Lengths.....	96
3.2.6.2	Effects of Varying Roughness Patch Lengths.....	102
3.2.6.3	The Hogg et al. (1996) Scaling	105
3.2.6.4	Curve Fits for the 305 mm Roughness Patch Wall Jet Flows.....	107
3.2.7	Rough Wall Jet Flow Inner Region Scaling	108
3.2.8	Rough Wall Jet Flow in Inner Coordinates.....	111
3.2.9	Turbulent Character of the Rough Wall Jet Flow in the Inner Region.....	113
3.2.10	Rough Wall Jet Velocity Spectra.....	114
3.2.11	Smooth and Rough Wall Jet Velocity Spectra Viewed Together.....	122
3.2.12	Relation of the Rough Wall Mean Velocity, Turbulence, and Spectral Data.....	125
3.2.13	Rough Wall Jet Flow Summary	126
4	Smooth and Rough Wall Jet Surface Pressure	128
4.1	Surface Pressure Measurement Setup	128
4.1.1	Surface Pressure Microphone Calibrations.....	128
4.1.2	Microphone Height and Placement Effects	133
4.1.3	Effects of Pinhole Size.....	135
4.1.4	Effects of Microphone Height and Placement on Surface Pressure	138

4.2	Smooth Wall Surface Pressure Fluctuations	142
4.2.1	Smooth Wall Test Cases	142
4.2.2	Smooth Wall Jet Surface Pressure Measurements.....	143
4.2.3	Smooth Wall Surface Pressure Summary	155
4.3	Rough Wall Surface Pressure Fluctuations	156
4.3.1	40 Grit Surface Pressure Measurements	157
4.3.2	180 Grit Surface Pressure Measurements	167
4.3.3	Surface Pressure Measurements for Varying Surface Roughness.....	174
4.3.4	Alternative Scaling Methods.....	183
4.4	Summary	188
5	Conclusions	191
	References.....	195

List of Symbols

Roman

A, B	Semilog region fit constants
A_w, A_y	Empirical flow parameter scaling constants
b	Nozzle height
C_f	Skin friction coefficient
C_i	Reynolds number dependent coefficient
f	Frequency (Hz)
G	Diffusion function as defined by Bradshaw <i>et al.</i> (1967)
G_{pp}	Single sided power spectrum of the pressure
G_{uu}	streamwise velocity power spectrum
H_1, H_2	Empirically determined constants for Hogg <i>et al.</i> (1996) scaling
J	Nozzle exit momentum
k	Nominal roughness size
k^+	Roughness Reynolds number based on k_s and u^*
k_g	Nominal roughness size obtained from standardized tables
$\overline{k_g}$	Mean roughness height
k_g^+	Roughness Reynolds number based on k_g and u^*
k_{rms}	RMS roughness height
k_s	Nikuradse equivalent sand grain roughness height
L_p	Roughness patch length
n, m	Empirical flow parameter scaling exponents
p	Pressure
p_{ref}	Reference pressure (20 μ Pa)
$\overline{q^2}$	Turbulent kinetic energy
Q_m	Dynamic pressure at velocity maximum
Re_j	Nozzle exit Reynolds number
Re_x	Reynolds number base on streamwise distance
R_T	Ration of inner to outer timescales
S	Nozzle exit span
U	Mean streamwise velocity
u', u	Mean fluctuating streamwise velocity
u^*	Skin friction velocity

U^+	Mean streamwise velocity normalized on wall variables
u^2	Streamwise normal stress
U_e	Edge velocity
U_m	Maximum velocity
U_o	Nozzle exit velocity
V	Mean velocity normal to flow surface
v', v	Mean fluctuating normal velocity
x	Streamwise distance from the nozzle exit
x_i	Downstream position of the leading edge of the roughness patch
x_o	Virtual origin
y	Normal distance from flow surface
y^+	Mean normal distance from flow surface normalized on wall variables
$y_{1/2}$	Mixing layer half height
$y_{1/2}^+$	Local Reynolds number based on $y_{1/2}$ and u^*
z	Spanwise distance from nozzle centerline

Greek

δ	Boundary layer thickness
δ^*	Displacement thickness
$\Phi(\omega)$	Power spectral density of the surface pressure
γ	Reynolds number dependent exponent
ν	Kinematic viscosity
θ	Momentum thickness
ρ	Density
Re_δ	Local Reynolds number based on δ
Re_θ	Local Reynolds number based on θ
τ	Shear stress
τ_δ	Shear stress at height of boundary layer thickness
τ_{max}	Maximum shear stress
τ_w	Wall shear stress
ω	Frequency (rad/s)

Abbreviations and Other Items of Interest

<i>dB</i>	Decibels
<i>FFT</i>	Fast Fourier Transform
<i>SPL</i>	Sound Pressure Level
$\left(\overline{pv} + \frac{1}{2}\overline{\rho q^2 v}\right)$	Turbulent diffusion

List of Figures

Figure 1.1 Schematic of the wall jet flow employed in the current test facility	2
Figure 1.2 Goody empirical model for the surface pressure spectrum for a range of timescale parameters.....	15
Figure 2.1 Schematic of the Virginia Tech wall jet tunnel in the acoustically treated configuration (dimensions in mm)	19
Figure 2.2 Top view schematic of settling chamber and aluminum plate layout (dimensions in mm)	20
Figure 2.3 Diagram of the cubic curve used in the contraction section	20
Figure 2.4 Schematic of nozzle exit and plate junction	22
Figure 2.5 Schematic of the Virginia Tech wall jet tunnel acoustic enclosure being removed (dimensions in mm).....	23
Figure 2.6 Schematic of the Virginia Tech wall jet tunnel in the aerodynamic testing configuration (dimensions in mm)	23
Figure 2.7 schematic showing the nozzle and acoustic baffle (dimensions in mm).....	24
Figure 2.8 Picture of nozzle exit and surrounding acoustic enclosure	25
Figure 2.9 Picture showing the traverse and rail mount system in the aerodynamic measurement configuration.....	26
Figure 2.10 Schematic of flattened Pitot probe.....	27
Figure 2.11 Auspex AUHW-100 single wire probe	28
Figure 2.12 Hotwire mounting assembly schematic.....	29
Figure 2.13 Single sensor hotwire measurement system setup.....	29
Figure 2.14 Picture of TSI 1125 calibrator.....	30
Figure 2.15 Sennheiser KE 4-211-2 electret condenser microphone	31
Figure 2.16 Setup scheme for each microphone used in a given measurement.....	32
Figure 2.17 Schematic of desired microphone positioning	33
Figure 2.18 5 x 5 mm plot of measured surface of 40 grit sand paper roughness sample produced by MicroPhotonics Inc.	34
Figure 2.19 Integrated sound pressure levels measured in the acoustic enclosure at different jet exit speeds for the smooth wall	35
Figure 3.1 Vertical nozzle exit profiles taken just aft (38.1 mm) of the nozzle exit.....	40
Figure 3.2 Vertical nozzle exit profiles taken just aft (38.1 mm) of the nozzle exit.....	41
Figure 3.3 Nozzle exit profiles normalized on the nozzle height and nozzle exit velocity.....	42

Figure 3.4 Vertical nozzle exit profiles examining the uniformity of the nozzle exit flow; blue × corresponds to the nozzle centerline or $z = 0$; green × corresponds to a spanwise location $z = -305$ mm; red × corresponds to a spanwise location $z = +305$ mm.....	43
Figure 3.5 Horizontal nozzle exit velocity profile normalized on the nozzle exit velocity and the nozzle span, S	44
Figure 3.6 profiles normalized on U_0 and nozzle span, S , showing the variation with streamwise distance downstream.....	45
Figure 3.7 Horizontal profiles normalized on U_0 and nozzle span, S , showing the effect of nozzle exit velocity.....	45
Figure 3.8 Horizontal velocity profiles normalized on U_0 and S investigating the effect of variations in nozzle height, b	46
Figure 3.9 Vertical profiles showing the effect of spanwise position, z ; × symbols denote a streamwise profile location of $x = 953$ mm; □ symbols denote a streamwise profile location of $x = 1867$ mm.....	46
Figure 3.10 Normalized velocity profiles showing the effect of the spanwise position, z	47
Figure 3.11 Current normalized mean profiles compared with previous studies; the Abrahamsson et al. (1994) data (AJL) was taken at a jet Reynolds number of 10,000; the Wygnanski et al. (1992) data (WKH) was taken at a jet Reynolds number of 19,000.....	48
Figure 3.12 All measured profiles normalized on outer variables, U_m and $y_{1/2}$	49
Figure 3.13 Narasimha et al. (1973) proposed scaling showing the variation of U_m	50
Figure 3.14 Narasimha et al. (1973) proposed scaling showing the variation of $y_{1/2}$	51
Figure 3.15 Nondimensional vertical mean velocity profiles showing the effects of axial measurement location, x	51
Figure 3.16 The decay of the velocity maximum vs. downstream distance.....	52
Figure 3.17 Measured wall jet maximum velocities vs. estimated values for all test cases.....	53
Figure 3.18 Measured $y_{1/2}$ values vs. estimated values for all test cases.....	54
Figure 3.19 Nondimensional boundary layer length scales vs. x/b for.....	55
Figure 3.20 Nondimensional boundary layer length scales vs. x/b for all test cases seen above viewed tighter.....	55
Figure 3.21 Measured length scale values compared with the boundary layer thickness.....	56
Figure 3.22 Measured boundary layer length scales vs. the estimated length scales.....	57
Figure 3.23 Normalized wall jet profiles showing the effects of varying Re_j and the streamwise distance downstream of the nozzle exit.....	57
Figure 3.24 Normalized wall jet profiles showing the effects of varying the initial flow conditions while holding the ratio of nozzle exit and streamwise distance Reynolds numbers constant.....	59
Figure 3.25 Measured boundary layer length scales for test cases where the ratio of nozzle exit and streamwise distance Reynolds numbers is held constant but the initial flow conditions are varied.....	59
Figure 3.26 Turbulence profiles normalized on outer scaling parameters; Abrahamsson et al. (1994) noted as AJL and Eriksson et al. (1998) noted as EKP.....	60
Figure 3.27 All turbulence profiles from current study normalized on outer scaling parameters.....	61
Figure 3.28 Normalized turbulence profiles investigating the effects of axial position.....	62
Figure 3.29 Normalized turbulence profiles of varying nozzle exit velocity at two streamwise locations.....	62

Figure 3.30 Normalized Normal stress profiles showing the effects of varying the initial flow conditions while holding the ratio of nozzle exit and streamwise distance Reynolds numbers constant.....	63
Figure 3.31 Wall jet and turbulent boundary layer turbulence intensity profile comparison; $Re_\delta = 84000$ for Klebanoff (1955) data.....	64
Figure 3.32 Wall jet profiles normalized on outer variables.....	65
Figure 3.33 Skin friction predictions of George et al. (2000), Bradshaw and Gee (1960) data fit, and Schultz and Grunow (1940) correlation.....	67
Figure 3.34 Clean plate mean velocity profiles compared with George et al. (2000) prediction.....	68
Figure 3.35 Comparison of wall jet profiles with TBL semilog region fit and George et al. (2000) fit.....	69
Figure 3.36 Comparison of all measured wall jet profiles with TBL semilog region and data fit from the current data.....	69
Figure 3.37 Turbulence profiles normalized on inner variables showing the effects of variations in the streamwise profile location.....	71
Figure 3.38 Turbulence profiles normalized on inner variables showing the effects of variations in the nozzle exit velocity.....	71
Figure 3.39 Turbulence profiles normalized on inner variables showing the effects of variations in the nozzle exit height.....	72
Figure 3.40 All measured smooth wall jet velocity spectra taken at δ^* , δ , $y_{1/2}$	73
Figure 3.41 All measured smooth wall jet velocity spectra taken at δ^* , δ , $y_{1/2}$ normalized on outer variables, U_m and $y_{1/2}$	74
Figure 3.42 All measured smooth wall jet velocity spectra taken at δ^* , δ , $y_{1/2}$ normalized on outer variables, u^* and $y_{1/2}$	75
Figure 3.43 All measured smooth wall jet velocity spectra taken at δ^* , δ , $y_{1/2}$ using the inner scaling presented in Ueda and Hinze (1975).....	76
Figure 3.44 Smooth wall jet dimensional velocity spectra and nondimensional velocity spectra scaled on U_m and $y_{1/2}$	77
Figure 3.45 Smooth wall velocity spectra with varying nozzle height, b	78
Figure 3.46 Smooth wall velocity spectra with varying nozzle height, x	78
Figure 3.47 Schematic of boundary layer flow encountering abrupt change in surface condition.....	83
Figure 3.48 Calculated outgoing flow characteristic for wall jet flow with $Re_j = 21000$ and $x/b=99$ (blue) along with schematic of incoming flow and roughness patch.....	85
Figure 3.49 Rough wall jet mean velocity profiles normalized on outer scaling variables.....	87
Figure 3.50 Rough wall jet mean velocity profiles normalized on outer variables near the wall.....	88
Figure 3.51 Rough wall jet mean velocity profiles (test condition A) normalized on outer variables showing the effects of patch length.....	89
Figure 3.52 Rough wall jet mean velocity profiles (test condition A) normalized on outer variables showing the effects patch length near the wall.....	89
Figure 3.53 Rough wall jet mean velocity profiles normalized on outer variables showing the effects of nozzle exit speed near the wall.....	90
Figure 3.54 Rough wall jet mean velocity profiles normalized on outer variables showing the effects of nozzle exit height near the wall.....	91

Figure 3.55 Turbulence profiles (test condition C) for wall jet flows with varying roughness sizes normalized on the outer variables, U_m and $y_{1/2}$	92
Figure 3.56 Turbulence profiles (test condition C) for wall jet flows with varying roughness sizes normalized on the outer variables, U_m and $y_{1/2}$ near the velocity maximum and below	92
Figure 3.57 Turbulence profiles (test condition A) of rough wall jet flows with varying roughness patch length compared with smooth wall jet profiles normalized on the outer variables, U_m and $y_{1/2}$	93
Figure 3.58 Turbulence profiles of varying nozzle exit velocities for smooth and rough wall jet flows normalized on the outer variables, U_m and $y_{1/2}$	94
Figure 3.59 Turbulence profiles (test condition A) of varying nozzle height for smooth and rough wall jet flows normalized on the outer variables, U_m and $y_{1/2}$	95
Figure 3.60 Rough and smooth wall jet flow U_m (measured vs. smooth wall estimations)	97
Figure 3.61 Rough and smooth wall jet flow $y_{1/2}$ (measured vs. smooth wall estimations).....	97
Figure 3.62 Rough and smooth wall jet flow δ (measured vs. smooth wall estimations)	97
Figure 3.63 Rough and smooth wall jet flow δ^* (measured vs. smooth wall estimations).....	98
Figure 3.64 Rough and smooth wall jet flow θ (measured vs. smooth wall estimations)	98
Figure 3.65 Normalized U_m as a function of normalized RMS roughness height	99
Figure 3.66 Normalized $y_{1/2}$ as a function of normalized RMS roughness height.....	99
Figure 3.67 Normalized δ as a function of normalized RMS roughness height	99
Figure 3.68 Normalized δ^* as a function of normalized RMS roughness height.....	100
Figure 3.69 Normalized θ as a function of normalized RMS roughness height	100
Figure 3.70 Nondimensional boundary layer thickness vs. k_{rms} (test conditions A – E).....	101
Figure 3.71 δ^* for smooth and rough wall jet flows (measured vs. smooth wall estimation)	102
Figure 3.72 Measured U_m vs. smooth wall estimation for varying roughness patch lengths.....	103
Figure 3.73 Measured δ vs. smooth wall estimation for varying roughness patch lengths	103
Figure 3.74 Measured δ^* vs. smooth wall estimation for varying roughness patch lengths	104
Figure 3.75 Normalized boundary layer thickness vs. normalized distance from the nozzle exit; (red: 40 Grit test cases, blue: 180 Grit test cases, black: smooth wall test cases).....	104
Figure 3.76 Normalized displacement thickness vs. normalized distance from the nozzle exit; (red: 40 Grit test cases, blue: 180 Grit test cases, black: smooth wall test cases).....	105
Figure 3.77 Dimensionless δ^* vs. dimensionless downstream distance for rough wall flow	106
Figure 3.78 Dimensionless θ vs. dimensionless downstream distance for rough wall flow.....	106
Figure 3.79 Measured vs. estimated δ^* for rough wall jet flows	107
Figure 3.80 Measured vs. estimated θ for rough wall jet flows	108
Figure 3.81 Skin friction coefficient estimate for rough wall jet flows.....	110
Figure 3.82 Skin friction estimates vs. nominal sand grain size.....	111
Figure 3.83 Rough wall jet profiles in inner coordinates	112
Figure 3.84 Nominal and equivalent sand grain roughness size comparison.....	113
Figure 3.85 Normal stress profiles in inner coordinates showing the effect of roughness size	113
Figure 3.86 Normal stress profiles in inner coordinates showing the effect of patch length	114
Figure 3.87 All measured smooth wall jet velocity spectra taken at δ^* , δ , $y_{1/2}$	115

Figure 3.88 All measured rough wall jet velocity spectra taken at δ^* , δ , $y_{1/2}$ normalized on outer variables, U_m and $y_{1/2}$	116
Figure 3.89 All measured rough wall jet velocity spectra taken at δ^* , δ , $y_{1/2}$ using the inner scaling presented in Ueda and Hinze (1975)	116
Figure 3.90 Dimensional rough wall jet velocity spectra of varying k_g at δ^* , δ , and $y_{1/2}$ (left to right)	117
Figure 3.91 Rough wall jet velocity spectra scaled on U_m and $y_{1/2}$ at δ^* , δ , and $y_{1/2}$ (left to right)	118
Figure 3.92 Rough wall jet spectra scaled on u^* and δ^* at δ^* , δ , and $y_{1/2}$ (left to right)	118
Figure 3.93 All measured rough wall jet velocity spectra taken at δ^* , δ , $y_{1/2}$ scaled on u^* and δ^*	119
Figure 3.94 Rough wall velocity spectra scaled on U_m , u^* , and k_g	120
Figure 3.95 Dimensional rough wall velocity spectra at δ^* , δ , and $y_{1/2}$ (left to right) showing effects of variations in U_o	120
Figure 3.96 Dimensional rough wall velocity spectra at δ^* , δ , and $y_{1/2}$ (left to right) showing effects of variations in b	121
Figure 3.97 Dimensional rough wall velocity spectra at δ^* , δ , and $y_{1/2}$ (left to right) showing effects of variations in roughness patch length.....	121
Figure 3.98 Smooth and rough wall jet velocity spectra.....	123
Figure 3.99 Velocity spectra scaled on U_m and $y_{1/2}$ at δ^* , δ , and $y_{1/2}$ (left to right)	123
Figure 3.100 Velocity spectra taken at δ^* scaled on U_m and δ^* , δ , and $y_{1/2}$ (left to right).....	124
Figure 3.101 Velocity spectra scaled on u^* and δ^* and $y_{1/2}$ (left to right).....	125
Figure 4.1 Picture of microphone calibration setup	128
Figure 4.2 Magnitude calibration for a typical measurement microphone; M_{cal} is the magnitude of the calibration for microphone fitted with a 0.25 mm pinhole	129
Figure 4.3 Magnitude calibrations for measurement microphones used in the current study	130
Figure 4.4 Smoothed and original calibration comparison.....	131
Figure 4.5 Original and current microphone pinhole calibrations.....	132
Figure 4.6 Original and high frequency smoothed calibrations for current measurement microphone calibration	132
Figure 4.7 Clean plate surface pressure trusted reference test case	133
Figure 4.8 Effects of microphone height relative to Nylon bushing.	134
Figure 4.9 Effects of microphone bushing assembly height relative to aluminum plate.	134
Figure 4.10 Calibrations for microphones with varying pinhole diameter	136
Figure 4.11 Smooth wall surface pressure spectra at nozzle exit speeds of 20, 40 and 60 m/s	137
Figure 4.12 Microphone installation schematic showing microphone positioning relative to the pre-punched holes in the roughness patches	139
Figure 4.13 Microphone height variation test; clean plate surface pressure spectra	140
Figure 4.14 Installation variation at constant microphone height surface pressure spectra; microphone heights were $2.05k_g$ below the tops of the roughness (top plot) and $0.85 k_g$ below the tops of the roughness (bottom plot).....	141
Figure 4.15 Smooth wall surface pressure spectra taken at $x = 1302$ mm over a range of nozzle exit speeds	144
Figure 4.16 Surface pressure spectra scaled on inner variables (v/u^* , u^* , and τ_w).....	145

Figure 4.17 Smooth wall surface pressure spectra scaled on outer variables (δ , U_m , and τ_w)	147
Figure 4.18 Smooth wall surface pressure spectra scaled on outer variables (δ , U_m , and Q_m)	147
Figure 4.19 Smooth wall jet surface pressure spectra compared with Chase-Howe model for turbulent boundary layer surface pressure spectra	148
Figure 4.20 Smooth wall jet surface pressure spectra compared with Goody (2004) empirical model for turbulent boundary layer surface pressure spectra	150
Figure 4.21 Smooth wall surface pressure spectra taken at $x = 1302$ mm (foremost microphone measurement position)	151
Figure 4.22 Smooth wall surface pressure spectra taken at $x = 1505$ mm (aft most microphone measurement position)	152
Figure 4.23 Smooth wall surface pressure spectra taken at varying x locations	153
Figure 4.24 Smooth wall surface pressure spectra taken at varying x locations	153
Figure 4.25 Smooth wall surface pressure spectra taken at varying x locations	154
Figure 4.26 Smooth wall surface pressure spectra taken at varying x locations scaled on outer and inner variables (top and bottom, respectively)	155
Figure 4.27 Surface pressure microphone setup (dimensions in mm)	157
Figure 4.28 Dimensional surface pressure spectra at $x = 1302, 1403,$ and 1505 mm (top to bottom, respectively)	158
Figure 4.29 40 grit surface pressure spectra normalized on inner variables (v/u^* , u^* , and τ_w) at $x = 1403$ mm	159
Figure 4.30 Smooth (blue) and 40 grit (red) surface pressure spectra normalized on inner variables (v/u^* , u^* , and τ_w) taken at the same range of initial flow conditions and x microphone locations (1403 mm)	160
Figure 4.31 40 grit surface pressure spectra normalized on outer variables (δ , U_m , and τ_w) at $x = 1403$ mm	160
Figure 4.32 Smooth (blue) and 40 grit (red) surface pressure spectra normalized on outer variables (δ , U_m , and τ_w) taken at the same initial flow conditions and x microphone locations (1403 mm)	161
Figure 4.33 40 grit surface pressure scaled on (k_{rms} , u^* , and τ_w) as suggested by Blake (1970)	162
Figure 4.34 40 grit surface pressure spectra scaled on (k_s , u^* , and τ_w) and divided by the skin friction coefficient, C_f , as suggested by Aupperle and Lambert (1970)	163
Figure 4.35 40 grit surface pressure spectra at constant initial flow conditions and varying microphone location	164
Figure 4.36 40 grit surface pressure spectra at constant initial flow conditions and varying microphone location scaled on inner (v/u^* , u^* , and τ_w) and outer (δ , U_m , and τ_w) variables (top and bottom, respectively)	165
Figure 4.37 40 grit surface pressure spectra at constant initial flow conditions and varying location scaled on roughness variables (k_{rms} , u^* , and τ_w) and (k_s , u^* , and τ_w) variables proposed by Blake (1970) and Aupperle and Lambert (1970) (top and bottom, respectively)	166
Figure 4.38 40 grit surface pressure spectra at constant initial flow conditions and varying microphone location	167

Figure 4.39 Dimensional surface pressure spectra at $x = 1302, 1403,$ and 1505 mm (top to bottom, respectively).....	168
Figure 4.40 180 grit surface pressure spectra normalized on inner variables ($v/u^*, u^*,$ and τ_w) at $x = 1403$ mm	169
Figure 4.41 Smooth (blue) and 180 grit (red) surface pressure spectra normalized on inner variables ($v/u^*, u^*,$ and τ_w) taken at the same initial flow conditions and x microphone locations (1403 mm)	169
Figure 4.42 180 grit surface pressure spectra normalized on outer variables ($\delta, U_m,$ and τ_w) at $x = 1403$ mm	170
Figure 4.43 Smooth (blue) and 180 grit (red) surface pressure spectra normalized on outer variables ($\delta, U_m,$ and τ_w) taken at the same initial flow conditions and x microphone locations (1403 mm)	171
Figure 4.44 180 grit surface pressure scaled on ($k_{rms}, u^*,$ and τ_w) as suggested by Blake (1970)	171
Figure 4.45 180 grit surface pressure spectra scaled on ($k_s, u^*,$ and τ_w) and divided by the skin friction coefficient, C_f , as suggested by Aupperle and Lambert (1970)	172
Figure 4.46 180 grit surface pressure spectra at constant initial flow conditions and varying microphone location	172
Figure 4.47 180 grit surface pressure spectra at constant initial flow conditions and varying microphone location scaled on inner ($v/u^*, u^*,$ and τ_w) and outer ($\delta, U_m,$ and τ_w) variables (top and bottom, respectively).....	173
Figure 4.48 180 grit surface pressure spectra at constant initial flow conditions and varying microphone location scaled on roughness variables ($k_{rms}, u^*,$ and τ_w) and ($k_s, u^*,$ and τ_w) proposed by Blake (1970) and Aupperle and Lambert (1970) (top and bottom, respectively)	174
Figure 4.49 Surface pressure spectra for wall jet flow with constant initial flow conditions over rough patches 305 mm long of varying roughness heights	175
Figure 4.50 A closer look at the surface pressure spectra for wall jet flow with constant initial flow conditions over rough patches 305 mm long of varying roughness heights in the low to mid frequency range	176
Figure 4.51 Surface pressure spectra for wall jet flow with constant initial flow conditions over rough patches 305 mm long of varying roughness heights at 3 streamwise microphone measurement locations.	177
Figure 4.52 Surface pressure spectra for wall jet flow with varying nozzle exit velocity over rough patches of varying roughness heights at the center microphone measurement location ($x = 1403$ mm)	178
Figure 4.53 Surface pressure spectra of wall jet flows having constant initial flow conditions and varying rough surface sizes scaled on outer variables ($\delta, U_m,$ and τ_w)	179
Figure 4.54 Surface pressure spectra of wall jet flows having constant initial flow conditions and varying rough surface sizes scaled on inner variables ($v/u^*, u^*,$ and τ_w).....	179
Figure 4.55 Surface pressure scaled on ($k_{rms}, u^*,$ and τ_w) as suggested by Blake (1970) for test cases with constant initial flow conditions and varying roughness size	180
Figure 4.56 Surface pressure spectra scaled on ($k_s, u^*,$ and τ_w) and divided by the skin friction coefficient, C_f , as suggested by Aupperle and Lambert (1970) for test cases with constant initial flow conditions and varying roughness size	181

Figure 4.57 Surface pressure scaled on $(k_{rms}, u^*, \text{ and } \tau_w)$ as suggested by Blake (1970) for test cases with varying roughness size at $U_o = 20, 40, \text{ and } 60 \text{ m/s}$ (red, blue, and black, respectively)..... 182

Figure 4.58 Surface pressure spectra scaled on $(k_s, u^*, \text{ and } \tau_w)$ and divided by the skin friction coefficient, C_f , as suggested by Aupperle and Lambert (1970) for test cases with varying roughness size at $U_o = 20, 40, \text{ and } 60 \text{ m/s}$ (red, blue, and black, respectively)..... 182

Figure 4.59 Empirical scaling of surface pressure spectra taken at 40 grit test cases of varying nozzle exit velocity..... 185

Figure 4.60 Empirical scaling of surface pressure spectra taken at 180 grit test cases of varying nozzle exit velocity..... 185

Figure 4.61 Empirical scaling of surface pressure spectra taken at 40 grit test cases of varying microphone measurement position and constant initial flow conditions of $U_o = 60, 40, \text{ and } 20 \text{ m/s}$ (top to bottom)..... 186

Figure 4.62 Empirical scaling of surface pressure spectra taken at constant initial flow conditions and varying surface roughness 188

List of Tables

Table 1.1 List of notable smooth and rough wall jet flow studies	3
Table 2.1 Measured and estimated roughness parameters	34
Table 2.2 Uncertainties in measured quantities in current study	36
Table 2.3 Uncertainties in calculated or estimated quantities	37
Table 3.1 Smooth wall jet conditions for velocity profile measurements	39
Table 3.2 Rough wall jet flow test cases	81
Table 4.1 Range of flow conditions for the smooth wall surface pressure measurements at microphone measurement position #1 ($x = 1302$ mm).....	142
Table 4.2 Range of flow conditions for the smooth wall surface pressure measurements at microphone measurement position #5 ($x = 1505$ mm).....	143
Table 4.3 Microphone position numbers and corresponding locations for smooth wall tests.....	143

1 Introduction and Problem Description

1.1 Motivation

Wall jet flows are quite common in engineering applications. Examples include cooling jets over turbo-machinery components and sluice gate flows. A more recent use for wall jets has come in the realm of aeroacoustics by Grissom (2007) and Grissom *et al.* (2006). In these studies a wall jet flow over a patch of roughness is used because the wall jet flow offered a flow configuration where acoustic measurement equipment could be mounted outside of the flow, and the flow could be exhausted into an acoustically treated environment. Both of these considerations combined to yield a higher signal to noise ratio than that found in conventional flow facilities that generate conventional boundary layer flows. However, the wall jet flow is not as well studied or documented as the ordinary turbulent boundary layer flow, particularly as it relates to surface pressure fluctuations or to the presence of surface roughness.

1.2 Wall Jet Physical Description

Launder and Rodi (1981) defined a wall jet as “a shear flow directed along a wall where, by virtue of the initially supplied momentum, at any station, the streamwise velocity over some region within the shear flow exceeds that of the free stream”. Schwartz and Cosart (1960) define a wall jet as “a jet of fluid which impinges onto a wall at an angle from 0 to 90 degrees”, and note that the wall jet flow is a member of a class of self preserving flows such as jets, wakes, and free mixing layers. These definitions allow for the possibility of some external stream of fluid into which momentum is added. In the case of the current work, the flow is known as a plane turbulent wall jet in still air. In this flow, the jet exhausts over a plane wall from a nozzle into the undisturbed laboratory environment. The jet exhaust is parallel to the wall surface yielding an angle of impingement of 0 degrees. In Figure 1.1 below, one can see a simple schematic of the wall jet flow. Flow from the nozzle exit is exhausted into the still air of the laboratory creating a shear layer between the high momentum fluid exiting the nozzle and the fluid at rest in the lab. As this shear layer develops with downstream distance, the still fluid environment is entrained by the shear layer forming a mixing layer that begins to extend downward into the exhausted jet fluid. A boundary layer between the plate and the fluid exiting the nozzle is also formed, and as the flow develops downstream, both the mixing shear layer and the boundary layer grow and approach one another. At some point downstream of the nozzle exit the two meet and the wall jet flow becomes what is considered to be fully developed. Narasimha *et al.* (1973) suggest that this distance downstream is on the order of 30 times the height of the nozzle slot for a uniform nozzle flow. A study by Hall and Ewing (2005) provides experimental data to suggest that the flow becomes fully developed at between 20 and 25 times the nozzle exit height downstream of the nozzle exit of uniform slot height. In Figure 1.1 below, U_o denotes the nozzle exit velocity, b denotes the nozzle exit height, U_m is the maximum velocity in the streamwise

direction at any given x (streamwise distance aft of the nozzle exit) location, δ (the height of the velocity maximum above the plate) is taken to be the boundary layer thickness (this will be discussed in more detail below), and $y_{1/2}$ is the height above the plate at which the streamwise velocity decreases from the velocity maximum to half the maximum velocity, U_m .

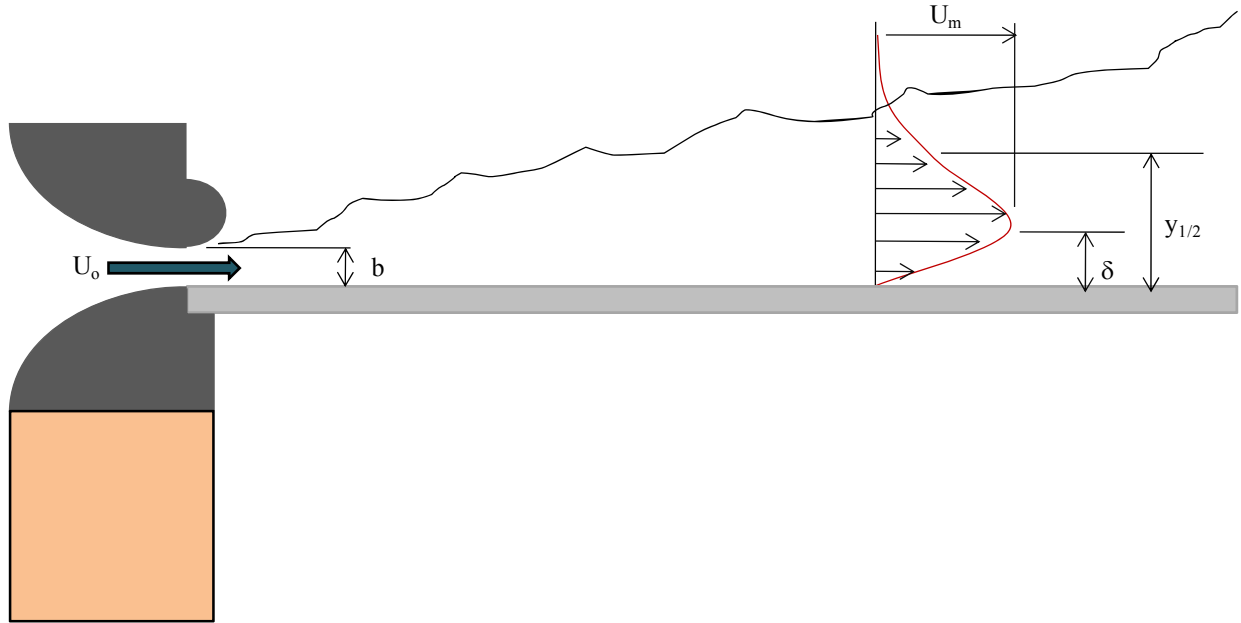


Figure 1.1 *Schematic of the wall jet flow employed in the current test facility*

The fully developed wall jet flow propagates downstream and spreads causing δ to increase as well as $y_{1/2}$. It is believed that the turbulent structures spawned by the mixing shear layer extend well down below the velocity maximum affecting the mean flow and turbulent characteristics of this boundary layer flow.

1.3 Review of Previous Work

1.3.1 Wall Jet Review

1.3.1.1 *Wall Jet Experimental Study Overview*

Wall jets have been extensively studied over the years. This is most likely due to the fact that wall jet type flows occur so often in nature and in engineering applications. Another reason for the widespread study of wall jets could be that in spite of all of the studies designed to understand wall jet flows, there has historically been disagreement amongst various workers on how to scale the wall jet and, particularly, on the estimation of the skin friction. To date, relatively little has been done in the way of studies of rough wall jet flows, and what little has been done is limited in the variation of roughness type or in the range of jet Reynolds numbers tested. The flow conditions for several wall jet studies of note (for both smooth and rough wall jets) are compiled in Table 1.1 below. This table contains the nozzle exit dimensions (b is the nozzle height, and S is the nozzle span), nozzle exit Reynolds number, Re_j , the local Reynolds number based on δ , Re_δ , the distance of the measurements from the nozzle exit normalized on the

nozzle exit height, and comments of interest regarding the studies listed. All listed smooth and rough wall cases are studies of plane turbulent wall jets in a still fluid environment with the angle between the jet and the flow surface set at zero degrees. Several of the more recent studies were conducted in open flume type test facilities, and thus, there is a free surface some distance above the flow surface. These studies are noted in the table below. The nominal roughness size, k , for the rough wall jet studies is also included.

Study Reference	b (mm)	S (mm)	Re_j ($\times 10^3$)	Re_δ ($\times 10^3$)	x/b	k (mm)	Comments
Smooth Wall							
Förthmann (1934)	30	65	53	14.7 - 19	3 - 33		Earliest known wall jet work
Sigalla(1958)	8	132	20 - 40		4 - 70		
Bradshaw and Gee (1960)	0.46		6.08	2.88 - 12.5	339 - 1459		
Schwarz and Cosart (1961)	25.4	610	13.5, 20, 30, and 41.6		29 - 85		
	6	900	11, 18, and 25	4.9 - 7.4, 6.9 10.9 8.8 - 14.4	33 - 209		
Tailland and Mathieu (1967)							
Wyganski et al. (1992)	0 - 10	600	3 - 30		30 - 140		
Eriksson et al. (1998)	9.6	1450	9.60		5 - 200	LDA data taken in open flum type facility	
Tachie et al. (2002)	10	788	7.5 - 14	2.7 - 7.7	0 - 100	LDA data taken in open flum type facility	
Rough Wall							
Rajaratnam (1967)	20 - 53.6		19.4 - 102		5 - 68	1 - 11	LDA data in open flume type facility
Hogg et al. (1996)	20 - 53.6		19.4 - 102		5 - 68	1 - 11	Data from Rajaratnam (1967)
Tachie et al. (2004)	6 - 10	800	5.9 - 12.5		20 - 80	1.2	LDA data in open flume type facility
Ead and Rajaratnam (2004)	25.4 - 50.8	446	76 - 143		2 - 60	12.7	LDA data in open flume type facility

Table 1.1 List of notable smooth and rough wall jet flow studies

These are some of the notable studies of wall jet flows conducted over the years. This is not by any means a complete list of previous studies, but this list contains most of the experimental studies found to be of interest in the current work. A formal review of the available wall jet literature will be given below.

1.3.1.2 *The Beginning*

The first work conducted on wall jet flows appears to have been done by Förthman (1936). However, as noted earlier, Glauert (1956) was the first to use the name “wall jet”. Very early on, workers approached the wall jet problem with the hope that a similarity solution could be identified to describe the entire flow. Glauert (1956) was the first worker to realize that the entire plane turbulent wall jet flow cannot conform to a single similarity solution. He divided the flow into two regions, an inner and an outer region, that were defined to be the region of the flow below the local maximum velocity of the wall jet and the region above the local maximum. Later authors have questioned Glauert’s (1956) point of separation between the inner and outer regions, but the fact remains that he was the first to propose such a separation.

1.3.1.3 *The Outer Layer*

In 1960, Schwarz and Cosart published a study on plane, turbulent, incompressible wall jets. This study states that the wall jet flow can be correlated by a single velocity scale, U_m , and by a single length scale, δ , over the entire range of conditions tested. This choice of length scale and velocity scale on which to normalize the velocity profiles is very similar to the length and velocity scales that are used in nearly all other subsequent major studies to collapse the velocity

profiles in the outer region. In fact, work done by Launder and Rodi (1981), Wygnanski *et al.* (1992), George *et al.* (2000), and numerous others shows that a velocity scale of U_m and a length scale of $y_{1/2}$ collapse the mean velocity profiles of a wall jet flow very well, and it is only upon very close inspection of profiles near the wall that one can see that this scaling does not apply to the wall jet flow everywhere. The length scale, $y_{1/2}$, has been commonly used for over 4 decades, and while this length scale varies from the length scale, δ , which was proposed by Schwarz and Cosart (1960) the results show the same behavior of the velocity profiles. This suggests that the variation of the boundary layer thickness and that of $y_{1/2}$ with variations in flow conditions are the same and that the two are proportional to one another.

While the works of many who have studied wall jets adopt the length and velocity scales mentioned above, most only show experimental data to support the use of these scales. However, a study by George *et al.* (2000) rigorously shows that these scales can be considered to be correct length and velocity scales on which to normalize wall jet outer flows. George *et al.* (2000) employ the asymptotic invariance principle in order to determine the scaling laws for wall jets. The asymptotic invariance principle as defined by George (1995) can be described as follows. In the governing equations for wall jets, there are terms that are Reynolds number dependent but are neglected. These terms are really only absent when the Reynolds number approaches infinity. This means that the solutions to the full governing equations are also Reynolds number dependent and only lose this dependency when the Reynolds number is infinite. George *et al.* (2000) starts with the equation of motion and boundary conditions appropriate to a plane wall jet with constant properties at high Reynolds number given by Irwin (1973):

$$U \frac{\partial U}{\partial x} + V \frac{\partial V}{\partial y} = \frac{\partial}{\partial y} [\langle -uv \rangle + v \frac{\partial U}{\partial y}] - \left\{ \frac{\partial}{\partial x} [\langle u^2 \rangle - \langle v^2 \rangle] \right\} \quad (1.1)$$

where $U \rightarrow 0$ as $y \rightarrow \infty$ and $U = 0$ as $y = 0$. Irwin obtained this equation by integrating the y momentum equation across the boundary layer. This is the same equation that governs the plane free jet and the turbulent boundary layer with no pressure gradient, but the boundary conditions vary for these flows. George *et al.* (2000) chooses to omit the normal stresses in equation 1.1 stating that they are negligible to second order. When this is done, equation 1.1 reduces to

$$U \frac{\partial U}{\partial x} + V \frac{\partial V}{\partial y} = \frac{\partial}{\partial y} [\langle -uv \rangle] \quad (1.2)$$

where $U \rightarrow 0$ as $y \rightarrow \infty$ for the outer region and

$$0 = \frac{\partial}{\partial y} [\langle -uv \rangle + v \frac{\partial U}{\partial y}] \quad (1.3)$$

where $U = 0$ when $y = 0$ at the wall. George *et al.* (2000) also states that the neglected terms in both of the above equations vanish identically only in the limit of infinite Reynolds number. George *et al.* (2000) applies the asymptotic invariance principle to equations 1.2 and 1.3 above for wall jet flows, and then solutions were searched for that reduced to full similarity solutions in the limit of an infinite Reynolds number. These solutions were sought for the inner layer and for the outer layer. This analysis yields the appropriate scaling parameters for both finite and infinite Reynolds number cases. For the outer region these parameters are found to be U_m and

$y_{1/2}$. The only difference is that for the finite Reynolds number cases (which are all real physical cases) the length and velocity scales are dependent on the Reynolds number. This result is not unexpected as other workers such as Wygnanski *et al.* (1992) and Narasimha *et al.* (1973) show a Reynolds number dependence for the outer scaling parameters when they present their scaling on the jet momentum.

Several of the major studies have also proposed length and velocity scales to normalize the normal stress profiles. Launder and Rodi (1981), Eriksson *et al.* (1998), and George *et al.* (2000) among others all propose the use of U_m and $y_{1/2}$ as the velocity and length scales, respectively, for normalizing the normal stress profiles. Agreement between studies is rather poor, and Launder and Rodi (1981) show little collapse of the experimental data that they collected from other studies. Eriksson *et al.* (1998) show reasonable collapse of the longitudinal normal stress profiles and fair agreement with the previous study of Abrahamsson *et al.* (1994). The lateral normal stress profiles normalized on the proposed outer variables collapsed as well, but did not agree with the Abrahamsson *et al.* (1994) study. George *et al.* (2000) who present the data of Eriksson *et al.* (1998) and Abrahamsson *et al.* (1994) do not compare these results with any past studies, but do show a very tight collapse of their longitudinal and lateral normal stress profiles on U_m and $y_{1/2}$.

1.3.1.4 *The Inner Layer*

Obtaining length and velocity scales for the outer region has not seemed to be much of a problem in past works. However, the ability of these outer length and velocity scales to scale the near wall portions of the wall jet flow has been shown to be lacking by Schwarz and Cosart (1960) and Wygnanski *et al.* (1992) to name a few. The question might be asked, what are the length and velocity scales associated with the inner region and what is the extent of this inner region? Schwarz and Cosart (1960) showed variation in the normalized profiles very near the wall, but they could not discern any systematic variation. They determined that the outer scales held down to y/δ equal to 0.005. They also make mention of the fact that velocity in the inner layer (Schwarz and Cosart (1960) defined the inner layer to be the region between the wall and the maximum velocity) was considered to vary as the classic one-seventh power of the distance from the wall by the very early pioneers of wall jet studies, Förthman (1934), Glauert (1956), and Sigalla (1958). Schwarz and Cosart (1960) experimentally determined the power to be $1/(14 \pm 1)$, and that this power holds from y/δ equal to 0.01 to 0.13. Förthman (1934), Glauert (1956), and Sigalla (1958) all considered the wall jet inner layer to be analogous to that of a classical turbulent boundary layer. This explains their use of the one-seventh power in their descriptions of the wall jet inner layer. Schwarz and Cosart (1960) do not deal with the region of the flow heavily affected by viscosity. Wygnanski *et al.* (1992) show results that indicate that the distance above the wall at which the scaling applicability of the outer variables described above breaks down is much higher than that observed by Schwarz and Cosart (1960) showing small but noticeable deviations between the scaled wall jet flows out to near height of maximum velocity, δ . They suggest that there is some Reynolds number dependence on the scaling behavior of the near wall flow. This is later supported by the analysis of George *et al.* (2000).

Probably the most prevalent approach to dealing with the inner layer has been to attempt to deal with it in terms of a law of the wall type formulation. This approach has been especially common in the more recent papers. Wygnanski *et al.* (1992), Eriksson, *et al.* (1998), and George *et al.* (2000) all attempt to show that the wall jet behavior is, at least to some degree, like that of

a classical turbulent boundary layer, namely that it has a laminar sublayer region and a log law region:

$$U^+ = y^+ \quad (1.4)$$

for the laminar sublayer region and

$$U^+ = A \text{Log}(y^+) + B \quad (1.5)$$

for the semilog region. For classical turbulent boundary layers, A is usually taken to be equal to 5.6 and B is taken to be 4.9. When this approach is adopted, it necessitates that u^* , the friction velocity, is the appropriate velocity scale for the inner layer. These authors show a log law like behavior in their wall jet measurements and they also show that there is a laminar sublayer region in wall jet flows. However, when the U^+ vs. y^+ profiles are plotted, it is very clear from Wygnanski *et al.* (1992) and from Eriksson *et al.* (1998) that the constants associated with the wall jet profiles vary from the traditional turbulent boundary layer constants significantly and that these wall jet constants also vary amongst different wall jet studies. In fact, Eriksson *et al.* (1998) reports values of 2.44 and 5.0 for A and B , respectively while Wygnanski *et al.* (1992) reports values of A ranging from 3.9 to 4.75 and values of B ranging from 5.5 to 9.5.

Schwarz and Cosart (1960) noted some major differences between classical turbulent boundary layers and the inner region of wall jet flows that may account for these differences. First of all, the outer layer has a very intermittent character and this could affect the inner region. Secondly, the structure of the inner layer is likely modified by the turbulence and entrainment from the outer layer. Also, it is shown in various studies that the skin friction in a wall jet varies in a different way than that of a classical turbulent boundary layer and is also very difficult to measure or estimate correctly. If the skin friction measurements or estimates are not correct, then any attempt to scale the inner regions of wall jets on u^* will also be in error. Indeed, obtaining a reliable estimate or measurement for the skin friction seems to be the most difficult problem facing any of the previous studies and also appears to be one of the biggest sources of disagreement between studies. Methods for estimating or measuring the skin friction will be discussed in more detail below.

1.3.1.5 Wall Jet Parameter Relations

Even though wall jet flows have been shown to be difficult to describe entirely, the behavior of flow variables such as U_m , δ , $y_{1/2}$, etc. as functions of control variables like U_o , x , and b is greatly desired because wall jet flows have many engineering applications. Narasimha *et al.* (1973) proposed that after the wall jet flow has become fully developed (most workers consider this condition to be met at x/b equal to around 30) the details of the initial conditions are not relevant, but alternatively only a gross nozzle exit momentum parameter that is in some sense dynamically equivalent to the initial conditions is relevant. The authors propose that for a wall jet, the parameter of choice is the jet momentum scale, J , defined as follows:

$$J = U_o^2 b \quad (1.6)$$

Narasimha *et al.* (1973) show that U_m , δ , and $y_{1/2}$ are all functions of x and the jet momentum, and by fitting experimental data they come up with the following relations:

$$\frac{U_m v}{J} = A_u \left(\frac{Jx}{v^2} \right)^n \quad (1.7)$$

$$\frac{y_{1/2} J}{v^2} = A_y \left(\frac{Jx}{v^2} \right)^m \quad (1.8)$$

where x is the distance downstream of the origin at which the properties are to be calculated, A_u and A_y are found by Narasimha *et al.* (1973) to be 4.6 and 0.595, respectively, and n and m were found to be -0.506 and 0.91, respectively. Wygnanski *et al.* (1992) applied this momentum scaling to their data and found values of 0.557 and 9.246 for A_u and A_y and values of -0.428 and 0.804 for n and m . Wygnanski *et al.* (1992) note that the constants A_u and A_y are very dependent on the values chosen for n and m . Both Wygnanski *et al.* (1992) and Narasimha *et al.* (1973) plot the left hand side of equations 1.7 and 1.8 vs. what is in parentheses on the right hand side and show a good collapse of the data. They then used these plots to find suitable values of the constants and exponents in order to fit their data.

The use of the momentum scaling resulting in equations 1.7 and 1.8 is a quite useful result because by rearranging these equations, one can obtain an expression relating the maximum velocity and $y_{1/2}$ to the jet exit Reynolds number and the Reynolds number based on x . These expressions are as follows:

$$\frac{U_m}{U_o} \sim Re_j^{n+1} Re_x^n \quad (1.9)$$

$$\frac{y_{1/2}}{b} \sim Re_j^{m-2} Re_x^m \quad (1.10)$$

where x_o is the virtual origin location relative to the nozzle exit. Narasimha *et al.* (1973) also state that the boundary layer thickness is a constant multiple of $y_{1/2}$.

1.3.1.6 Combined Inner/Outer Layer Solutions

One of the more recent developments in wall jet work has been the work by George *et al.* (2000) toward defining an expression for a velocity profile over the entire inner and overlap regions. It is important to note that George *et al.* (2000) defines the inner region as $y^+ < 30$ unlike Schwarz and Cosart (1960) who consider everything below the velocity maximum as the inner region. George *et al.* (2000) used the asymptotic invariance principle discussed above to analyze the inner region of the wall jet flow and determined that the velocity scale was u^* . This agrees with the results of numerous other studies. However, George *et al.* (2000) reasoned that the similarity solutions that were obtained for the inner and outer regions had to be related in a region between the two regions. More than this, both the similarity solutions obtained for the inner and outer regions must describe the flow between the regions as long as the Reynolds number is finite. George *et al.* (2000) present a composite form of the overlap solutions derived in their work which is valid from $0 \leq y^+ \leq 300$, and it is as follows:

$$\frac{U}{u^*} = \left(y^+ + c_4 y^{+4} + c_5 y^{+5} \right) \exp(-d y^{+6}) + C_i y^{+\gamma} \left[1 + \gamma a^+ y^{+^{-1}} + \frac{1}{2} \gamma (\gamma - 1) a^{+2} y^{+^{-2}} \right] [1 - \exp(-d y^{+6})] \quad (1.11)$$

The derivation of this relation and those immediately following which were not trivial are explained in great detail in George *et al.* (2000) and will not be presented here. The crux of what they did was to use the asymptotic invariance principle to yield a scaling law for the overlap region of wall jets in the form of a power law. They then used a Taylor series expansion of the mean velocity very near the wall and also of the power law found for the overlap region in order to obtain equation 1.11 above. The constants c_4 and c_5 were experimentally determined by George *et al.* (2000). The damping parameter, d , was chosen to be equal to 8×10^{-8} and is responsible for the changeover from the portion of equation 1.11 above dominated by the inner region to the portion of this equation dominated by the overlap region. The constant a^+ is a parameter used for similar analyses of classical turbulent boundary layers and has been found to be approximately equal to -16. George *et al.* (2000) justifies the use of this parameter and others that will be presented below that are used in classical boundary layer analyses by presenting agreement in experimental data between the inner region flow for wall jet flows to that of ordinary turbulent boundary layer flows. The unknowns that are left are u^* , γ , and C_i . The latter two are Reynolds number dependent and must be calculated for a given flow. The friction velocity can be solved for using the following equation given by George *et al.* (2000) obtained from manipulation of the overlap region solutions that were derived:

$$\frac{u^*}{U_m} = \frac{C_o}{C_i} (D y_{1/2}^+)^{-\gamma} = \frac{C_{o\infty}}{C_{i\infty}} [D y_{1/2}^+]^{-\gamma_\infty} \exp[A/(\ln D y_{1/2}^+)^{\alpha}] \quad (1.12)$$

On the right hand side of this equation, one will notice several parameters that have not been discussed. The parameter, A , is a classical boundary layer parameter found by George and Castillo (1997) to be 2.9. The parameter, α , is also a boundary layer parameter determined by George and Castillo (1997) and was found to be 0.46. The parameters γ_∞ , D , and $C_{o\infty}$ were found to be 0.0362, 1.0, and 56.7 by George and Castillo (1997), and the parameter $C_{i\infty}$ was found to be 1.30 by fitting the overlap solutions to data obtained by Karlsson *et al.* (1993). All of these parameters were used by George *et al.* (2000) to test their composite expression for the velocity profile by applying these parameters to the data of Karlsson *et al.* (1993). With these parameters the friction velocity, u^* , can be solved for implicitly (because $y_{1/2}^+ = y_{1/2} u^* / \nu$) using the far right hand side and the far left hand side of equation 1.12. Once the friction velocity is obtained, the parameter, γ , can be solved for by:

$$\gamma = \gamma_\infty + \frac{\alpha A}{(\ln D y_{1/2}^+)^{1+\alpha}} \quad (1.13)$$

Then C_i can be solved for using the left hand side, and middle portions of equation 1.12. With these parameters solved for, equation 1.11 can be used to determine the velocity profile of the wall jet flow in the very near wall and overlap regions. This approach has been applied to experimental data by George *et al.* (2000) and the skin friction velocities obtained by this approach collapse the velocity profiles over a range of jet exit Reynolds numbers and conditions very well. More importantly, this collapse indicates a reliable way to obtain the friction velocity,

something that until these studies was difficult to accomplish. Previous attempts to obtain the skin friction velocity, and hence the skin friction, will be discussed in the section below.

1.3.1.7 *Other Skin Friction Correlations*

As mentioned above, George *et al.* (2000) has employed a method of obtaining the friction velocity. This is a relatively new approach and in the past other approaches have been used to obtain the skin friction. The importance of skin friction is vital because it has been established that the inner and overlap regions scale on the friction velocity. The work of Sigalla (1958) is referenced as the first study to attempt to tackle the skin friction problem. He obtained a measure of the skin friction as though the region below the velocity maximum were analogous to a classical turbulent boundary layer. Sigalla correlated his data as follows:

$$C_f = 0.0565(U_m \delta / \nu)^{-\frac{1}{4}} \quad (1.14)$$

which can be rearranged as done by Schwarz and Cosart (1960) to show that

$$C_f \propto (x)^{-0.111} \quad (1.15)$$

Schwarz and Cosart (1960) presented their result for the skin friction obtained from a momentum balance:

$$C_f = 1.109 \times 10^{-2} \quad (1.16)$$

Schwarz and Cosart claimed that the skin friction is independent of x and at worst varies very slightly with the jet Reynolds number. More recent studies seem to take the work of Sigalla (1958) as being useful, and some workers such as Hari (1973) actually employ equation 1.14 above to obtain the skin friction in their work.

Launder and Rodi (1981) present a thorough review of the attempts made to obtain reliable skin friction results. They state that because the skin friction coefficient, C_f , is such a minor contributor to the growth of the wall jet a momentum balance approach is not likely to yield plausible results. Launder and Rodi (1981) present results from several studies employing various methods to calculate the skin friction. One of the ways used to find the skin friction was to measure the velocity gradient in the viscous sublayer. This method was used by Tailland and Mathieu (1967) and the work of this particular study was also referenced in Wagnanski *et al.* (1992). Another method to obtain the skin friction was to use a Preston tube as done by Bradshaw and Gee (1960). Direct measurement techniques were also discussed, and results from Alcaraz (1977) were presented. These studies along with others were reviewed by Launder and Rodi (1981) and found to be only in reasonable agreement with one another. However, the data from Alcaraz (1977) and that of Bradshaw and Gee (1960) were in good agreement and the range of measurement position from the nozzle relative to the nozzle height varied greatly between the two studies. An empirical fit to the data of these two studies is given below

$$C_f = 0.0315 Re_m^{-0.182} \quad (1.17)$$

Eriksson *et al.* (1998) later proposed an empirical fit to their data of the same form as that in equation 1.17. Their skin friction relation was found to be

$$C_f = 0.0179Re_m^{-0.113} \quad (1.18)$$

Wyganski *et al.* (1992) present skin friction results obtained by measuring the slope of the velocity gradient near the wall, and their results are in fair agreement with those of Tailand and Mathieu (1967), and they provide their own skin friction relation

$$C_f = 2 \frac{U_o^2}{U_m^2} A_\tau Re_j^{k-2} Re_x \quad (1.19)$$

where A_τ was found to be 0.146 and the exponent k was determined to be -1.07.

1.3.1.8 *Effects of Roughness on the Wall Jet Flow*

Little work has been done on plane turbulent wall jet flows over rough surfaces. The bulk of what has been done deals with the erosion of the surfaces of flows below sluice gates. In 1967, Rajaratnam set out to conduct research on wall jet flows over surfaces with deterministic roughness patterns extending from the nozzle exit. Most of the roughnesses used were woven wire meshes or two-dimensional ridges of different types. The thickness of the wire meshes and ridges varied from 1.016 to 11.05 mm (ranging from 2% of the nozzle exit height to almost 53% of the nozzle height). The initial jet Reynolds number ranged from 19000 to 100000 and the measurement locations ranged from 2 to 60 times the nozzle height downstream of the nozzle exit. In this study, the author uses a “melted down” or average roughness height to describe the characteristic roughness length. Rajaratnam (1967) does show that the presence of roughness not only increases the boundary layer thickness, δ , but that it also increases its rate of change with x . Rajaratnam (1967) also shows that the wall jet flows over roughness do not obey the one-seventh power law for turbulent boundary layers and that there is a systematic variation of the velocity profiles in the region below the maximum velocity with the ratio of x to the nozzle height, b . Rajaratnam (1967) shows that while the maximum velocity for a smooth wall jet flow occurs at a $y/y_{1/2}$ of 0.16, the maximum occurs at $y/y_{1/2}$ equal to anywhere from 0.25 to 0.40 for rough wall jet flows depending on the roughness. Finally, the author proposes that the maximum velocity varies with the roughness height as follows

$$\frac{U_m}{U_o} = C - 0.54 \log \left(\frac{x}{k_e} \right) \quad (1.20)$$

where k_e is the melted down roughness height and C is an empirically determined constant that varies with the roughness condition. The author shows the results of plotting equation 1.20 along with experimentally collected maximum velocity data indicating that his hypothesis is correct. When examining wall jet flows submerged in shallow depths Ead and Rajaratnam (2004) choose to use the Nikuradse equivalent roughness to describe the rough surfaces used.

Ead and Rajaratnam (2004) showed that for a large surface roughness extending from the nozzle exit ($k/\delta \approx 1/12 - 1$ where k is the nominal roughness size), the wall jet profiles scaled on the standard U_m and $y_{1/2}$. However, $y/y_{1/2}$ value seen to correspond with the velocity maximum in this study was equal to 0.35 while that seen in smooth wall jet flows has been shown to be 0.14 – 0.16.

Hogg *et al.* (1996) have extended the Narasimha *et al.* (1973) parameter scaling and have developed a flow parameter scaling that accounts for the roughness size for wall jets over rough surfaces enabling a continuous interpolation of experimental data with changes in the streamwise distance from the nozzle proposing that

$$\frac{\delta}{b} = B_y \left(\frac{x}{b}\right)^n \left(\frac{b}{k}\right)^{2(n-1)} \quad (1.21)$$

where B_y and n are empirically determined constants and k is the roughness height. Hogg *et al.* (1996) assume that the flow is fully rough. They also assume that the dependence of δ/b and U_m/U_o are only dependent upon the downstream distance x/b and that the flow is governed by the initial momentum flux, J , and a measure of the turbulent viscosity which they propose to be $U_o k$ where k is the roughness length. Experimental results taken from the Rajaratnam *et al.* (1967) study mentioned above were presented by Hogg *et al.* (1996) scaled according to equation 1.21 demonstrating the ability to scale the boundary layer thickness on the roughness size, k .

Tachie *et al.* (2004) also tested a wall jet flow over a rough surface. They used 1.2 mm nominal diameter sand grains as the rough surface extending from the nozzle exit. The roughness Reynolds number ($k^+ = k_s u^* / \nu$) for the tests conducted ranged from 25 – 53. The jet exit Reynolds numbers ranged from 6000 to 12500. This study showed that the maximum velocity was slightly lower for rough wall cases than for smooth wall cases. This study also showed that the boundary layer thickness increases significantly when roughness was present, but that $y_{1/2}$ was not appreciably changed. Tachie *et al.* (2004) showed the normalized profiles on outer variables and showed that the $y/y_{1/2}$ value at which the maximum velocity occurred for the rough wall profiles was about 0.21 whereas for smooth wall jet flows this value was seen to be about 1.6. Tachie *et al.* (2004) then set out to investigate the inner region. They fit their rough wall data to the power law formulation proposed in George *et al.* (2000) below to fit their rough wall data in the overlap region and obtain values for C_i and γ .

$$U^+ = C_i (y^+ + a^+)^{\gamma} \quad (1.22)$$

George *et al.* (2000) used equation 1.22 along with a Taylor series expansion of the mean velocity in the laminar sublayer region to obtain equation 1.11. Noting that the skin friction coefficient, $C_f = 2(u^*/U_m)^2$, Tachie *et al.* (2004) used the results for C_i and γ to solve for the skin friction by using equation 1.12. Tachie *et al.* (2004) show that the skin friction coefficient is anywhere from 15% to 30% greater for the rough wall cases than for the smooth wall cases depending on the local Reynolds number, and the skin friction decreases with Reynolds number slower for the rough wall cases than for the smooth wall cases.

Dey and Sarkar (2005) attempt to deal with smooth wall jet flows encountering sudden changes in surface roughness. They provide an empirical relationship describing the behavior of the maximum velocity and the boundary layer thickness as a function of the streamwise distance downstream of the origin of the roughness given the flow conditions at this origin. They did not provide a detailed account of how the empirically determined constants and exponents were determined, and they did not present a data comparison to support their empirical relations. It was attempted to leverage this empirical method in the current study, but the scaling method proposed by Hogg *et al.* (1996) was determined to be more useful.

1.3.2 Wall Pressure Fluctuations Under Conventional Turbulent Boundary Layers

1.3.2.1 Overview

There have been no previous studies of wall pressure fluctuations under wall jet boundary layers with smooth or rough surfaces. For this reason prior work on wall pressure fluctuations under conventional two-dimensional flat plate ordinary turbulent boundary layers over a smooth and rough surface is reviewed in this section.

1.3.2.2 Smooth Wall Surface Pressure

The power spectral density spectrum of the pressure $\Phi(\omega)$ is of interest because it provides an indication of the energy contributed to the surface pressure fluctuations by turbulent eddies of varying sizes. Of particular interest is the scaling behavior of the spectral density. There are numerous studies investigating the surface pressure fluctuations under conventional turbulent boundary layer flows. The current review is by no means exhaustive, but instead makes extensive use of the reviews of Goody (2004) and Goody and Simpson (2002).

The surface pressure spectral density for conventional turbulent boundary layers has several features that should be noted. At very low frequencies ($< 100 - 200$), the spectral levels are highest and indicate the dominance of large turbulent eddies that are convected in the wake region of the boundary layer flow. As the frequency is increased, there begins to be seen a region where the spectral levels vary with a theoretical f^1 variation (experimental results show an approximate $f^{0.7}$ frequency variation) where the dominance of convected eddies in the log region of the flow is manifested in the spectrum. This region varies in its frequency extent depending on the Reynolds number of the flow. Finally, at high frequencies, the locally convected eddies near the wall in the viscous sublayer become dominant, and the spectral levels of the surface pressure begin to roll off and take on an f^5 variation. The spectral levels vary with the flow conditions of the turbulent boundary layer, but these regions of spectral behavior are always present.

Goody and Simpson (2000) provide a review of various spectral scaling attempts, and show comparison of data from several studies scaled in selected ways. The experimental data presented by Goody and Simpson (2000) range in Reynolds number based on the momentum thickness from 3400 to 23400. The data of Goody and Simpson (2000) along with the presented data from McGrath and Simpson (1987), Blake (1970), Farabee and Casarella (1991) among others, show good collapse at high frequencies when the spectra are normalized on inner boundary layer variables as follows:

$$\frac{\Phi(\omega)u^{*2}}{\tau_w^2\nu} \quad (1.23)$$

and the frequency is normalized as:

$$\frac{\omega\nu}{u^{*2}} \quad (1.24)$$

where ν/u^* is the length scale, u^* (the skin friction velocity) is the velocity scale, and τ_w is the wall shear stress. These scaling variables are shown by Goody and Simpson (2000) to scale the spectra in the high frequency region ($\frac{\omega\nu}{u^{*2}} > 0.15$) where the surface pressure spectra are dominated by smaller near wall turbulent eddy motions. They also show some collapse of the presented spectra in the frequency region between the very low and high frequencies and note that this region is considered to be an overlap region which will be discussed more below.

The scaling of the surface pressure spectra on outer variables with the intention of collapsing the low frequency spectral regions has also been a topic of interest. The choice of the length, velocity, and pressure scales vary from study to study. Goody and Simpson (2000) provide a review of the choices of these scales adopted by several studies and note that Blake (1970) and others use δ^* as a length scale, U_e (edge velocity) as a velocity scale, and Q_e (dynamic pressure at the edge of the boundary layer) as a pressure scale in an attempt to scale the low frequency pressure spectrum while other workers such as Farabee and Casarella (1991) have adopted δ , u_τ , and τ_w , as the outer length, velocity, and pressure scales, respectively. Goody and Simpson (2000) adopted the outer scaling variables used by Farabee and Cassarella (1991) so that the nondimensional spectrum is as follows:

$$\frac{\Phi(\omega)u^*}{\tau_w^2\delta} \quad (1.25)$$

and the frequency is normalized as:

$$\frac{\omega\delta}{u^*} \quad (1.26)$$

Goody and Simpson (2000) also note that of the eight possible scaling combinations from the outer length, velocity, and pressure scales noted above, none collapse the surface pressure spectra at very low frequencies ($\frac{\omega\delta}{u^*} < 50$). However, there is a spectral collapse in the frequency region between the low and high frequencies which was shown to exist between data taken from Goody and Simpson (2000) as well as from McGrath and Simpson (1987), Blake (1970), Farabee and Cassarella (1991) among others. This region of spectral collapse is considered to be the overlap region. Early workers such as Bradshaw (1967), and more recent workers such as Blake (1986) have proposed that there is an overlap region in the surface pressure spectrum of turbulent boundary layer flow at sufficiently high Reynolds number where the inner and outer scaling variables scale the pressure spectrum. This proposition is supported by data presented in both Blake (1986) and Goody and Simpson (2000).

Both the inner and outer variable spectral scalings mentioned above yield spectral collapse overlap region, and the inner scaling variables collapse the surface pressure spectra at high frequencies. The spectral variation with frequency of the normalized spectra in these regions is also of interest. Blake (1986) provides a theoretical discussion suggesting that the surface pressure spectrum should vary as ω^{-1} in the overlap region, and he goes on to suggest that the high frequency spectral character should vary with ω^{-5} . This high frequency variation is supported by all of the studies presented in Goody and Simpson (2000). However, the variation in the overlap region presented is not a variation with ω^{-1} . Goody (2004) notes that the experimentally determined frequency variation in the overlap region varies from $\omega^{-0.7}$ to $\omega^{-0.8}$

depending on the study. Goody (2004) also presents experimental data that shows that the extent of the overlap region is dependent on the Reynolds number.

Goody (2004) presents an empirical model for the surface pressure spectra. His model is based off of a model which he calls the Chase-Howe model. The Chase-Howe model given below was presented by Howe (1998) who attributes it to Chase (1980).

$$\frac{\Phi(\omega)U_e}{\tau_w^2\delta^*} = \frac{2\left(\frac{\omega\delta^*}{U_e}\right)}{\left[\left(\frac{\omega\delta^*}{U_e}\right)^2 + 0.0144\right]^{\frac{3}{2}}} \quad (1.27)$$

This model does not predict the high frequency variation with ω^{-5} that is seen in the experimental data and suggested theoretically by Blake (1986), but does reflect the ω^{-1} variation predicted for frequencies in the overlap region. The Goody (2004) empirical model seen below was designed to account for the $\omega^{-0.7}$ variation in the overlap region seen experimentally and also the ω^{-5} predicted and seen experimentally.

$$\frac{\Phi(\omega)U_e}{\tau_w^2\delta} = \frac{3.0\left(\frac{\omega\delta}{U_e}\right)^2}{\left[\left(\frac{\omega\delta}{U_e}\right)^{0.75} + 0.5\right]^{3.7} \left[(1.1R_T^{-0.57})\left(\frac{\omega\delta}{U_e}\right)\right]^7} \quad (1.28)$$

The parameter R_T is a ratio of inner to outer timescales:

$$\frac{\left(\frac{\delta}{U_e}\right)}{\left(\frac{\nu}{u_*^2}\right)} = \frac{\left(\frac{u_*\delta}{\nu}\right)}{\sqrt{\frac{c_f}{2}}} = R_T \quad (1.29)$$

Goody (2004) attributes Reynolds number effects on the surface pressure spectrum to this parameter. Notice that the edge velocity has been used for the velocity scale in both the Chase-Howe models and the Goody empirical model which differs from the outer scaling velocity adopted by Farabee and Cassarella (1991) and Goody and Simpson (2000) above. Also notice that the length scale for the Goody (2004) empirical model is taken to be the boundary layer thickness whereas the length scale used in the Chase-Howe model is taken to be the displacement thickness. Goody (2004) compares his model with experimental data from Farabee and Cassarella (1991) and with data from Blake (1970) and shows good agreement. The local Reynolds number based on the momentum thickness for these two studies varied by a factor of nearly 4 (3386 to 13200 from the Farabee and Cassarella (1991) data to the Blake (1970) data), and the timescale parameter, R_T , varied from 47.11 to 120.7 between the two studies. The agreement between the Goody (2004) model and the experimental data taken at different flow conditions would indicate that this empirical model is robust and predicts the surface pressure spectrum for turbulent boundary layer flows quite well. The Goody (2004) model for a range of the timescale parameter (R_T) values is shown in Figure 1.2 below.

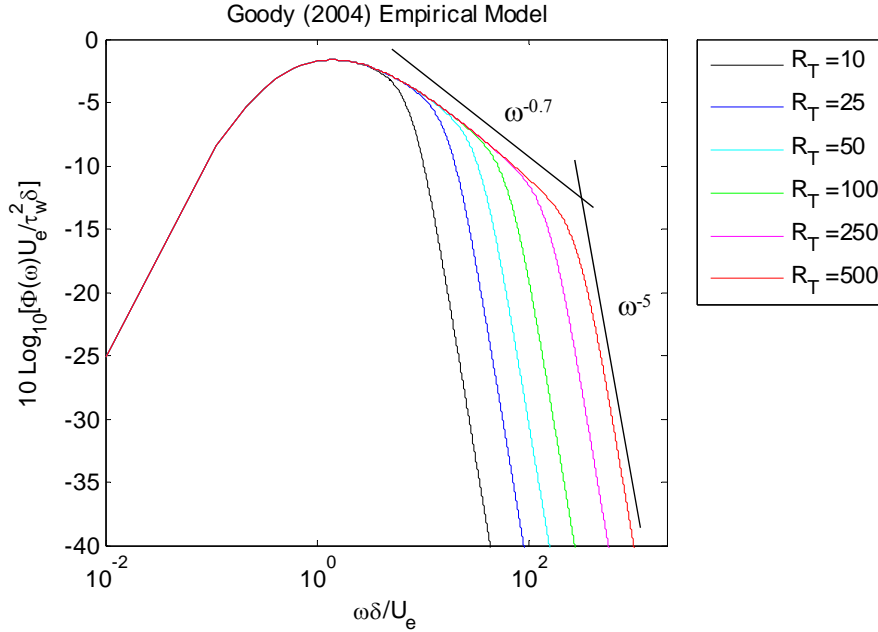


Figure 1.2 Goody empirical model for the surface pressure spectrum for a range of timescale parameters.

Notice that the region in which there is a $\omega^{-0.7}$ variation is the overlap region, and at high frequencies, the predicted spectrum has a ω^{-5} variation. Also notice that as the timescale parameter increases (this corresponds to an increase in local Reynolds number) the extent of the overlap region increases as well showing the ability of the Goody (2004) model to predict surface pressure spectra for varying flow conditions.

1.3.2.3 Rough Wall Surface Pressure

As noted above, the available literature applicable to the surface pressure spectral density of ordinary turbulent boundary layer flows over rough surfaces is scarcer than that relating to the smooth wall surface pressure of turbulent boundary layer flows. Two studies that seem to be standards in the area of rough wall surface pressure spectra are those of Blake (1970) and Aupperle and Lambert (1970). In both of these studies the authors note a change in both the spectral shape and spectral levels of the surface pressures associated with varying surface roughnesses. The variation in level accompanied by the addition of surface roughness as well as the frequency range for which this level variation occurs is dependent on the characteristics of the surface roughness. The surface pressure spectra presented by both Blake (1970) and Aupperle and Lambert (1970) show a larger change in spectral level at lower frequencies. This is not surprising given that the roughnesses used in these studies were large. The roughness Reynolds number ($k_s u^* / \nu$) was found to range from 236 – 670 in the Blake (1970) study and from 500 to almost 3300 in the Aupperle and Lambert (1970) study. These ranges of roughness Reynolds number indicate fully rough flows.

In both of these studies, the authors attempt to incorporate roughness length scales into the spectral scaling of the surface pressure. The spectral scaling proposed by Blake (1970) is given as follows:

$$\frac{\Phi(\omega)u^*}{\tau_w^2 \overline{k_g}} \quad (1.30)$$

and the frequency is normalized as:

$$\frac{\omega \overline{k_g}}{u^*} \quad (1.31)$$

where $\overline{k_g}$ is the mean roughness height. Blake (1970) reports some collapse of the surface pressure spectra at high frequencies.

The scaling suggested by Aupperle and Lambert (1970) is given as follows:

$$\frac{\Phi(\omega)u^*}{\tau_w^2 k_s C_f} \quad (1.32)$$

and the frequency is normalized as:

$$\frac{\omega k_s}{u^*} \quad (1.33)$$

where k_s is the Nikuradse equivalent sand grain roughness height. Both of these proposed scaling bring in some measure of the roughness size into the scaling of the surface pressure spectra. The scaling proposed by Aupperle and Lambert used the skin friction coefficient as a scaling parameter in addition to the incorporation of the Nikuradse equivalent sand grain roughness height (this will be discussed in more detail in later chapters).

1.4 Objectives and Experimental Approach

While a significant effort to understand wall jet flows over smooth surfaces has been seen in the available literature, there has been relatively little work done in the area of wall jet flows over rough surfaces. The majority of the work done to address rough wall jet flows deal with deterministic roughness or sand grain roughness that is large relative to the boundary layer thickness. Most of these studies investigate wall jet flows over rough surfaces that extend from the nozzle source to the measurement location, and the study by Dey and Sarkar (2005) was not seen to be applicable to the current study. Also, while the surface pressure fluctuations under conventional two-dimensional flat plate turbulent boundary layers has been studied in detail by numerous workers, there is a complete lack of any work regarding the surface pressure fluctuations under smooth wall jet flows. There is also a scarcity of rough wall surface pressure fluctuation measurements in the literature even for conventional turbulent boundary layers, and, to the knowledge of the author, there have been no studies where the surface pressure fluctuations under rough wall jet flows have been measured.

Given the lack of knowledge in these areas, the objectives of this study are as follows:

- Investigate behavior of wall jet flows over short roughness patches whose roughness grain size is not large relative to the boundary layer thickness
- Investigate smooth wall jet surface pressure fluctuation spectral character and scaling

- Investigate wall jet surface pressure fluctuation spectral character and scaling over rough surfaces of varying grain size

A single hotwire anemometry system will be used to take mean velocity, velocity spectra, and normal stress profiles of the wall jet flow in a smooth wall condition for a range of flow conditions and streamwise locations. Velocity spectra taken for each measured test case at measurement heights off of the plate of $y = y_{1/2}$, δ , and δ^* (to be defined later), will be given, and scaling attempts will show the applicability of certain length and velocity scales at very different locations in the wall jet flow.

The surface pressure fluctuations will be measured for the smooth wall jet flow for a range of initial flow conditions and streamwise measurement locations to determine the form of the surface pressure spectral density. Comparisons will be drawn between the surface pressure spectral behavior seen in the turbulent wall jet flow and that of ordinary turbulent boundary layer.

The effects of rough surfaces on the wall jet flow were investigated as well. In order to determine the variation of the wall jet flow with variations in surface roughness, rough patches of various sand grain roughnesses were constructed from sand paper. The roughness type tested in this study was of a stochastic type (there was no pattern roughness tested). The roughness elements that comprise these patches are small compared to the boundary layer thickness ($k_g/\delta < 1/10$, where k_g is the nominal roughness size). Single hotwire measurements were taken directly behind each roughness patch (about 9 mm aft of the trailing edge of the roughness patches), and the wall jet flow was measured for a range of initial flow conditions. The variation of wall jet flow parameters such as the maximum flow velocity and the boundary layer length scales with the change in roughness size were examined, and the effects of roughness on the normal stresses seen in the wall jet flow were also observed. The effects of rough surfaces on the wall jet flow were also examined by measuring the velocity spectra in the same way as for the smooth wall jet flow taken at the same measurement heights as for the smooth wall velocity spectra. These spectra are scaled in various ways in order to show the dependence of the flow at different distances from the flow surface.

Finally, the surface pressure spectral character of the wall jet flow over rough surfaces was investigated by placing measurement transducers at several streamwise locations along the rough patches. The decay of the surface pressure with streamwise distance was investigated, as was the change in the surface pressure spectra with changes in the roughness size. The scaled behavior of the rough wall jet surface pressure spectra was analyzed by applying various smooth wall scaling schemes as well as proposed scaling schemes for rough wall turbulent boundary layers.

2 Wall Jet Tunnel and Instrumentation

This chapter will describe, in detail, the experimental test facility and all instrumentation devices used to obtain the data discussed in the following pages and chapters of this document. Section 2.1 will describe the wind tunnel test facility used to generate the wall jet flow that has been studied. Section 2.2 will describe the various measurement systems that were used to obtain mean velocity profiles and selected turbulence and spectral measurements. Section 2.3 will describe the measurement systems used to obtain surface pressure measurements. Section 2.4 will describe the various types of roughnesses used in the experiments that are discussed in later chapters. Section 2.5 will describe the facility's basic acoustic characteristics, and Section 2.6 will give the uncertainty estimates for various measured and calculated quantities used in the current study. All experiments and data presented in this dissertation were obtained in the measurement facility to be described below between May 2005 and March 2008.

2.1 Virginia Tech Wall Jet Tunnel

2.1.1 The Facility Itself

The construction of the Virginia Tech wall jet tunnel began in 2005. Preliminary measurements were very promising regarding the facility's usefulness in the measurement of two dimensional wall jets and the roughness noise they can produce. After the facility was proven to be conceptually viable, a series of improvements and alterations were applied to the facility. These changes were intended to improve flow qualities, reduce vibration, improve signal to noise ratio, etc. The improved testing facility was completed in the summer of 2006 and has not been significantly altered since that time.

The Virginia Tech wall jet tunnel produces a plane turbulent wall jet flow. Figure 2.1 (adapted from Grissom *et al.* 2007) shows a schematic of the testing facility. Air is blown through a flexible rubber hose from a centrifugal fan into an acoustically treated settling chamber. The air is accelerated through a nozzle and exhausted over a flat aluminum plate. Depending on the configuration, the flow exiting the nozzle is exhausted over the plate into the lab (aerodynamic configuration) or into an acoustically treated chamber (acoustic configuration).

Flow is delivered to the settling chamber from a centrifugal blower via the flexible rubber hose shown in Figure 2.1. The blower is a Cincinnati Fan model HP-8D20. The motor is a 15 HP electric motor, and the fan (a 20 by 65 mm fan) is able to produce 0.945 m³/s worth of volumetric flow rate against 7500 Pa of back pressure. This fan was chosen based on an earlier conceptual design for a channel flow, so the blower characteristics were not optimum for this facility and flow, but they were adequate. The blower was also fitted with a SSA-8 steel discharge silencer. This silencer reduced the broadband noise in the fan exhaust by as much as 10 dB.

Once the air flow reaches the settling chamber through the flexible rubber hose, it must pass through three sections of the settling chamber. The inner cross section of each of these

sections is roughly 1220 mm by 1220 mm. Each section of the settling chamber was constructed with 25.4 mm thick MDF. All inside walls of the aft two sections are acoustically treated with 102 mm egg-crate foam.

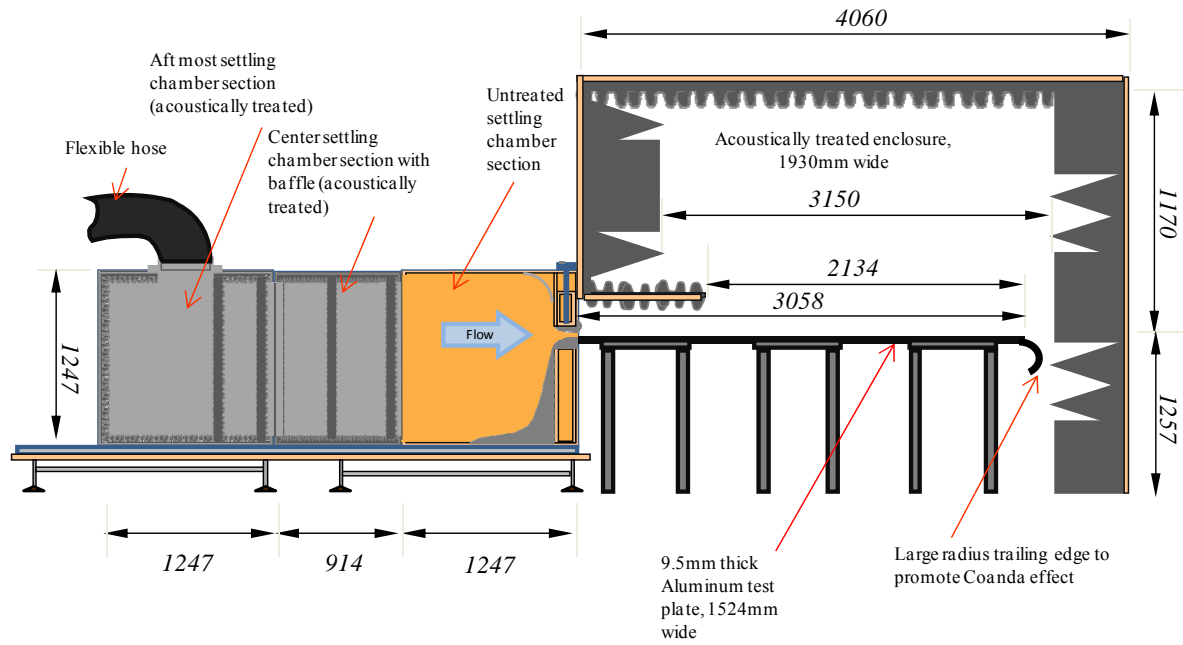


Figure 2.1 Schematic of the Virginia Tech wall jet tunnel in the acoustically treated configuration (dimensions in mm)

The aft two sections are also equipped with treated baffles designed to eliminate direct line of sight between the rubber hose exit and the nozzle exit. The treated baffles are 610 mm. wide, 25.4 mm thick, run vertically from the bottom of the section to the top, and are completely covered with 102 mm egg-crate foam. Each of the sections is joined together with external latches, and is sealed. The openings between sections are 610 mm wide and occupy the entire height of the section. After the air flow snakes its way through the aft two sections of the settling chamber, it enters the forward most section which is not acoustically treated. A top view schematic of the settling chamber is shown in Figure 2.2 below.

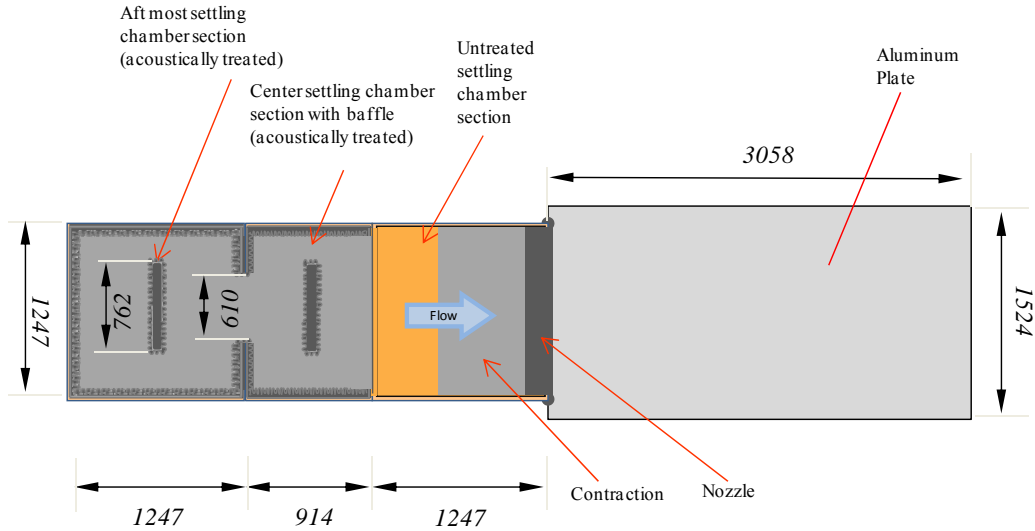


Figure 2.2 Top view schematic of settling chamber and aluminum plate layout (dimensions in mm)

The acoustically untreated forward section of the settling chamber is the same size as the aft sections and is equipped with a contraction along its lower surface. The contraction on the lower surface of the settling chamber and the lower portion of the nozzle were designed according to methods proposed by Fang *et al.* 2001. The design and construction of the nozzle contraction (both upper and lower sections) is described briefly below. The cubic equation suggested by Fang *et al.* is:

$$y = (h_1 - h_2) \left[1 - \frac{1}{X_m^2} \left(\frac{x}{L} \right)^3 \right] + h_2 \quad (2.1)$$

The variables in this equation are described in Figure 2.3 below.

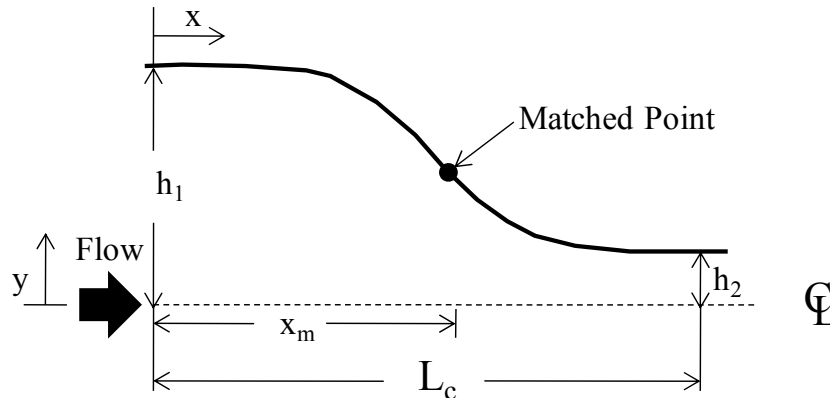


Figure 2.3 Diagram of the cubic curve used in the contraction section

The lower portion of the contraction and nozzle were designed to create a flow path defined by this cubic curve. For this facility, the dimension h_2 is a variable (i.e. the nozzle height can be altered) but this dimension was chosen to be the nozzle half height for a 12.7 mm nozzle height because this nozzle height was the nozzle height most often used during the tests conducted in the testing facility. The length, L_c , was set to be half of the inside length of the settling chamber section or 610 mm, and h_1 was set to be the height of the nozzle center line off of the bottom of the section minus 76 mm to account for the presence of acoustic foam should it ever be necessary to apply foam to this section ($h_1 = 681$ mm). For the current configuration, the matchpoint length, x_m , was determined so as to force the shape of the lower nozzle to mimic as closely as possible the elliptic shape of the nozzle of the previous test facility design iteration. The best value for this length was determined to be 254 mm. These parameters determined the shape of the lower portion of the nozzle used in the testing facility. No cubic fit was used for the upper portion of the nozzle because the upper portion of the nozzle had to be adjustable to allow for the change of nozzle height. The upper portion of the nozzle was designed to simply be a quarter ellipse with a semi major axis of 305 mm and a semi minor axis of 152 mm. This portion of the nozzle was fitted with a mechanism to allow for its vertical movement. This mechanism made it possible to test at nozzle heights varying from 0 mm to 102 mm. At the top corner of the nozzle section of the settling chamber there is a 152 mm diameter piece of aluminum perforate that forms an arc between the top and forward most portions of this settling chamber section. The space behind the perforate is packed with fiberglass creating a contraction in order to prevent stall in the corner of the nozzle section of the settling chamber.

The nozzle portions were fabricated from PVC and milled using a CNC milling machine according to the specifications just discussed. The milling machine was able to produce a surface that was accurate to within 0.0127 mm. The nozzle exit is 1207 mm wide in the spanwise direction and has a nearly constant opening height across the width. The top outside and side edges of the nozzle exit are fitted with rounded lips of diameter 76 mm. These lips are present to reduce edge noise that might contaminate far field acoustic measurements taken in this flow facility. The bottom edge of the nozzle exit is joined with the aluminum plate over which the wall jet flow develops. This junction was carefully designed to eliminate exposed edges caused by mismatches in the plate and nozzle junction which were less than 0.25 mm in size. Any mismatch in the nozzle exit and the aluminum plate was smoothed by applying and sanding automotive body filler. A schematic of the junction between the aluminum plate and the nozzle exit can be seen in Figure 2.4 below.

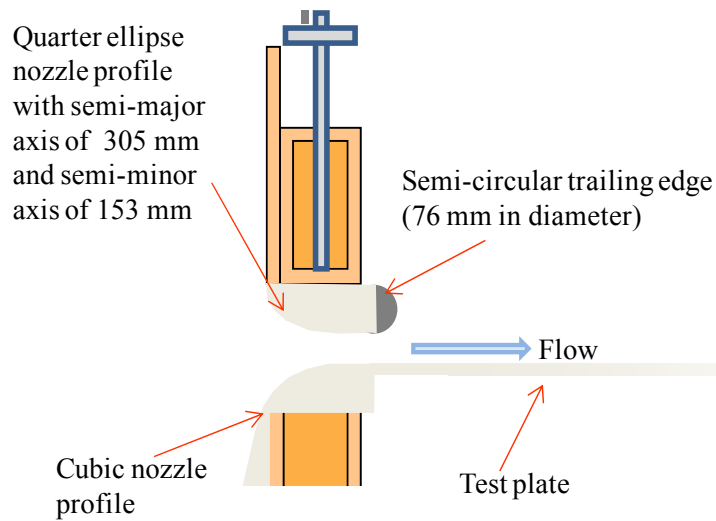


Figure 2.4 Schematic of nozzle exit and plate junction

The flow through the nozzle is exhausted out over an aluminum plate that is 9.5 mm thick, 1524 mm wide and 3058 mm long. This is a polished plate and surface imperfections were removed with automotive body filler and a lot of sanding and buffing. The plate is mounted on three steel stands bolted to the floor. The plate is set to be nominally 1245 mm off of the floor, and it is leveled. The aft edge of the plate is fitted with a rounded trailing edge of radius 102 mm in order to reduce edge noise and produce a Coanda effect to redirect the flow downward and away from a potentially noisy interaction with the acoustic wedges on the aft wall of the acoustic enclosure. During wall pressure or acoustic measurements the plate is enclosed in an acoustically treated room. The acoustically treated configuration is seen in Figure 2.1 above. During an aerodynamic test the plate is not covered, and the enclosure is rolled away. In this configuration, the settling chamber and aluminum plate and supports remain stationary, but the acoustic enclosure is completely removed as seen in Figure 2.5 and Figure 2.6 below.

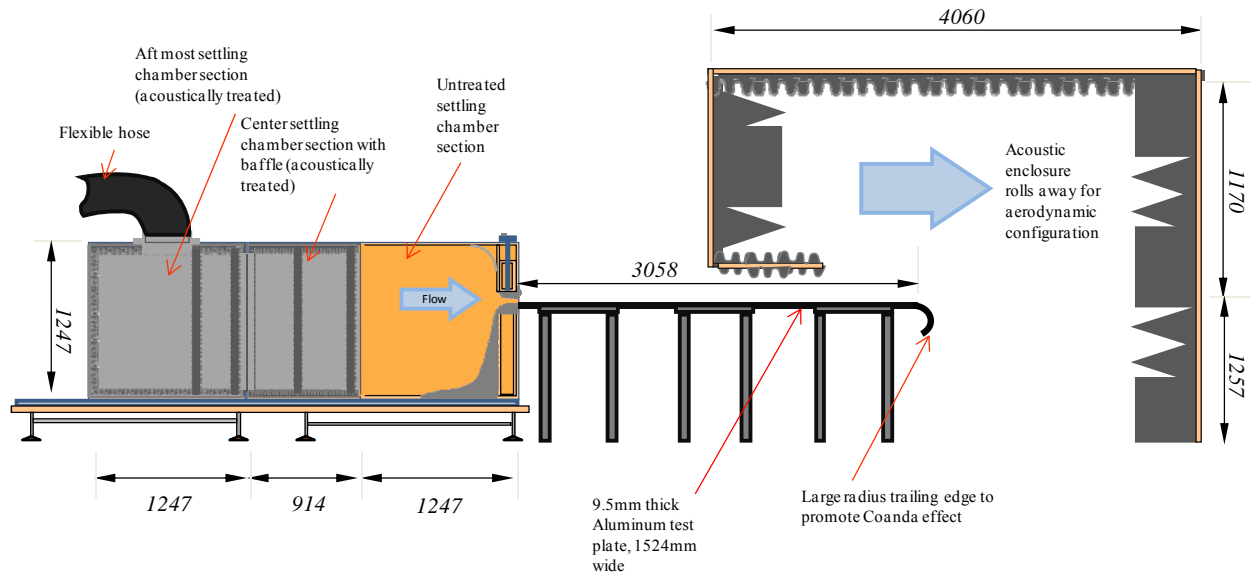


Figure 2.5 Schematic of the Virginia Tech wall jet tunnel acoustic enclosure being removed (dimensions in mm)

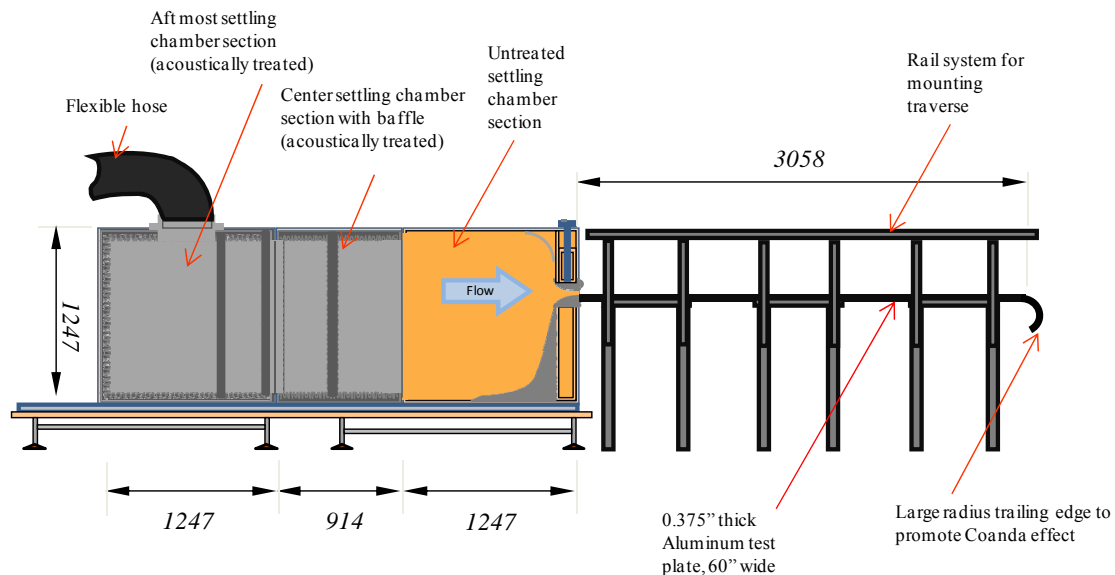


Figure 2.6 Schematic of the Virginia Tech wall jet tunnel in the aerodynamic testing configuration (dimensions in mm)

In the acoustically treated configuration, microphone measurements can be made from inside the acoustically treated enclosure that can be rolled forward and backward to cover the aluminum plate. This enclosure completely surrounds the plate. It mates with the settling chamber sections, and the only area open to the lab space outside the enclosure is a 152 mm gap between the enclosure and the floor that goes all the way around the enclosure. The dimensions of the acoustic enclosure are given in Figure 2.1 above. The inside of the enclosure is lined

primarily with the same 102 mm egg-crate foam that the settling chamber is lined with. However, on the aft end 305 mm x 610 mm x 457 mm acoustic foam wedges were used. In the forward portion of the enclosure, there is an acoustic baffle that forms a shelf above the plate. This shelf is acoustically treated with 102 mm egg crate foam, and microphones can be mounted in the space above the shelf in order to measure flow generated noise on the plate. The shelf serves to shield microphones from any jet noise caused by the airflow out of the nozzle contraction. Figure 2.7 below shows this portion of the enclosure in more detail. It also shows the nozzle exit region in more detail. It is in this acoustically treated configuration that surface pressure or far field noise measurements are made for a variety of conditions. It is these surface pressure measurements that will be the subject of discussion in a later chapter.

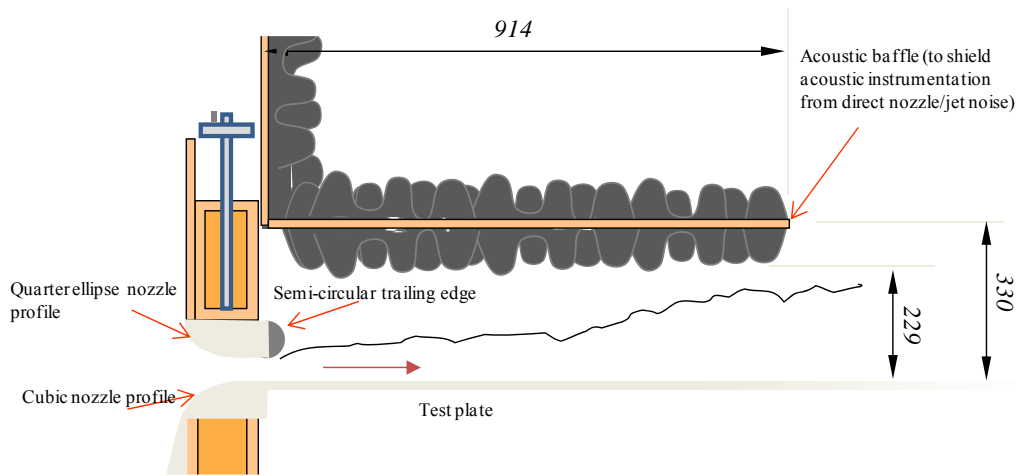


Figure 2.7 schematic showing the nozzle and acoustic baffle (dimensions in mm)

Figure 2.8 shows a picture of the inside of this enclosure in the clean plate configuration. One can see the rounded lip integrated with three sides of the nozzle exit. The acoustic baffle shown in Figure 2.7 above that forms a shelf can also be seen in Figure 2.8 below.

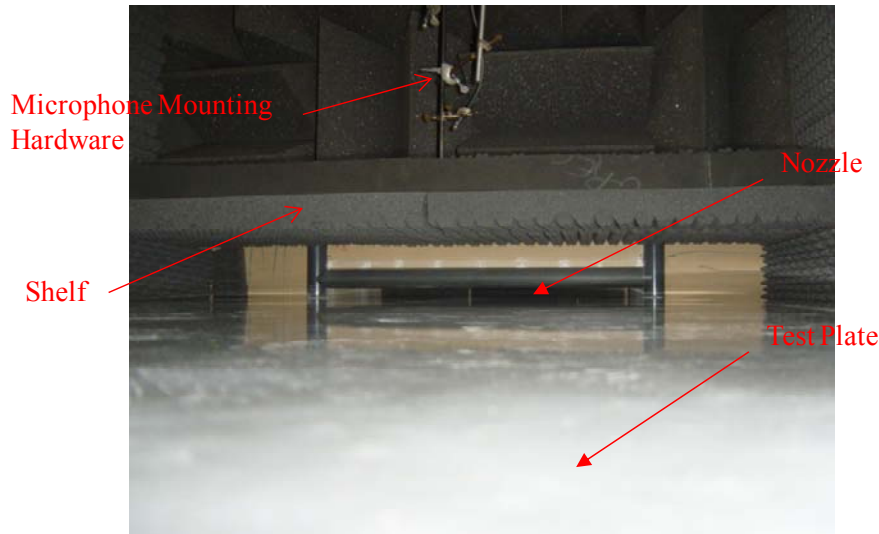


Figure 2.8 *Picture of nozzle exit and surrounding acoustic enclosure*

When aerodynamic measurements are desired, the acoustic enclosure rolls away from the plate, and the airflow is exhausted out over the plate and is exposed to the open lab space. In this configuration, aerodynamic measurements are made by mounting a traverse on a rail system and using a hotwire anemometer system or Pitot or Pitot-static probe system. In Figure 2.9 one can see the testing facility in its aerodynamic configuration. In this figure, the plate is viewed from the nozzle, and the acoustic enclosure that has been rolled away from the rest of the wall jet tunnel can be seen in the background. The figure shows the aft portion of the plate, the rail mounts for the traverse, the traverse, and a hotwire probe over a patch of sand grain roughness.

2.1.2 Facility Instrumentation and Hardware

Atmospheric pressure was obtained using a Kahlsico Mk 2 type M2236 precision aneroid barometer (accuracy: ± 0.05 mBar). The temperature inside the lab was measured with a AcuRite digital thermometer (accuracy: $\pm 0.1^\circ\text{F}$). The temperature inside the settling chamber was also measured with this thermometer for test cases measured with the flattened Pitot probe measurement system and taken as a measure of the flow temperature, but for tests taken using a single hotwire system the flow temperature was measured with a Omega DP80 thermistor (accuracy: $\pm 0.1^\circ\text{F}$) and recorded with the data acquisition system. This allowed for the measured quantities to account for flow temperature variations during each test case run whereas, for the Pitot measurements, the flow temperature at the start of the run was taken as the flow temperature throughout the test. The temperature variation during a test case was never more than 2°F . Nozzle exit speeds were calculated by measuring the pressure difference in the settling chamber pressure and the ambient pressure. This pressure difference was measured with Setra 239 pressure transducer with a range of ± 2.5 psid (accuracy: $\pm 0.14\%$ full-scale). The uncertainty in nozzle exit speed was calculated to be $\pm 2.4\%$ for a nozzle exit velocity of nominally 20 m/s and $\pm 0.6\%$ for a nozzle exit speed of 60 m/s.

The traverse used was made in house. It is a 2 axis traverse and is powered by Compumotor model S57-83-MO stepper motors. It is controlled by the data acquisition software (to be discussed below) through Parker PDX13 drivers. The traverse is placed outside of the

flow above the shear layer present in wall jets. Only the probe stem and the probe itself extend into the wall jet flow.

The traverse and rail system shown in Figure 2.9 allows for movement of the measurement probe in 3 directions. The measurement probe can be moved in the streamwise (or x) direction along the length of the plate manually so that measurements can be taken at any location along the plate ranging from $x = 0$ mm at the nozzle exit to $x = 2590$ mm aft of the nozzle exit. The measurement probe can be moved in the y and z directions over a broad range of values in increments as small as 0.0127 mm.

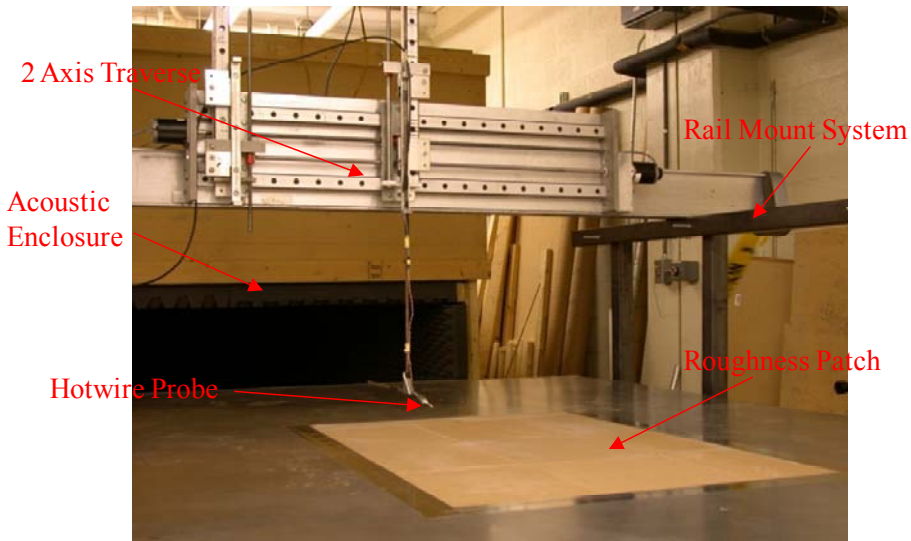


Figure 2.9 *Picture showing the traverse and rail mount system in the aerodynamic measurement configuration*

2.1.3 Data Acquisition System

All measurement systems used an Agilent data acquisition system. Signals were digitized by Agilent 1432 A 16 bit A/D converters. These A/D converters are capable of a simultaneous sampling at a rate of up to 51.2 kHz on any one of 16 channels. Each A/D converter has signal conditioning and anti-aliasing capabilities. A VXI CT-100C mainframe is used to house these devices. The A/D converters not only sample signals from the measurement systems, but they also can be used to sample signals from reference temperature and pressure transducers. The sampled data was transferred by an HP E8491B module to an HP NX5000 Notebook computer via firewire interface. The notebook computer was used to run Agilent VEE data acquisition software that was programmed in house. Sampling and signal conditioning schemes differ from measurement system to measurement system and will be discussed below in detail.

2.2 Aerodynamic Measurement Systems

In the measurement of wall jets the mean velocity is a quantity of interest. Indeed, one can understand much about a wall jet flow with just a simple mean velocity measurement, and many of the first measurements taken in this study were made with a simple flattened Pitot probe. However, the majority of the data collected was obtained using a single sensor hotwire anemometry system. This system allowed for the measurement of basic turbulence quantities and velocity spectra.

2.2.1 Flattened Pitot Measurement System

This fairly simple system was used early on to measure the mean velocity profiles of the wall jet flow produced by this facility. The system consisted of three major components: a flattened Pitot probe, pressure transducers, and a data acquisition unit. The probe was constructed in house. Figure 2.10 shows a schematic of the probe and probe tip.

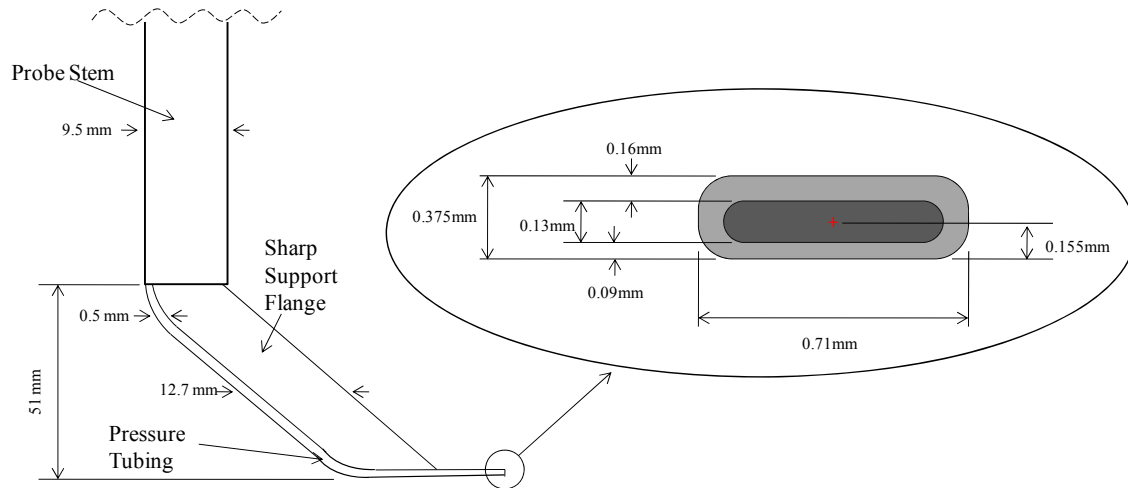


Figure 2.10 Schematic of flattened Pitot probe

The probe was designed with a thin sharp support flange to provide structural support while maintain a low profile so as not to generate a lot of drag or flow interference. The probe was connected to a Setra 239 pressure transducer of range $\pm 5''$ WC (accuracy: $\pm 0.14\%$ full scale) via Tygon tubing. This pressure transducer measured the difference in the Pitot pressure and the ambient pressure in the lab. The output voltage from this transducer was sampled with the HP 1432A A/D converters described above and the digitized signal was recorded using Agilent VEE software. The software converted the voltages measured to pressure using a known slope and offset specific to that transducer. Also recorded for each test case was the pressure difference between the settling chamber and the lab. This pressure difference was measured with the pressure transducer of range ± 2.5 psid discussed above. Profiles were taken by measuring some 50-60 points through the wall jet flow. The Pitot profiles were measured with a sampling rate of 6400 Hz, and 50 records of 1024 samples each were recorded.

The origin of the flattened Pitot probe was determined with the use of an electrical connection between the aluminum plate and the probe tip. The Pitot probe was wired to a hand

held multimeter equipped with an audio beeper that indicates a closed circuit. The probe was positioned close to the plate surface, and then the air flow was turned on. Then the probe was stepped down in increments of 0.001 inches (or 0.025 mm) until the audio indicator was engaged. Then the probe was raised 0.025 mm from that location. This position was considered to be the baseline point of each measurement, and the probe tip center was considered to be 0.15 mm from the plate \pm 0.025 mm. This method was found to be very reliable in previous airfoil trailing edge boundary layer measurements, see Camargo *et al.* (2005).

2.2.2 Hotwire Anemometry

The majority of the velocity measurements were obtained using hotwire anemometry. In addition to mean flow quantities, hotwires can be used to measure turbulence quantities such as the normal stresses, and they are able to obtain velocity spectra to reveal the distribution of turbulence energy with frequency. The basic premise of hot-wire anemometry is that if a thin wire (sensor) is exposed to an airflow, the resistance of that wire fluctuates as its temperature fluctuates. Most hotwire systems employ a constant temperature anemometer (CTA) technique. In this technique, the CTA attempts to keep the sensor, which is connected to a bridge circuit much like a Wheatstone bridge circuit, at a constant temperature. As the speed of the flow over the wire changes, the heat transfer rate of the sensor changes as well, and, thus, the temperature changes. In order for the sensor to stay at a constant temperature, the CTA must supply more current, and hence more voltage, to the sensor. This voltage which varies with the velocity of the flow across the sensor is recorded by the data acquisition system used.

For the experiments discussed below, a single sensor Auspex AHWU-100 hotwire probe was used (Figure 2.11). The sensor is an etched tungsten wire 1mm long and of diameter 5 μ m.

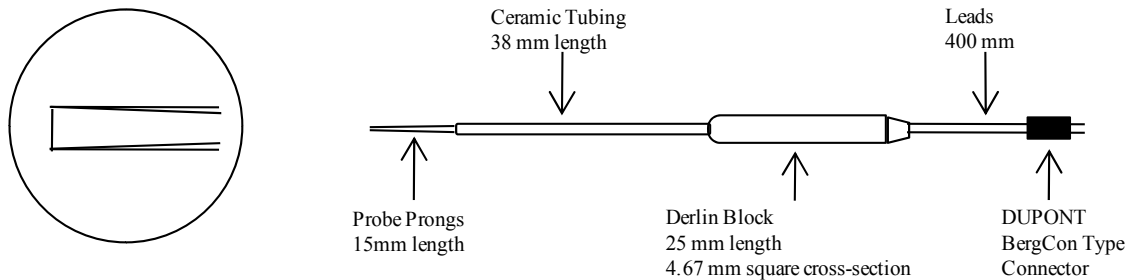


Figure 2.11 Auspex AUHW-100 single wire probe

The hotwire probe was used in conjunction with a Dantec 90C10 Streamline CTA unit using an overheat ratio of 1.7. The Dantec CTA unit was operated using Streamware software. Because the hotwire system is highly dependent on the flow temperature, tests were conducted in a temperature controlled laboratory, and the room temperature as well as the flow temperature was monitored closely. Figure 2.12 below shows the hotwire mounting assembly.

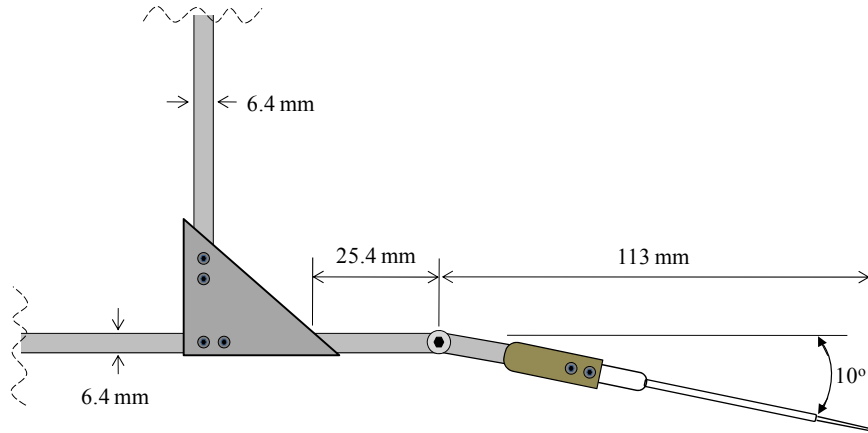


Figure 2.12 Hotwire mounting assembly schematic

Figure 2.13 shows the instrumentation associated with the single wire. It is important to note that the Dantec CTA unit has built into it capability for customized amplification and signal conditioning. For all hotwire measurements presented in the current study, a sampling rate of 51200 Hz was used to obtain 100 records of 8192 samples each.



Figure 2.13 Single sensor hotwire measurement system setup

The mounted hotwire probe configuration can be seen in Figure 2.9 above. Moving the hotwire probe small distances accurately was not a problem because of the positioning capabilities of the traverse mentioned above. Positioning the probe initially, however, was more difficult. The hotwire probe was positioned optically using a cathetometer. The cathetometer was placed slightly above the aluminum plate level, and the probe was lowered until it and its reflected image could be seen. The hotwire probe was moved to about 0.5 mm off of the aluminum plate where the crosshairs of the cathetometer were placed on the probe tip. Then the cathetometer was translated downward until the crosshairs were in line with the probe tip of the reflected

image. The distance the cathetometer was moved was divided by two and the resulting distance was taken to be the probe's distance from the aluminum plate. Then the probe was positioned to the desired height off of the aluminum plate using the traverse. The uncertainty in the true position of the hotwire probe after being set in this way was experimentally determined by plotting the measured velocity profiles on a Clauser type plot and varying the distance from the wall, y , until the points in the laminar sublayer and overlap regions agreed from profile to profile. The resulting uncertainty was determined to be ± 0.13 mm or around 0.005 inches.

2.2.3 Hotwire Calibration Methods

All hotwire probes were calibrated before each day of testing and then again after the testing was completed. The basic calibration procedure used was to relate the bridge circuit output voltages with the effective flow velocities seen by each sensor by using King's law which is shown in equation 2.2 below.

$$E^2 = A + BU_{eff}^{0.45} \quad (2.2)$$

Here, E is the output voltage of the bridge circuit and A and B are constants. For the single wire hotwire probes the calibration was conducted using a TSI 1125 calibrator shown in Figure 2.14 below.

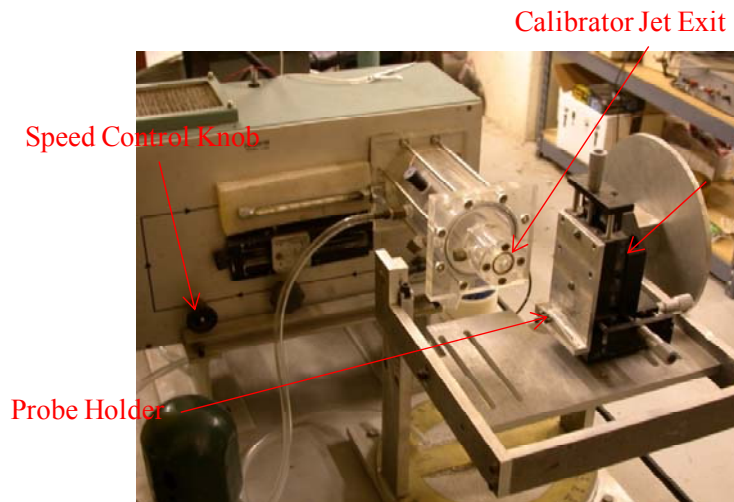


Figure 2.14 Picture of TSI 1125 calibrator

The probe tip is placed in a jet of diameter 6.4 mm produced by the calibrator. The exit speed of this jet is measured and varied over a range of velocities and the voltage from the hotwire bridge is recorded. For single wire probes with the sensor perpendicular to the flow, the velocity in the streamwise direction, u , is equal to the effective velocity, U_{eff} . This calibration is then used to convert the recorded voltages from experiments into velocities. Because the lab temperature varied slightly over the course of a day of testing, an interpolation of the measurements between the beginning and ending calibrations was employed to reduce errors associated with ambient

temperature drift. These corrections were usually very small and were under $\pm 3\%$ of the measured quantities.

2.3 Surface Pressure Measurement Systems

For surface pressure measurements, Sennheiser KE 4-211-2 electret condenser microphones shown in Figure 2.15 below were used. These microphones have a nominal sensitivity of 10mV/Pa, and they have a frequency response that is flat to within 1dB from 100 Hz to 10 kHz, and they can be calibrated over a larger frequency range. They have an external diameter of approximately 5.1 mm, and they have a pinhole that is 1 mm in diameter. These microphones can detect signals with SPL levels of as much as 125 dB, and the microphones are not sensitive to vibration. The Sennheiser microphones require a 5 V DC power supply, and the output voltage from the microphones is amplified by 10 times with in-house amplification circuits.

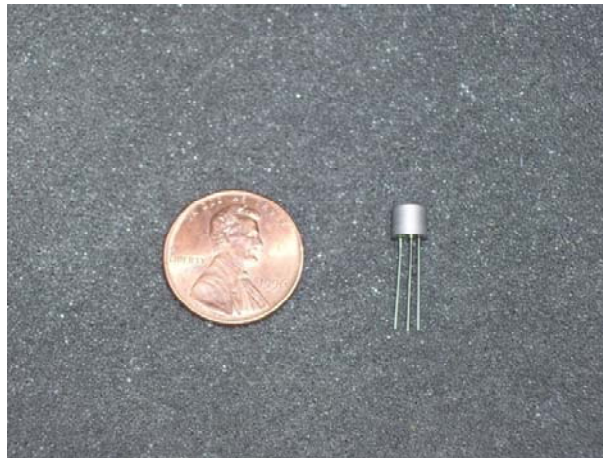


Figure 2.15 *Sennheiser KE 4-211-2 electret condenser microphone*

The microphones signals are recorded by the data acquisition system described above. Figure 2.16 below shows a schematic of the microphone system. Of course, it is of vital importance to any microphone measurement system that a reliable calibration system and procedure can be employed. The calibration procedure used in the current study will be discussed in detail in Chapter 4 below where the calibration results are presented.

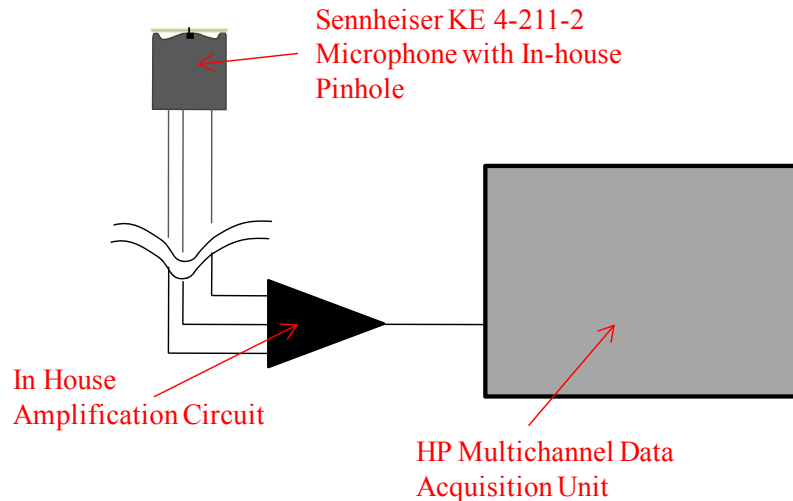


Figure 2.16 Setup scheme for each microphone used in a given measurement

All of the Sennheiser microphones were inserted into nylon bushings that had outer diameters of 9.5 mm and inner diameters slightly larger than the 5.1 mm diameter of the Sennheiser microphones. Also of note is the fact that the Sennheiser microphones used in this study have been fitted with pinholes of smaller diameter than those provided by the factory. This was done to eliminate spatial averaging associated with large pinholes in surface pressure measurements. The new pinholes were created by drilling 0.25 mm holes in a 0.13 mm thick disc of Mylar that was adhered to the head of the Sennheiser microphone casing using 5 minute epoxy that was applied in a very small amount with a toothpick. The effects of the addition of these pinholes will be discussed in detail in Chapter 4 below.

Another key aspect of the surface pressure measurement system is the chosen microphone height. Once the desired streamwise positions of the microphones were determined for each of the measurements conducted, the KE 4-211-2 microphones had to be placed so that the pin holes were flush with the surface (clean plate measurement cases) or at the roughness tops (roughness cases). This was done by placing a flat block of metal on the roughness patch and pushing the microphone and bushing assembly up through pre-punched holes in the roughness patch until the microphone and bushing assembly touched the metal block. Then the microphones were glued into place from the bottom of the plate using hot glue. Figure 2.17 below illustrates the desired placement of the microphones. A discussion on the reasoning behind the chosen microphone heights for each roughness test case will be presented later in chapter 4.

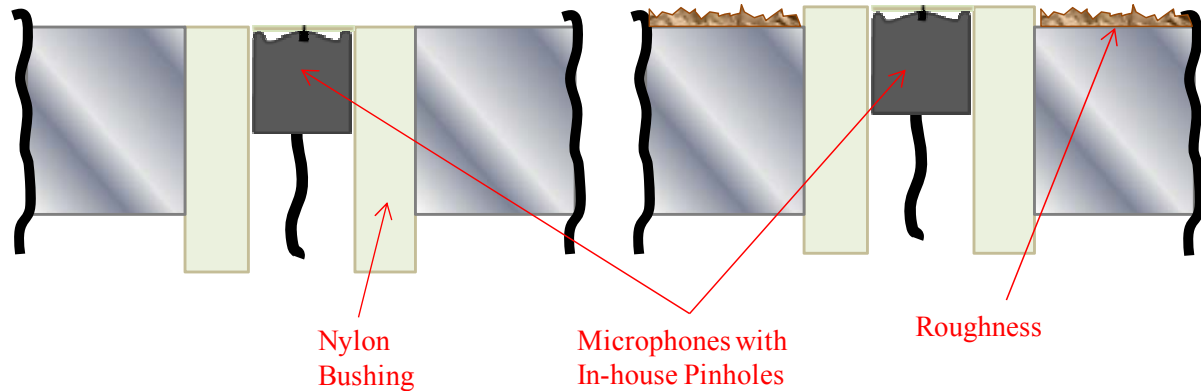


Figure 2.17 Schematic of desired microphone positioning

2.4 Roughness

The surfaces tested ranged from 220 grit sheets to 20 grit sheets. Most of the sheets were made from a thin paper backing with aluminum oxide grit distributed over the surface of the paper manufactured by Gator Grit®. However, some of the sheets used were made of a thicker paper backing and distributed grit that were manufactured by Norton®. Table 2.1 below shows the roughness properties of each random roughness tested in detail. In this table, the roughness sheets that were made of the thicker paper backing are designated as Floor Sanding roughness sheets. It is important to note that nominal grain sizes (k_g) were inferred from the grit number using standardized tables. The RMS height (k_{rms}) values were obtained from measurements made by MicroPhotonics Inc. using white light profilometry that can be used to obtain complete 3-dimensional documentation of the surface shapes as seen in Figure 2.18 below. In this figure, the measurement step size was 15 microns.

The correlation function and sparseness values, λ , were determined from these measurements. L is the integral of the correlation coefficient function from zero displacement (where the coefficient is 1) to the point where the coefficient first falls through 0.1. The sparseness λ is defined as the ratio of the projected area of the rough surface perpendicular to the wall to that parallel to the wall. The grain densities are inferred by counting grains in images of the white-light profilometry or scanner images of the rough surfaces, and overall thickness of the roughness sheets was measured using a caliper. The nominal grain size (k_g) appears to be a roughly constant multiple of the r.m.s. surface elevation, the ratio varying from 2.5 to 4.6. The integral scale is roughly equal to the nominal grain size, and would indicate that there is little grain to grain correlation in the surface distribution. The sparseness values show a variation of about a factor of 5 from the 20-grit floor sanding sheet to the 60-grit Aluminum oxide paper.

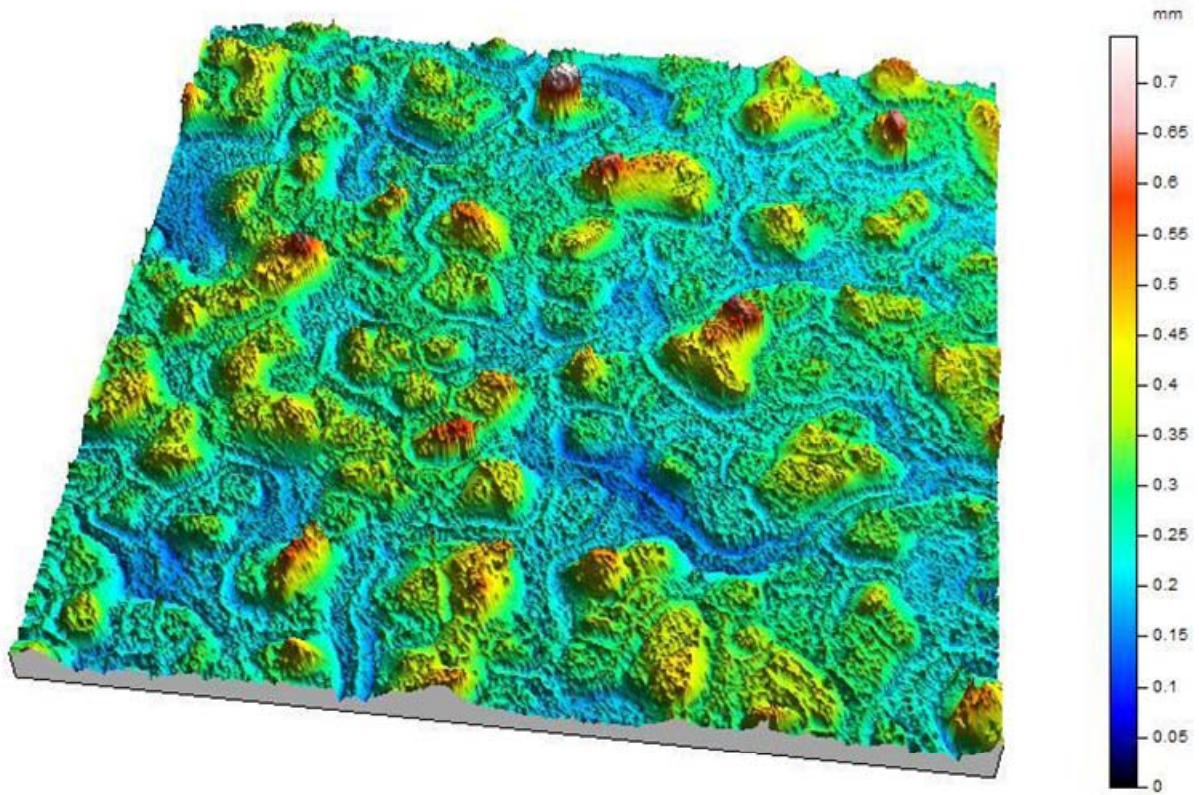


Figure 2.18 5 x 5 mm plot of measured surface of 40 grit sand paper roughness sample produced by MicroPhotonics Inc.

Type	Grit	Sheet thickness (mm)	Nominal grain size k_g (mm)	Grain density per mm ²	RMS roughness size k_{rms} (mm)	k_g/k_{rms}	Integral scale L (mm)	L/k_{rms}	Sparseness λ
Al Oxide	40	0.76	0.425	1.4	0.145	2.94	0.547	3.78	2.13
Al Oxide	60	0.58	0.265	2.6	0.106	2.50	0.266	2.51	1.08
Al Oxide	80	0.44	0.19	4.3	0.066	2.88	0.204	3.10	1.34
Al Oxide	100	0.38	0.14	10.6	0.041	3.39	0.163	3.94	2.64
Al Oxide	150	0.33	0.092	24	0.029	3.21	0.100	3.47	2.19
Al Oxide	180	0.29	0.082	34	0.024	3.35	0.079	3.24	2.19
Al Oxide	220	0.29	0.068	43	0.017	3.93	0.103	5.97	3.90
Floor Sanding S413	20	1.27	0.95	0.23	0.206	4.60	1.253	6.07	5.27
Floor Sanding H425	36	1.13	0.53	1.5	0.187	2.84	0.568	3.04	2.69
Floor Sanding H425	60	0.81	0.265	4.9	0.076	3.47	0.315	4.12	1.69
Floor Sanding H425	80	0.66	0.19	6.2	0.071	2.66	0.222	3.11	1.60

Table 2.1 Measured and estimated roughness parameters

All roughness patches used in the current experiment were attached to the aluminum plate surface using very thin (0.075 mm) double sided tape. The roughness patches used measured 305 mm in streamwise extent, and 610 mm in spanwise extent. For the 40 grit and 180 grit cases longer patches were investigated and these patches measured up to 914 mm in streamwise extent. These longer patches are also 610 mm in spanwise extent. The edges of all of these roughness patches were taped with aluminum foil tape that was 0.15 mm thick. The leading edge step size of the leading edge of the roughness patches is taken to be roughly the backing thickness of the sand paper used to make the roughness patches and ranges from 0.29 to 1.29 mm.

2.5 Testing Facility Basic Acoustic Characteristics

This testing facility was designed to be an acoustic as well as an aerodynamic testing facility. Therefore the basic acoustic character of the facility in its acoustically treated configuration is worthy of comment. To determine the acoustic character of the facility, a B & K 4190 ½" microphone was mounted at the aft edge of the shelf area in the acoustic enclosure 914 mm above the plate surface at a streamwise distance downstream of the nozzle exit of 914 mm on the spanwise centerline of the test plate. The plate was without roughness. The flow was turned on and noise measurements were taken at a number of nozzle exit speeds. The integrated SPL levels were calculated, and Figure 2.19 below shows that these SPL levels scale well with U^8 .

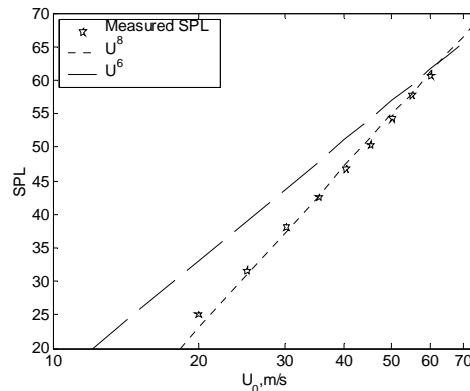


Figure 2.19 *Integrated sound pressure levels measured in the acoustic enclosure at different jet exit speeds for the smooth wall*

This indicates that the jet noise from the nozzle dominates the noise spectrum of this facility when there is no roughness present and, thus, that edge noise is not a dominant noise source in this facility. These results are important to the current study in that they indicate that any surface pressure measurements taken will not be contaminated by acoustic radiation originating from the flow over edges specific to the facility itself. It is difficult to make any statements about how quiet the overall noise level inside the facility is without comparing clean plate noise measurement with noise measurements of the facility when roughness is present. This kind of measurement is not the main focus of the measurements discussed in later chapters, but this type

of measurement is discussed in detail in Grissom (2007), and his data shows that the noise level of the facility described above is quite low.

2.6 Uncertainty Estimates

Uncertainty estimates of measured and estimated quantities to be presented in the following chapters were obtained and are discussed presently. The uncertainties of measured quantities are given in Table 2.2 below.

Measured Quantity Uncertainties		
Streamwise Velocity (Pitot)	u (m/s)	± 0.39
Streamwise Velocity (SHW)	u (m/s)	± 0.14
Normal Stress	u'^2 / U_m^2	± 0.0018
Spectral Density (SPL)	S_p (dB)	± 2.5

Table 2.2 Uncertainties in measured quantities in current study

The uncertainty of the velocity measurements taken using a Pitot probe was determined using a jitter analysis. The Pitot probe velocity measurement uncertainty were dominated by uncertainties associated with the calibration of the pressure transducer. The effects of uncertainties in the ambient temperature and pressure were found to be small. The velocity measurements taken with the single hotwire system were found to have an uncertainty of ± 0.14 m/s. Three main contributors to the uncertainty in the velocity and normal stress measurements were taken into account. These were the statistical uncertainty, the uncertainty associated with the calibration, and the uncertainty associated with the normalization. The mean velocity and turbulence uncertainties were calculated using method described in Ma (2003). The pressure spectral density measurements were determined to have an uncertainty of ± 2.5 dB. This uncertainty was comprised of the uncertainty due to placement of the transducer, the uncertainty due to the flow conditions, and the uncertainty of measurement system. The uncertainty associated with the transducer placement was determined to be approximately ± 1.0 dB. The spectral density varies with the velocity, u , to the fifth power. Given the uncertainty of the local flow velocity, the corresponding uncertainty of the spectral density was estimated to be ± 0.25 dB. The uncertainty of the measurement system was determined by taking successive calibrations of the same microphone which yielded an uncertainty in the spectral density of ± 1.25 dB. The root sum square of these uncertainties yield an uncertainty of approximately ± 2.25 dB in spectral density above.

There were also several calculated and estimated quantities whose uncertainties are presented below in Table 2.3. The boundary layer thickness was chosen as the height of the maximum velocity of the wall jet flow, and the uncertainty determining this height was estimated to be ± 3 mm. The uncertainties for the other boundary layer length scales shown below were calculated using a jitter analysis procedure. The definitions of these length scales will be given in a later chapter. The uncertainties in the calculated values these length scales stem from uncertainties in the probe position, uncertainties in the boundary layer thickness, and

uncertainties in the measured maximum velocity. For the displacement thickness and the momentum thickness, the major contributor to the uncertainty was determined to be the uncertainty in the probe position. For the mixing layer half height, the major contributor was seen to be the uncertainty of the measured maximum velocity.

The smooth wall skin friction estimates were determined to have an uncertainty of $\pm 5\%$. This uncertainty was estimated because the proximity of the George *et al.* (2000) skin friction correlation used was with that of other skin friction correlations considered to be reasonable (such as the Bradshaw and Gee (1967) correlation). For the rough wall skin friction coefficient estimates, a momentum balance approach was used and will be described in detail below. The estimated uncertainty of the rough wall skin friction estimates was determined to be approximately $\pm 8\%$ of the measured value. Jitter analysis reveals that uncertainties in the boundary layer thickness and in the momentum thickness measurements were determined to affect the uncertainty of the skin friction coefficient the most for the rough wall cases.

Calculated/Estimated Quantity Uncertainties		
Boundary Layer Thickness	δ (mm)	± 3
Displacement Thickness	δ^* (mm)	± 0.25
Momentum Thickness	θ (mm)	± 0.19
Mixing Layer Half Height	$y_{1/2}$ (mm)	± 1.9
Skin Friction Coefficient (Smooth Wall)	C_f	$\pm 5\%$
Skin Friction Coefficient (Rough Wall)	C_f	$\pm 8\%$

Table 2.3 *Uncertainties in calculated or estimated quantities*

3 Velocity Field of the Wall Jet With and Without Roughness

3.1 Smooth Wall Jet

3.1.1 Smooth Wall Jet Test Conditions

The smooth wall jet experimental data presented in this study were collected for range of flow conditions. Conditions were varied by changing the nozzle exit height or nozzle exit speed. Two nozzle heights were used (12.7 mm, and 25.4 mm). The nozzle exit speeds examined were nominally 20 and 30 m/s for the 25.4 mm nozzle height and 30, 40, and 60, m/s for the 12.7 mm nozzle height. These nozzle exit velocities and associated nozzle heights were chosen because they covered a large range of the facility operating envelope and because the effects of nozzle exit height on the measured wall jet flow could be investigated by holding the nozzle exit speed at 30 m/s and varying the nozzle height. For each of these flow conditions velocity and turbulence profiles were taken at a range of streamwise locations. In Table 3.1 below, the initial flow conditions are given as well as the boundary layer length scales and local flow conditions measured at the indicated test cases. However, before the table summarizing the initial and measured flow conditions can be presented, some of the flow parameters must be introduced formally.

At this time the author would like to formally introduce various boundary layer length scales that will be referred to throughout the rest of this document. The length scales $y_{1/2}$ is defined as the distance from the wall to the height above the velocity maximum where the flow velocity has decreased to half of the maximum velocity, and δ , otherwise noted as the boundary layer thickness is defined as the distance from the wall to the height at which the maximum flow velocity occurs at a given streamwise location. Two other boundary layer length scales that will be referred to in the coming analysis are the displacement and momentum thicknesses, δ^* and θ .

$$\delta^* = \int_0^\delta \left(1 - \frac{u}{U_m}\right) dy \quad (3.1)$$

$$\theta = \int_0^\delta \left(1 - \frac{u}{U_m}\right) \frac{u}{U_m} dy \quad (3.2)$$

where the edge velocity used in the definitions of these length scales for regular turbulent boundary layers has been replaced by the maximum velocity, U_m .

The coordinate system used throughout this study can be described as follows. The origin is placed at the nozzle exit (junction between the aluminum plate and the nozzle) on the plate surface at the spanwise center of the nozzle. The streamwise dimension, x , is measured from the origin and increases with downstream distance from the nozzle exit. The vertical

dimension, y , is measured positive from the plate surface, and the spanwise dimension, z , is measured from the spanwise centerline of the flow facility.

Test Condition	U_o (m/s)	b (mm)	x (mm)	z (mm)	Re_j	$y_{1/2}$ (mm)	δ (mm)	δ^* (mm)	θ (mm)	Re_δ	Re_θ
A	30.0	12.7	953	0	20972	80	13.0	0.79	0.60	8552	394
A	29.9	12.7	1257	0	20893	101	13.7	1.06	0.83	7921	478
A	30.1	12.7	1410	0	21059	114	15.2	1.00	0.78	8165	419
A	29.9	12.7	1562	0	20902	127	19.7	1.22	0.91	10078	468
A	29.9	12.7	1867	0	20971	156	23.4	1.55	1.19	10915	556
A	29.6	12.7	2172	0	20735	178	27.8	2.47	1.89	12569	852
B	39.7	12.7	953	0	27714	80	10.8	0.71	0.53	9296	461
B	39.7	12.7	1257	0	27699	105	13.0	0.90	0.69	9831	525
B	39.8	12.7	1410	0	27747	116	15.9	1.00	0.78	11311	554
B	39.9	12.7	1562	0	27823	125	18.2	1.21	0.95	12358	647
B	39.7	12.7	1867	0	27781	152	24.1	1.34	1.04	14666	631
B	39.6	12.7	2172	0	27631	173	24.1	1.43	1.10	14598	669
C	59.9	12.7	953	0	41644	84	10.8	0.91	0.56	14528	760
C	60.2	12.7	1257	0	41895	106	14.5	1.03	0.70	17016	819
C	59.8	12.7	1410	0	41571	118	15.2	1.18	0.80	16661	882
C	59.6	12.7	1562	0	41618	125	17.4	1.16	0.82	18066	854
C	59.7	12.7	1867	0	41536	150	19.7	1.43	0.98	18445	924
C	59.8	12.7	2172	0	41642	182	23.4	1.74	1.22	21068	1097
D	20.1	25.4	953	0	27996	90	12.2	0.86	0.65	7596	401
D	20.0	25.4	1257	0	27920	113	17.4	1.14	0.90	9356	483
D	19.9	25.4	1410	0	27755	125	15.9	1.08	0.82	7856	403
D	19.8	25.4	1562	0	27686	132	18.9	1.27	0.95	8989	453
D	19.7	25.4	1867	0	27636	160	22.6	1.34	1.02	9893	444
D	20.5	25.4	2172	0	28637	187	27.8	1.70	1.32	11493	547
E	29.7	25.4	953	0	41472	90	12.2	0.81	0.61	11087	551
E	29.9	25.4	1257	0	41721	112	15.9	1.09	0.86	12880	696
E	30.0	25.4	1410	0	41691	124	15.2	1.32	1.03	11403	773
E	30.0	25.4	1562	0	41780	137	17.4	1.38	1.04	12595	750
E	29.6	25.4	1867	0	41362	160	23.4	1.48	1.13	15091	732
E	30.0	25.4	2172	0	41974	179	25.6	1.84	1.49	15507	900
F	21.2	12.7	38	0	16255	-	5.0	0.35	0.17	6430	222
F	30.6	12.7	38	0	23457	-	3.3	0.28	0.13	6097	249
F	40.0	12.7	38	0	30655	-	4.4	0.26	0.13	10535	310
F	22.0	25.4	38	0	33714	-	7.6	0.37	0.19	10141	251
F	30.6	25.4	38	0	46916	-	5.8	0.31	0.16	10673	304
F	38.2	25.4	38	0	58593	-	5.0	0.26	0.14	11581	321
F	30.6	12.7	38	305	23470	-	6.4	0.30	0.16	11747	290
F	30.7	12.7	38	-305	23549	-	4.4	0.28	0.14	8092	254
F	30.6	12.7	38	-	23471	-	-	-	-	-	-
G	30.1	12.7	953	0	23065	79	9.4	0.98	0.73	7310	566
G	40.3	12.7	953	0	30871	80	16.4	1.06	0.80	16628	811
G	19.8	25.4	953	0	30390	89	13.2	0.94	0.69	9888	516
G	29.7	25.4	953	0	45562	93	16.4	0.94	0.71	17280	746
G	29.9	12.7	953	-	22923	-	-	-	-	-	-
G	39.9	12.7	953	-	30551	-	-	-	-	-	-
G	20.0	25.4	953	-	30668	-	-	-	-	-	-
G	30.0	25.4	953	-	45902	-	-	-	-	-	-
G	29.9	12.7	953	406	22932	81	14.5	1.04	0.79	11237	611
G	29.8	12.7	1867	0	22840	152	24.6	2.29	1.74	13999	991
G	39.3	12.7	1867	0	30127	154	20.2	1.64	1.24	14591	896
G	19.7	25.4	1867	0	30170	154	18.9	1.81	1.35	10620	758
G	29.6	25.4	1867	0	45402	158	20.2	1.75	1.36	15974	1075
G	29.9	12.7	1867	-	22896	-	-	-	-	-	-
G	39.8	12.7	1867	-	30495	-	-	-	-	-	-
G	19.8	25.4	1867	-	30385	-	-	-	-	-	-
G	29.9	25.4	1867	-	45786	-	-	-	-	-	-
G	29.9	12.7	1867	-406	22917	138	23.4	1.83	1.38	13005	770

Table 3.1 Smooth wall jet conditions for velocity profile measurements

The test cases presented in Table 3.1 above are grouped into seven main test conditions. Conditions A through E designate one set of nominal initial flow conditions. For example, all of the measured data from test condition A were taken for a nozzle exit velocity of, nominally, 30 m/s, and a nozzle exit height of 12.7 mm. Test conditions F and G denote the measured flow

very near the nozzle exit (flow was measured 38.1 mm aft of the nozzle exit) and two-dimensionality tests, respectively. Note that for the G test conditions in the table above there are several entries that do not have a z value listed. These measurements were horizontal profiles taken across the span of the flow.

In the pages that follow, measurements of the smooth wall jet flow will be presented and discussed. First, the measurements of the flow at the nozzle exit will be presented. Then tests demonstrating the two-dimensionality of the wall jet flow will be presented. This will be followed by a brief section comparing the current wall jet flow with that typically seen in other wall jet studies. An investigation into the streamwise development, variation with initial flow conditions, and similarity of the wall jet flow will then be given. The skin friction for the smooth wall jet flow will be estimated using the method of George *et al.* (2000), and will be discussed briefly followed by a discussion of the wall jet flow below the velocity maximum (or inner region). The wall jet flow will be presented in inner coordinates, and both the mean flow and turbulent character of the wall jet flow near the wall will be discussed. The velocity spectra for the smooth wall jet flow will also be presented and discussed.

3.1.2 The Nozzle Exit

The flow that forms the wall jet is exhausted through a rectangular opening 1207 mm wide with a height, b , which can be varied. Vertical mean velocity profiles were taken at a distance, x , of 38.1 mm aft of the nozzle exit with a flattened Pitot probe for both 12.7 mm and 25.4 mm nozzle heights. The profiles could not be taken directly at the nozzle exit due to the geometry of the probe and the round lip on the upper portion of the nozzle exit. These profiles can be seen in Figure 3.1 and in Figure 3.2 below.

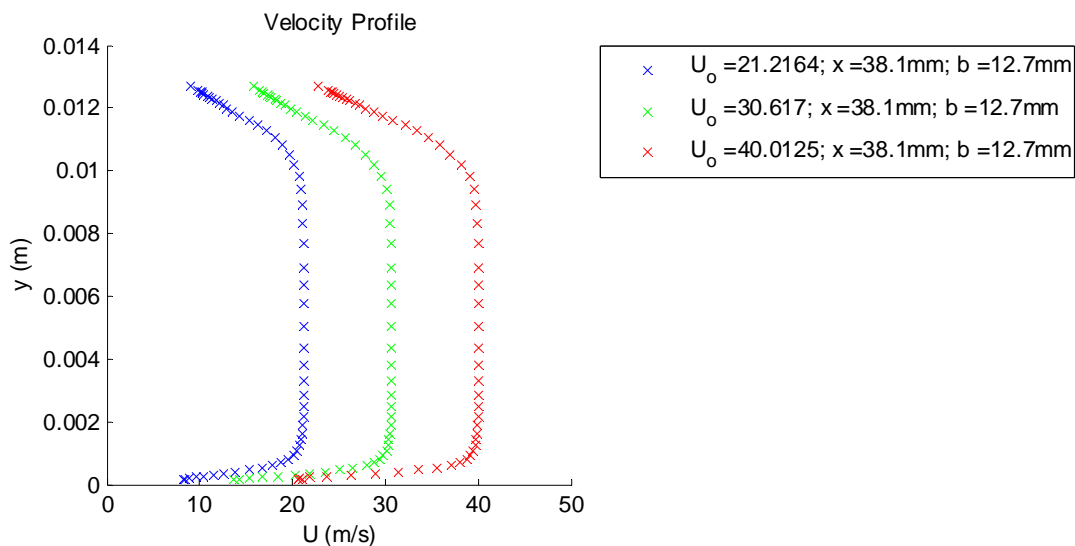


Figure 3.1 Vertical nozzle exit profiles taken just aft (38.1 mm) of the nozzle exit.

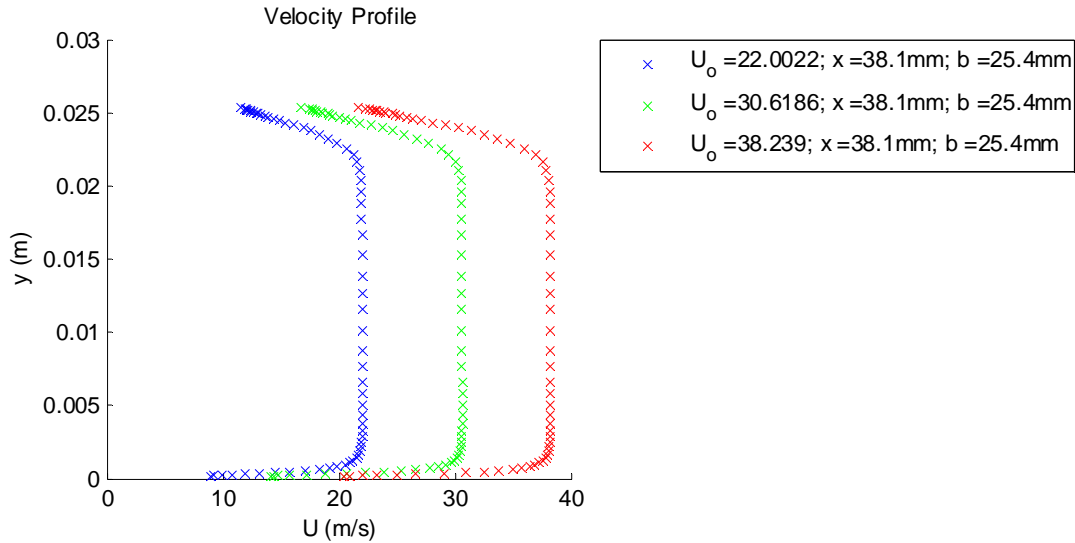


Figure 3.2 Vertical nozzle exit profiles taken just aft (38.1 mm) of the nozzle exit.

In both of the figures above, the profiles were taken for nozzle exit speeds of 20, 30, and 40 m/s and are taken from the measurements of test condition F in the table above. The nozzle exit speed was limited by the capacity of the centrifugal fan for this test case. The nozzle exit Reynolds numbers, Re_j (based on b and U_o), varied from 16000 to 58500 for the nozzle exit profiles shown above.

There is a sharp increase in velocity at the bottom of the profiles followed by a region of nearly constant velocity cover the major portion of the profiles. Then there is a decrease in velocity at the top of the profile that is more gradual than the increase at the bottom. This gradual region of velocity decrease is present due to the rounded lip of the upper portion of the nozzle shown in Figure 2.4 above and the fact that the profile is taken 38.1 mm aft of the nozzle exit. The flow is very uniform over nearly the entire nozzle height and varies by less than ± 0.05 m/s.

Figure 3.3 shows the velocity profiles from Figure 3.1 normalized on the measured nozzle exit velocity and nozzle height.

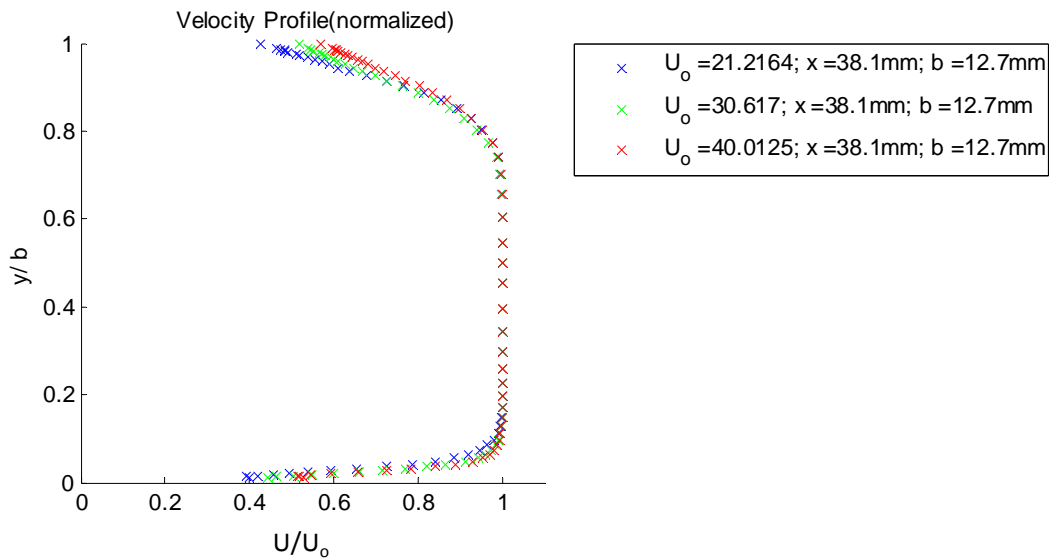


Figure 3.3 Nozzle exit profiles normalized on the nozzle height and nozzle exit velocity

The height in the profiles at which the gradual decrease in velocity begins is roughly 83% of the nozzle height for the cases where b is equal to 25.4 mm and 69% of the nozzle height when b is equal to 12.7 mm. This difference is likely due to the fact that the nozzle exit profiles were taken some small finite distance downstream of the nozzle exit, and that the profiles taken for a nozzle height of 12.7 mm are taken effectively farther downstream relative to the nozzle height than the profiles taken at a nozzle height of 25.4 mm.

The uniformity of the nozzle in the spanwise direction was also investigated to ensure that the flow being produced from the nozzle exit was as close to being uniform and two-dimensional as possible. In order to show that the nozzle exit flow was uniform, vertical profiles were taken off centerline for an initial flow velocity of 30 m/s and a nozzle height of 12.7 mm. These are compared in Figure 3.4 below

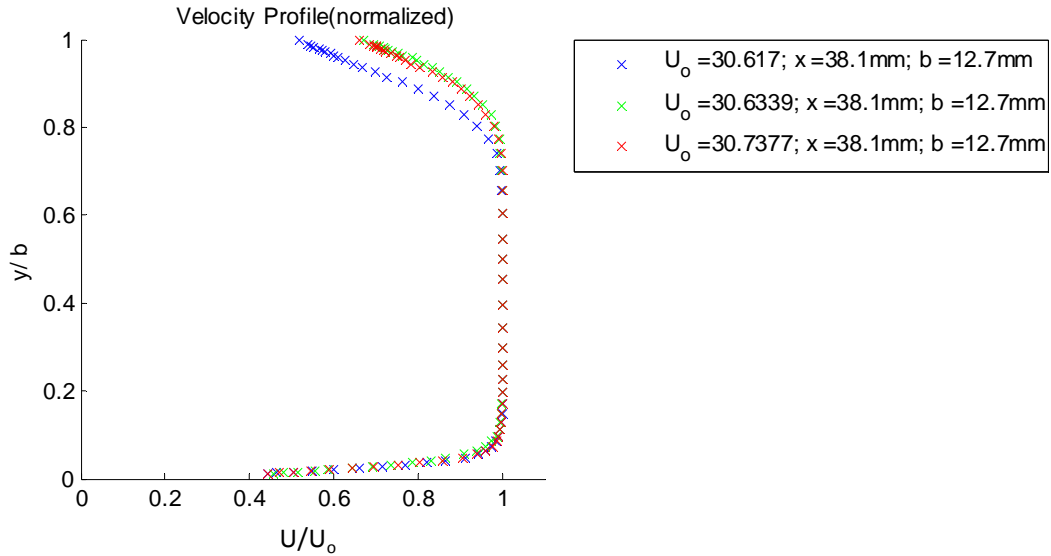


Figure 3.4 Vertical nozzle exit profiles examining the uniformity of the nozzle exit flow; blue × corresponds to the nozzle centerline or $z = 0$; green × corresponds to a spanwise location $z = -305\text{ mm}$; red × corresponds to a spanwise location $z = +305\text{ mm}$

The flow is quite uniform over a range of spanwise locations. However, there is a difference in the profile taken at the centerline and the other profiles in the figure. The velocity profile reveals a narrower jet at the centerline than at the other two profile locations. It is believed that this effect is due to the joint at the center of the PVC nozzle. While great care was taken to join the two pieces together as seamlessly as possible, oil flow visualization showed slight deviations in separation location along the upper portion of the nozzle exit near the centerline. However, as will be shown below, this effect is local and does not affect the two-dimensional nature of the flow downstream.

Finally, a horizontal profile was taken at the nozzle half height at the same initial flow conditions as those in Figure 3.4 above. This profile is shown in Figure 3.5 below and shows that the flow is very uniform across the entire span of the nozzle. The velocity is very uniform across the span of the nozzle exit and varies by less than $\pm 0.5\%$.

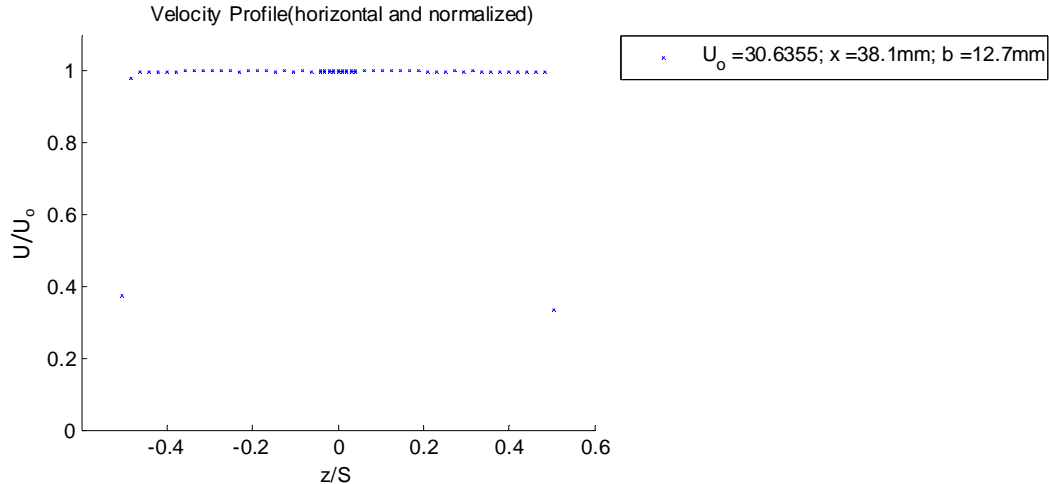


Figure 3.5 Horizontal nozzle exit velocity profile normalized on the nozzle exit velocity and the nozzle span, S

3.1.3 Two Dimensionality of the Flow

The wall jet is not a fundamentally two dimensional flow. The flow is exhausted into still air from a nozzle exit and a shear layer is created at the boundary of the still air and the moving stream. Entrainment of the still air occurs along this shear layer causing the jet to spread, and thus a fraction of the momentum in the streamwise direction is redirected into the spanwise direction causing a velocity component in the spanwise direction outward from the centerline of the nozzle. Very near the nozzle, this induced velocity starts near the spanwise limit of the nozzle exit, but as the flow develops downstream spanwise velocity components would be expected to be induced closer and closer to the nozzle centerline. Studies of the lateral spreading of the wall jet have been conducted by Naib (1968), Sforza and Herbst (1970), and Craft and Launder (2000) among others. While the lateral spreading of wall jet flows is of interest, it is a phenomenon that has been studied extensively and was not considered to be of primary importance in the current study. In the current study, it is not only advantageous to consider the wall jet flow as having a mean two dimensional character for analysis purposes, but necessary to have a region of the wall jet flow over the plate where there are no significant lateral velocity components for the measurements of the rough wall surface pressure fluctuations to be discussed later. In order to map the region of mean two dimensional flow, horizontal profiles were taken at two locations downstream of the nozzle exit over a range of conditions. Vertical profiles were taken off-centerline and compared with those at the same streamwise location on the nozzle centerline to examine two-dimensionality.

Figure 3.6 shows horizontal profiles taken at three different streamwise locations of x equal to 38, 953, and 1867 mm downstream of the nozzle exit for a nozzle height, b , of 12.7 mm and a nozzle exit velocity, U_o , of 30 m/s. The profiles seen in the figure below were taken from test conditions F and G in Table 3.1 above. The profile closest to the nozzle exit was taken at a height above the plate equal to half of the nozzle height, or 6.35 mm. The other two profiles were taken at the height of the velocity maximum, δ , obtained from vertical mean velocity profiles taken at the same initial flow conditions yielding $y = 9.4$ mm at $x = 943$ mm and $y = 14.6$ mm at $x = 1867$ mm. These heights were the measured boundary layer thicknesses

associated with the vertical measured profiles on the spanwise centerline for the G test cases listed in the table above.

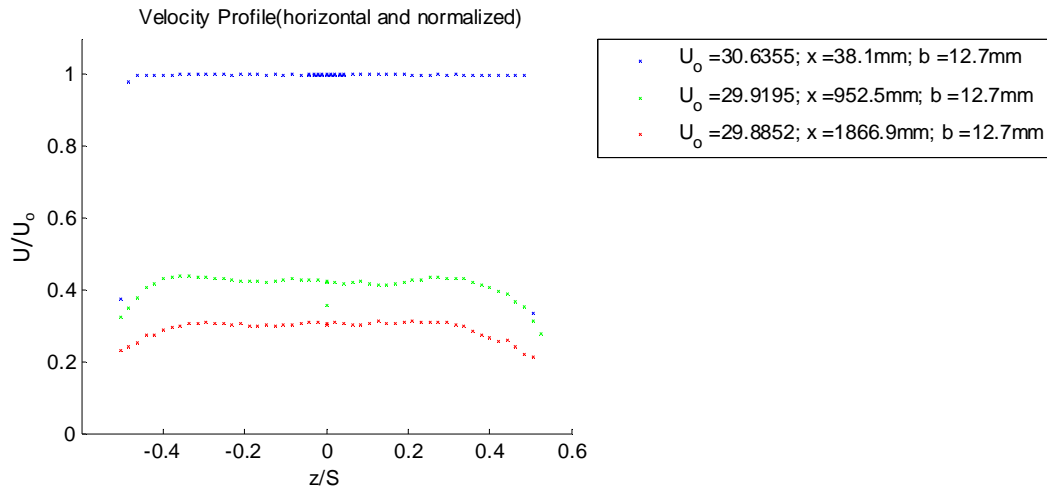


Figure 3.6 profiles normalized on U_o and nozzle span, S , showing the variation with streamwise distance downstream

As the distance downstream from the nozzle exit is increased, the region of spanwise uniformity shrinks to just over $0.8 S$ (975 mm) at $x = 953$ mm and to $0.67 S$ (817 mm) at $x = 1867$

Changing the nozzle exit velocity from 30 to 40 m/s (Figure 3.7) does not significantly change the size of this two-dimensional region.

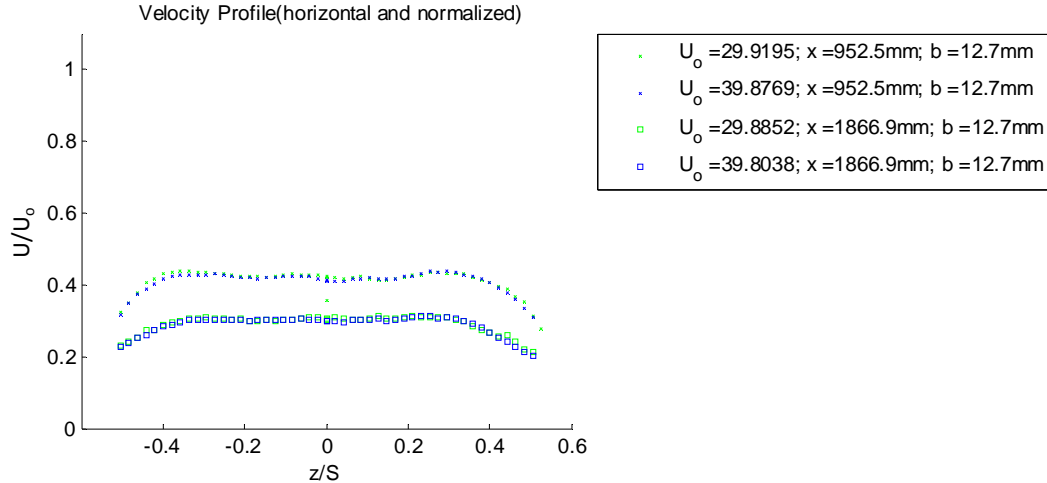


Figure 3.7 Horizontal profiles normalized on U_o and nozzle span, S , showing the effect of nozzle exit velocity

Changing the nozzle height for a nozzle exit speed of 30 m/s results in a higher maximum velocity but causes almost no change in the spanwise extent of the two dimensional flow.

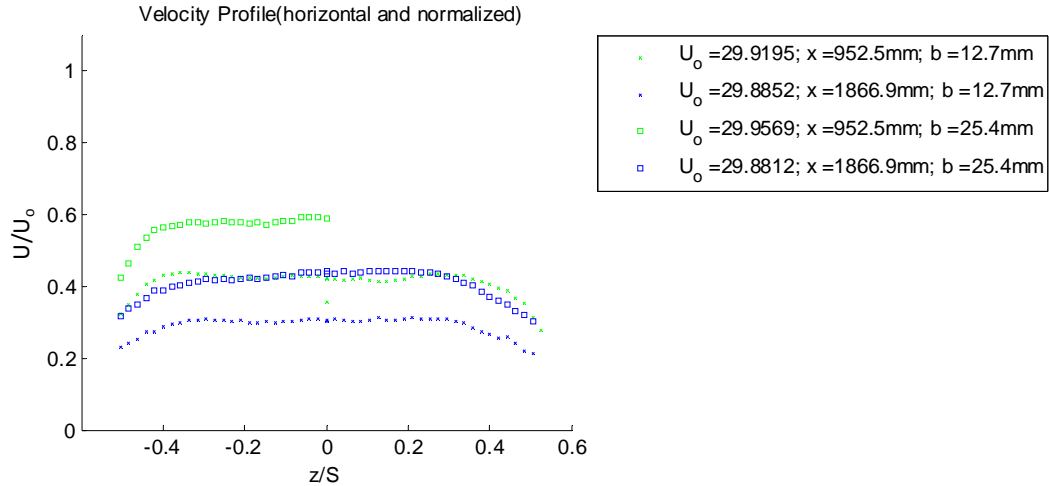


Figure 3.8 Horizontal velocity profiles normalized on U_o and S investigating the effect of variations in nozzle height, b

Vertical profiles were taken at the spanwise limits of the two-dimensional region indicated in the figures above and compared with profiles taken at center span for the same nominal conditions. This was done for a nozzle height of 12.7 mm and a nominal nozzle exit speed of 30 m/s at x locations of 953 and 1867 mm downstream of the nozzle exit (see Table 3.1).

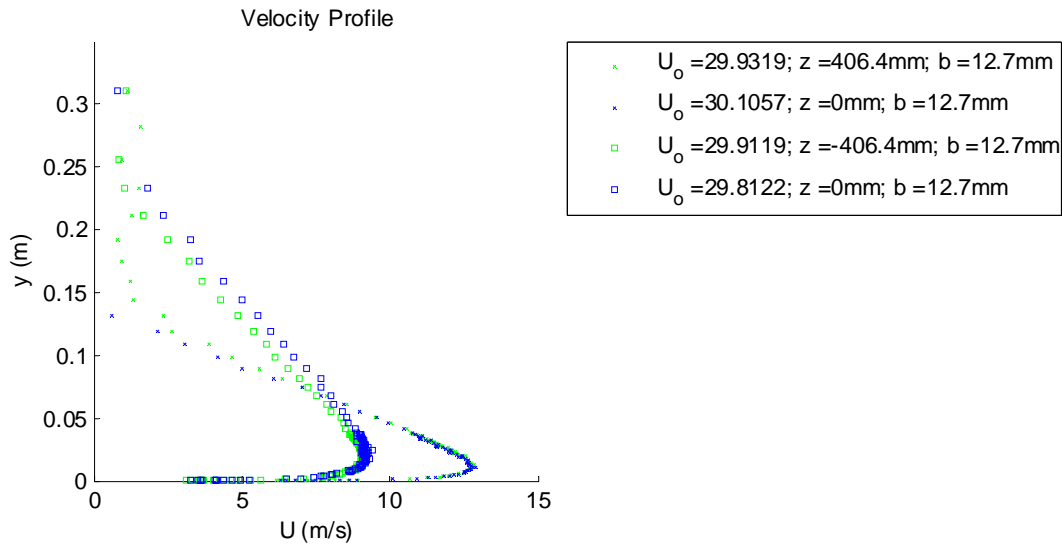


Figure 3.9 Vertical profiles showing the effect of spanwise position, z ; \times symbols denote a streamwise profile location of $x = 953$ mm; \square symbols denote a streamwise profile location of $x = 1867$ mm

The off-center span profiles show fair agreement with those taken at the center span, especially throughout the lower portion of the profile and into the lower portion of the shear layer. The profiles seen above in Figure 3.9 appear to be indicative of typical wall jet velocity profiles and normalize well on U_m and $y_{1/2}$ as shown in Figure 3.10 below. The normalized profiles below show behavior that is consistent with that observed by numerous workers who have studied wall

jet flows. The form of the current wall jet flow compared with that seen in prior studies is discussed in more detail in the following section.

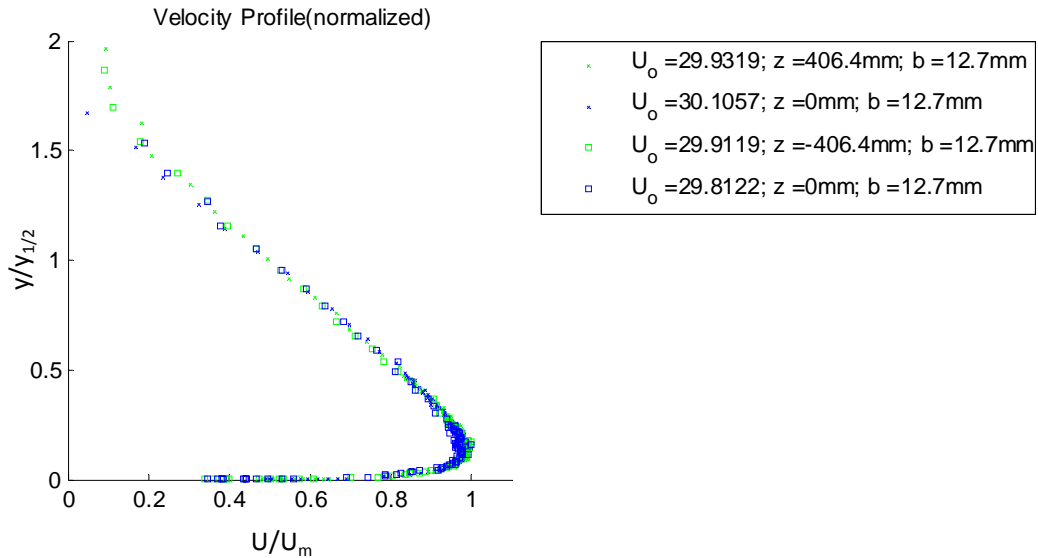


Figure 3.10 Normalized velocity profiles showing the effect of the spanwise position, z

It is concluded, therefore, that there is a region roughly 810 mm wide that extends at least 1867 mm downstream of the nozzle exit over which the flow behaves like a mean two-dimensional flow. Any tests that involved rough surfaces conducted by the author, or by Grissom (2007) or Grissom *et al.* (2006 and 2007), were conducted by placing the rough surfaces in this region on the aluminum plate.

3.1.4 Overall Wall Jet Characteristics

One of the first useful observations of wall jets from various workers was that mean vertical profiles tended to collapse when they were normalized on the maximum velocity, U_m , and on the height above the maximum velocity at which the flow velocity decreases to half of the maximum, $y_{1/2}$ (these wall jet quantities are defined in Figure 1.1 above). This scaling is really only valid away from the wall surface because near the wall the profiles scale differently due to viscosity. However, if one plots mean velocity profiles normalized in this way, they do tend to collapse regardless of their initial conditions in regions away from the wall. Data from the current study was compared with that from other studies. In Figure 3.11 below, one can see several profiles plotted on top of one another.

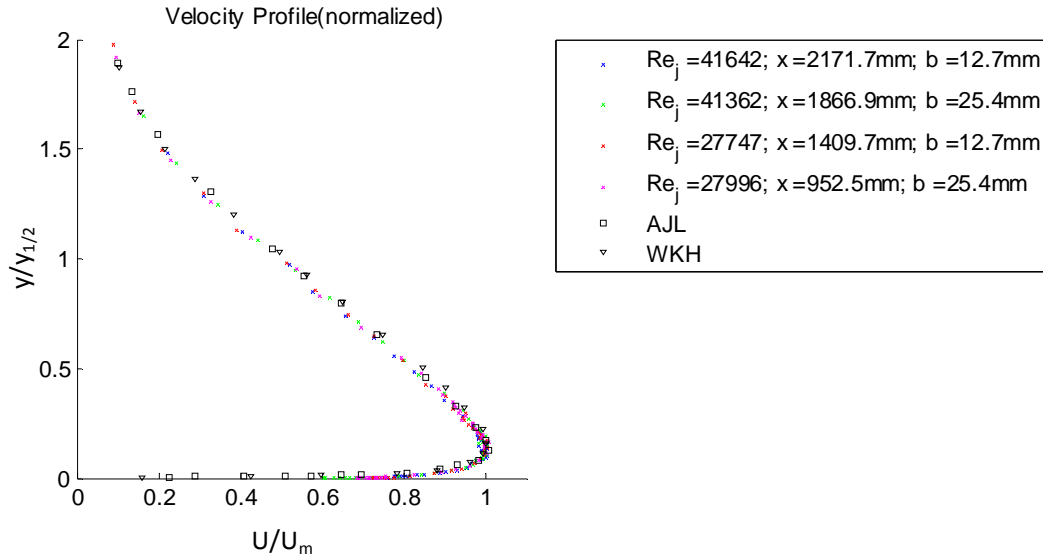


Figure 3.11 Current normalized mean profiles compared with previous studies; the Abrahamsson et al. (1994) data (AJL) was taken at a jet Reynolds number of 10,000; the Wagnanski et al. (1992) data (WKH) was taken at a jet Reynolds number of 19,000

The current profiles in Figure 3.11 above were taken over a range of nozzle exit Reynolds numbers and x locations. The nozzle exit Reynolds numbers ranged from 28000 to 41500 while the jet exit Reynolds numbers from the past studies shown ranged from 10000 to 19000. The profiles from the current study shown were taken at 4 of the 5 main test conditions presented in Table 3.1 above (B, C, D, and E). The x positions presented in this figure extend from 953 mm to 2172 mm downstream of the nozzle exit. All profiles presented and all surface pressure measurements presented below were measured inside of this range of streamwise distances from the nozzle exit. One can see that even though the initial flow conditions of the profiles shown vary widely, the profiles still collapse into a tight band out to a height over $y/y_{1/2}$ equal to 2.

When all measured profiles are plotted in this way, the results can be seen in Figure 3.12 below. The profiles collapse very well regardless of initial flow conditions.

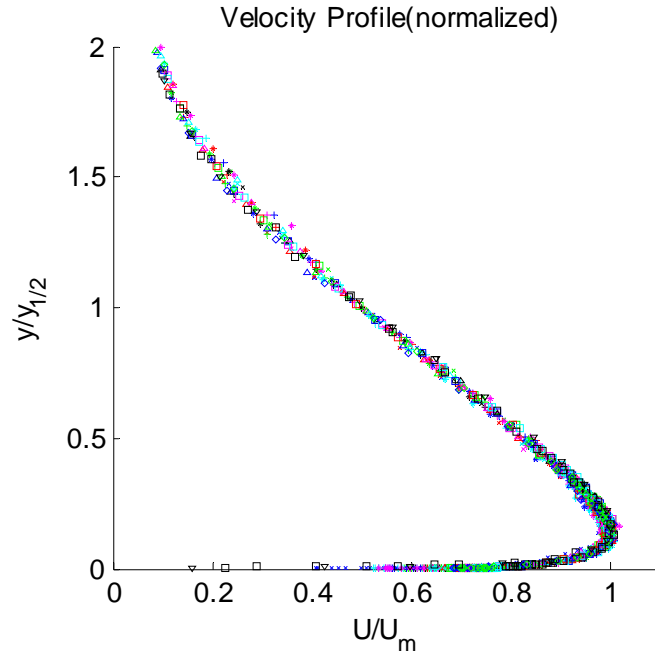


Figure 3.12 All measured profiles normalized on outer variables, U_m and $y_{1/2}$

Another way in which wall jets are often characterized involves a scaling on the nozzle exit momentum. This approach was used by Narasimha *et al.* (1973) and employed by Wygnanski *et al.* (1992) afterwards. This approach is quite useful because from it relations estimating flow properties of the wall jet as a function of downstream distance from the nozzle can be developed and are given as equations 1.9 and 1.10 above. These relations will be discussed in more detail later. A comparison with the results of Narasimha *et al.* (1973), Wygnanski *et al.* (1992), and the results from the current study will be investigated. In Figure 3.13 below, the fits proposed by Narasimha *et al.* (1973) and Wygnanski *et al.* (1992) for the dependency of the maximum wall-jet velocity on $\frac{(x-x_o)bU_0^2}{\nu^2}$ are plotted along with the measured data from the current study (all data from test conditions A – E noted in Table 3.1 above) and a fit from the current study. Note the data presented below is referenced as clean plate data in the legend indicating that these data are smooth wall data. The nozzle exit momentum flux can be well approximated by $U_o^2 b$ and x_o is the location of the virtual origin which is considered to be the actual origin in the current flow and is equal to 0. The exponent, n , from equation 1.7 above was experimentally found to be equal to -0.512, and the constant A_u was found to be 3.75. Wygnanski *et al.* (1992) and Narasimha *et al.* (1973) presented values of -0.428 and -0.506, respectively for n .

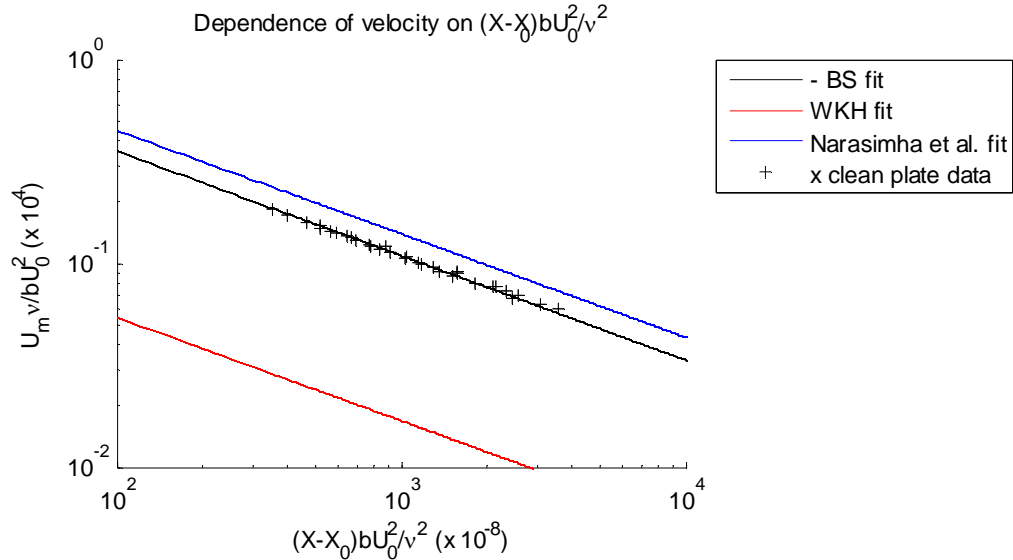


Figure 3.13 *Narasimha et al. (1973) proposed scaling showing the variation of U_m*

In Figure 3.14 below, the scaling proposed by Narasimha *et al.* (1973) was applied to the current data to show the variation of $y_{1/2}$. Again, the fits presented by Wygnanski *et al.* (1992) and Narasimha *et al.* (1973) are shown as well. The exponent, m , from equation 1.8 was found to be 0.914, and the constant A_y was found to be 1.52. Wygnanski *et al.* (1992) and Narasimha *et al.* (1973) presented values of 0.804 and 0.91, respectively for m .

The agreement of the slope between the results from the current study and those of Wygnanski *et al.* (1992) and Narasimha *et al.* (1973) (which is what counts) is near perfect. Still the experimental results from this study are bracketed by those of the other two studies mentioned. If one applies the scaling shown in Figure 3.11 above or that proposed by Narasimha *et al.* (1973) to the current study's data, a very strong case could be made stating that the current flow is indeed consistent with wall jet flows studied previously by various other workers. This is an important result because it determines the kind of flow that is being dealt with. Now knowledge of wall jet flows can be leveraged in the analysis of rough wall jet flows, surface pressure characteristics, and radiated noise characteristics.

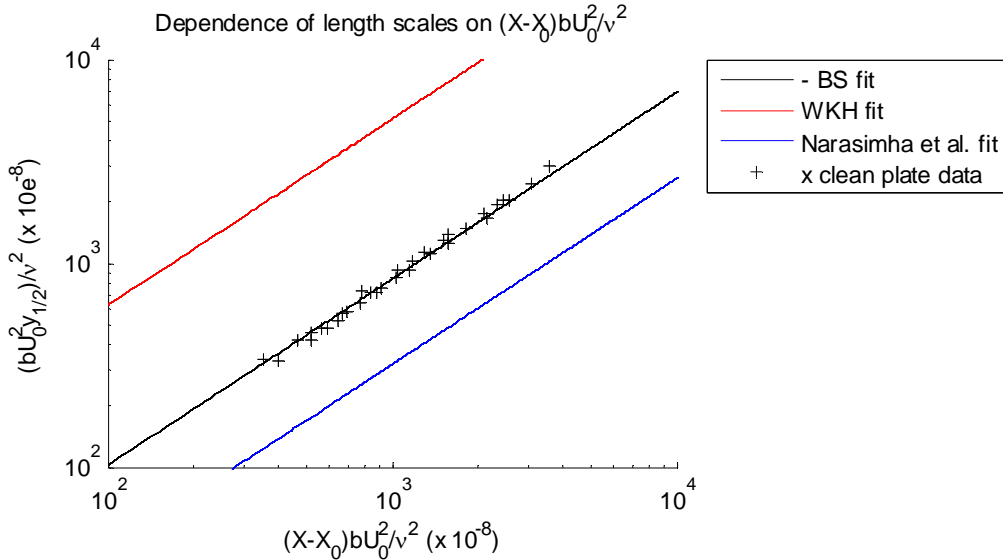


Figure 3.14 Narasimha et al. (1973) proposed scaling showing the variation of $y_{1/2}$

3.1.5 Streamwise development of the Wall Jet

When one considers the effects of the streamwise location of the measurement on the results it is expected that the wall jet profiles will show a velocity decay and an increase in $y_{1/2}$ as the measurement location is moved downstream. This is expected because of the loss of momentum due to viscosity and due to the entrainment of the still laboratory air by the shear layer. Given these considerations it is no surprise to see these expected trends born out in the profiles shown in Figure 3.15 below. These profiles were taken at test condition A (referenced in Table 3.1 above). Profiles taken at other initial flow conditions show the same kind of variation with downstream distance.

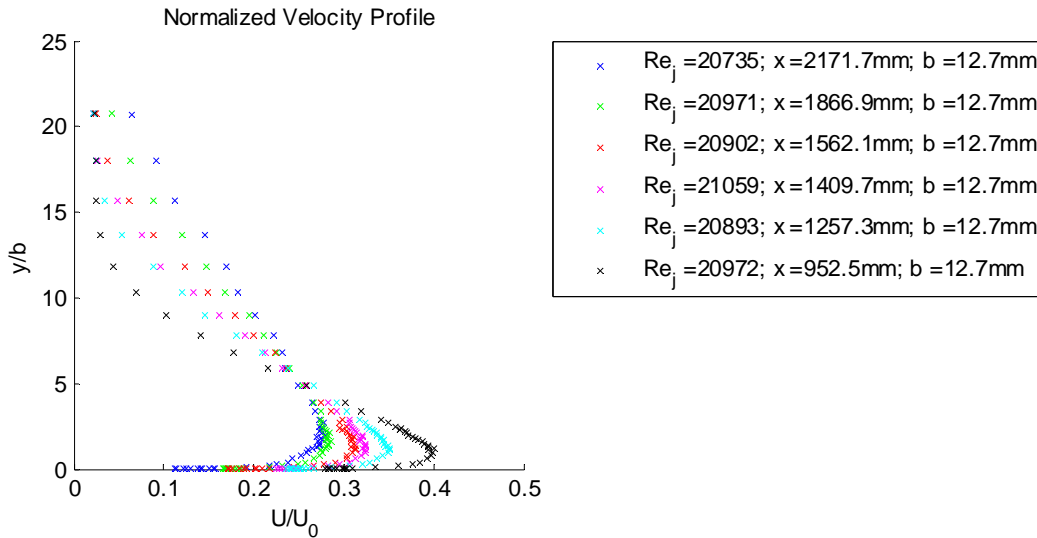


Figure 3.15 Nondimensional vertical mean velocity profiles showing the effects of axial measurement location, x

The behavior of the maximum flow velocity with downstream distance is seen in Figure 3.16 below. Here, the maximum velocity is plotted non-dimensionally against the nondimensional streamwise distance downstream. The nondimensional maximum velocities shown were obtained for the same test cases as seen in Figure 3.15 above.

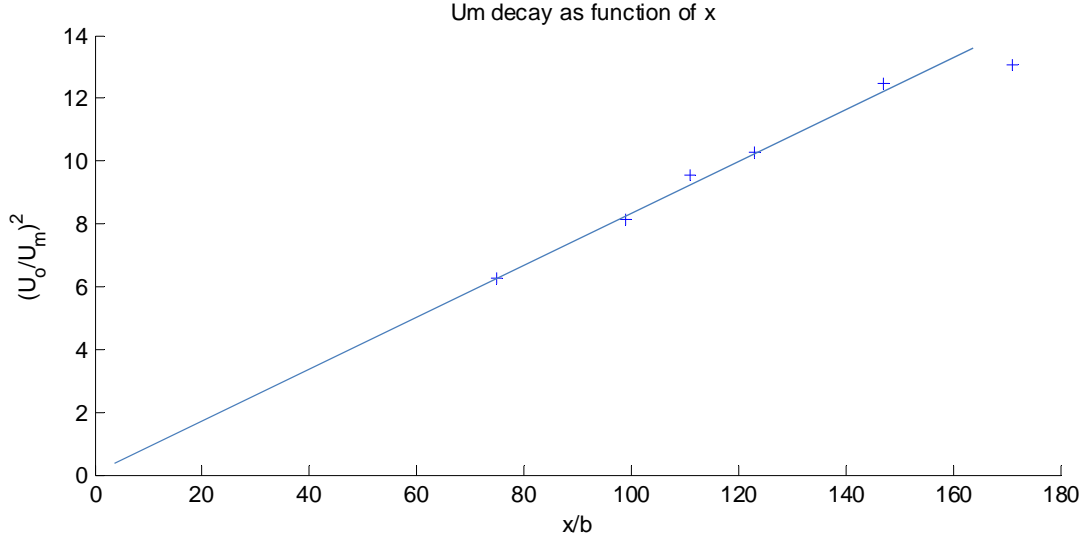


Figure 3.16 The decay of the velocity maximum vs. downstream distance

From Figure 3.16 the maximum velocity can be seen to decay closely as the downstream distance to the -0.5 power. Wagnanski *et al.* (1992) use a power law formulation and suggest that the maximum velocity varies as the downstream distance to the -0.47 power, and Narasimha *et al.* (1973) propose a -0.506 variation using a power law formulation. Data from the current study shows a -0.512 variation with downstream distance in the following section.

3.1.6 Wall Jet Self Similarity

From the discussion in chapter 1, relations for the maximum velocity, U_m , as well as $y_{1/2}$ are determined. Equations 1.7 and 1.8 give these relations and can be rearranged to show how U_m and $y_{1/2}$ are dependent on the nozzle exit Reynolds number and the Reynolds number based on the distance downstream of the origin:

$$\frac{U_m}{U_o} = A_u Re_j^{n+1} Re_x^n \quad (3.3)$$

$$\frac{Y}{b} = A_y Re_j^{m-2} Re_x^m \quad (3.4)$$

where A_u and A_y are empirically determined constants, m and n are empirically determined exponents, and Y is the boundary layer length scale of interest (δ , δ^* , θ , $y_{1/2}$). A_u was determined to be 3.75, and n was found to be -0.512. The exponent m was found to be 0.914 for all boundary layer length scales because these length scales are shown to be constant multiples of one another or very nearly so in Figure 3.21 and Figure 3.22 below. The constant A_y was

determined to be 1.52, 0.2138, 0.0105, and 0.0077 for $y_{1/2}$, δ , δ^* , and θ , respectively. Given these empirically determined constants and exponents, estimations of the maximum velocity and boundary layer length scales can be obtained for any given set of initial flow conditions and streamwise position. This allows for a continuous interpolation of flow parameters between test cases or an estimation of flow parameters in the absence of measured data.

For all of the measurement cases in the current study, the measured values of the maximum velocity were compared with those estimated by this method. The results are shown in Figure 3.17 below. The results indicate that the estimated values of the maximum velocity are slightly higher than the measured values, but the curve fit shown is consistent with the measured maximum velocities presented in Grissom *et al.* (2007) as well as those shown here. There is good agreement with the measured and estimated values of maximum velocity in the wall jet flows analyzed, and one can confidently estimate the maximum velocity of a wall jet flow in this facility knowing only the initial flow conditions and streamwise position. It should be noted that the data shown below covers a range of initial nozzle exit speeds and heights ranging from 20 – 60 m/s and 12.7 – 25.4 mm, respectively. The most outlying point on this figure shows a difference of less than 1.25 m/s in the measured and estimated values for maximum velocity.

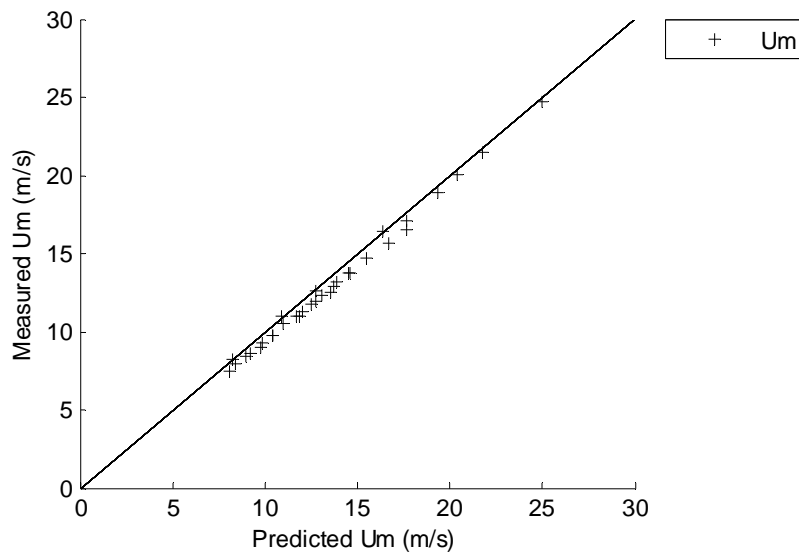


Figure 3.17 Measured wall jet maximum velocities vs. estimated values for all test cases

The same procedure was applied in the estimation of the length scale $y_{1/2}$. The results are shown in Figure 3.18 below.

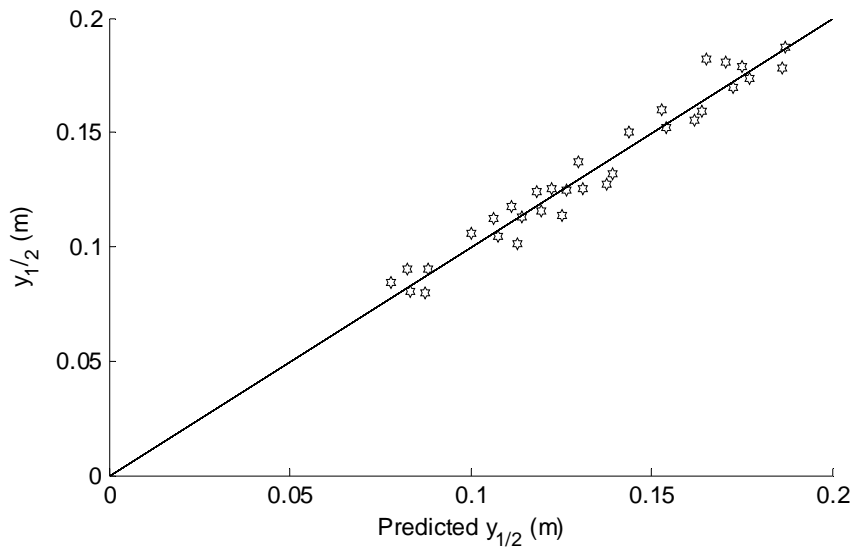


Figure 3.18 Measured $y_{1/2}$ values vs. estimated values for all test cases

One can see from Figure 3.18 above that the estimated values of $y_{1/2}$ are quite good as well. The most outlying point shows a difference less than 17 mm, or to within 9% of the measured value, between the measured and estimated values. This is substantially larger than the uncertainty for $y_{1/2}$ which was estimated to be ± 1.85 mm. However, this method of estimating the flow properties is still a very useful method because it allows for the scaling of the surface pressure measurements taken in the current wall jet flows without necessitating the aerodynamic measurements to go along with the pressure fluctuation measurement cases.

George *et al.* (2000) suggests that the length scale $y_{1/2}$ could just as easily be replaced by δ with no loss of generality implying that δ is a constant multiple of $y_{1/2}$. If this is true of δ , then perhaps it is true of other boundary layer length scales such as δ^* and θ . To test this, these boundary layer length scales were measured for all of the wall jet vertical profiles taken in test conditions A – E (referenced in Table 3.1 above) and plotted against the downstream distance. These measured values are presented in Figure 3.19 below.

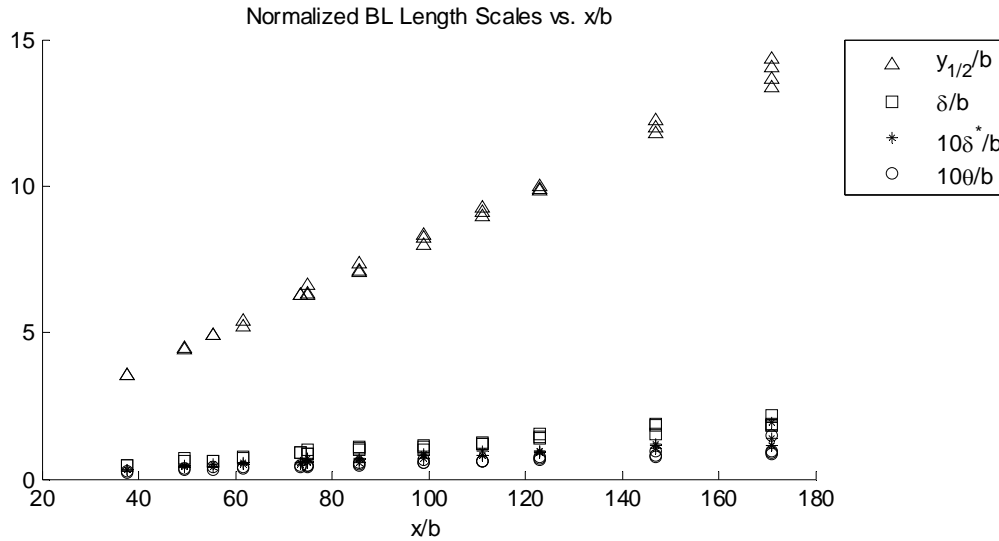


Figure 3.19 Nondimensional boundary layer length scales vs. x/b for

From this figure it is difficult to determine if a case could be made for considering the other boundary layer length scales to be constant multiples of $y_{1/2}$. If the boundary layer, displacement, and momentum thicknesses are viewed on a larger scale as shown below in Figure 3.20, there is seen a dependence on the initial flow speed which is evidenced by the groupings of the data points at several of the x/b locations. However, the measured boundary layer, displacement, and momentum thickness data does not suggest an exponential variation with downstream distance that is any different than that seen for $y_{1/2}$. In light of these observations, it seems that it would be acceptable to consider the boundary layer length scales as being constant multiples of one another for estimation purposes.

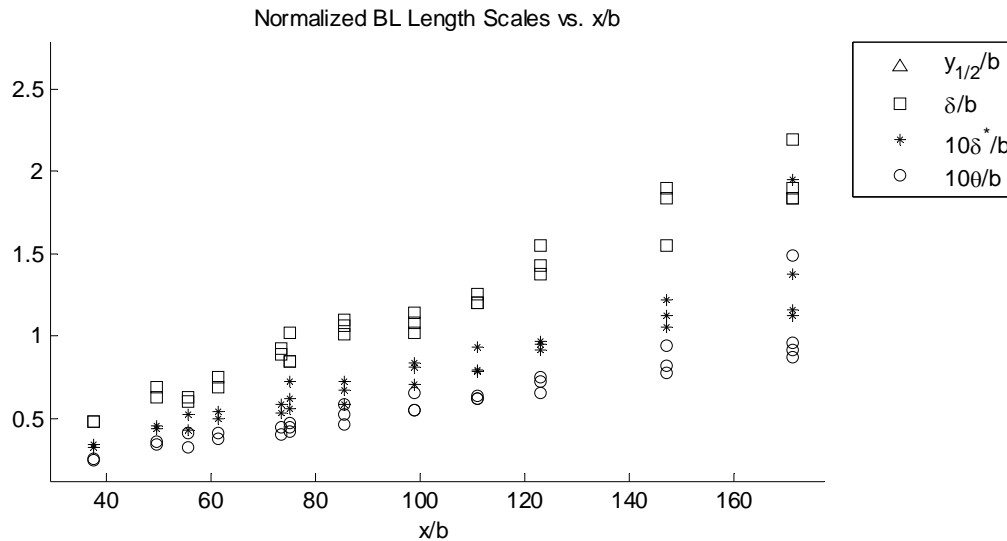


Figure 3.20 Nondimensional boundary layer length scales vs. x/b for all test cases seen above viewed tighter

If all of the boundary layer length scales are multiplied by some constant scale factor specific to each length scale are compared with, say, the boundary layer thickness, the results can

be seen in Figure 3.21 below. The empirically determined scale factors that show the best agreement are seen in the legend. In this figure the displacement and momentum thicknesses along with $y_{1/2}$ are multiplied by these empirically determined scale factors and plotted against the value of δ specific to each test case. For example, the linear fit of the measured data showed that δ is equal to 14.3% of $y_{1/2}$.

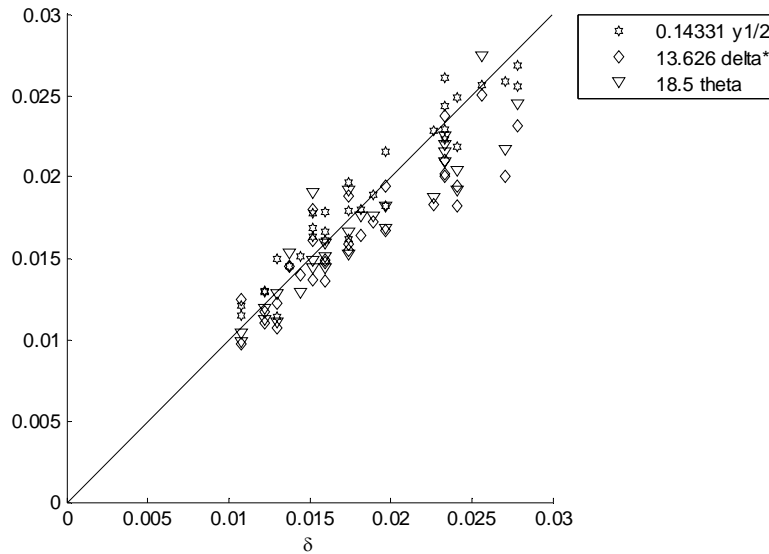


Figure 3.21 Measured length scale values compared with the boundary layer thickness

There is a general agreement seen between the various scaled length scales seen in the figure above although the correlation is not as good as is desirable. However, the approximate constant multiple relationship between the boundary layer parameters seen above was deemed sufficient for use in the estimation of boundary layer parameters for test cases where no aerodynamic data was available. The estimation method described above was applied to the boundary layer length scale data and the results are given below in Figure 3.22. Notice also that the scale factors relating the boundary layer length scales are presented in Figure 3.21 above and Figure 3.22 below. The estimations seen below agree within 0.4 mm (23%) for the displacement thickness for the most outlying point, within 0.25 mm (18%) for the momentum thickness for the most outlying point, within 3 mm (13%) for the boundary layer thickness for the most outlying point, and within 17 mm for $y_{1/2}$ for the most outlying data point. Note the uncertainty associated with the displacement and momentum thicknesses was estimated to be ± 0.25 mm and ± 0.19 mm, while that of the boundary layer thickness was determined to be ± 3 mm.

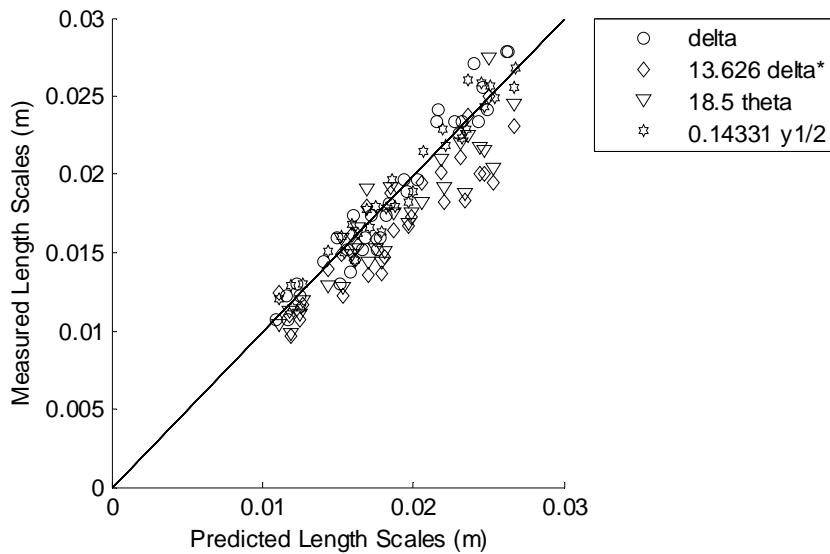


Figure 3.22 *Measured boundary layer length scales vs. the estimated length scales*

3.1.7 Effects of Initial Flow Conditions on the Wall Jet Flow

In this section, the effects of varying the initial flow conditions will be investigated further. In Figure 3.23 below, the velocity profiles normalized on the nozzle exit velocity and nozzle height are shown for test cases where the nozzle exit speed is varied while the nozzle height is held constant. The profiles shown in this figure were taken at two separate streamwise locations and are from test conditions A – C referenced in Table 3.1 above.

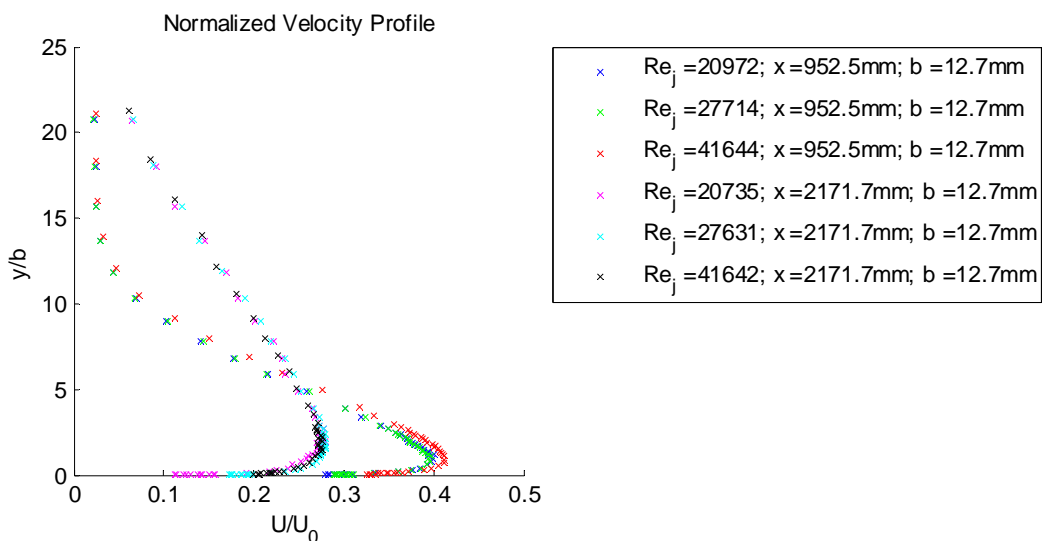


Figure 3.23 *Normalized wall jet profiles showing the effects of varying Re_j and the streamwise distance downstream of the nozzle exit*

The character of the wall jet as it develops downstream for varying nozzle exit speeds can be seen above. It is not surprising that the nozzle exit velocity scales the profiles taken at each streamwise location nor that the nozzle exit velocity does nothing to scale the profiles at different streamwise locations. It has already been established by the work of Narasimha *et al.* (1973) that the wall jet flow is dependent on the nozzle exit velocity in the form of the jet exit momentum as well as the streamwise position in the form of the Reynolds number based on the downstream x location.

In Figure 3.24 below, wall jet profiles normalized on the nozzle exit speed and on the nozzle exit height are presented for test cases where the ratio of the nozzle exit and streamwise distance Reynolds numbers are held constant. In the figure below, the blue profile was taken at a given x location, nozzle height, and nozzle exit speed. The green profile was taken at a nozzle exit Reynolds number $Re_j = \frac{U_o b}{\nu}$ and streamwise distance Reynolds number $Re_x = \frac{U_o x}{\nu}$ double that of the blue profile. These conditions were obtained by doubling the nozzle height and approximately doubling the streamwise measurement location while holding the nozzle exit velocity approximately constant. The red profile was taken at nozzle exit and streamwise distance Reynolds number double that of the blue profile as well. These conditions were obtained by doubling the nozzle exit velocity while leaving the nozzle exit height and measurement location equal to that of the blue profile. Since the velocity scale in the streamwise distance Reynolds number is the nozzle exit velocity, the x location remained constant for this profile. The profiles shown below were taken at test conditions A, E, and C for the blue, green, and red profiles, respectively.

The ratio of the nozzle exit Reynolds number and the Reynolds number based on the downstream location is held constant, and the profiles normalized on the initial flow conditions at the nozzle nearly identical. Moreover, when this ratio is held constant, the measured boundary layer length scales remain essentially constant as seen in Figure 3.25 below. This is consistent with expectations given the variation of the boundary layer length scales with the jet exit Reynolds number and the streamwise distance Reynolds number indicated by equation 3.4 above (the boundary layer length scales are dependent upon the product of these two Reynolds numbers that are each raised to a power close to -1 when the empirically determined exponent, m is considered). Given this and the fact that the maximum velocity is dependent upon the ratio of the nozzle exit Reynolds number and the streamwise Reynolds number each raised to a power near 0.5 (as suggested by equation 3.3 along with the empirically determined exponent, n), the agreement of the normalized profiles in Figure 3.24 is no surprise.

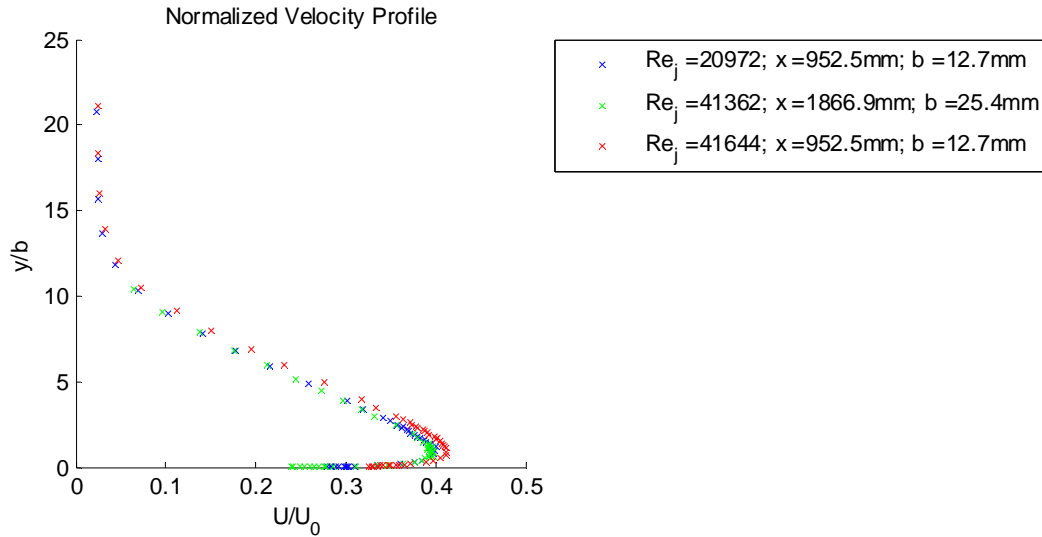


Figure 3.24 Normalized wall jet profiles showing the effects of varying the initial flow conditions while holding the ratio of nozzle exit and streamwise distance Reynolds numbers constant

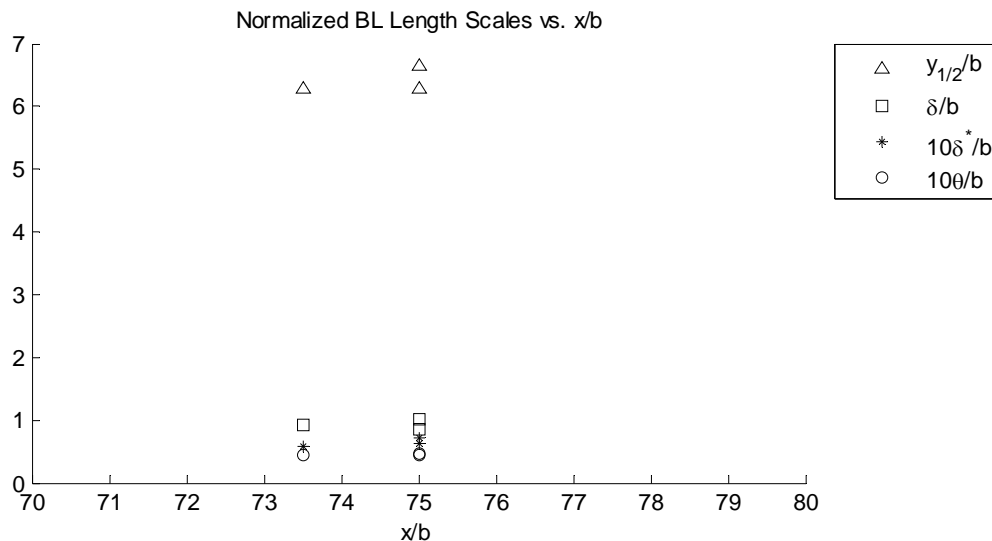


Figure 3.25 Measured boundary layer length scales for test cases where the ratio of nozzle exit and streamwise distance Reynolds numbers is held constant but the initial flow conditions are varied

3.1.8 Turbulent Character of the Wall Jet Flow

George *et al.* (2000) derived outer scalings for wall jet parameters and have applied these length and velocity scales to turbulent data taken from Abrahamsson *et al.* (1994). The length scale derived by George *et al.* (2000) was $y_{1/2}$ and the velocity scale was U_m . In Figure 3.26 below, the normal stress profiles of the component of velocity in the streamwise direction from test condition A as referenced in Table 3.1 above are shown. The data shown is representative of the rest of the experimental data set and is compared with experimental data from Abrahamsson *et al.* (1994) and from Eriksson *et al.* (1998) at nozzle exit Reynolds numbers of 10000 and

9600, respectively. The normal stress profiles are normalized on the scaling parameters derived by George *et al.* (2000).

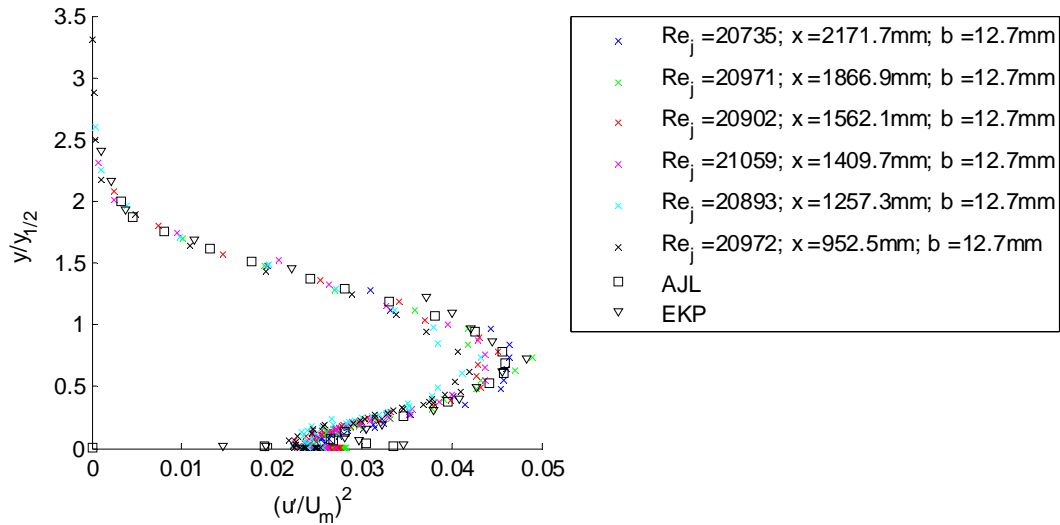


Figure 3.26 *Turbulence profiles normalized on outer scaling parameters; Abrahamsson et al. (1994) noted as AJL and Eriksson et al. (1998) noted as EKP*

The profiles from the current study are vertical profiles for a single nozzle exit velocity and nozzle height over a range of axial locations. The data from Abrahamsson *et al.* (1994) and Eriksson *et al.* (1998) were taken at a distance of 100 nozzle heights downstream of the nozzle exit. The data from the current study was taken at distances downstream of the nozzle exit ranging from 75 nozzle heights to 170 nozzle heights. Notice that the profiles collapse well except near the wall. The spread shown in the data from the current study is no larger than that presented by Eriksson *et al.* (1998) while the data presented by George *et al.* (2000) from Abrahamsson *et al.* (1994) over a range of distances downstream collapses tighter than that of the current study. The scatter of the data near the wall is not unexpected because the profiles have been normalized on outer variables. In a later section, an investigation into the near wall behavior of these turbulence profiles will be presented. All of the measured turbulent profiles are presented normalized on outer variables in Figure 3.27 below. The normal stress profiles scale well on outer variables except very near the wall showing about a 7 – 8 % variation in the bulk of the data at the mixing layer peak value.

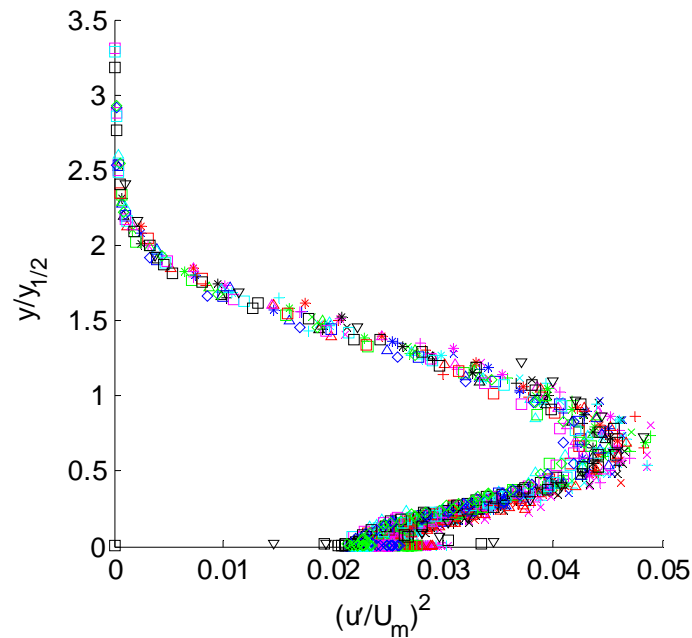


Figure 3.27 All turbulence profiles from current study normalized on outer scaling parameters

During the investigation of the turbulence characteristics of the wall jet flow, the effects of nozzle exit speed, nozzle height and axial position were considered. In Figure 3.28 below, the profiles from test condition A listed in Table 3.1 above are shown to illustrate the effects of downstream distance on the normal stress profiles normalized on the nozzle exit velocity and nozzle height. The maximum turbulence intensity decreases as the downstream distance increases, but the height of the maximum turbulence intensity increases as the measurement location is moved downstream. The normal stress profiles are clearly becoming more diffuse as the flow moves downstream. Also, it is evident that the maximum turbulence intensity occurs at a height greater than the height of maximum velocity, δ seen for the same conditions in Figure 3.15 above.

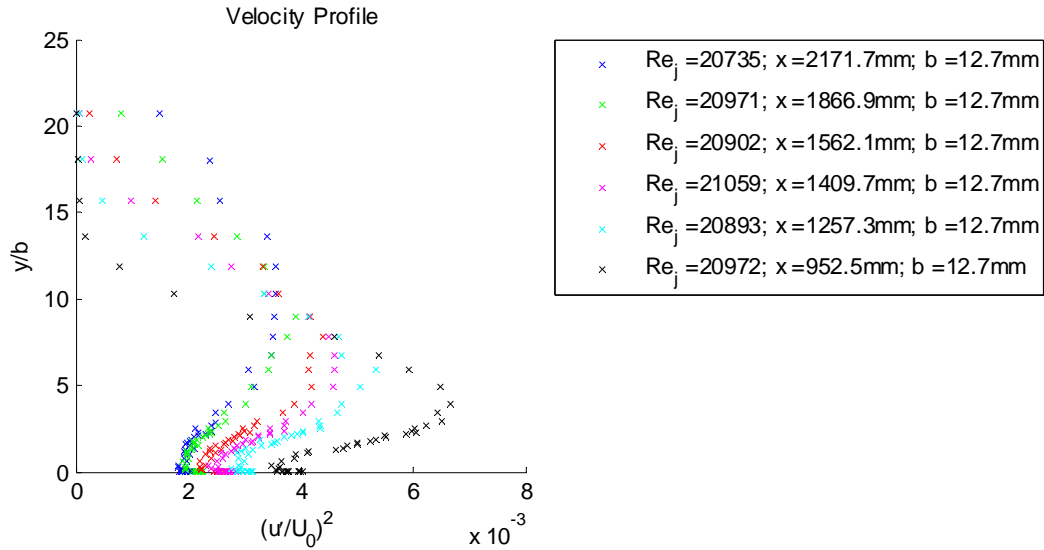


Figure 3.28 Normalized turbulence profiles investigating the effects of axial position

In Figure 3.29 below, turbulence profiles taken at constant nozzle height and the normal stress profiles normalized on nozzle exit conditions for varying nozzle exit speed are shown for two streamwise locations. As for the wall jet mean velocity profiles seen in Figure 3.23 above, the normal stress profiles seem to scale on the nozzle exit velocity at each of the two streamwise locations shown.

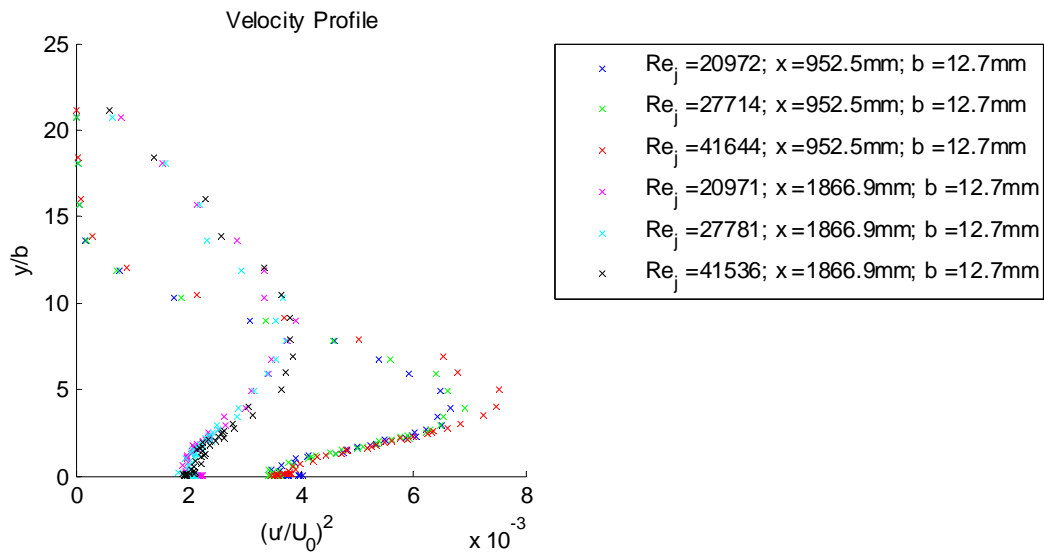


Figure 3.29 Normalized turbulence profiles of varying nozzle exit velocity at two streamwise locations

Now if the same approach is taken with the normal stress profiles as was taken for the wall jet profiles shown in Figure 3.24 above, the results are seen in Figure 3.30 below. The collapse of these profiles is not good near the maximum normal stress in the mixing layer indicating that that the relationship between the normal stresses of wall jet flows of various

initial flow conditions cannot be related to a simple ratio of nozzle exit and downstream distance Reynolds number as for the mean velocity profiles.

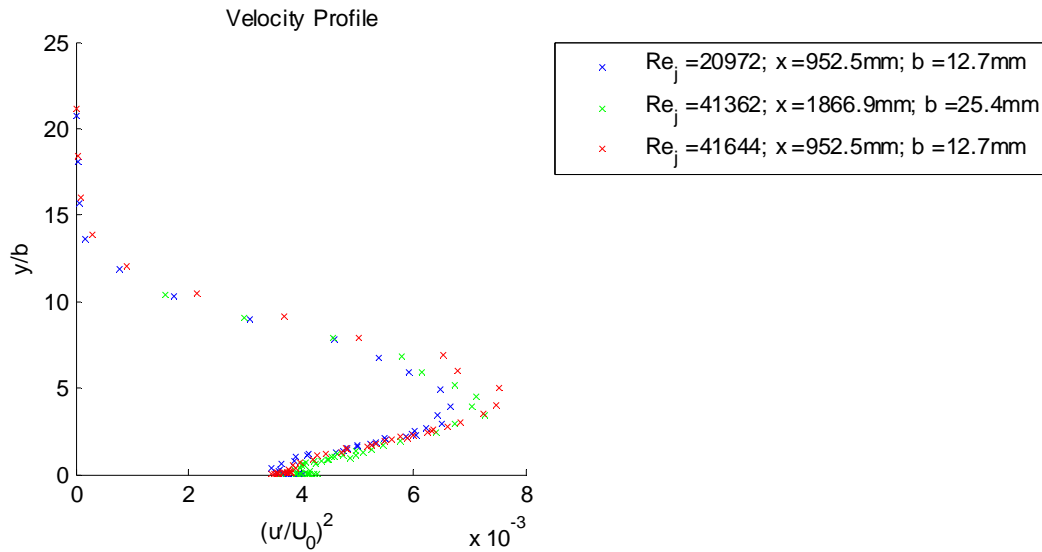


Figure 3.30 Normalized Normal stress profiles showing the effects of varying the initial flow conditions while holding the ratio of nozzle exit and streamwise distance Reynolds numbers constant

As discussed in Chapter 1 one of the ongoing questions relating to wall jets is whether or not the portion of the wall jet flow below the velocity maximum can be thought of or treated in the same way as a canonical turbulent boundary layer. Investigations into the near wall behavior of a wall jet compared to that of a turbulent boundary layer will be discussed in detail in a later section, but a comparison of the turbulence profiles for a wall jet flow and for that of a turbulent boundary layer will be presented here. In Figure 3.31 below, experimental data from the current study is compared with the turbulent boundary layer data of Klebanoff (1955). The data from the current study shown was taken for a range of nozzle exit speeds. The data will be normalized on U_e and δ for the boundary layer profile and U_m and δ for the wall jet profiles. For turbulent boundary layers δ represents the height at which the flow reaches $0.99 U_e$. The most analogous velocity scale to the turbulent boundary layer's U_e in the wall jet flow is U_m .

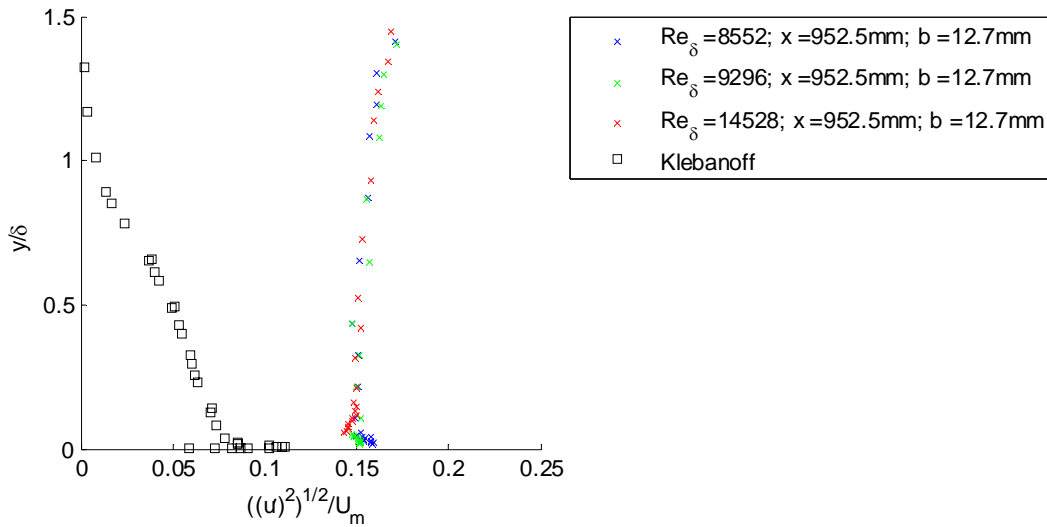


Figure 3.31 Wall jet and turbulent boundary layer turbulence intensity profile comparison; $Re_{\delta} = 84000$ for Klebanoff (1955) data

The profiles shown present data out to y/δ equal to 1.5. It is clear that the turbulence intensity from the wall jet is markedly different than that from the turbulent boundary layer. This is evident by the fact that the wall jet and boundary layer profiles do not collapse when normalized. Also of interest is the fact that the boundary layer turbulence intensity plots reach a maximum near the wall and then decrease to nearly zero at y/δ equal to 1 while the turbulence intensity profiles for the wall jet also reach a maximum, but they decrease a little and then increase steadily as y/δ is increased. The main difference in a wall jet and a turbulent boundary layer flow is the presence of a mixing layer in the upper portion of the wall jet flow. The figure above indicates that the mixing layer plays a major role in the turbulence intensity of the wall jet profiles and that because the turbulent boundary layer lacks this mixing layer, the difference between the two types of turbulence intensity profiles is marked. It would seem that regardless of the similarities of the lower portion of the wall jet flow to a turbulent boundary layer flow, there are some characteristics that are fundamentally different. The discussion above is quite important in light of the fact that there is great disagreement in the literature concerning the similarity between the wall jet flow below the velocity maximum and that of a regular turbulent boundary layer. Early on in the literature, the similarity between the two was taken as a given, but later as researchers began to measure velocity profiles near the wall, the notion that these flows are not the same began to become more prevalent. The most common point of contention lies in the presentation of log law profiles as some researchers present data showing a good fit with the common semilog region form of the regular turbulent boundary layer while others show a semilog region that is not consistent with the established turbulent boundary layer semilog region. Possible reasons for the differing observations have been proposed to be the difficulty in measuring the wall jet skin friction coefficient. In light of the turbulence intensity discussion above, the two flows are certainly different, and as will be shown below, the mean velocity profiles below the velocity maximum show similarities with those of the turbulent but do not have the same variation in the semilog region.

3.1.9 Wall Jet Flow in the Inner Region

Discussion in the preceding sections focused on the wall jet flow over a smooth flow surface and how various flow parameters scale on outer region variables. The fact that the wall jet flow profiles only scale on outer variables over a limited portion of the profiles' extent was mentioned earlier. The region where the U_m and $y_{1/2}$ scalings are valid is away from the wall where viscosity is a minor player. It was also stated above that the boundary layer, momentum, and displacement thicknesses (δ , δ^* , θ) for the wall jet flow were calculated in a way analogous to that of the calculation of these thicknesses for canonical turbulent boundary layers. These observations from the preceding sections lead one to ask some questions about wall jet flows. First, how does the inner region of a wall jet flow scale? Second, does the region of the wall jet flow up to and including the velocity maximum behave like a turbulent boundary layer as some have suggested? Last, if this region is different from turbulent boundary layers, how does it behave, and how is it different from the turbulent boundary layer?

The fact that the outer scaling variables do not scale the flow near the wall is clearly illustrated in Figure 3.32 below where the profiles from test condition A are presented. One can see that the collapse of the profiles is really not as good near the wall as it is away from the wall. The profiles shown below vary in the streamwise distance Reynolds number, and as the streamwise distance is increases, the profiles are generally retarded more and more very close to the wall. There is some scatter in this trend, but this effect does appear to be real and present. It is also interesting to note that the outer scaling variables do a nice job as close to the plate as $y/y_{1/2}$ equal to 0.01.

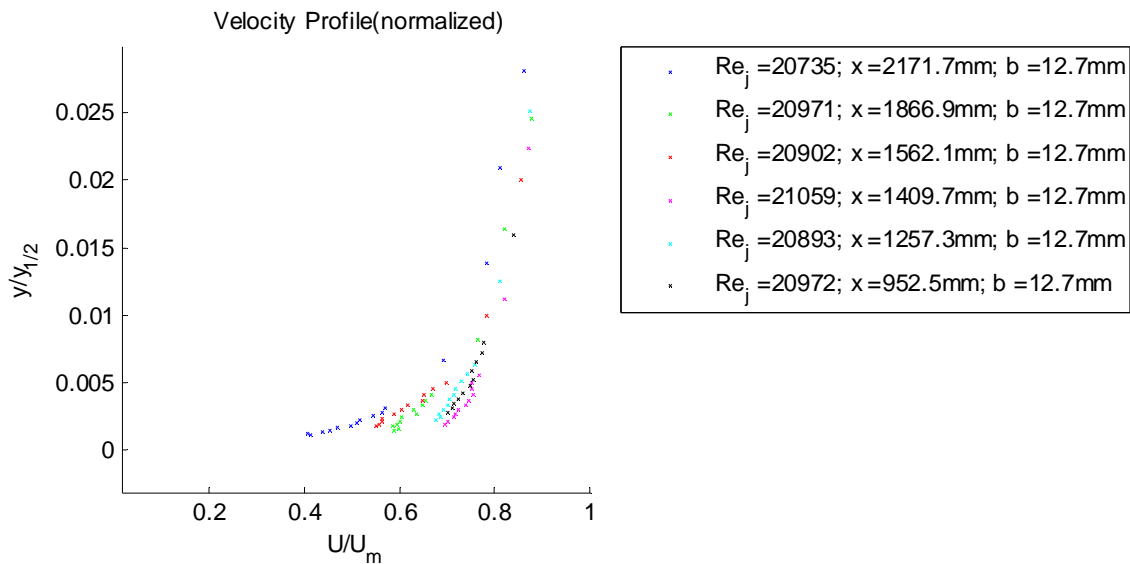


Figure 3.32 Wall jet profiles normalized on outer variables

3.1.10 Skin Friction

In the common turbulent boundary layer, there is an inner sublayer, a buffer region, and a log law region where the characteristic velocity scale is the skin friction velocity, u^* . Therefore, it stands to reason that this could be a possible characteristic velocity scale for the inner portion

of the wall jet flow, and indeed the skin friction velocity must be the velocity scale in the viscous sublayer. It makes sense to at least investigate this velocity scale given the fact that there is disagreement in the literature regarding whether or not the wall jet behaves like a canonical turbulent boundary layer over some portion of the flow below the velocity maximum. Many workers have attempted to get the skin friction (and hence the friction velocity) in a wall jet flow. Launder and Rodi (1981) give an overview of the results from numerous studies and show a very wide variation amongst the skin friction data. The skin friction results shown in Launder and Rodi (1981) were obtained using a variety of methods and measurement techniques and show differences amongst the data sets of nearly 40%. Of the data presented, that of Bradshaw and Gee (1960) seems to agree closer with several of the other data sets and is considered to one of the better estimates presented. The results of Bradshaw and Gee (1960) were obtained with a Preston tube, and a fit was applied to the data to give the following relationship:

$$C_f = 0.0315Re_m^{-0.182} \quad (3.5)$$

George *et al.* (2000) used the asymptotic invariance principle to show that the skin friction velocity has to be the velocity scale in the inner region of a wall jet flow and they provide a method to obtain this velocity scale. The George *et al.* (2000) method of obtaining the skin friction velocity, u^* , was described in more detail above in Chapter 1. Basically, George *et al.* (2000) use assumption that the wall jet flow and a turbulent boundary layer flow are identical very close to the wall to develop equations 1.12 and 1.13 that enable one to calculate the skin friction velocity. George *et al.* (2000) provide some justification for this by comparing near wall ($y^+ < 100$) LDA data for both a wall jet and a turbulent boundary layer flow taken at the same test conditions. Equations 1.12 and 1.13 indicate that the skin friction velocity is a function of the local Reynolds number, $y_{1/2}^+$ whose velocity scale is the skin friction velocity yielding an implicit equation for the skin friction velocity that can be easily solved as the length scale $y_{1/2}$ is known.

In the present study, the skin friction coefficient was estimated using the method from George *et al.* (2000). This estimate along with the fit from Bradshaw and Gee (1960), and the fit from Schultz and Grunow (1940) for regular turbulent boundary layers are shown in Figure 3.33 below for comparison.

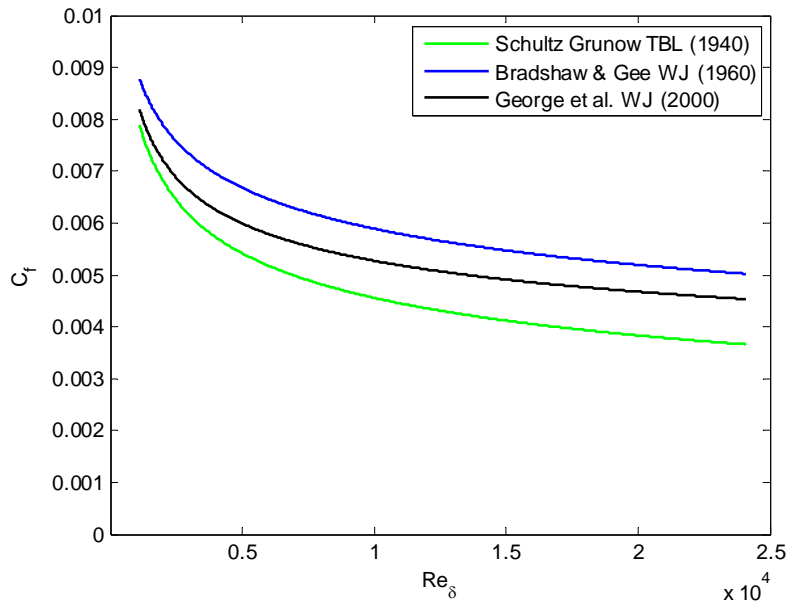


Figure 3.33 Skin friction predictions of George *et al.* (2000), Bradshaw and Gee (1960) data fit, and Schultz and Grunow (1940) correlation

The Bradshaw and Gee (1960) and George *et al.* (2000) methods yield higher results than are seen in normal turbulent boundary layers. One should also note that the George *et al.* (2000) prediction is, on average, 10% lower than that predicted by Bradshaw and Gee (1960). When looking at the agreement of the wall jet skin friction correlations above with the predictions of Bradshaw and Gee (1960), one would seem to think that calculated skin friction values above are in pretty good agreement, especially when one considers the large spread of experimental data shown in Launder and Rodi (1981) as this suggests significant uncertainty in the skin friction and any associated correlation fits by various researchers.

3.1.11 Wall Jet Flow in Inner Coordinates

A common way to present turbulent boundary layer data is to plot the velocity profiles in inner coordinates, U^+ and y^+ , where $U^+ = \frac{U}{u^*}$ and $y^+ = \frac{yu^*}{\nu}$. The latter is a Reynolds number based on the length scale, y , and the velocity scale, u^* .

George *et al.* (2000) assumed that the wall jet flow in the overlap region described in Chapter 1 above could be described by a power law and they proposed a composite solution that is given in equation 1.11 above. This form blends the laminar sublayer region with the semilog region of the wall jet flow. Nearly all of the constants in equation 1.11 are the same as those of a regular turbulent boundary layer, and the authors make arguments in favor of these choices. However, the constant, C_i , and the exponent, γ , are dependent on $y_{1/2}^+$ ($y_{1/2}u^*/\nu$). From equations 1.11, 1.12, and 1.13 one can present velocity profiles in inner coordinates. The real questions are, does this prediction match well with experimental data, and do the profiles scaled on inner variables behave in the same way as a canonical turbulent boundary layer in the semilog region?

In order to answer the first question, mean velocity profiles were generated from data taken in the present study and compared with the associated predictions from the George *et al.* (2000) method. In Figure 3.34 below, four profiles from test condition A are shown with the accompanying predictions. The x location of these profiles was varied as indicated to give a range of local Reynolds numbers for a given set of initial flow conditions.

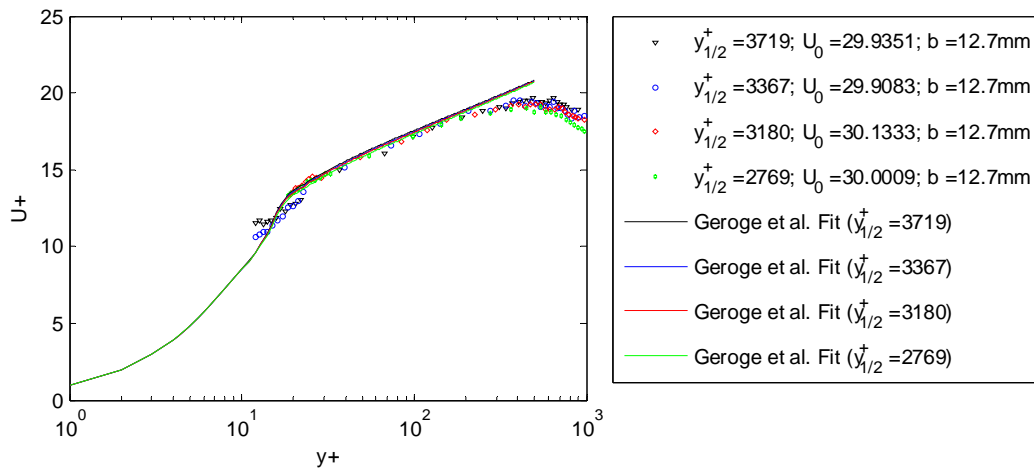


Figure 3.34 Clean plate mean velocity profiles compared with George *et al.* (2000) prediction

The experimental data match well with the predictions, although the predictions are slightly higher than the experimental results in the semilog region. It is also important to note that the applicability of the prediction begins to deteriorate as the y position approaches the boundary layer thickness, or the height of maximum velocity, for the wall jet, but this prediction of George *et al.* (2000) was not intended to predict the outer region flow. The agreement between the predictions and measured profiles is important not only because it lends credibility to the George *et al.* (2000) predictions, but because it supports the method of George *et al.* (2000) for obtaining the skin friction velocity, u^* .

In answer to the second question, a much larger selection of the available data was investigated. In Figure 3.35 below, profiles for which the range of conditions varies widely are shown. In Figure 3.36 below, all of the measured profiles are shown. The profiles shown in Figure 3.35 are representative of the rest of the available data set and were taken from test conditions A, C, and E. Profiles from additional measured cases agree well with those shown in Figure 3.35 and are left out for clarity, but are shown in Figure 3.36. The nozzle heights represented in these profiles range from 12.7mm to 25.4 mm. The nozzle exit speeds vary from

approximately 30 m/s to 60 m/s, and the streamwise locations of the profiles shown in Figure 3.35 below range from 37.5 – 171 nozzle heights downstream.

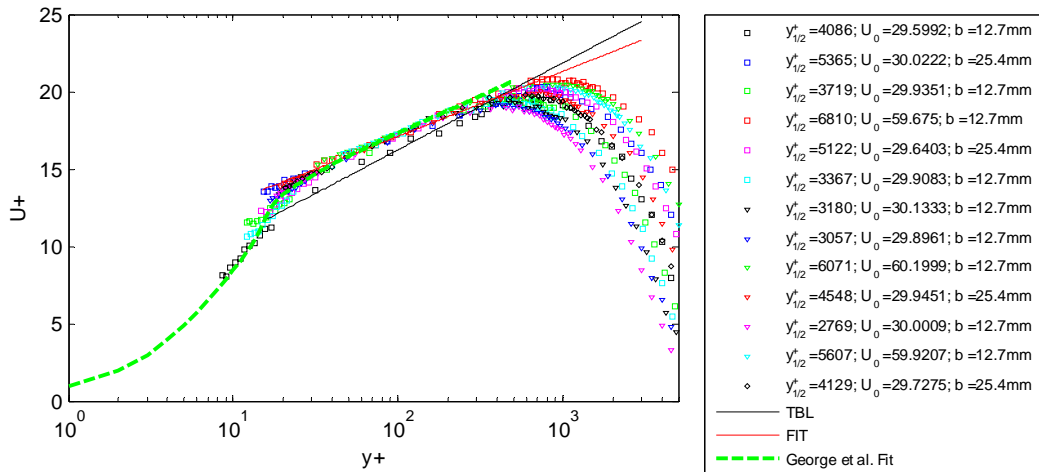


Figure 3.35 Comparison of wall jet profiles with TBL semilog region fit and George *et al.* (2000) fit.

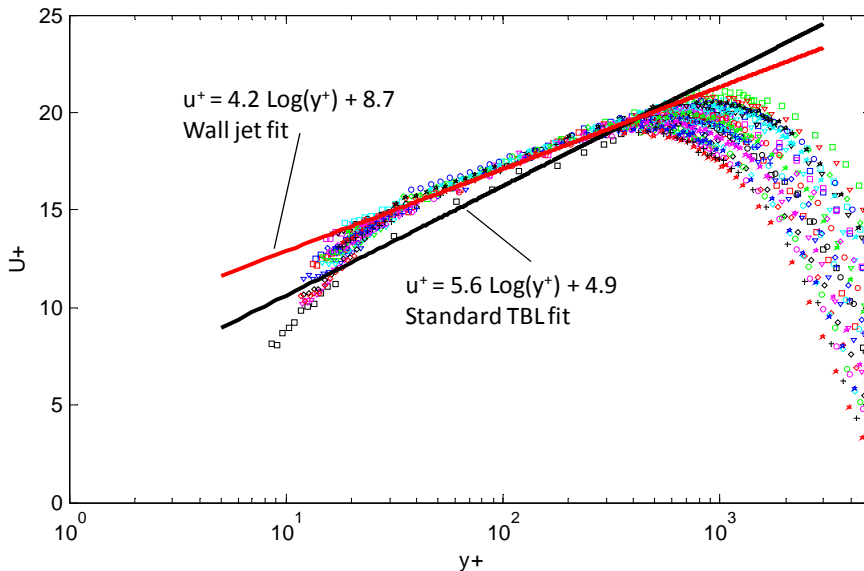


Figure 3.36 Comparison of all measured wall jet profiles with TBL semilog region and data fit from the current data

As can be seen in Figure 3.35 and Figure 3.36 above, the profiles taken experimentally agree well with one another in the semilog region and also show agreement with the George *et al.* (2000) predictions in the inner portions of the wall jet flow over the wide variation of the flow conditions. However, there does appear to be a slight difference in the slope of the George *et al.* (2000) prediction and the experimental data. Even though this difference in slope is seen to be small, it was unexpected because the George *et al.* (2000) correlation for the skin friction was used, and because the George *et al.* (2000) prediction was determined using their skin friction correlation along with other experimentally determined constants. However, the few test cases that George *et al.* (2000) used to validate their prediction are shown to begin to diverge slightly

starting at a y^+ value of around 80 – 100. Thus, it is believed that the small difference in the slope seen in the current data and the George *et al.* (2000) prediction in the semilog region is consistent with the results shown by George *et al.* (2000).

There does appear to be one outlier represented by the black square symbols, but even this profile shows fair agreement with the rest. This outlier was taken at test condition A at a streamwise distance downstream of the nozzle of 2172 mm. No justification for the anomalous behavior of this profile can be given so it is included in the presented data. The wall jet profiles plotted this way do not agree well with the semilog region fit for a conventional turbulent boundary as proposed by Clauser (1956):

$$U^+ = 5.6 \log(y^+) + 4.9 \quad (3.6)$$

While the experimental data in Figure 3.34 and Figure 3.35 agrees well with the George *et al.* (2000) composite profile, it is sometimes advantageous for certain data analyses to use a simple fit of the semilog region (this type of fit was used in the estimation of the equivalent sand grain roughness height that will be discussed below). A simple fit to the wall jet data shown above is given here:

$$U^+ = 4.2 \log(y^+) + 8.7 \quad (3.7)$$

This fit seems to match well with the data shown above in Figure 3.35 and Figure 3.36 where all of the experimental data is presented. In Figure 3.36 there is a well defined semilog region where all measured profiles (with the exception of the one outlier) collapse nicely. Given the discussion above, the wall jet flow may behave in an identical way as the turbulent boundary layer does in the laminar sublayer as suggested by George *et al.* (2000), but the wall jet does behave differently, albeit in a similar fashion, than a turbulent boundary layer in the semilog region. This is no surprise given that there is no theoretical justification for expecting the wall jet flow to behave like a turbulent boundary layer in the semilog region.

3.1.12 Turbulent Character of the Wall Jet in the Inner Region

In section 3.1.8 above there was discussion regarding the turbulent character of the wall jet in the outer region of the flow. It was shown that turbulence profiles scale well on the outer variables U_m and $y_{1/2}$. In the current section an investigation into the behavior of turbulence profiles when normalized on inner variables will be conducted. George *et al.* (2000) presents the data of Karlsson *et al.* (1993) which shows that the turbulence profiles scale very well on the skin friction velocity, but only for values of y^+ less than 10. Outside of this range, the profiles separate. All measurements in the present study were made for values of y^+ greater than 10. In Figure 3.37, Figure 3.38, and Figure 3.39 below turbulence profiles are shown as the profile streamwise location, nozzle exit speed, and the nozzle exit height are varied, respectively. The profiles shown in Figure 3.37 were taken from test condition A. The profiles from Figure 3.38 were taken from test conditions A – C. The profiles seen in Figure 3.39 were taken from test conditions A and E.

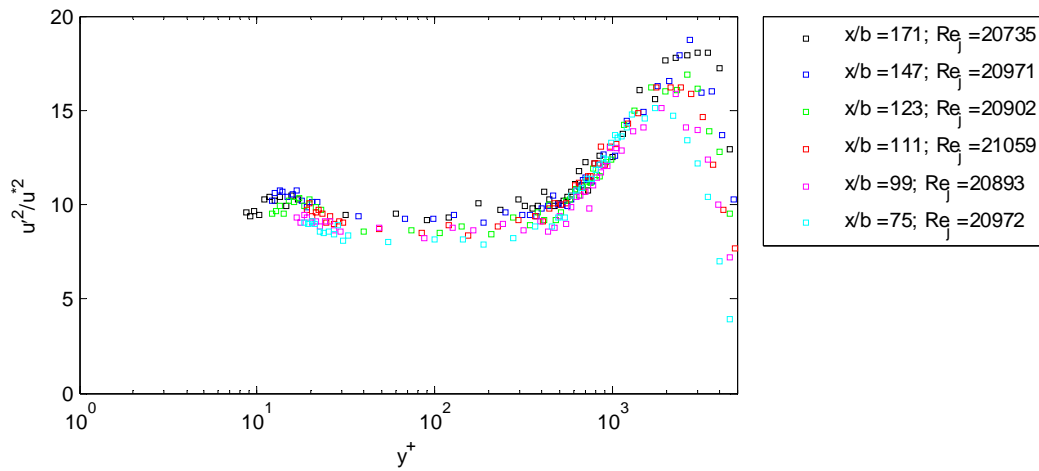


Figure 3.37 Turbulence profiles normalized on inner variables showing the effects of variations in the streamwise profile location

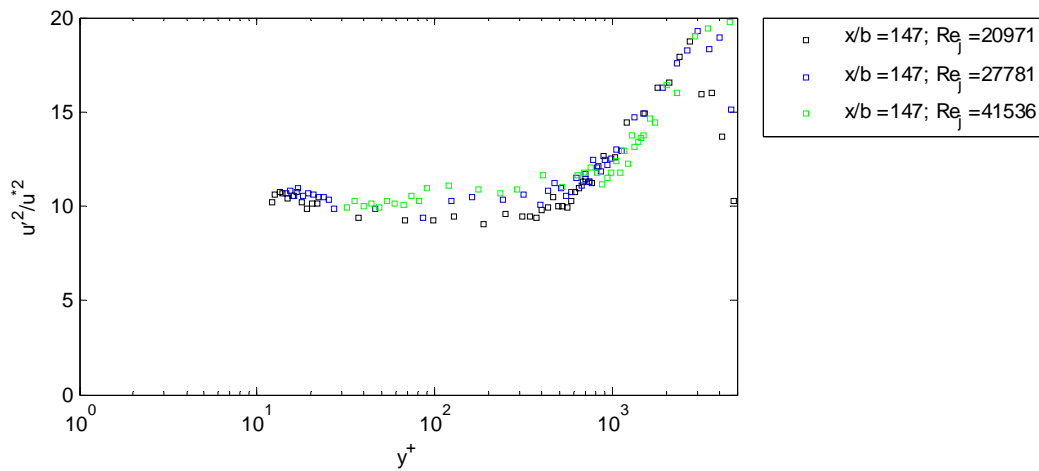


Figure 3.38 Turbulence profiles normalized on inner variables showing the effects of variations in the nozzle exit velocity

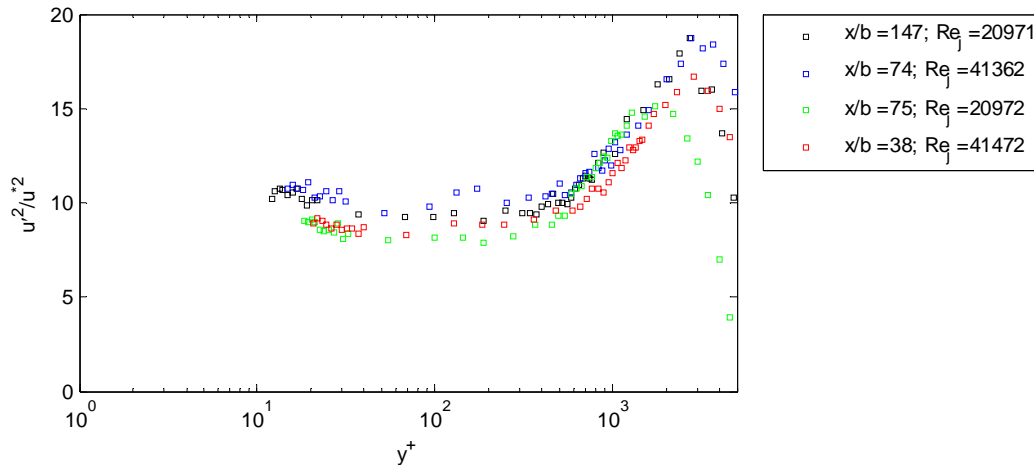


Figure 3.39 *Turbulence profiles normalized on inner variables showing the effects of variations in the nozzle exit height*

The profiles shown in Figure 3.37, Figure 3.38, and Figure 3.39 above are presented in the same way as the data of Karlsson *et al.* (1993) presented by George *et al.* (2000) and are representative of the current data set. The normal stress profiles from other test conditions show similar scaling behavior to those seen in Figure 3.37, Figure 3.38, and Figure 3.39. The data presented by George *et al.* (2000) was taken at a nozzle exit Reynolds number of 9600, and covered a range of streamwise distances normalized on the nozzle exit height from 40 to 100. In Figure 3.37 above, the data presented was taken for a nozzle exit Reynolds number of approximately 21,000, and the normalized streamwise distance varied between 75 and 171. There is a progression seen in the normalized turbulent profiles showing higher turbulence levels as the streamwise distance is increased. George *et al.* (2000) note this same trend. However, George *et al.* (2000) showed a larger spread in the normal stress profiles at the near wall peak location of y^+ equal to 11 than in the current study. In the George *et al.* (2000) study, the normalized streamwise distance was increased by 150% whereas in the current study, the increase in normalized downstream distance was 125%. The spread in the current data is about 65% of that seen in George *et al.* (2000), but the same trend is present. The data presented by George *et al.* (2000) was obtained with LDA, and thus it was possible to measure closer to the wall surface. George *et al.* (2000) notes very good agreement between the profiles presented below a y^+ equal to 7, but the data from the current study cannot confirm this.

Figure 3.38 and Figure 3.39 would indicate that the nondimensional normal stress profiles do not behave in a similar way at y^+ greater than 11 for a given nondimensional streamwise distance, and that they can be scaled on inner variables for a given nozzle exit Reynolds number with only limited success.

3.1.13 Smooth Wall Jet Velocity Spectra

In order to investigate the behavior of the smooth wall spectra more closely, the velocity spectra for various smooth wall jet flows were analyzed over a range of conditions. The velocity spectra, G_{uu} , normalized on the nozzle exit velocity, U_o , are plotted against ω for all measured smooth wall profiles (test conditions A – E).

$$\frac{G_{uu}}{U_o^2} \text{ vs. } \omega \quad (3.8)$$

The spectra shown were taken at the displacement thickness height, the boundary layer thickness height, and mixing layer half height, $y_{1/2}$.

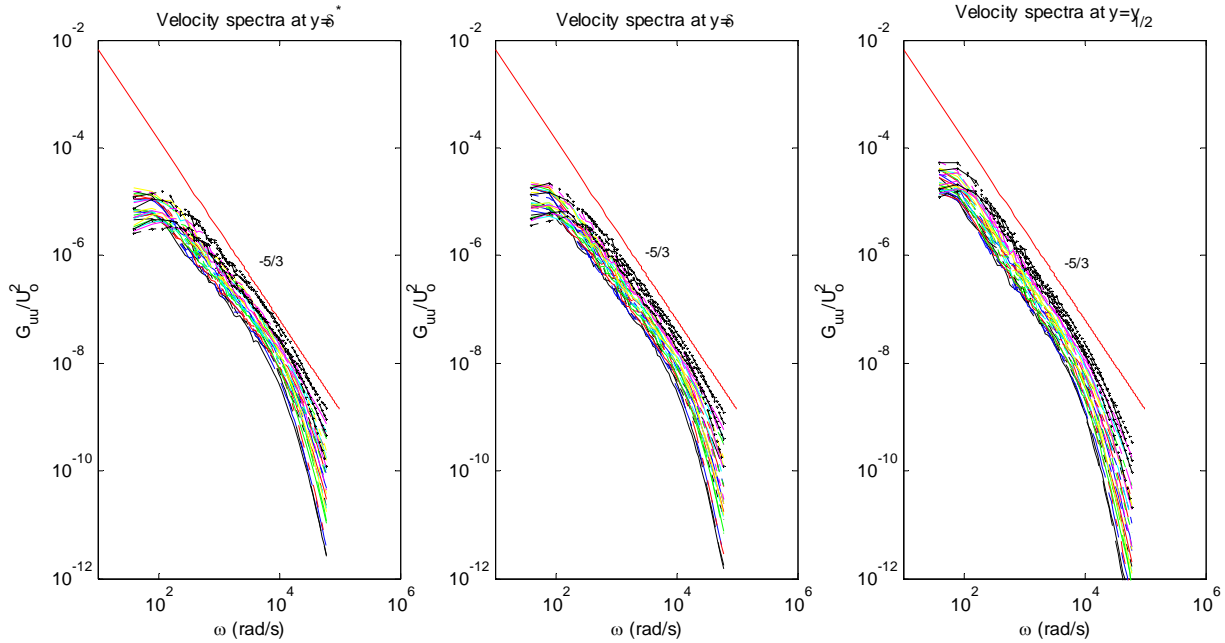


Figure 3.40 All measured smooth wall jet velocity spectra taken at δ^* , δ , $y_{1/2}$

The velocity spectra fall into a thick band and at each measurement height, and show a spectral region that varies with $\omega^{-5/3}$ followed by a ω^{-7} roll off with frequency. The extent of the $-5/3$ region increases as the probe position is moved away from the wall as the larger more energetic turbulent motions become more dominant. Note also that the spectral levels at low frequencies increase as the probe position is moved away from the wall indicating the dominance of the larger turbulent structures away from the wall, while the spectral levels at high frequencies increase as the probe position is moved toward the wall where the smaller, higher frequency, turbulent motions are more dominant.

It was desired to determine the variables that scaled the smooth wall jet velocity spectra. The outer variables U_m and $y_{1/2}$ were seen to scale the mean velocity and turbulence profiles well except very near the wall where the skin friction velocity u^* was seen to scale the flow well for the mean velocity profiles, but not necessarily for the turbulence profiles. In Figure 3.41 below, the smooth wall jet spectra shown above are plotted nondimensionally and are scaled on outer flow variables:

$$\frac{G_{uu}}{U_m y_{1/2}} \text{ vs. } \frac{\omega y_{1/2}}{U_m} \quad (3.9)$$

In Figure 3.42 below, the smooth wall jet profiles are plotted nondimensionally and are scaled on u^* and $y_{1/2}$:

$$\frac{G_{uu}}{u^* y_{1/2}} \text{ vs. } \frac{\omega y_{1/2}}{u^*} \quad (3.10)$$

The skin friction velocity was investigated because it was thought using this velocity scale might collapse the spectra at high frequencies near the wall. The use of $y_{1/2}$ as the length scale was maintained because it seemed to scale the mean velocity profiles and the normal stress profiles well even close to the wall.

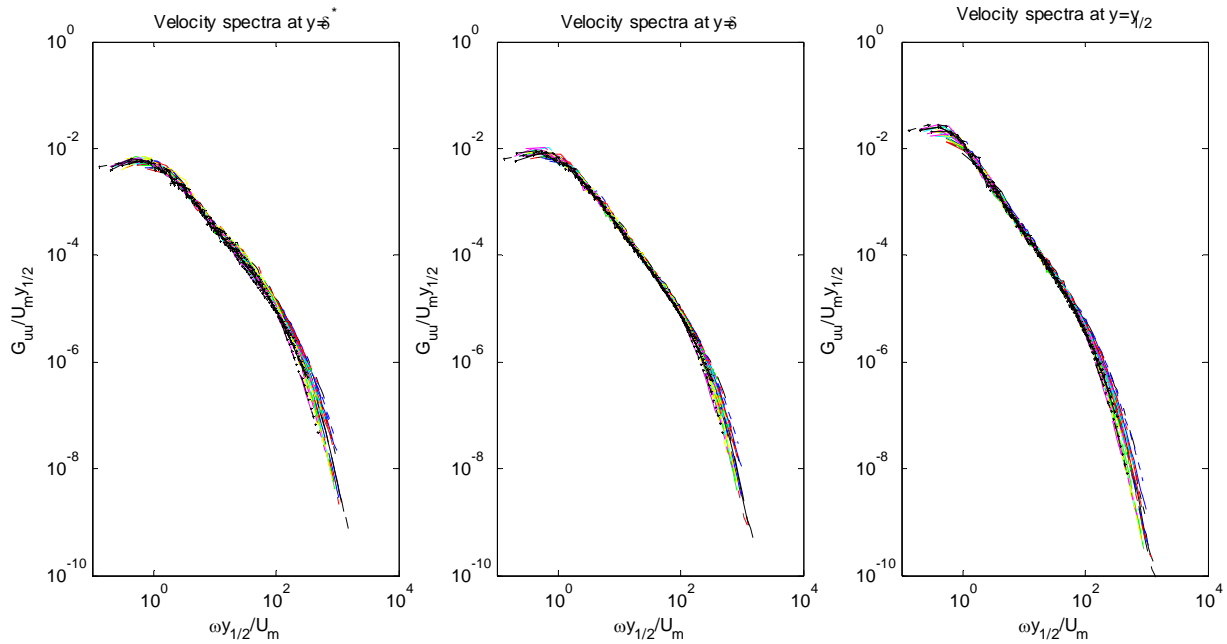


Figure 3.41 All measured smooth wall jet velocity spectra taken at δ^* , δ , $y_{1/2}$ normalized on outer variables, U_m and $y_{1/2}$

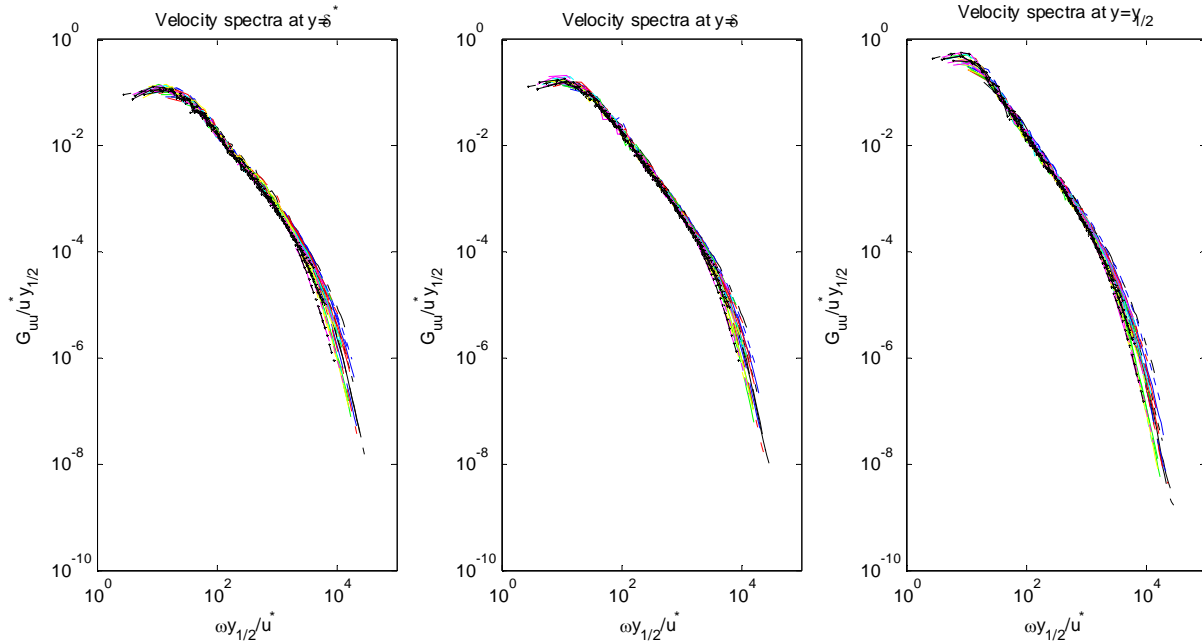


Figure 3.42 All measured smooth wall jet velocity spectra taken at δ^* , δ , $y_{1/2}$ normalized on outer variables, u^* and $y_{1/2}$

The maximum velocity and the skin friction velocity both scale the smooth wall jet velocity spectra well. There appears to be a slight improvement in the collapse of spectra when the maximum velocity is used as a velocity scale, but any differences are difficult to determine given the logarithmic scale of the plots. Other boundary layer length scales were investigated as scaling variables, but no improvement was seen even for the spectra taken at the displacement thickness height. This should be no surprise because for the smooth wall jet flow, the boundary layer length scales were shown to be constant multiples of one another.

The inner spectral scaling adopted by Ueda and Hinze (1975) was also applied to the velocity spectra with the exception that the normalizing velocity scale of $\overline{u'^2}$ used by Ueda and Hinze (1975) was replaced with the maximum velocity in the wall jet flow. The scaling used is given as follows:

$$\frac{u^{*2} G_{uu}}{\nu U_m^2} \text{ vs. } \frac{\omega \nu}{u^{*2}} \quad (3.11)$$

In Figure 3.43 below, the smooth wall velocity spectra were scaled according to Ueda and Hinze (1975). It can be seen that the spectra scale very well in the high frequency region. In the $-5/3$ region, the spectra do not collapse quite as well as those scaled on the outer variables seen in Figure 3.41 above, and at low frequencies, the spectra scaled on outer variables collapse noticeably tighter than those employing the inner scaling of Ueda and Hinze (1975). This indicates that the outer flow variables scale the velocity spectra that are dominated by larger higher energy turbulent structures, and that high frequency spectral regions dominated by very small scale low energy turbulent structures in the flow are scaled best by using the inner timescale, ν/u^{*2} .

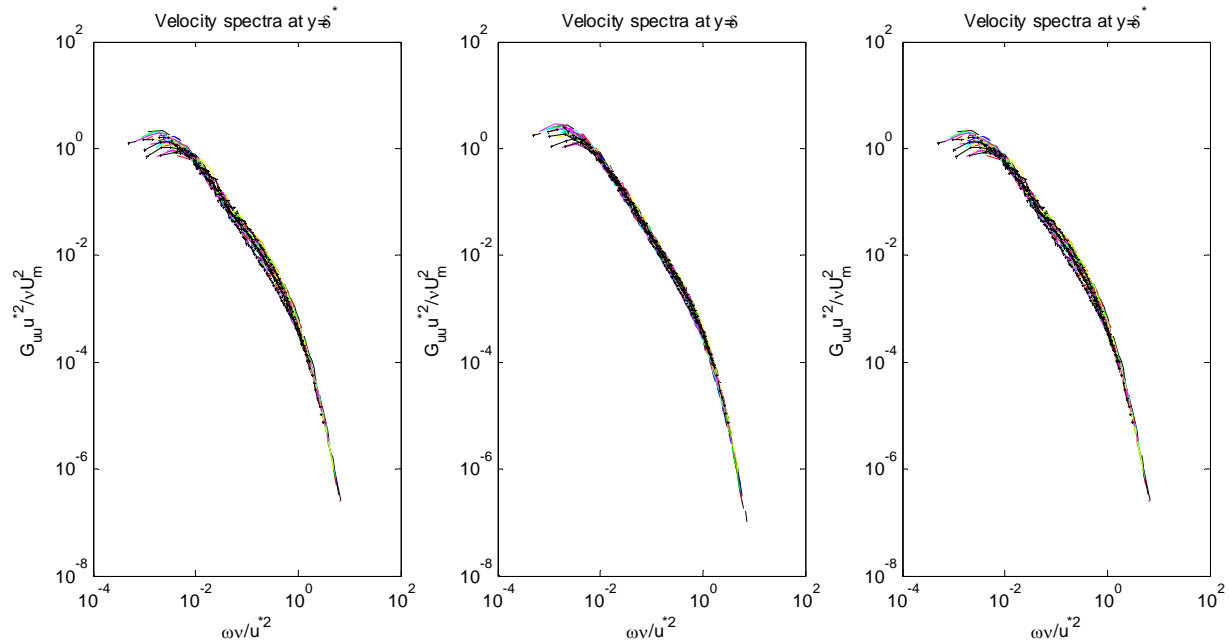


Figure 3.43 All measured smooth wall jet velocity spectra taken at δ^* , δ , $y_{1/2}$ using the inner scaling presented in Ueda and Hinze (1975)

The effects of varying the flow velocity are seen in shown in detail in Figure 3.44 below. Both the dimensional and nondimensional spectra (scaled on outer variables) are shown. The spectra shown were taken over a range of nozzle exit speeds of approximately, 30, 40, and 60 m/s (test conditions A – C) at the boundary layer thickness height. In these figures there are spectra from two streamwise locations (953 and 1867 mm aft of the nozzle exit). Spectra from two streamwise locations were shown in order to increase the number of spectra available for comparison from 3 to 6. The effects of the streamwise location will be examined in more detail below. One can see that the dimensional spectra seem to be grouped together depending on their streamwise location until the spectra begin to diverge from one another. This diversion occurs at about 1500 Hz (~ 9400 rad/s). Also notice that the increase in nozzle exit speed does not appear to greatly affect the level of the spectra at frequencies below this diversion point.

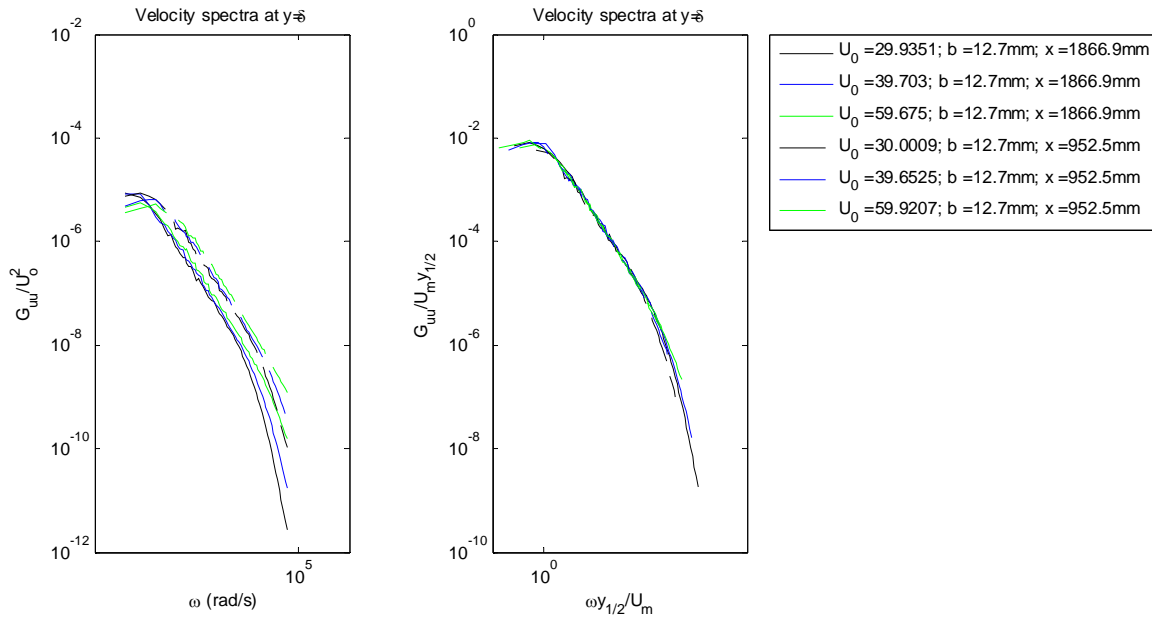


Figure 3.44 Smooth wall jet dimensional velocity spectra and nondimensional velocity spectra scaled on U_m and $y_{1/2}$

Smooth wall velocity spectra showing the effects of varying both the nozzle exit height and the streamwise measurement location are shown dimensionally and scaled on U_m and $y_{1/2}$ in Figure 3.45 and Figure 3.46 below. The observations made from these two figures really don't add anything new to what has already been discussed for smooth wall jet spectra behavior. However, it is interesting to see how the dimensional spectra vary in these two figures. In Figure 3.45 the spectra shown were measured at two streamwise locations for nozzle heights of 12.7 mm and 25.4 mm (test conditions A and E). The reason that spectra from two streamwise locations were presented was to provide more profiles for the scaled comparison. It is interesting to note that both the decrease in streamwise distance from the nozzle exit and the increase in nozzle height cause the spectra to shift upward. This is due to the fact that as the wall jet flow develops downstream, the large scale turbulent eddies lose their energy to the smaller eddies through the energy cascade. One could think of increasing the nozzle height as a decrease in the effective streamwise position relative to the nozzle exit, explaining why the spectral levels rise with an increase in nozzle height. Again, the scaled profiles seem to agree with one another nicely.

In Figure 3.46 below, the spectra shown were taken from profiles where the nozzle exit velocity was held constant at approximately 30 m/s, the nozzle height was held at 12.7 mm, and the streamwise measurement location was varied from 953 mm to 2172 mm (test condition A). From this figure, one can see that as the streamwise distance from the nozzle exit is increased, the spectral levels shift downward, and at higher frequencies, these levels tend to drop off faster than for the spectra taken closer to the nozzle exit. Again, this is due to the energy cascade. These spectra scale well on U_m and $y_{1/2}$ as seen with all other smooth wall jet velocity spectra.

From the above discussion, one can conclude that the smooth wall spectra can be effectively scaled on U_m and $y_{1/2}$ which are the same parameters that scale the mean velocity profiles. This scaling holds for spectra taken as close to the wall as the height of the displacement thickness which, for the profiles referenced in the smooth wall velocity spectra

discussion above correspond to y^+ values of between 35 and 70. Putting the spectra taken at δ^* well down into the overlap region between the outer and viscous regions of the wall jet flow. However, at very high frequencies, the spectra scale very well on the inner scaling presented in Ueda and Hinze (1975).

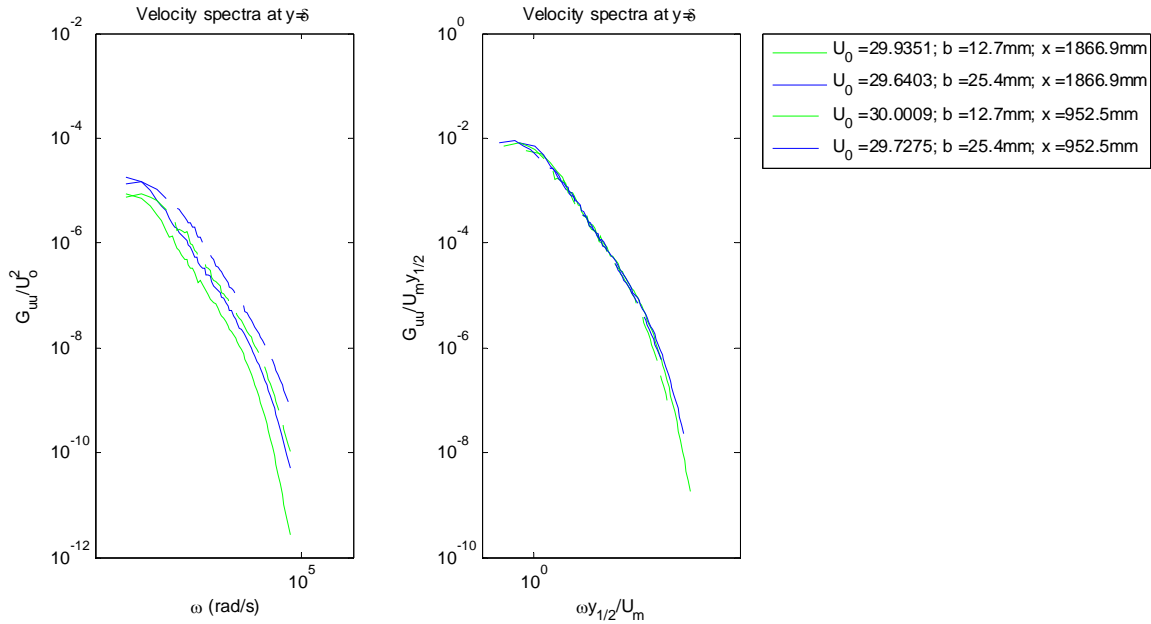


Figure 3.45 Smooth wall velocity spectra with varying nozzle height, b

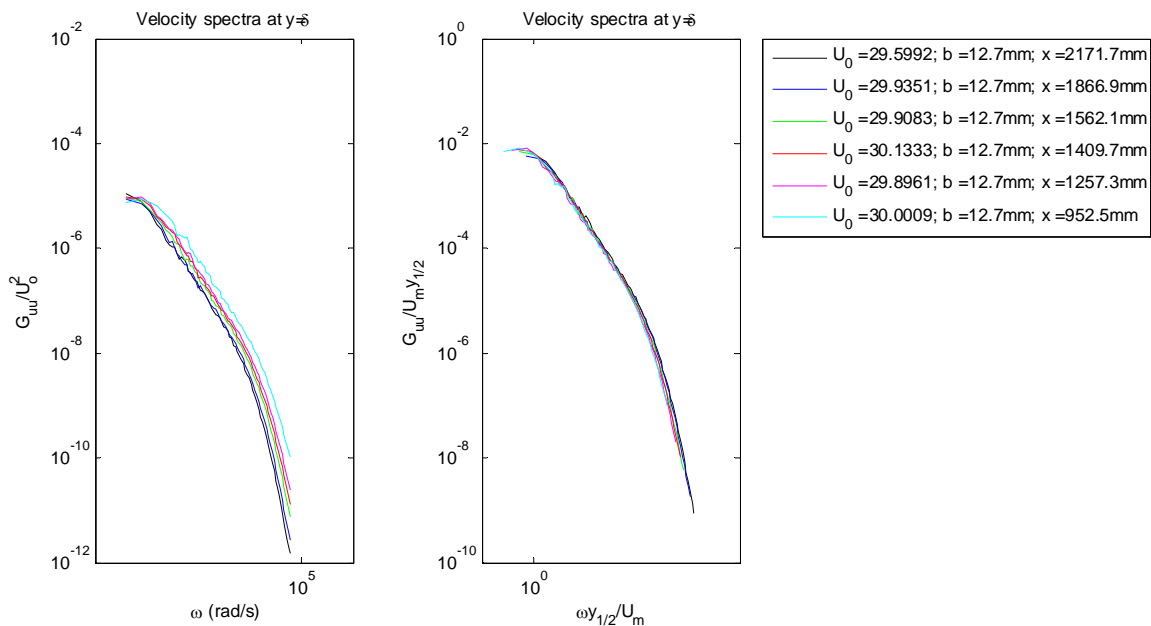


Figure 3.46 Smooth wall velocity spectra with varying nozzle height, x

3.1.14 Relation of the Smooth Wall Mean Velocity, Turbulence, and Spectral Data

When viewed collectively, the presented smooth wall jet measurements above can provide some insight into the nature of the flow in the current study. The smooth wall jet flow has been shown to scale on outer variables except very near the wall. The mean velocity also shows a scaling on wall variables near the wall, and there is an overlap region where the mean velocity scales on both inner and outer variables. The turbulent normal stress profiles also scale well on outer variables. However, they do not scale as well on wall variables over the range of available data. This result has also been noted by George *et al.* (2000) who show that the normal stress profiles only scale well on wall variables below a y^+ of about 7. This would suggest that the large, high energy turbulent structures present in the outer and mixing layers are affecting the turbulent character even very close to the wall.

Given the collapse of the normal stress profiles on outer variables, it is no surprise that the velocity spectra scale on outer variables as well. The velocity spectra presented were taken at three probe heights from the wall: one out in the mixing layer, one at the boundary layer height, and one at the displacement thickness height. The velocity spectra taken at each of these three heights all scale on the outer variables indicating that the large high energy turbulent motions are the dominant motions even as the wall is approached. The displacement thickness height lies around y^+ ranging from 35 – 70 depending on the flow test case, and from the results of the normal stress profiles and the results given by George *et al.* (2000) one would not expect any improved scaling over the outer variables at this height off of the flow surface. The velocity spectra were shown to scale very well at high frequencies on the inner scaling presented in Ueda and Hinze (1975), but this scaling did not collapse the velocity spectra at low to mid frequencies as well as the outer scaling, again indicating that the larger more energetic turbulent motions are dominant in the wall jet flow.

3.1.15 Smooth Wall Jet Flow Summary

From the discussion in the sections above, there are important conclusions regarding wall jet behavior over a smooth surface. First, the wall jet mean velocity and turbulence profiles can be shown to scale on the outer scaling variables, U_m and $y_{1/2}$, in the outer portions of the flow, but the ability of these outer scaling parameters to collapse the data deteriorates as the wall surface is approached. Second, relations describing the behavior of these scaling parameters and other boundary layer length scales as a function of initial flow conditions and streamwise location can be obtained using the momentum scaling and associated analysis proposed by Narasimha *et al.* (1973). Third, the skin friction velocity, u^* , was shown to scale the inner region of the wall jet mean velocity profiles from the wall through the log layer, and the method of George *et al.* (2000) for obtaining the skin friction velocity was shown to provide proper inner scaling for mean velocity profiles that agreed well with the composite velocity profile formulation proposed by George *et al.* (2000). Fourth, while the wall jet flow below the velocity maximum behaves in many ways like a canonical turbulent boundary layer (such as sharing a common laminar sublayer and possessing a log layer) it is, in fact, different from a turbulent wall jet flow in some key respects. This is evidenced by the fact that the semilog region of a regular turbulent

boundary layer does not fit the experimental wall jet data well and by the fact that the turbulence intensity profiles for a wall jet are significantly different in character than those of a turbulent boundary layer.

When looking at the smooth wall jet velocity spectra, one can conclude that the outer variables, U_m and $y_{1/2}$, scale the spectra effectively even as close to the wall as the displacement thickness height. Also, there appears to be little difference in the scaled behavior of the velocity spectra taken at the chosen boundary layer length scale heights. This supports the observations of earlier sections indicating that the boundary layer length scales are essentially constant multiples of one another and have the same dependence on initial flow conditions. This also suggests that for smooth wall jet turbulent flows the velocity spectra are determined by the higher energy large turbulent motions associated with the outer flow. Indeed, the turbulence character of the mixing layer modifies the flow structure even near the wall and appears to prevent the normal stress profiles from scaling on wall variables, at least down to a y^+ of 10 – 12. Below this height from the wall, the current study can provide no data for analysis.

3.2 Rough Wall Jet Flow Characteristics

3.2.1 Rough Wall Jet Test Conditions

The wall jet flow was measured for a range of initial test conditions and with the addition of rough patches to the flow surface. The rough patches were of a random sand grain type and varied in their surface character. The test conditions for the rough wall experiments in the current study are given in Table 3.2 below. The streamwise measurement location, x , is given as well as the roughness patch length, L_p . It should be noted that the roughness patch leading edge is always at a streamwise location downstream of the nozzle exit of 1257 mm. All rough wall measurements given in this table were taken directly behind the roughness patches.

Test Condition	U_o (m/s)	b (mm)	x (mm)	L_p (mm)	Re_j	$y_{1/2}$ (mm)	δ (mm)	δ^* (mm)	θ (mm)	Re_δ	Re_θ	Grit	k_g (mm)	k_s (mm)	k_{rms} (mm)	k_g^+	k_+
A	30.0	12.7	1562	305	14979	130	22.7	3.75	2.03	13085	1166	20	0.95	1.60	0.21	41.0	69.0
A	30.0	12.7	1410	152	22844	116	23.4	2.34	1.55	13602	899	40	0.43	1.00	0.13	18.6	43.9
A	29.8	12.7	1562	305	30426	129	28.6	2.76	1.97	16268	1118	40	0.43	1.00	0.13	15.6	36.7
A	29.9	12.7	1867	610	30998	160	31.7	3.30	2.33	15521	1142	40	0.43	1.00	0.13	13.1	30.8
A	29.9	12.7	2181	914	45388	188	29.6	3.59	2.49	13132	1103	40	0.43	1.00	0.13	13.2	31.0
A	29.8	12.7	1562	305	57832	128	23.6	1.88	1.37	13656	792	100	0.01	0.07	0.04	4.3	2.0
A	30.0	12.7	1562	305	22919	131	21.8	1.77	1.22	12231	684	180	0.08	0.04	0.02	2.5	1.3
A	30.1	12.7	1867	610	22971	158	24.5	2.33	1.61	12529	824	180	0.08	0.04	0.02	2.5	1.3
A	30.2	12.7	2172	914	22884	181	29.9	2.51	1.77	13757	818	180	0.08	0.04	0.02	2.2	1.1
B	39.9	12.7	1410	152	22872	119	21.3	2.31	1.51	16164	1147	40	0.43	1.00	0.13	25.2	59.4
B	40.0	12.7	1562	305	22871	136	26.5	2.63	1.85	19168	1337	40	0.43	1.00	0.13	20.4	48.1
B	39.9	12.7	1867	610	15358	164	33.8	3.81	2.69	22474	1790	40	0.43	1.00	0.13	17.8	41.9
B	40.0	12.7	2181	914	23065	191	34.8	4.18	2.90	21656	1802	40	0.43	1.00	0.13	16.4	38.5
B	39.9	12.7	1562	305	30871	135	17.4	1.71	1.17	12684	856	180	0.08	0.04	0.02	3.6	1.8
B	40.0	12.7	1867	610	30390	157	20.9	1.94	1.39	13974	926	180	0.08	0.04	0.02	3.3	1.7
B	40.1	12.7	2172	914	45562	180	29.9	2.27	1.64	18440	1015	180	0.08	0.04	0.02	2.6	1.3
C	60.0	12.7	1562	305	60362	136	23.4	3.79	2.13	26419	2408	20	0.95	1.60	0.21	80.1	134.9
C	59.9	12.7	1562	305	22923	137	22.4	3.42	2.02	25340	2284	36	0.53	1.30	0.19	43.6	107.0
C	59.8	12.7	1562	305	30551	140	26.5	2.97	2.10	29723	2358	40	0.43	1.00	0.13	32.9	77.5
C	60.0	12.7	1562	305	30668	134	22.4	2.55	1.71	25692	1970	60	0.27	0.44	0.11	19.3	32.1
C	60.1	12.7	1562	305	45902	132	22.4	2.52	1.61	26102	1882	60	0.27	0.26	0.08	18.5	18.2
C	60.0	12.7	1562	305	22932	135	22.4	2.30	1.52	26525	1805	80	0.19	0.16	0.07	12.6	10.6
C	59.8	12.7	1562	305	22937	134	20.3	1.70	1.18	22681	1319	100	0.01	0.07	0.04	8.1	3.8
C	60.0	12.7	1562	305	22984	140	23.4	1.85	1.33	26497	1501	150	0.09	0.06	0.03	5.2	3.1
C	60.1	12.7	1562	305	15251	133	19.2	1.54	1.07	22091	1224	220	0.07	0.03	0.02	3.8	1.7
D	19.8	25.4	1562	305	22840	141	26.5	4.15	2.31	14067	1226	20	0.95	1.60	0.21	39.5	66.5
D	19.7	25.4	1410	152	30127	131	24.4	2.31	1.52	13283	825	40	0.43	1.00	0.13	16.7	39.3
D	19.5	25.4	1562	305	30170	139	24.4	2.73	1.90	12631	985	40	0.43	1.00	0.13	15.5	36.6
D	19.9	25.4	1867	610	45402	168	33.8	3.24	2.30	15649	1065	40	0.43	1.00	0.13	11.7	27.4
D	19.8	25.4	2181	914	60494	197	34.8	3.75	2.63	14860	1123	40	0.43	1.00	0.13	11.4	26.7
D	19.5	25.4	1562	305	22896	136	20.9	1.90	1.35	10747	693	100	0.01	0.07	0.04	4.3	2.0
D	20.2	25.4	1562	305	30495	145	22.7	2.10	1.48	11996	781	180	0.08	0.04	0.02	2.7	1.4
D	19.9	25.4	1867	610	30385	163	20.9	2.00	1.38	10037	662	180	0.08	0.04	0.02	2.4	1.2
D	19.9	25.4	2172	914	45786	189	33.4	2.69	1.96	14409	844	180	0.08	0.04	0.02	1.9	1.0
E	30.0	25.4	1562	305	22917	147	23.4	4.15	2.31	18295	1807	20	0.95	1.60	0.21	61.0	102.8
E	29.9	25.4	1410	152	22910	135	20.3	2.51	1.67	16093	1329	40	0.43	1.00	0.13	29.6	69.6
E	29.8	25.4	1562	305	22920	147	27.6	2.92	2.05	20499	1525	40	0.43	1.00	0.13	22.9	53.8
E	29.9	25.4	1867	610	20804	180	34.8	3.25	2.29	23655	1552	40	0.43	1.00	0.13	15.8	37.3
E	30.0	25.4	2181	914	42065	201	42.1	4.46	3.12	27466	2035	40	0.43	1.00	0.13	14.7	34.7
E	29.7	25.4	1562	305	27722	145	24.5	1.98	1.44	18292	1076	100	0.01	0.07	0.04	6.0	2.8
E	30.1	25.4	1562	305	21048	143	24.5	2.15	1.59	19123	1243	180	0.08	0.04	0.02	3.9	2.0
E	30.1	25.4	1867	610	27929	168	25.4	2.55	1.85	18178	1322	180	0.08	0.04	0.02	3.5	1.8
E	30.3	25.4	2172	914	27824	193	27.2	2.26	1.67	18279	1124	180	0.08	0.04	0.02	3.0	1.6

Table 3.2 Rough wall jet flow test cases

As with the smooth wall test cases, the rough wall test cases are divided into test conditions designated A through E and are the same initial flow conditions that were described for the smooth wall test cases above. In the table above, each test condition represents a particular set of initial flow conditions, namely, the nozzle exit velocity and the nozzle height. Many of the same flow parameters given for the smooth wall flow were measured and are presented in this table for the rough wall flow. The roughness patch grit designation is given for each measurements presented above. This designation ranges from 20 to 220 in the current study and is nothing more than a measure of how big the roughness grains are on the sand paper patches used in this experiment. The higher the grit number, the smaller the grain size. The values of k_g presented are the nominal sizes of the sand grains obtained from standardized tables. The values of k_s presented are the calculated Nikuradse equivalent sand grain roughness sizes for each of the rough surfaces presented. The equivalent sand grain roughness size is determined empirically by fitting the semilog region of the wall jet flow over rough surfaces by the method presented in Aupperle and Lambert (1970) for turbulent boundary layers which was modified to account for the differences in the wall jet semilog region behavior with respect to that of a turbulent boundary layer seen above in Figure 3.36. The values of k_{rms} given in the table were

obtained from the measurements of MicroPhotonics that are discussed in Chapter 2 above. Also given in the table above are k_g^+ and k^+ where $k_g^+ = \frac{k_g u^*}{\nu}$ and $k^+ = \frac{k_s u^*}{\nu}$. These values are important because, for turbulent boundary layers, ranges of these parameters have been proposed that correspond to the flow behavior over rough surfaces. Nikuradse proposed that for $k^+ < 5$, the flow was considered to be hydrodynamically smooth, meaning that the roughness elements were within the laminar sublayer. For $5 \leq k^+ \leq 70$, the flow in turbulent boundary layers is considered to be transitionally rough, and for $k^+ \geq 70$, the flow is fully rough.

In order to create wall jet flows over rough surfaces, patches of sand-grain roughness were adhered to the aluminum plate that is the flow surface. The roughnesses used in the current study are described in detail above in Chapter 2. The roughnesses used were either standard aluminum oxide sand paper of varying grits or aluminum oxide floor sanding belts of varying grits. The major portion of the experimental data was taken with rough patches extending 610 mm in the spanwise direction and 305 mm in the streamwise direction. These rough patches were placed on the spanwise center of the aluminum plate with the leading and trailing edges of the roughness patches located at 1257 mm and 1562 mm aft of the nozzle exit, respectively (this streamwise location was chosen due to the inner geometry of the current facility's acoustic enclosure which contained a shelf (described in Chapter 2 above).

The patch edges created an effective step relative to the aluminum plate surface that ranged from 0.29 mm to 1.27 mm (this is just the backing thickness of the sand paper). This step height was between 30% and 120 % of the size of the measured displacement thickness at the leading edge of the roughness patches. It should be noted, however, that the steps associated with the addition of the roughness patches were smoothed at the leading edge by using aluminum foil tape. The aluminum tape was pressed so that it conformed to the roughness elements on the roughness patch, and was applied in such a way as to make the transition from the smooth flow surface to the rough surface occur over a streamwise distance of approximately 2.5 mm. The step size was not considered to be a dominant effect compared to the change in roughness size because measurements of the displacement thickness and momentum thickness for varying roughness size and nearly constant leading edge step size showed a clear variation with the roughness size.

There was also data taken for patches that extended further downstream than those mentioned above. These experimental data sets were taken to investigate the effect of the wall jet flow with an increase in streamwise distance from the roughness leading edge.

3.2.2 Considerations for Abrupt Changes in Surface Condition

One consideration that will be important to keep in mind is the fact that the flow in the current study is a smooth wall jet flow that encounters an abrupt change in surface roughness. One would expect for the effects of the sudden addition of roughness to the flow surface to evolve and develop from the point of origin of the rough surface. Smits and Wood (1985) provide a review of the behavior of conventional turbulent boundary layers with sudden changes in the surface condition. They propose that there is an outward propagation of the disturbance characterized by the growth of an inner layer beneath the existing boundary layer. The effects of the change in the surface are seen in this inner layer while outside of this inner layer, the flow remains uninfluenced and behaves as an undisturbed boundary layer flow. The inner layer grows outward with streamwise distance downstream of the origin of the change in surface condition and eventually permeates the entire boundary layer causing the boundary layer flow over the

changed surface condition to become fully developed. The streamwise distance necessary for the boundary layer to become fully developed is estimated by Smits and Wood (1985) to be between 10 and 20 times the boundary layer thickness at the origin of the change in surface condition depending on the severity of the perturbation.

Bradshaw *et al.* (1967) notes the incompressible time averaged continuity, boundary layer momentum, and the turbulence energy equations below for a turbulent boundary layer form a parabolic set of equations and note that there are three characteristics associated with this set of equations.

$$\frac{\partial U}{\partial x} + \frac{\partial V}{\partial y} = 0 \quad (3.12)$$

$$U \frac{\partial U}{\partial x} + V \frac{\partial U}{\partial y} = -\frac{1}{\rho} \frac{dP}{dx} + \frac{1}{\rho} \frac{\partial \tau}{\partial y} \quad (3.13)$$

$$\frac{1}{2} \rho \left(\frac{U \overline{\partial q^2}}{\partial x} + \frac{V \overline{\partial q^2}}{\partial y} \right) - \frac{\tau \partial U}{\partial y} + \frac{\partial}{\partial y} \left(\overline{p v} + \frac{1}{2} \overline{\rho q^2 v} \right) + \rho \varepsilon = 0 \quad (3.14)$$

The first term in equation 3.14 is the advection term, and the second term is the production term. The third term in the turbulence energy equation is the turbulent diffusion term, and the last term is the dissipation.

Of the three characteristics given by Bradshaw *et al.* (1967), the last outward characteristic of the undisturbed flow was noted to have the physical significance of being the apparent penetration point trajectory for flows that encounter an abrupt change in surface condition by Simpson (1971). In other words, the flow above this outgoing characteristic is unaltered by the presence of an abrupt change in surface condition while the flow below is affected by this change. In Figure 3.47 below, a schematic of this flow behavior noted by Bradshaw *et al.* (1967), Simpson (1971), and Smits and Wood (1985) is shown for a conventional turbulent boundary layer flow.

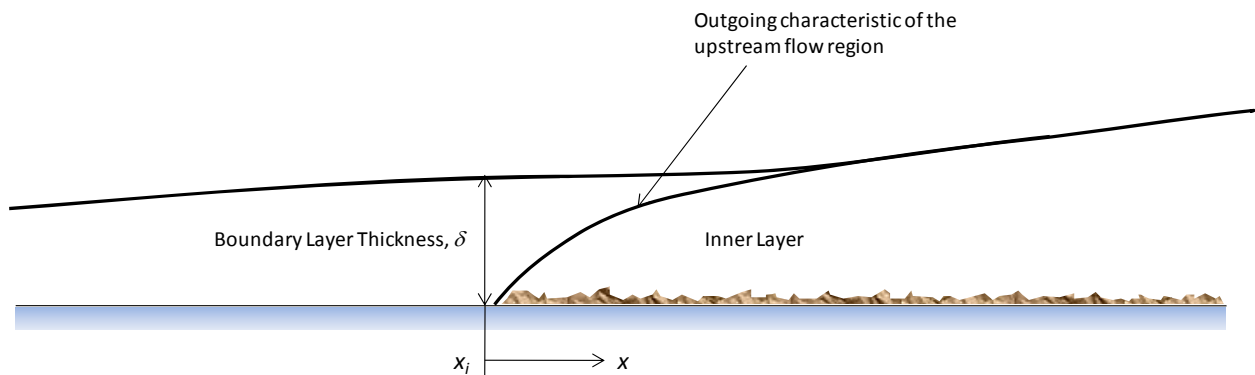


Figure 3.47 Schematic of boundary layer flow encountering abrupt change in surface condition

Simpson (1971) integrated the outgoing characteristic equation to obtain a relation for the y vs. $x - x_i$ position of the outward going characteristic, and this relation is given as follows:

$$x - x_i = \int_{y=0}^y \frac{U dy}{V + \frac{pv + \frac{1}{2}\rho\overline{q^2}v}{\rho q^2} + \left[\left(\frac{pv + \frac{1}{2}\rho\overline{q^2}v}{\rho q^2} \right)^2 + \frac{2\tau}{\rho q^2} \left(\frac{\tau}{\rho} \right) \right]^{\frac{1}{2}}} \quad (3.15)$$

where V is the velocity normal to the flow surface, τ is the shear stress, and $\overline{q^2}$ is the turbulent kinetic energy.

It is supposed that a similar phenomenon is present for wall jet flows that encounter a sudden change in surface roughness as in the current study. It was also thought that equation 3.15 above, while developed for conventional turbulent boundary layer flows, might be used to give an estimate of the extent of the inner layer described by Smits and Wood (1985), and provide a physical discussion tool for noting what portions of the wall jet flow could be expected to be altered due to the presence of short roughness patches. Unfortunately, equation 3.15 requires information for which no measurements were made in the current study such as the velocity normal to the plate, V , the shear stress profiles, τ/ρ , and the turbulent kinetic energy profiles, $\overline{q^2}$. An estimate for the turbulent diffusion is also required in order to use equation 3.15 above.

It was decided that in order to make an estimate of the y vs. $x - x_i$ position of the outward going characteristic, the mean streamwise velocity profile from a representative test case of the current study would be used along with experimental data from other studies taken at similar flow conditions. The mean streamwise velocity profiles taken at the origin of the surface discontinuity for a nozzle exit Reynolds number of approximately 21000 at a normalized streamwise distance, x/b equal to 99 was used for U in the equation above. The V profiles were obtained from the interpolated experimental data of Eriksson *et al.* (1998) who give a V/U_m vs. $y/y_{1/2}$ wall jet profile taken at x/b equal to 70 for a nozzle exit Reynolds number of 9600. These flow conditions are not coincident with those of the streamwise velocity data taken from the current study, but Eriksson *et al.* (1998) note the similarity of the V velocity as long as the Reynolds number is sufficiently high. These data were then adjusted to correspond with the current conditions. The shear stress profiles were obtained from the interpolated experimental data of Abrahamsson *et al.* (1994) who give Reynolds stress profiles normalized on the skin friction velocity for a wall jet flow taken at x/b equal to 70 and a nozzle exit Reynolds number of 10000. Again, these flow conditions are not coincident with the flow conditions used in the current study to obtain the streamwise velocity, but the Reynolds stress was shown by the George *et al.* (2000) similarity analysis to scale very well on the skin friction velocity, and the Abrahamsson *et al.* (1994) data was adjusted to correspond to the flow conditions of the current study. The turbulent kinetic energy profile was obtained from the interpolated experimental data of Tailland (1970) who gives the turbulent kinetic energy normalized on the maximum velocity vs. $y/y_{1/2}$. This data was obtained for a nozzle exit Reynolds number of 18000 at x/b equal to 85. The turbulent kinetic energy has been noted to behave similarly sufficiently far downstream of the nozzle exit, and thus this data was also able to be adjusted to correspond with the current study flow conditions.

The turbulent diffusion was estimated using the diffusion function, $G(y/\delta)$, described in Bradshaw *et al.* (1967):

$$G = \frac{\overline{pv + \frac{1}{2}\rho q^2 v}}{\rho} \frac{1}{\left(\frac{\tau_{max}}{\rho}\right)^{\frac{1}{2}} \frac{\tau}{\rho}} \quad (3.16)$$

Bradshaw *et al.* (1967) give an empirical variation of G with the τ_{max}/U_∞^2 for turbulent boundary layers. It was this empirical relationship that was used to obtain an estimate of the turbulent diffusion for the wall jet flow.

These quantities were used along with equation 3.15 above to obtain insight on how the wall jet flow is likely to be affected by the sudden addition of roughness to the surface for the streamwise velocity flow conditions noted above (x/b equal to 99 and Re_j equal to 21000). Given that experimental data from various studies encompassing a variety of flow conditions were used along with the fact that the model for the turbulent diffusion used was developed for ordinary turbulent boundary layers, there is a large uncertainty in the calculated results for y vs. $x - x_i$ of the outgoing characteristic for the wall jet flow seen in Figure 3.48 below.

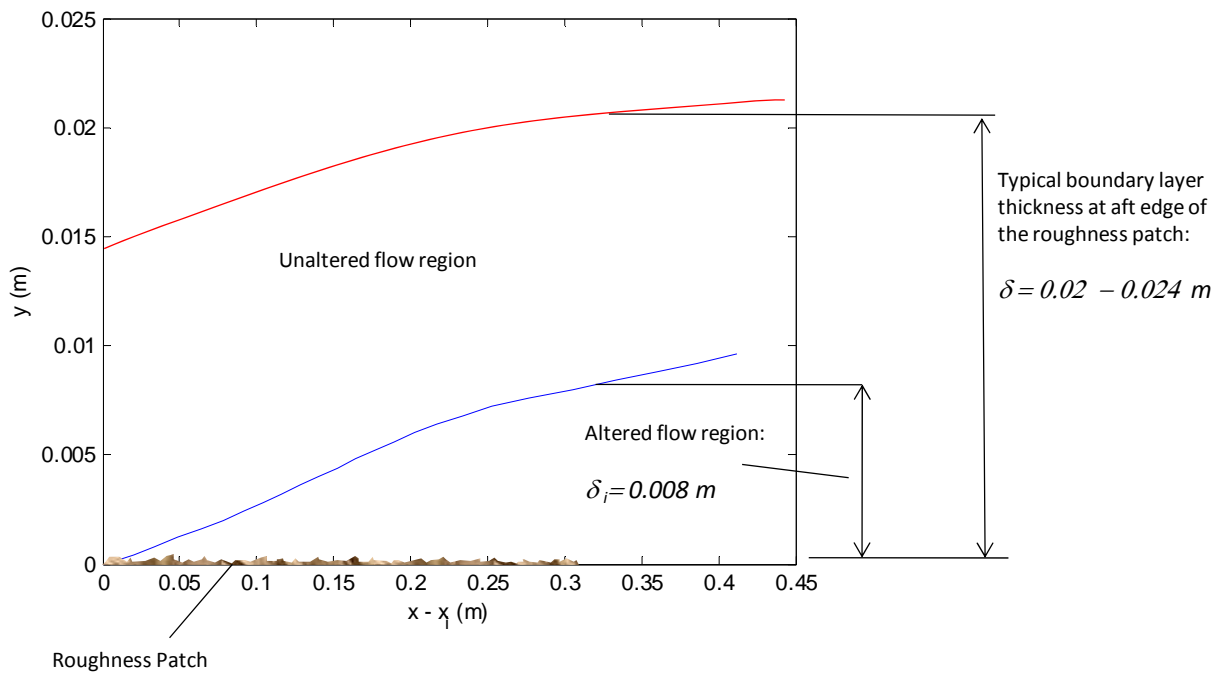


Figure 3.48 Calculated outgoing flow characteristic for wall jet flow with $Re_j = 21000$ and $x/b=99$ (blue) along with schematic of incoming flow and roughness patch

While there is some inherent uncertainty in the calculation above due to the use of experimental data from different studies and flow conditions and due to the use of a diffusion model created for turbulent boundary layers, the calculation in Figure 3.48 for the wall jet flow would indicate that the region of flow affected by the presence of the roughness is less than half of the height of a typical boundary layer thickness measurement at the aft edge of the 305 mm

roughness patches used in the current study indicating that the boundary layer thickness would not be affected by the presence of the rough patches used in the current study. Again, the calculation above is an estimation, and the extent of the inner layer that is estimated is subject to some uncertainty. However, this result can be useful in explaining flow parameter results and will be used as a discussion point in later sections. Other nozzle exit Reynolds numbers used in the current study were investigated, and the characteristic y value at the aft edge of the roughness patches was not seen to vary by more than 1.5 mm over this range of initial flow conditions. The results are left out in the figure above for clarity. It is also interesting to note that the inner region affected by the rough surface seems to develop more slowly than suggested by Smits and Wood (1985) taking much longer to reach a fully developed state.

3.2.3 Effects of Roughness Height on the Wall Jet Flow

Mean velocity profiles were taken at a single set of initial flow conditions from test condition C given in Table 3.2 above (U_o equal to approximately 60 m/s, b equal to 12.7 mm, and x equal to 1562 mm) behind roughness patches 305 mm in streamwise length. These roughness patches contained manufacturer sand-grain sizes ranging from 0.068 mm – 0.95 mm in diameter. The measured RMS roughness sizes that were obtained from MicroPhotonics range from 0.017 mm to 0.206 mm. These profiles (Figure 3.49) are normalized on the outer scaling variables discussed above in the previous sections. Given in the legend of this figure are the nozzle exit Reynolds number, the grit designation, and the roughness patch length, L_p , (all profiles were taken about 9 mm aft of the roughness patches which begin at a streamwise location of x equal to 1257 mm). Also presented is a clean plate profile taken at the same initial flow conditions (test condition C) and streamwise location. The flow conditions at the forward edge of the patch for this set of initial flow conditions were measured and the flow parameters are given in Table 3.1 above. At first glance the presence of roughness appears to have little or no effect on the normalized profiles, at least in the outer region of the wall jet flow. A closer look will show that near the wall the effects of the increasing roughness size are readily apparent. This is illustrated quite clearly in Figure 3.50 below. In this figure, it is very clear that as the roughness size is increased, the profiles begin to lift up off of the wall more and more as the velocity near the wall is reduced further and further. In other words, the smaller the roughness size, the fuller the profile.

Upon further investigation of Figure 3.50 below, it seems that it would be prudent to take a look at the effects of roughness on the height of maximum velocity. Nearly all rough wall jet studies mention that the presence of roughness increases the height of maximum velocity, or δ , in a wall jet flow. In smooth wall jet flows this height is generally considered to lie at a value of $y/y_{1/2}$ equal to 1.4 – 1.6 depending on which study is considered. For rough wall jet flows the reported height of maximum velocity varies from about $y/y_{1/2}$ equal to about 0.2 in Tachie *et al.* (2004) to nearly 0.38 in Ead and Rajaratnam (2004). The difference in the reported δ between these two studies is quite large. However, both studies support the notion that the boundary layer thickness is increased by the presence of roughness. In both of these studies, the roughness extends from the nozzle exit to the measurement location. It is apparent from Figure 3.49 that the boundary layer thickness does not occur at nearly the values of $y/y_{1/2}$ seen by Tachie *et al.* (2004) and Ead and Rajaratnam (2004). In fact from this figure it is difficult to say for sure that the boundary layer thickness is affected at all by the presence of the roughness patches. This is due to the fact that the roughness patches tested in the current study are of limited streamwise

length only extending some 15 - 20 boundary layer thicknesses downstream of their leading edge, and it is possible that the wall jet flows over the roughnesses in the current study have not had sufficient time to develop to a point where the effects of roughness are apparent. The effects of the roughness appear to be noticeable out to $y/y_{1/2}$ equal to approximately 0.125 from Figure 3.50 below. This corresponds to a y position of about 19 – 20 mm. Recall that the estimation of the outward going characteristic given above in Figure 3.48 would indicate that the extent of the effects of the rough surface at the trailing edge of the roughness patches should be about 8 – 9 mm. A one to one comparison of the current test flows and the estimate given is impossible due to the use of scaled experimental data from various studies and the use of a diffusion model developed for conventional turbulent boundary layers, and the results from Figure 3.50 would suggest that the y extent estimated for the outgoing characteristic is too small. The effects of roughness on the boundary layer thicknesses and maximum velocity will be discussed in more detail in a later section.

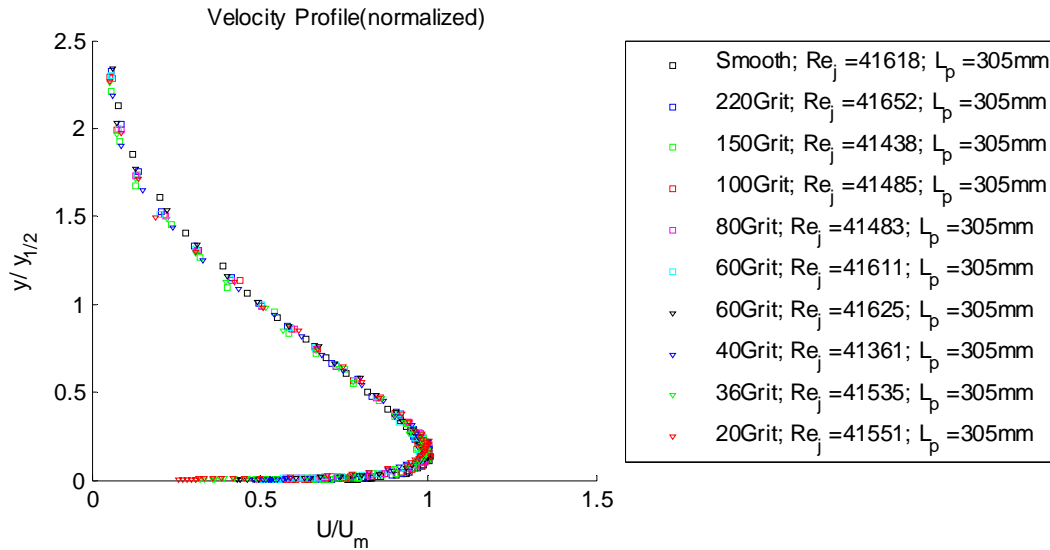


Figure 3.49 *Rough wall jet mean velocity profiles normalized on outer scaling variables*

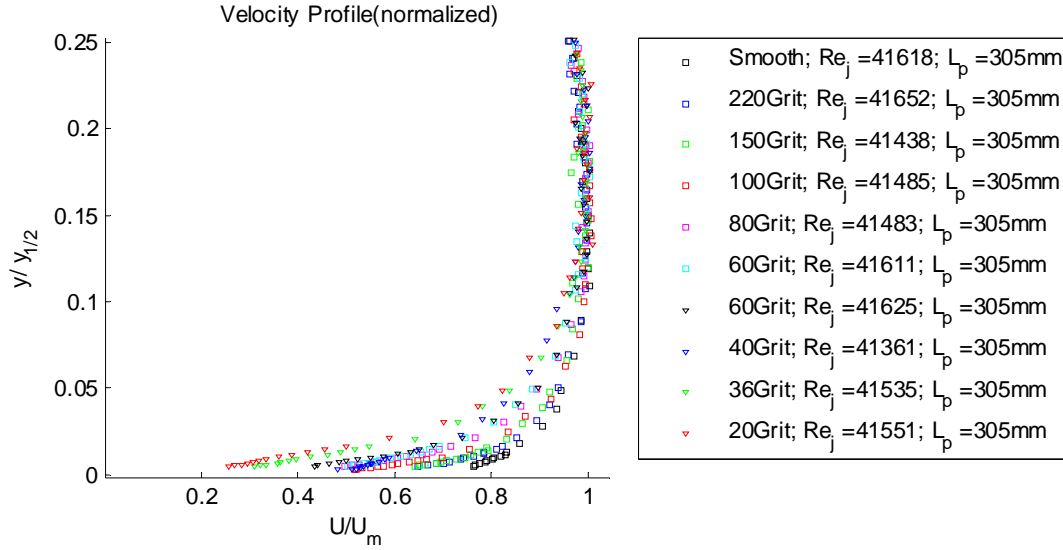


Figure 3.50 Rough wall jet mean velocity profiles normalized on outer variables near the wall

3.2.4 Effects of Initial Flow Conditions on the Rough Wall Jet Flow

As in the case of the smooth wall jet flow, the effects of the initial flow conditions U_o , b , and also variations in the patch length were investigated for the rough wall jet flow. The figures in the section below were all generated with the 40 grit ($k_g = 0.429$ mm; $k_{rms} = 0.156$ mm; $k_g/\delta \approx 0.025 - 0.033$ at the roughness patch leading edge) roughness patch. Similar figures were generated with a 180 grit (k_g equal to 0.041 mm; $k_{rms} = 0.02$ mm; $k_g/\delta \approx 0.0024 - 0.0031$ at the roughness patch leading edge) roughness patch, but the important results turn out to be the same between the two data sets. In fact, the only significant difference between the two is that the profiles generated for the 180 grit roughness were fuller than those for the 40 grit roughness, and this result has already been discussed in the section above. In Figure 3.54 the results of the analysis of the 180 grit profiles was added support the results from the 40 grit profiles.

Figure 3.51 shows mean velocity profiles taken directly behind roughness patches of varying streamwise extent. It is important to note that the roughness patch begins at a streamwise location of 1257 mm downstream of the nozzle exit. The 40 and 180 grit roughness cases were tested at patch lengths of up to 924 mm in length, and were longer than the rest of the roughness patches which were only 305 mm in length. These profiles were taken for a nozzle height of 12.7 mm at an x location and patch length that varied for a nozzle exit speed of approximately 30 m/s (test condition A).

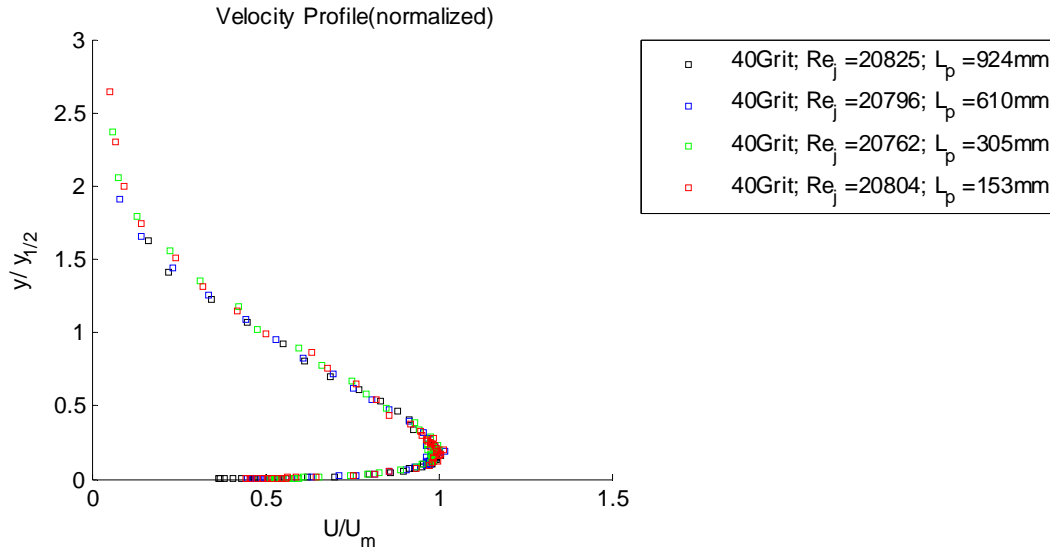


Figure 3.51 Rough wall jet mean velocity profiles (test condition A) normalized on outer variables showing the effects of patch length

There is no noticeable difference in the outer scaling behavior of the rough wall jet flow profiles shown above with the roughness patch length, but to illustrate this further, a closer look nearer to the wall is seen in Figure 3.52 below. No noticeable effect on the normalized profiles is seen as the patch length and measurement location varied. Also, any effect on the maximum velocity appears to be negligible. This result is in fair agreement with the limited literature regarding rough wall jet flows. The study by Tachie *et al.* (2004) shows a small variation of the maximum velocity for rough wall vs. smooth wall flows, but this difference between smooth and rough wall flows is not presented to be a function of downstream distance.

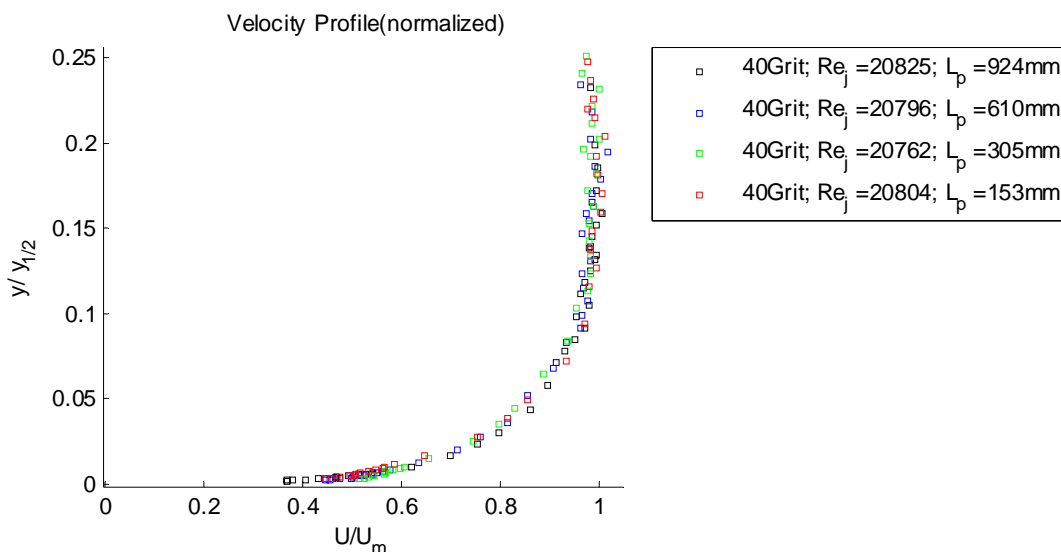


Figure 3.52 Rough wall jet mean velocity profiles (test condition A) normalized on outer variables showing the effects patch length near the wall

The effects of variation in nozzle exit velocity were also investigated for the 40 grit roughness test cases (test conditions A – C). Again, no noticeable effect of the variation in nozzle exit velocity can be seen in Figure 3.53 below.

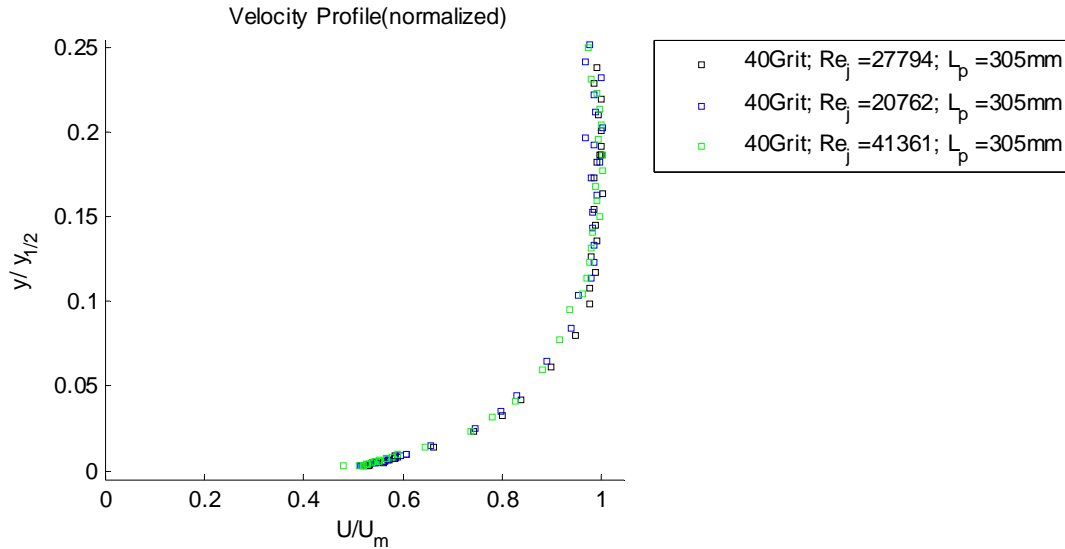


Figure 3.53 *Rough wall jet mean velocity profiles normalized on outer variables showing the effects of nozzle exit speed near the wall*

To analyze the effects of changing the nozzle height, profiles were taken behind two 305 mm long 40 grit and 180 grit roughness patches. The nozzle exit speed for these profiles was fixed at approximately 30 m/s while the nozzle height was varied between 12.7 mm and 25.4 mm (test conditions A and E, respectively). These profiles are shown in Figure 3.54 below, and show no noticeable effect of the change in nozzle height in the normalized profiles, but do show the effect of roughness. Again, the fuller profiles are those measured behind roughness patches whose roughness size is smaller.

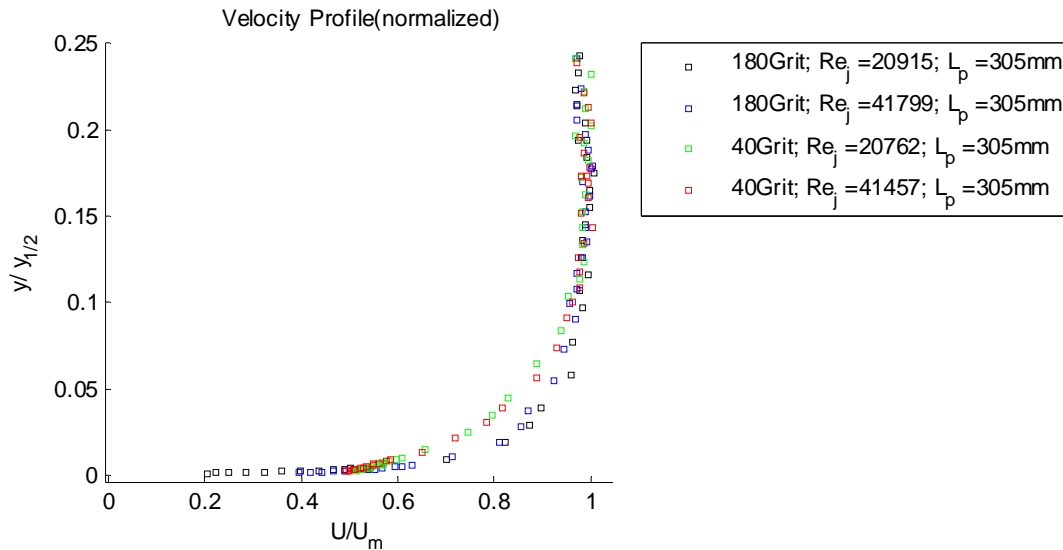


Figure 3.54 *Rough wall jet mean velocity profiles normalized on outer variables showing the effects of nozzle exit height near the wall*

3.2.5 Turbulent Character of the Rough Wall Jet Flow

The effects of variations in roughness size were investigated as they relate to the turbulent character of the wall jet flow. In Figure 3.55 below normal stress profiles normalized on outer variables are presented for wall jet flows over a range of rough surfaces. The nominal roughness heights of the sand-grain roughnesses used range from 0.068 mm to 0.95 mm, the measured RMS roughness sizes range from 0.017 mm to 0.206 mm, and the roughness Reynolds numbers based on the nominal roughness size vary from about 4 to about 80. For all profiles, the nozzle exit velocity and height were approximately 60 m/s and 12.7 mm, respectively (test condition C). All profiles were taken behind 305 mm long roughness patches that extend, in the streamwise direction, 10 – 20 times the boundary layer thickness at the leading edge of the patch. It is evident that there can be no consistent variation with roughness size can be seen in the outer regions of the normalized profiles. The outer variables collapse the normal stress profiles of the rough wall jet flows in the outer region to some extent, but the spread in the data near the wall is greater than that observed in the smooth wall normal stress profiles above. The smooth wall profile was taken at test condition C in Figure 3.55 and Figure 3.56 below.

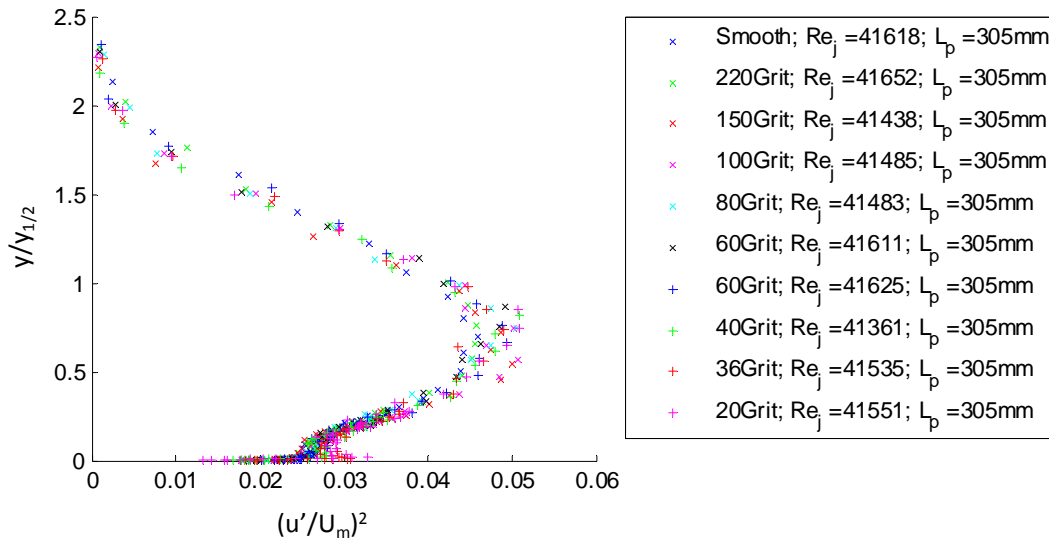


Figure 3.55 *Turbulence profiles (test condition C) for wall jet flows with varying roughness sizes normalized on the outer variables, U_m and $y_{1/2}$*

If the region below the velocity maximum (inferred to be roughly below $y/y_{1/2}$ equal to 0.15 from Figure 3.50 above) is looked at close, one can see in Figure 3.56 below that for some of the larger roughnesses, the turbulence intensity peak near the wall shows higher values, but as the roughness size is decreased, any clear progression of the normal stress profiles is lost.

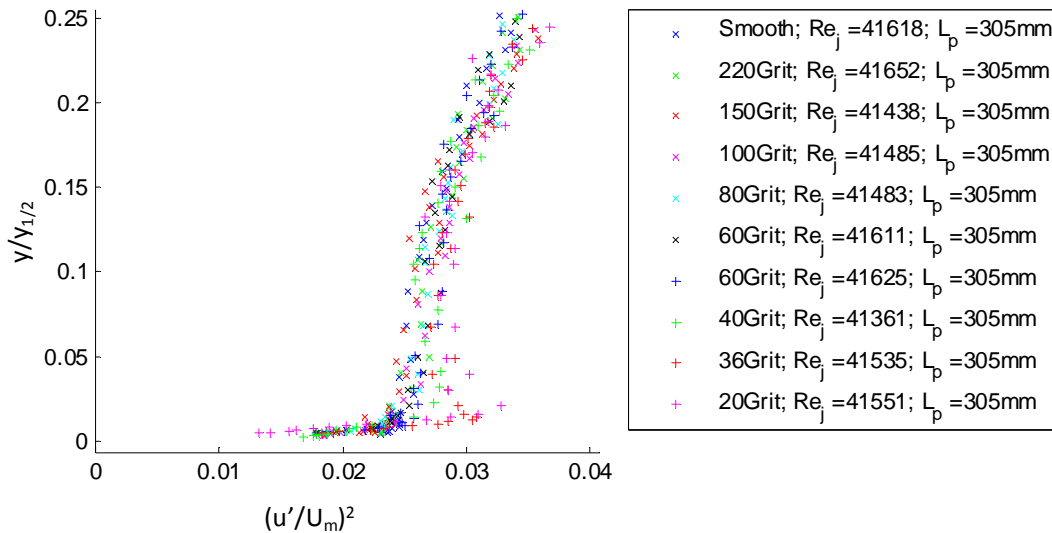


Figure 3.56 *Turbulence profiles (test condition C) for wall jet flows with varying roughness sizes normalized on the outer variables, U_m and $y_{1/2}$ near the velocity maximum and below*

From the analysis of the normal stress profiles in the outer region above, one may conclude that the presence of roughness does not affect the turbulent character in the outer regions of the wall jet flow. The normalized turbulence profiles in the outer region of the wall jet flow seem to be the same as those of a smooth wall jet flow, at least for the 305 mm roughness patches used in

the current study. However, very close to the wall, the normalized turbulence profiles show some dependence on the roughness condition. This indicates that the large turbulent motions associated with the mixing layer that dominated the smooth wall normal stress profiles are still dominant and are not noticeably affected by the surface roughness condition for the 305 mm roughness patches which cover a streamwise distance of approximately 20 times the boundary layer thickness at the leading edge of the patch and only 2.9 times the mixing layer half height, $y_{1/2}$, at the leading edge of the patch. However, the effects of the rough surface are seen to extend out to $y/y_{1/2}$ equal to 0.75 ($\approx 0.5\delta$) in the normal stress profiles scaled on inner variables. Perhaps this is because the effects of the sudden change in surface roughness have not reached a fully developed state, and the turbulent flow at, say the boundary layer thickness, is that of the undisturbed wall jet flow.

Normal stress profiles taken directly behind roughness patches of varying length were normalized on outer variables and plotted. These profiles were taken with nozzle heights of 12.7 mm and with nozzle exit velocities of approximately 30 m/s (test condition A). The rough patches investigated were 40 grit patches whose leading edge was located 1257 mm aft of the nozzle exit. The patch lengths varied from 305 mm to 914 mm. In Figure 3.57 below, these profiles were plotted alongside clean plate profiles taken at the same initial flow conditions (test condition A) and streamwise locations. All of these profiles have been normalized on outer variables. The outer variables seem to scale the turbulence profiles in the outer regions of the wall jet flow.

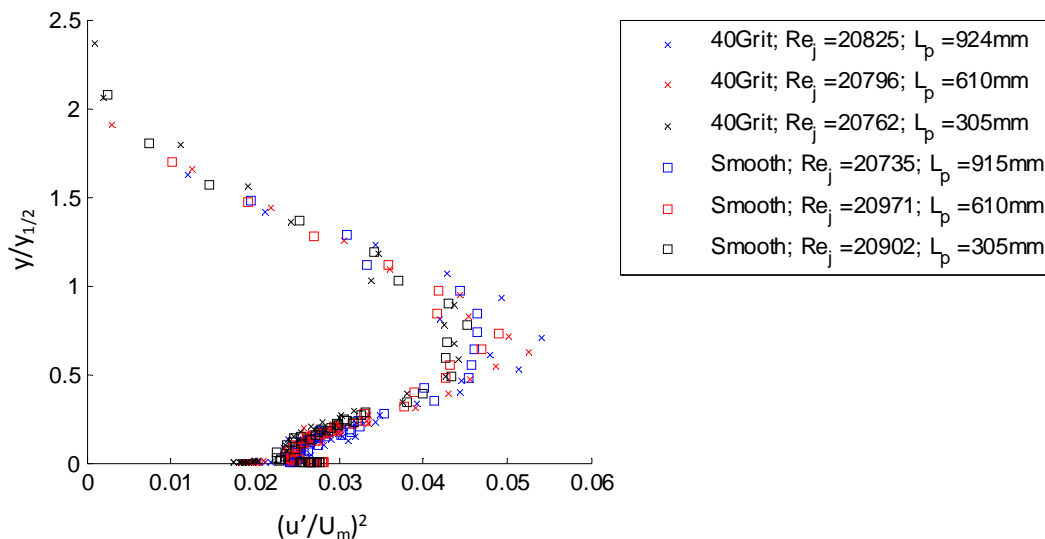


Figure 3.57 *Turbulence profiles (test condition A) of rough wall jet flows with varying roughness patch length compared with smooth wall jet profiles normalized on the outer variables, U_m and $y_{1/2}$*

In Figure 3.58 below, the nondimensional normal stress profiles for a wall jet flow over a 305 mm long patch of 40 grit roughness are presented. Smooth wall profiles are also presented at the same initial flow conditions (test conditions A – C). The nozzle height for these profiles was set at 12.7 mm and the nozzle exit speeds were nominally 30, 40, and 60m/s (test conditions A, B, and C).

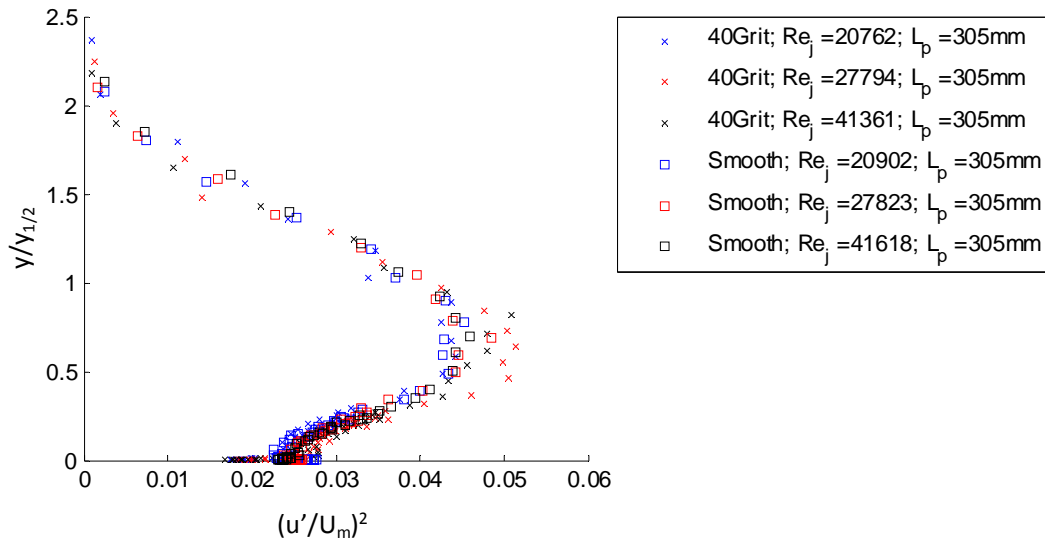


Figure 3.58 *Turbulence profiles of varying nozzle exit velocities for smooth and rough wall jet flows normalized on the outer variables, U_m and $y_{1/2}$*

These profiles are normalized on outer variables and collapse in a similar manner as the smooth wall profiles. It does appear that the collapse of the smooth wall data is somewhat tighter than that of the rough wall profiles and that the normal stress levels in the rough wall flows may show a higher maximum value in the mixing layer, but there is no real progression seen with the increase in the nozzle exit velocity.

The normal stress profiles for varying nozzle exit heights were plotted for both rough and smooth wall cases. The rough wall profiles were generated for flows over a 40 grit patch of roughness 305 mm in length. For both smooth and rough wall profiles, the nozzle exit velocity was nominally 30 m/s. The nozzle heights were varied from 12.7 mm to 25.4 mm (test conditions A and E for the smooth wall and rough wall profiles). These profiles normalized on outer variables are shown in Figure 3.59 below. The effects of the change in roughness cannot be seen in the figure below, but the effects of changing the nozzle height do appear to be present, but small, near the wall.

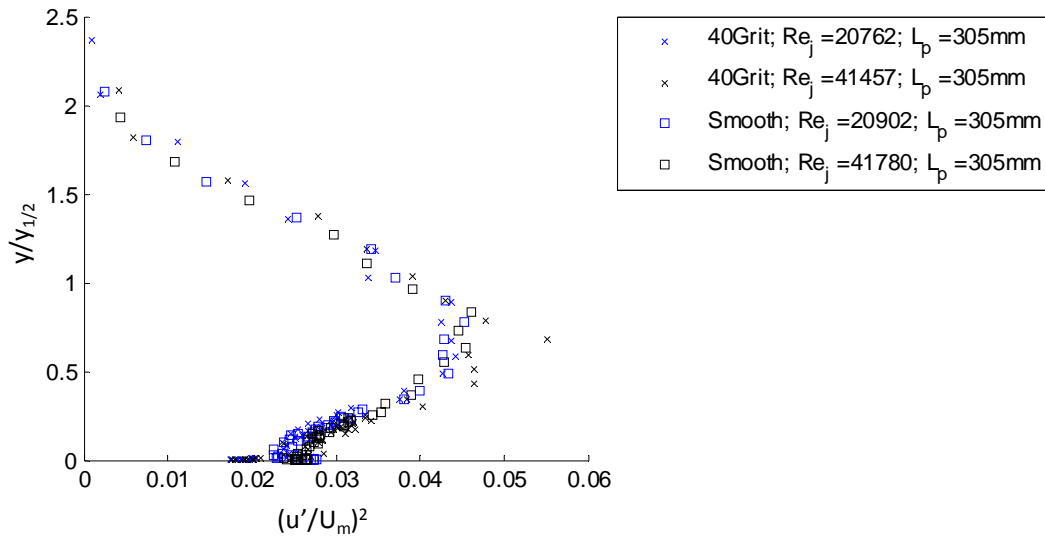


Figure 3.59 *Turbulence profiles (test condition A) of varying nozzle height for smooth and rough wall jet flows normalized on the outer variables, U_m and $y_{1/2}$*

Just the presence of roughness does not appear to change the scaling nature of the outer wall jet flow for cases of rough wall jet flows over 305 mm patches of roughness. The 40 grit roughness is not the roughest surface tested, but had sand-grain sizes larger than all but two of the rough surfaces tested. Therefore, one can say with reasonable confidence that the scaling nature of the outer region of the normal stress profiles is unaffected by the presence of the 305 mm roughness patches used in this study, and the effects of the patch length are only small in the outer portion of the nondimensional normal stress profiles if they exist at all. The roughness does appear to affect the inner portions of the nondimensional normal stress profiles significantly as long as the roughness is larger than the 60 grit roughness used in this study as indicated in Figure 3.56 above.

3.2.6 Rough Wall Jet Outer Flow Parameters

In section 3.1.6 above several smooth wall jet parameters were discussed in detail, and their behavior was discussed. The behavior of rough wall jet flow parameters is also of interest and will be discussed in detail in this section. In order to investigate the effects of roughness on wall jet flow parameters, a series of tests and analyses were conducted. First, the effects of varying roughness size on 305 mm roughness patches were investigated. These rough patches extended downstream about 15 – 20 times the boundary layer thickness at the leading edge. The rough patch leading edges were located 1257 mm ($x/b = 99$) aft of the nozzle exit. Then the effects of varying the patch length were investigated by taking velocity profiles directly behind rough patches varying in length from 153 mm – 914 mm ($L_p \approx 10 - 60$ times the boundary layer thickness at the leading edge of the patches). Again, these roughness patches of varying length were placed so that the leading edge was 1257 mm aft of the nozzle exit. After this was done, methods to estimate the boundary layer length scales are presented, and data will be shown to support these estimations.

3.2.6.1 *Effects of Roughness Variation for 305 mm Patch Lengths*

In Figure 3.60, Figure 3.61, Figure 3.62, Figure 3.63, and Figure 3.64 below, flow parameters from profiles taken behind 305 mm patches of 40 and 180 grit roughness over a range of nozzle exit speeds and heights were compared along with smooth wall jet parameters and the smooth wall curve fits discussed above. The range of nozzle exit speeds and heights was approximately 20 – 60 m/s, and 12.7 – 25.4 mm, respectively (all test conditions presented in Table 3.2 are present in these figures). Later, in Figure 3.65 through Figure 3.71 the variation of all roughness sizes will be given at a single initial flow condition (test condition C). Between these figures and the ones directly below, the major bulk of the experimental data is accounted for, and the results shown are indicative of the rest of the data set.

From Figure 3.60 one can see that the maximum velocity was measured to be very close to the smooth wall estimated values regardless of the roughness or lack thereof. Similarly, the measured values of $y_{1/2}$ shown in Figure 3.61 seem to be independent of the roughness and look to be more or less centered on the smooth wall estimated values. The difficulty in measuring $y_{1/2}$ accurately due to possible air currents in the laboratory could explain the large scatter of the data. This could also hide small variations of $y_{1/2}$ with the roughness height making them undetectable. Still, there really does not appear to be an effect of roughness on $y_{1/2}$ in the current experimental setup, and this is expected given the discussion of the effects of roughness given in section 3.2.2 above and given the results of Figure 3.50 above showing no effect of the roughness above $y/y_{1/2}$ equal to about 0.125.

Rough wall boundary layer parameters and flow conditions are compared to the previously established smooth wall curve fits in Figure 3.62, Figure 3.63, and Figure 3.64 below. In these figures, data from the smooth wall, 180 grit, and 40 grit surface conditions are presented because there are more data points at various test conditions tested for these surface conditions. The data presented were taken directly behind 305 mm roughness patches ($x = 1562$ mm) for test conditions A, B, D, and E. Also, these particular surface conditions make for a nice comparison because the 40 grit roughness is one of the largest roughnesses tested while the 180 grit roughness was the next to the smallest roughness surface condition tested. In Figure 3.62 the effects of the rough surfaces begin to become apparent. It is quite clear that the smooth wall boundary layer measurements agree well with the smooth wall estimations, but as the roughness size is increased from that in the 180 grit cases to that in the 40 grit cases, the boundary layer thickness appears to increase as well. This trend is continued with increased clarity in Figure 3.63 and Figure 3.64 below showing that closer to the flow surface the effects of roughness are more important which is to be expected.

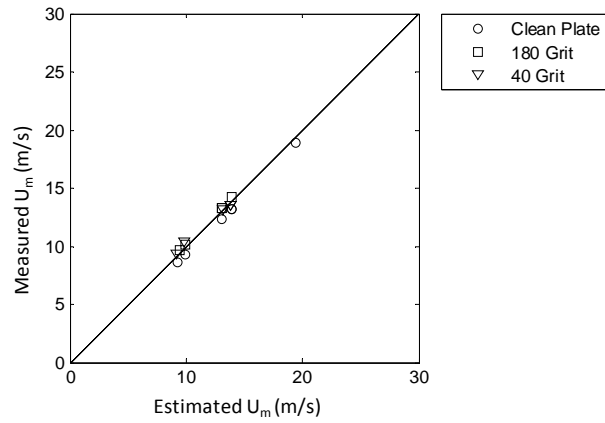


Figure 3.60 Rough and smooth wall jet flow U_m (measured vs. smooth wall estimations)

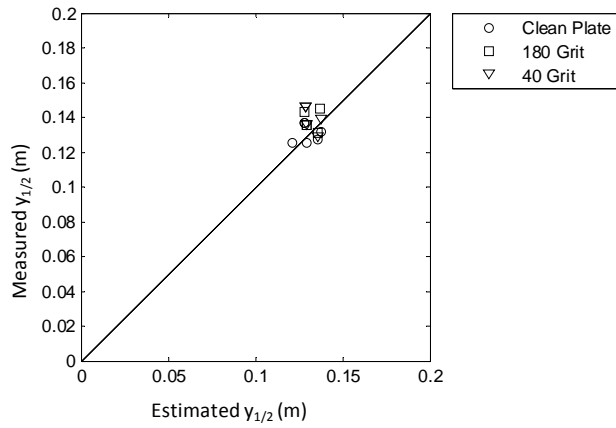


Figure 3.61 Rough and smooth wall jet flow $y_{1/2}$ (measured vs. smooth wall estimations)

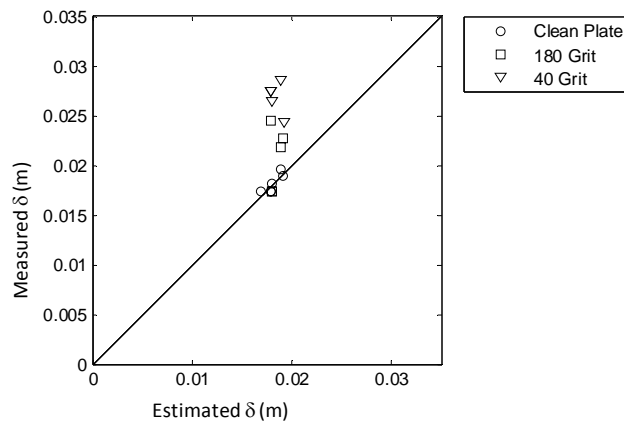


Figure 3.62 Rough and smooth wall jet flow δ (measured vs. smooth wall estimations)

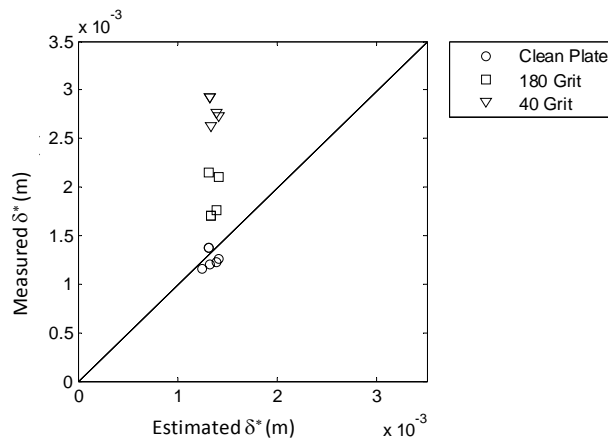


Figure 3.63 *Rough and smooth wall jet flow δ^* (measured vs. smooth wall estimations)*

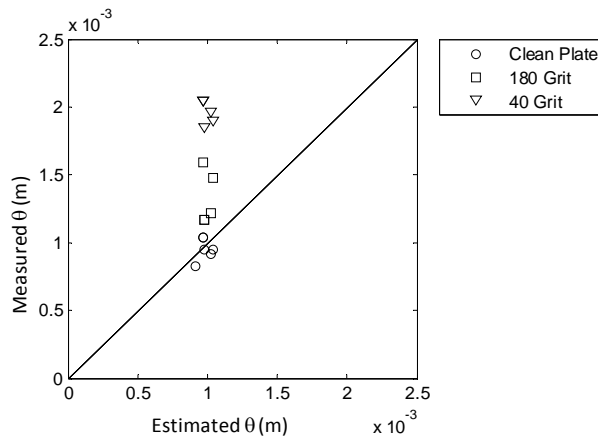


Figure 3.64 *Rough and smooth wall jet flow θ (measured vs. smooth wall estimations)*

To investigate the effects of roughness height further, flow parameters from profiles taken behind 305 mm patches of roughness of varying sizes were compared and plotted against the RMS roughness grain size normalized on the nozzle height, b . All of the flow parameters were obtained from velocity profiles taken with a nozzle exit height of 12.7 mm and for a nozzle exit velocity of approximately 60 m/s (test condition C). In Figure 3.65 below, the wall jet maximum velocity normalized on the nozzle exit velocity is shown for all flow cases.

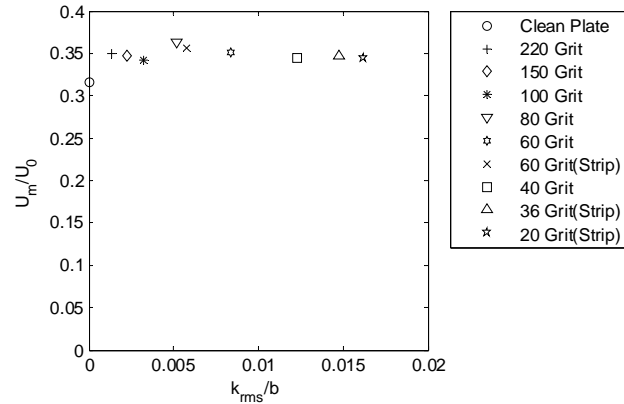


Figure 3.65 Normalized U_m as a function of normalized RMS roughness height

No apparent variation in the wall jet maximum velocity can be seen from Figure 3.65 above. In Figure 3.66, Figure 3.67, Figure 3.68, and Figure 3.69 below, the measured length scales discussed in section 3.1.6 above for the smooth wall flow are examined for wall jet flows over various roughnesses. These length scales were obtained from the same test cases as those of the maximum velocities shown in Figure 3.65 above.

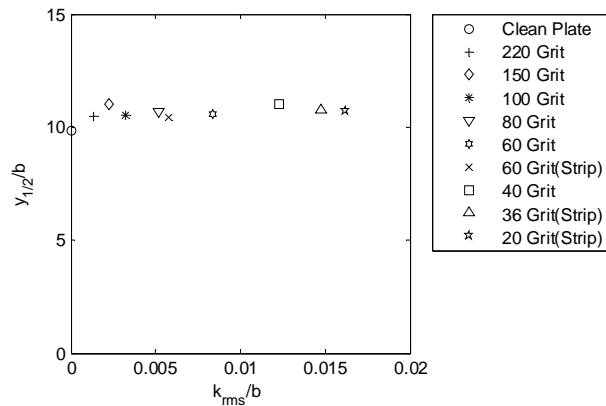


Figure 3.66 Normalized $y_{1/2}$ as a function of normalized RMS roughness height

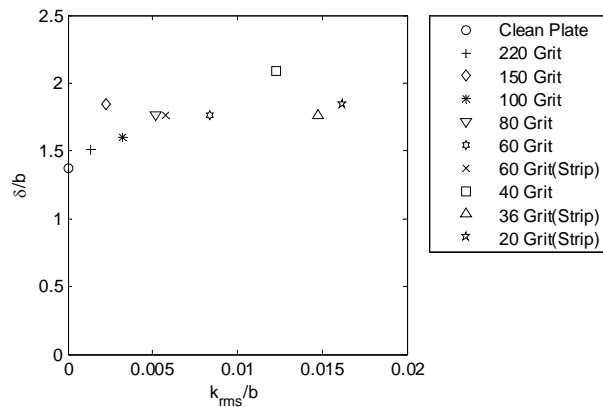


Figure 3.67 Normalized δ as a function of normalized RMS roughness height

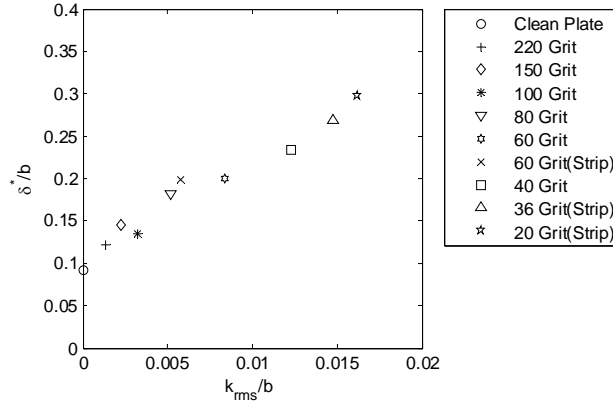


Figure 3.68 Normalized δ^* as a function of normalized RMS roughness height

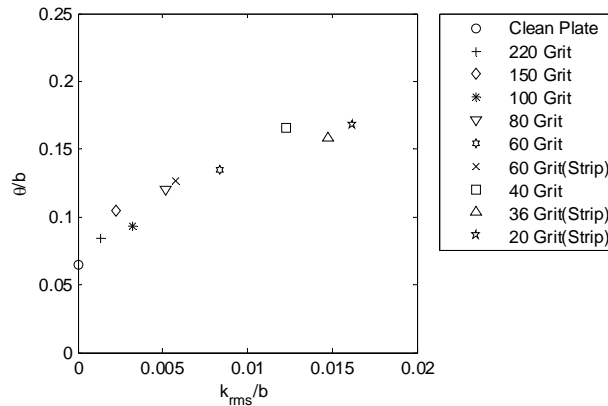


Figure 3.69 Normalized θ as a function of normalized RMS roughness height

Again, there is no definite variation of $y_{1/2}$ with the roughness size. However, the boundary layer thickness appears to increase as roughness is applied to the surface, but no definite trend is observable in Figure 3.67 above. This increase is on average 29.5% over the smooth wall boundary layer thickness. Figure 3.67 seems contradict Figure 3.62 above. One may also notice that in Figure 3.67 the largest boundary layer thicknesses measured were recorded for the 180 and 40 grit cases (rough surfaces represented in Figure 3.62) suggesting that perhaps the measured boundary layer thicknesses in Figure 3.62 are in error and too large. It is possible that this discrepancy is due to a poorly taped leading edge of the 40 and 180 grit rough surfaces, but this is unlikely due to the progressive behavior of the displacement and momentum thicknesses.

It is believed that the 29.5% average increase in boundary layer thickness is possibly due to the discontinuity of the smooth plate and the presence of a patch of finite thickness being applied to the plate rather than the actual size of the roughness on the patch, although the discussion in section 3.2.2 and the results seen in Figure 3.50 would suggest that the presence of the roughness is not seen by the flow at the boundary layer height due to the short length of the roughness patch. Perhaps the region of the flow affected by the roughness at the aft edge of the patch is quite close to encompassing the boundary layer height and thus makes for difficult identification of the effects of roughness on the boundary layer thickness. Another possible reason why the increase of boundary layer thickness with roughness size is not entirely clear lies

in the fact that measuring the boundary layer thickness is an inherently uncertain process because one needs to determine the location of the velocity maximum from the mean velocity profiles.

If all of the rough wall boundary layers measured behind 305 mm patches of roughness for all test conditions are plotted normalized on $y_{1/2}$ vs. k_{rms} the result is seen in Figure 3.70 below. The measured boundary layer thicknesses from the 40 grit cases seem to ride outside the norm, and the rest of the measured boundary layer thicknesses show an increase over the smooth wall boundary layer measurements indicated by data points plotted at k_{rms} equal to 0. The most outlying boundary layer thickness for the 40 grit roughness case was taken at test condition C.

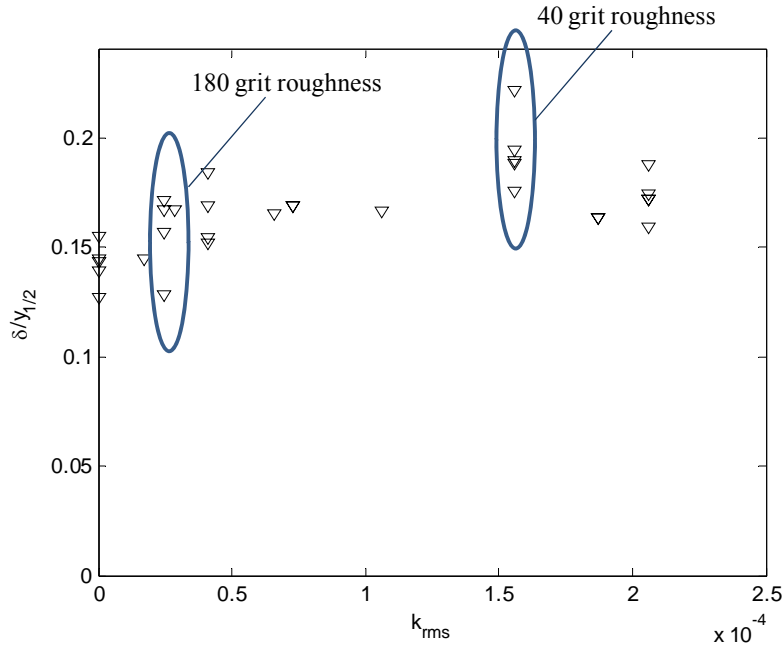


Figure 3.70 Nondimensional boundary layer thickness vs. k_{rms} (test conditions A – E)

The displacement and momentum thicknesses show a definite variation with roughness size. The momentum and displacement thicknesses more than double with an increase in roughness that is less than 7% of the nozzle height. Figure 3.71 below presents another way of looking at the displacement thickness data shown in Figure 3.68. The data shown was taken at test condition C (see Table 3.2). The displacement thickness shows a consistent variation with the increase in roughness size associated with the different roughnesses used. It is also clear that the displacement thickness for the flow over 20 grit roughness is almost four times the smooth wall measured and estimated values.

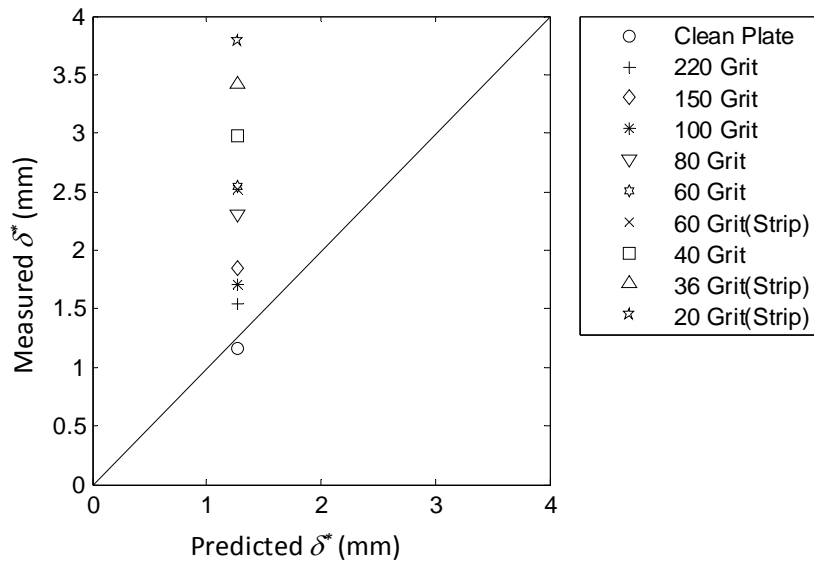


Figure 3.71 δ^* for smooth and rough wall jet flows (measured vs. smooth wall estimation)

3.2.6.2 Effects of Varying Roughness Patch Lengths

It was desirable to determine how the rough patch length affects the flow, so profiles taken at different patch lengths for the 40 and 180 grit cases were analyzed and the flow parameters obtained from the mean velocity profiles were examined. The parameters shown in Figure 3.72, Figure 3.73, and Figure 3.74 below were taken from profiles whose nozzle height was 12.7 mm and whose nozzle exit velocity was nominally 30 m/s (test condition A). The x location of the measured profiles is presented in the legend of the figures below. All profiles were taken directly behind (approximately 9 mm aft of the trailing edge) the roughness patches, and all roughness patches had their leading edge located at 1257 mm aft of the nozzle exit. The cases where the x measurement location is 2172 mm, for example, were taken behind roughness patches that are 914 mm long. Notice in Figure 3.72 there is very little or no noticeable effect of the patch length on the maximum flow velocity. The same observation held for $y_{1/2}$ and will not be shown here for the sake of brevity. The boundary layer thickness shown in Figure 3.73 is not seen to vary with the patch length in a consistent way, but does appear to be affected to some extent. In Figure 3.74 below, it appears that the displacement thickness does grow faster as the patch length increases than predicted by the smooth wall estimations for the 40 grit case. For the 180 grit measurements, this variation is not evident. This is likely due to the fact that the 180 grit roughness test cases have k^+ values that would indicate hydrodynamically smooth conditions. The momentum thickness analysis will not be shown because the same conclusions were drawn as for the displacement thickness. However, for the boundary layer, displacement, and momentum thicknesses, a larger data set was used to investigate the effects of the patch length further.

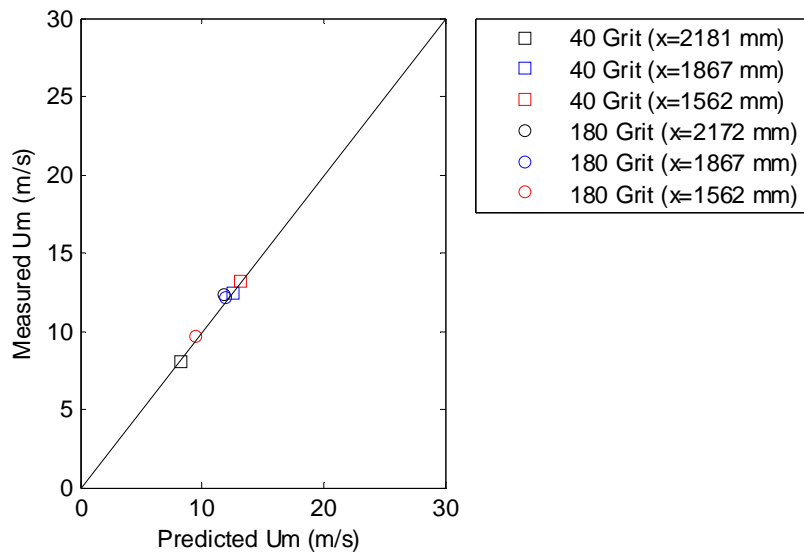


Figure 3.72 Measured U_m vs. smooth wall estimation for varying roughness patch lengths

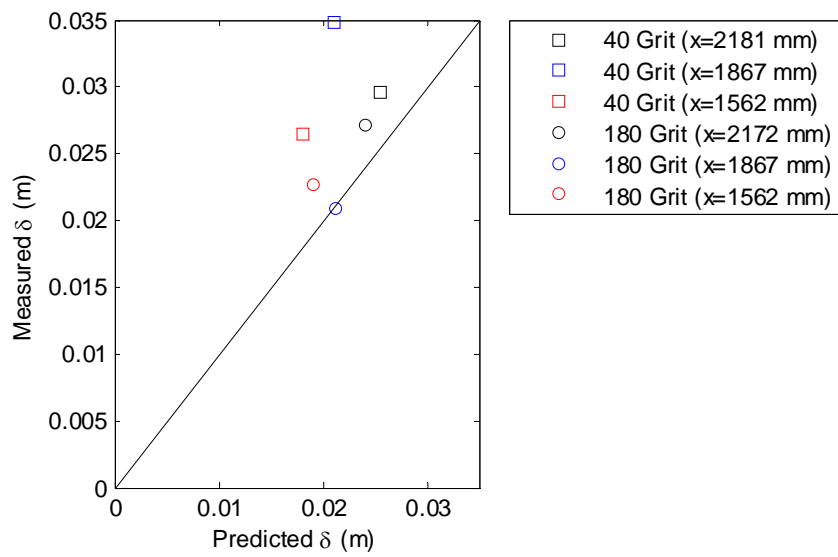


Figure 3.73 Measured δ vs. smooth wall estimation for varying roughness patch lengths

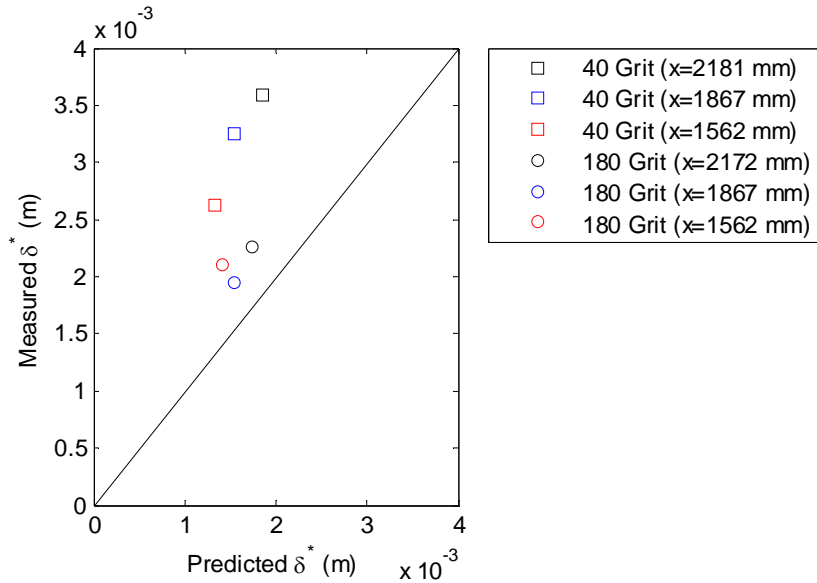


Figure 3.74 Measured δ^* vs. smooth wall estimation for varying roughness patch lengths

In order to investigate the effects of the roughness patch length further for the boundary layer, displacement, and momentum thicknesses, the measured data for nozzle exit speeds ranging from 20 – 40 m/s and nozzle heights ranging from 12.7 – 25.4 mm (test conditions A, B, D, and E) taken behind roughness patches of varying length were compared with the smooth wall data taken at the same initial flow conditions and measurement locations (test conditions A, B, D, and E). The results are shown in Figure 3.75 and Figure 3.76 below. The results were normalized on the nozzle height, and are presented as a function of nondimensional distance downstream of the nozzle exit.

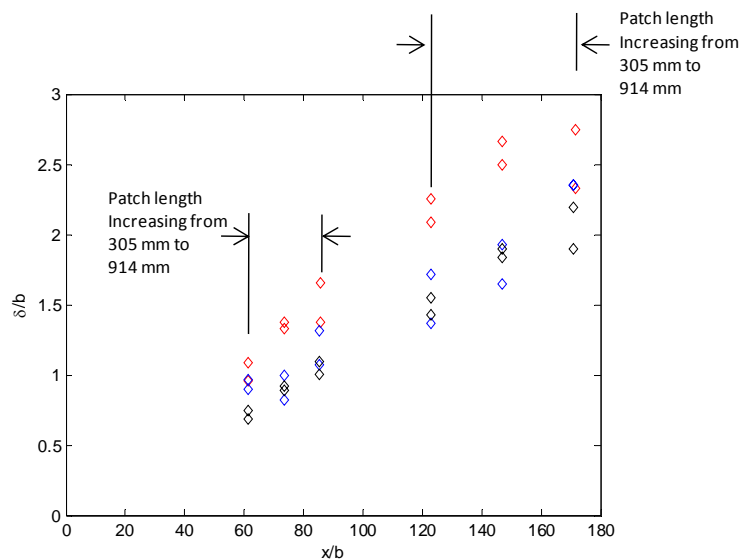


Figure 3.75 Normalized boundary layer thickness vs. normalized distance from the nozzle exit; (red: 40 Grit test cases, blue: 180 Grit test cases, black: smooth wall test cases)

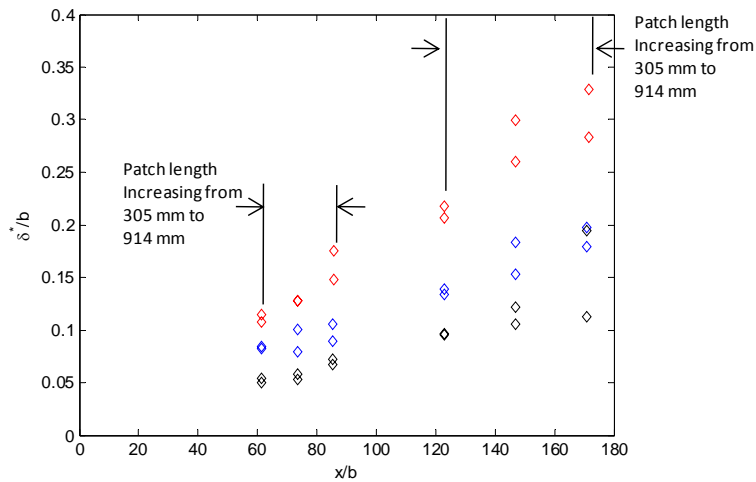


Figure 3.76 Normalized displacement thickness vs. normalized distance from the nozzle exit; (red: 40 Grit test cases, blue: 180 Grit test cases, black: smooth wall test cases)

In these figures, two groups of data can be seen (one group below x/b equal to 90 and one above x/b equal to 120). These groups correspond to data taken with different nozzle heights. Within these groups there can be seen data that correspond to three normalized streamwise distances, which correspond to successively longer patches of roughness. The spread in the data at each normalized streamwise distances is due to the change in initial velocity. The boundary layer and displacement thickness data was presented in this way to give an idea of how the displacement thickness and boundary layer thickness behave with normalized streamwise distance from the nozzle exit, and in particular, if this behavior is dominated by the change in patch length or the change in streamwise distance. From Figure 3.75 above, the boundary layer thickness can be seen to grow with the streamwise distance downstream faster with an increased roughness size, but it is not readily clear how important the patch length is to the variation of the boundary layer thickness due to the uncertainty of the boundary layer thickness measurement. The displacement thickness also shows an increased growth rate with the nondimensional distance downstream as the roughness size is increased. It was expected that the patch length would affect the displacement and momentum thickness growths in a noticeable way because these boundary layer length scales are much closer to the flow surface. However, this effect is not present in Figure 3.76 above with the clarity expected. In fact, it is believed that further investigation, beyond the scope of the current study, of the effect of roughness patches of limited extent on the boundary layer length scales is needed to better understand the effects of the roughness patch length.

3.2.6.3 The Hogg *et al.* (1996) Scaling

When the smooth wall jet parameters were discussed above, the fact that the parameter data can be scaled on the jet momentum as proposed by Narasimha *et al.* (1973) was used to develop the estimations that were presented for the smooth wall boundary layer, displacement, and momentum thicknesses as well as that of the maximum velocity and $y_{1/2}$ for various flow conditions and measurement locations. A similar scaling was proposed for the boundary layer thickness of rough wall jet flows by Hogg *et al.* (1997) and is discussed in Chapter 1, but this can

be extended to other boundary layer length scales. This type of scaling appears to be similar to the Narasimha *et al.* (1973) momentum scaling in that the parameter data is scaled on the jet exit momentum flux, J , but there are a few differences. First, this new scaling deals with the roughness size. Also, if one looks closely at the dimensionless downstream distance and dimensionless length scaling arrangements, it can be seen that the nozzle exit velocity in the denominator is canceled by the nozzle exit velocity implied by the nozzle jet exit momentum (J is equal to bU_o^2). U_m , $y_{1/2}$, and δ were shown not to vary with roughness size (for the short roughness patches) in the preceding sections while the displacement thickness and momentum thickness were seen to vary in a consistent way with the roughness size. In Figure 3.77 and Figure 3.78 below, the scaling proposed by Hogg *et al.* (1997) is applied to the current available rough wall jet flow displacement and momentum thicknesses from test conditions A - E.

In each of these figures a fit to the data has been presented in the form of a red line. There is a collapse of all of the parameter data seen in the figures below, and there is the potential for using experimental data curve fits in a similar way as the smooth wall estimations were developed.

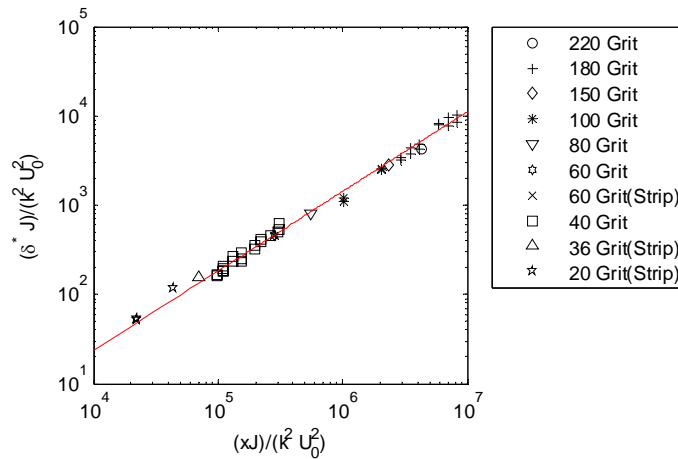


Figure 3.77 Dimensionless δ^* vs. dimensionless downstream distance for rough wall flow

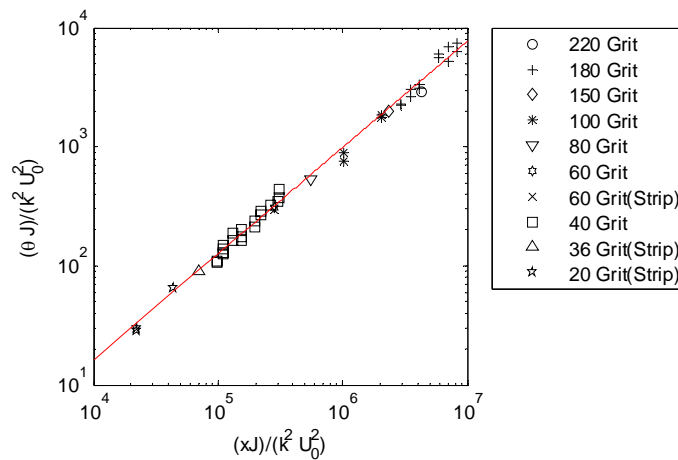


Figure 3.78 Dimensionless θ vs. dimensionless downstream distance for rough wall flow

The empirical fits in Figure 3.77 and Figure 3.78 above are given below:

$$\frac{\delta^*}{b} = H_1 \left(\frac{x}{b}\right)^m \left(\frac{b}{k}\right)^{2(m-1)} \quad (3.17)$$

$$\frac{\theta}{b} = H_2 \left(\frac{x}{b}\right)^n \left(\frac{b}{k}\right)^{2(n-1)} \quad (3.18)$$

where H_1 and H_2 are empirically determined constants (0.0065 and 0.0045, respectively) and m and n are the exponents fixing the slope of the fit. The exponents that fit the data for the nondimensional δ^* and θ length scales were both found to be 0.89.

3.2.6.4 Curve Fits for the 305 mm Roughness Patch Wall Jet Flows

For the scaling of surface pressure fluctuations in later chapters, it is necessary to have curve fits for the boundary layer flow parameters so that a continuous interpolation between measured flow parameters can be obtained. The Hogg *et al.* (1996) scaling above was used to obtain a curve fit for the displacement and momentum thicknesses. From these experimentally determined values of m and n and from equations 3.17 and 3.18 above, estimations for the rough wall jet displacement and momentum thicknesses were produced by use of a similar method to that used for the smooth wall estimations. In Figure 3.79 and Figure 3.80 below, one can see the measured values vs. the estimated values for the rough wall jet displacement thickness and momentum thickness.

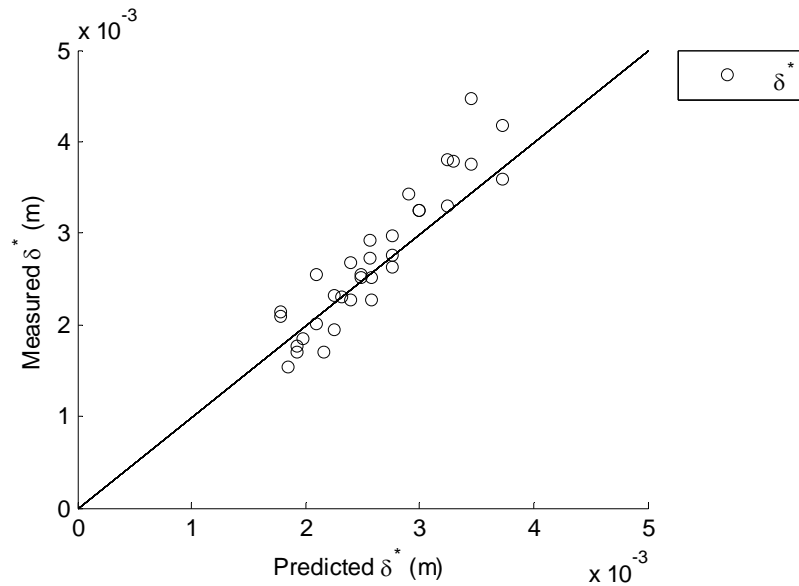


Figure 3.79 Measured vs. estimated δ^* for rough wall jet flows

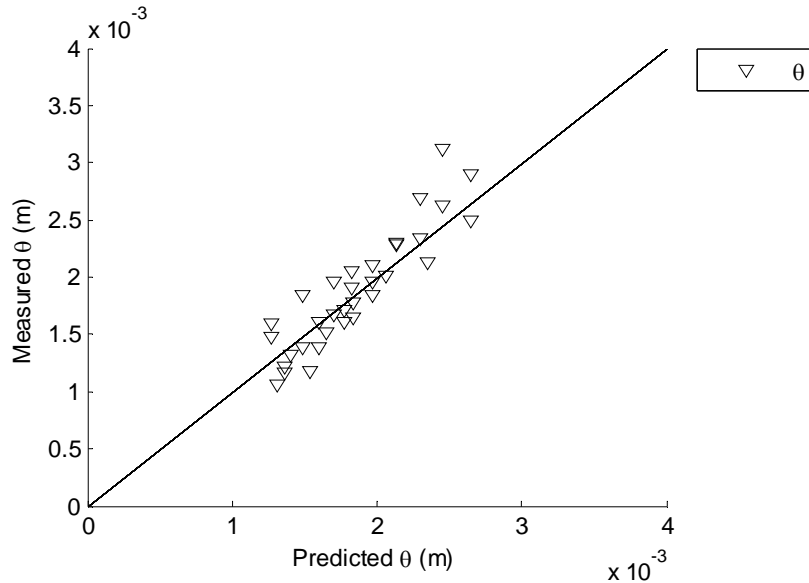


Figure 3.80 Measured vs. estimated θ for rough wall jet flows

The estimations for the displacement and momentum thicknesses show agreement between the estimated and measured rough wall jet displacement and momentum thicknesses. It should also be noted that other choices for the roughness length scale, such as k_{rms} , were investigated along with other scaling attempts to incorporate the flow velocity, but were not successful in improving the estimations seen in Figure 3.79 and Figure 3.80 above.

It was shown above that the maximum velocity and the mixing layer half height, $y_{1/2}$, did not show any variation with the roughness size so the smooth wall estimations have been adopted as the rough wall jet flow parameter estimations for these flow variables. The boundary layer thickness was also seen to be invariant with the roughness size, and the smooth wall estimation obtained from the Narasimha *et al.* (1973) scaling was used to estimate the boundary layer thickness for the surface pressure spectral scaling described in the following chapter. However, a scale factor was applied to the smooth wall scaling for the boundary layer thickness to account for the 29.5 % increase in boundary layer thickness seen in Figure 3.67 above when roughness patches of any size were applied.

3.2.7 Rough Wall Jet Flow Inner Region Scaling

The proper velocity scale for the inner portions of the smooth wall jet flow is the skin friction velocity, u^* . It is desired to present the rough wall jet profiles in inner coordinates as for the smooth wall jet profiles. With the addition of roughness, skin friction correlations dependent on simple flow parameters are no longer applicable, and another method of obtaining the skin friction is needed. Obtaining the skin friction (and, hence, the skin friction velocity) is not necessarily an easy undertaking for smooth wall jet flows as was discussed above. One cannot use a Preston tube to calculate the skin friction in rough wall flows because the laminar sublayer disappears entirely for roughnesses of even very small size. This leaves direct methods as a possible alternative for measuring the skin friction of rough wall jet flows. At the current time a skin friction balance that uses four very small load cells and floats on glycerin is being developed

and should be tested and ready for use by the summer of 2008. Until then, however, skin friction estimates will have to do. Thus, effort has been expended to produce the best estimate possible for rough wall skin friction estimates. The approach decided upon was to use a momentum balance across the roughness patch in order to estimate the skin friction of the flow. The method used is discussed in detail in Grissom *et al.* (2007). In short, the x momentum equation for a wall jet is integrated from the wall to δ yielding

$$\frac{\tau_w + \tau_\delta}{\rho} = \frac{dU_m^2 \theta}{dx} - (\delta - \delta^*) U_m \frac{dU_m}{dx} \quad (3.19)$$

where τ_w is the shear stress at the wall and τ_δ is the shear stress at the height of the boundary layer thickness. The δ term present in equation 3.19 above is present because for a wall jet flow the pressure gradient is zero.

Using this equation requires two assumptions. First, the maximum velocity must be considered to be independent of the surface roughness condition. This has been shown to be true for the current test cases examined for the 305 mm roughness patches. The other assumption is that τ_δ is also invariant with changes in surface roughness in the current study. The scaling of the normal stress profiles at the boundary layer edge with outer scaling parameters seen in the discussion above regardless of surface condition, suggest that this is a reasonable assumption. This will also be supported by the scaling of the velocity spectra for rough wall jet flows show in a later section below.

Now, if equation 3.19 is written for both smooth wall jet flows and rough wall jet flows and the difference between the two is taken, the following results:

$$\frac{\tau_w|_r - \tau_w|_s}{\rho} = \frac{dU_m^2 (\theta_r - \theta_s)}{dx} - [(\delta_r - \delta_s) - (\delta_r^* - \delta_s^*)] U_m \frac{dU_m}{dx} \quad (3.20)$$

Where the subscript r designates rough wall values and s denotes smooth wall properties. This can be integrated across the length of the roughness patch from the leading edge (x_1) to the trailing edge (x_2). The resulting relation is as follows:

$$\frac{f - f_s}{\rho} = U_m^2 [\theta_r(x_2) - \theta_s(x_2)] - \int_{x_1}^{x_2} [(\delta_r - \delta_s) - (\delta_r^* - \delta_s^*)] U_m \frac{dU_m}{dx} dx \quad (3.21)$$

where f is the total frictional force per unit span for the rough surface and f_s is the frictional force per unit span over the same area of the smooth surface. The subscripts r and s denote rough and smooth, respectively. From this equation, one can obtain an estimate of the difference between the rough and smooth wall jet flow skin friction values for a particular set run. Even if smooth wall jet mean profiles were not conducted for the same initial flow conditions as the rough wall jet flow of interest, the smooth wall parameter estimations discussed above can be used to obtain the smooth wall values required by equation 3.21. The boundary layer length scales in 3.21 are assumed to vary linearly. This is considered to be a fair approximation due to the relatively short patch length of the rough surface. To get the total skin friction, the correlation from George *et al.* (2000) was integrated over the streamwise extent of the roughness patch at each flow

condition of interest to obtain an estimate for the smooth wall skin friction, and then the difference between the smooth and rough wall jet skin friction values was added to the smooth wall skin friction estimate. In Figure 3.81 below, the skin friction values estimated from all of the measurements taken from test condition C and all other measurements taken for 305 mm roughness patches taken from test conditions A, B, D, and E are presented vs. the local flow Reynolds number along with George *et al.* (2000) estimate for the clean plate flows.

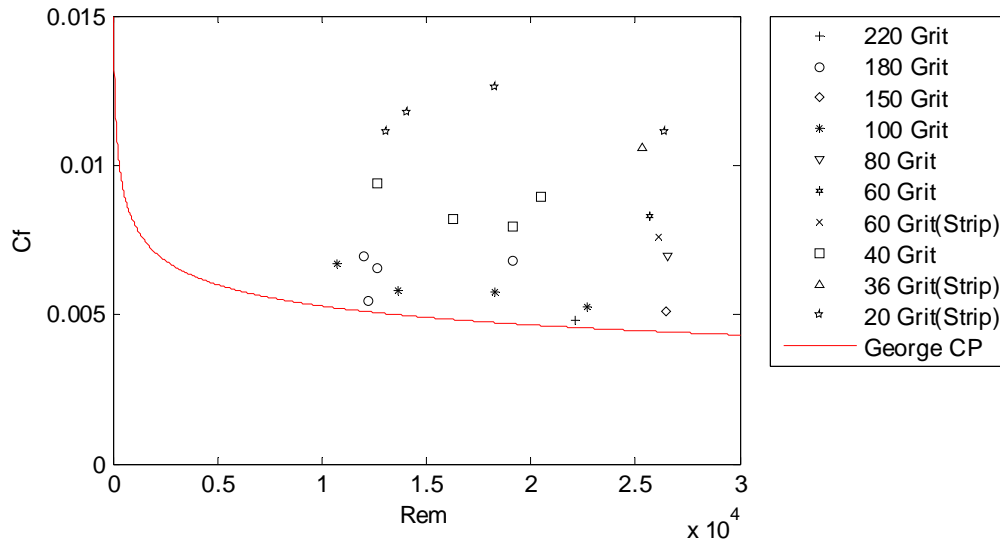


Figure 3.81 Skin friction coefficient estimate for rough wall jet flows

There is some scatter in the estimates shown above, but in general, the skin friction estimates rise with the roughness size which is expected. Also, the estimates for the 220, 180, 150, and 100 grit cases fall very nearly on the smooth wall estimate for the most part which is not surprising given that the k^+ values for these measured test cases are all below 5.

Seen another way, the skin friction coefficient values for test condition C are presented below against the nominal sand grain size, k_g .

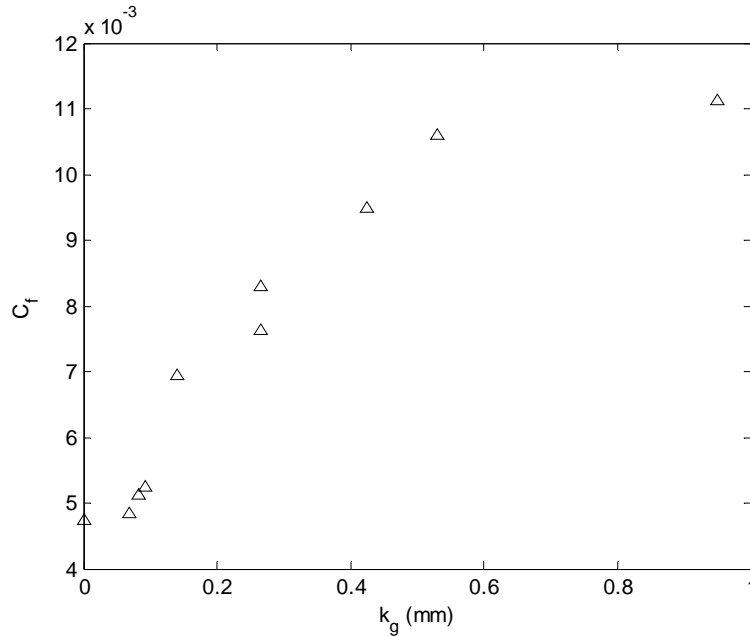


Figure 3.82 Skin friction estimates vs. nominal sand grain size

This figure shows a consistent variation with the roughness grain size. Skin friction estimates taken at similar roughness Reynolds numbers (k^+) by Tachie *et al.* (2004) show a reasonable agreement to within 8% – 9%.

These estimates of the skin friction coefficient were used to calculate the skin friction velocity which was used to scale the rough wall jet inner flow. The results of the analysis of the inner portion of the rough wall jet inner flow are presented below.

3.2.8 Rough Wall Jet Flow in Inner Coordinates

The smooth wall jet flow was presented in inner coordinates earlier in section 3.1.11 and was shown to scale well on the skin friction velocity which was obtained using the method described in George *et al.* (2000). Now the rough wall jet flow profiles will be presented in same way. In Figure 3.83 below, several profiles taken behind rough patches of varying roughness size (all 305 mm long) are shown. Each of these profiles was taken at test condition C. Also presented is a smooth wall profile taken at the same initial flow conditions.

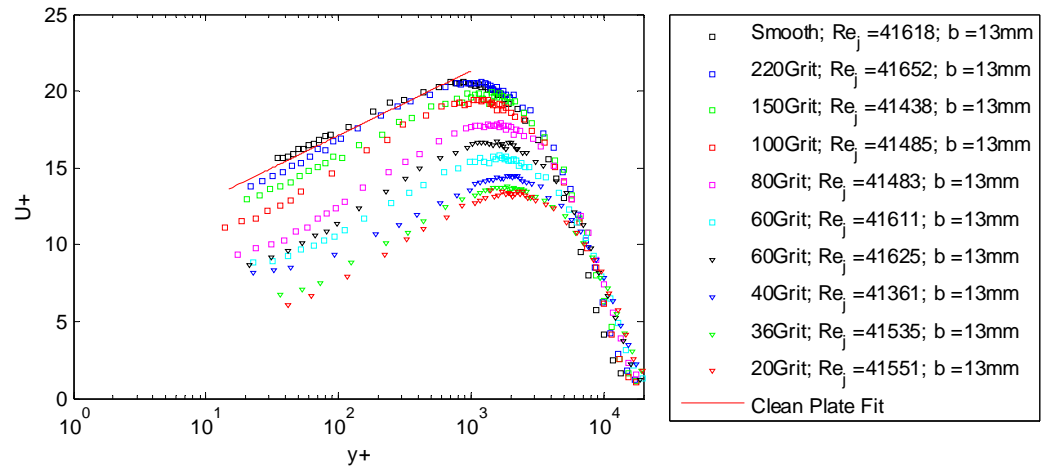


Figure 3.83 Rough wall jet profiles in inner coordinates

The smooth wall profile matches the smooth wall fit described previously in section 3.1.11 closely. One can also see that as the roughness size is increased from 220 grit roughness to 20 grit roughness, the profiles normalized on the skin friction velocity shift downward. They all collapse at large values of y^+ because they were all taken at the same set of initial flow conditions. It is also important to note that the slope of the log law region seems to remain unchanged regardless of the roughness size. This type of behavior is very similar to that seen in regular turbulent boundary layers as presented by Hama (1954). The profiles shown above are indicative of the rest of the profiles taken in this study. In the profiles taken from other test cases, the profiles shift with the roughness size and changes in Reynolds number as would be expected.

The equivalent sand grain roughness height, k_s , was determined by fitting the semilog region of the profiles above using the method described by Aupperle and Lambert (1970). The equation of the semilog fit is adapted from the smooth wall jet semilog fit given in Figure 3.36 above. The fit adapted to account for the equivalent sand grain roughness height is given as follows:

$$u^+ = 4.2 \text{Log}(y^+) - 4.2 \text{Log}\left(\frac{k_s u^*}{\nu}\right) + 8.7 \quad (3.22)$$

where k_s is the equivalent sand grain roughness height. A roughness Reynolds number is defined from this equivalent roughness size, $k^+ = k_s u^* / \nu$, and flows for a k^+ of less than 5 are considered to be hydrodynamically smooth in conventional turbulent boundary layers. For $5 \leq k^+ \leq 70$ the flow is considered to be transitionally rough and for $k^+ \geq 70$ the flow is considered to be fully rough. In Figure 3.84 below, the nominal roughness size and the equivalent sand grain size are presented vs. the RMS roughness size obtained from MicroPhotinics. It should be noted that the nominal roughness size is larger than the equivalent roughness size until a k_{rms} of about 0.075 mm is reached where the equivalent sand grain roughness size becomes larger than the nominal grain size suggesting that the equivalent roughness size is not physically tied to the geometric roughness size. The equivalent sand grain roughness sizes shown were calculated from the velocity profiles taken at test condition C.

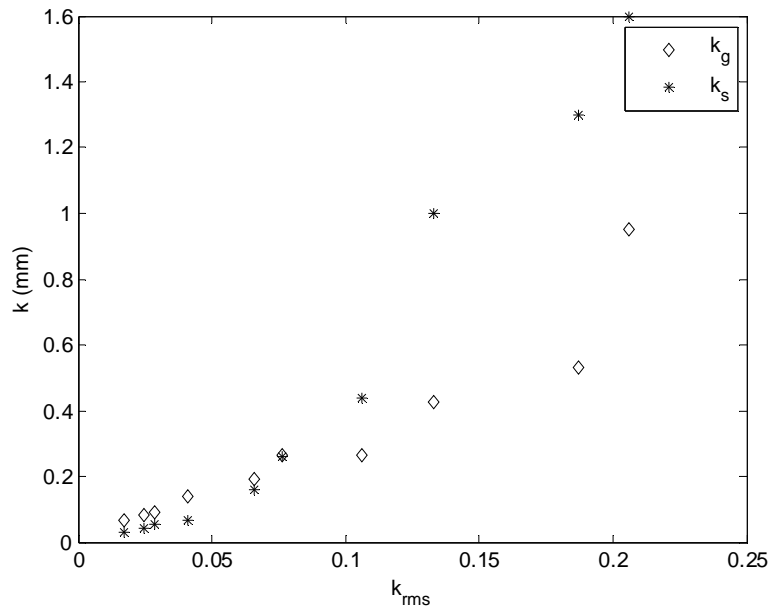


Figure 3.84 *Nominal and equivalent sand grain roughness size comparison*

3.2.9 Turbulent Character of the Rough Wall Jet Flow in the Inner Region

Just as the turbulent character of the smooth wall jet flow was investigated for the inner region, the rough wall jet turbulent flow character will be investigated for the inner region of the rough wall cases. In Figure 3.85 below, the normal stress profiles for several profiles taken behind 305 mm patches of roughness of varying roughness size are shown in inner coordinates. These profiles were taken for a nozzle height of 12.7 mm and a nozzle exit speed of approximately 60 m/s (test condition C). There is also a smooth wall profile plotted with the rough wall profiles.

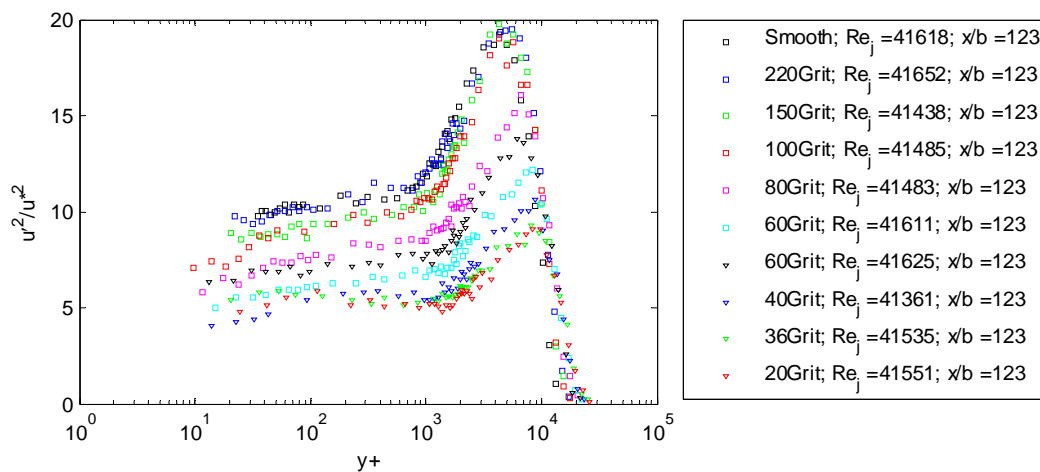


Figure 3.85 *Normal stress profiles in inner coordinates showing the effect of roughness size*

As the roughness is increased, the profiles shift downward and slightly to the right in the figure shown. The peak normalized normal stress values decrease with increasing roughness height,

and the profiles converge way out in the shear layer. Also, the peak normalized turbulence intensity values become smaller relative to the flattened region between y^+ equal to 10 and y^+ equal to 700 as the roughness size increases.

The effects of the streamwise distance downstream of the leading edge of the roughness patch on the turbulent character of the rough wall jet flow are investigated in Figure 3.86 below. There does not seem to be any collapse of the normal stress profiles, and there is no definite change as the patch length is increased. The profiles shown were all taken at a nozzle exit speed of approximately 30 m/s with a nozzle height of 12.7 mm (test condition A). The profiles were taken behind 305, 610 and 914 mm patches corresponding to x/b equal to 123, 147, and 172 in the legend. The same type of analysis was conducted for flow over 180 grit patches of varying lengths, and the results provide no evidence to counter the observations made from the investigation of Figure 3.86 below.

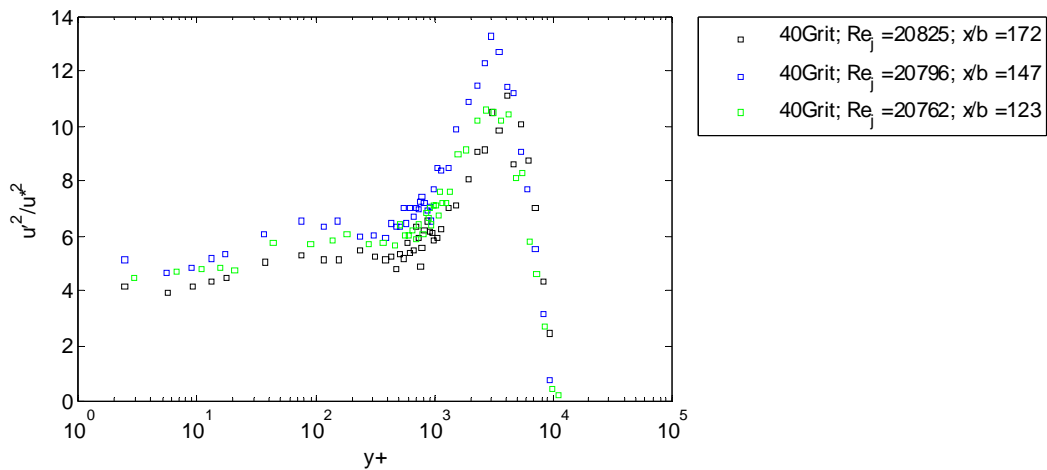


Figure 3.86 Normal stress profiles in inner coordinates showing the effect of patch length

3.2.10 Rough Wall Jet Velocity Spectra

The rough wall velocity spectra were measured for all measurement test cases at the measured boundary layer thickness height, the displacement thickness height, and the mixing layer half height, $y_{1/2}$. These spectra were taken for test conditions A – E and are shown in Figure 3.87 below. The spectra shown are presented in the same way as those in Figure 3.40 above:

$$\frac{G_{uu}}{U_o^2} \text{ vs. } \omega \quad (3.23)$$

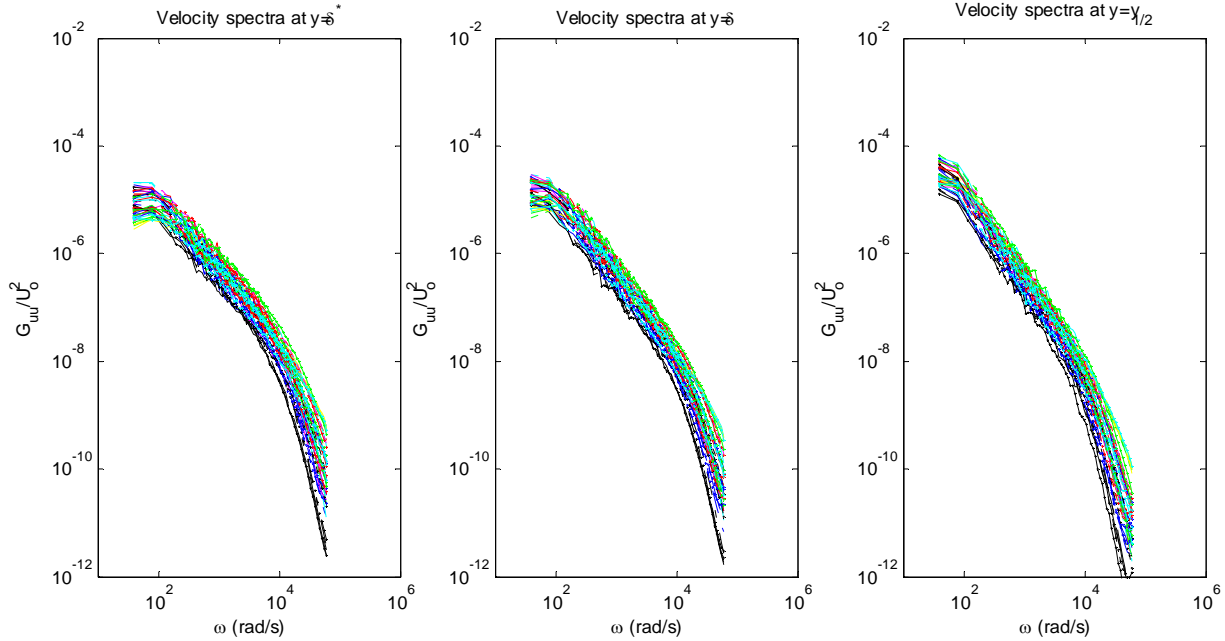


Figure 3.87 All measured smooth wall jet velocity spectra taken at δ^* , δ , $y_{1/2}$

The velocity spectra for rough wall jet flows show many of the same characteristics as those of the smooth wall flow. There is a $-5/3$ region followed by a -7 roll off with frequency. The spectral levels increase at low frequencies with probe distance from the wall, and increase at high frequencies as the probe distance from the wall decreases.

The spectra shown above were scaled on the outer variables discussed above for the smooth wall velocity spectra and are shown in Figure 3.88 below. The spectral scaling in this figure is as follows:

$$\frac{G_{uu}}{U_m y_{1/2}} \nu S. \frac{\omega y_{1/2}}{U_m} \quad (3.24)$$

The rough wall surface pressure spectra were also scaled according to the smooth wall scaling proposed by Ueda and Hinze (1975) in order to see if the high frequency spectral regions could be collapsed as for the smooth wall case (Figure 3.89). It was expected, and will be shown in Figure 3.89 below, that this scaling would not collapse the spectra at high frequencies in light of the inability of inner variables to scale the normal stress profiles in the overlap region as discussed above. Again, the Ueda and Hinze (1975) scaling is as follows:

$$\frac{u^{*2} G_{uu}}{\nu U_m^2} \nu S. \frac{\omega \nu}{u^{*2}} \quad (3.25)$$

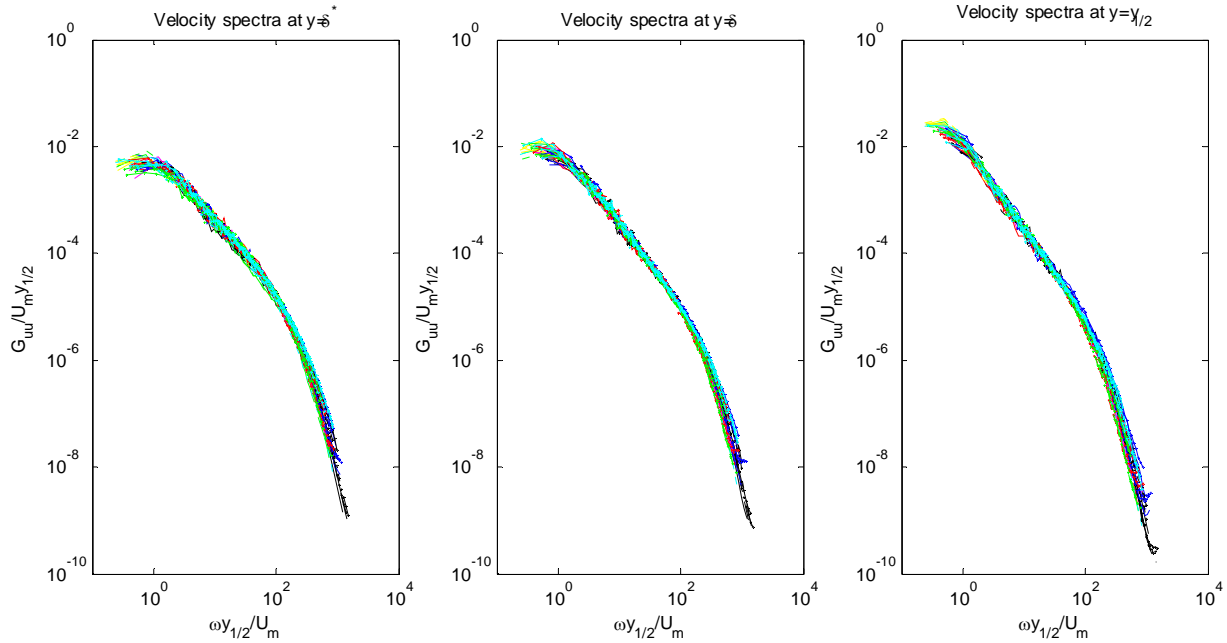


Figure 3.88 All measured rough wall jet velocity spectra taken at δ^* , δ , $y_{1/2}$ normalized on outer variables, U_m and $y_{1/2}$

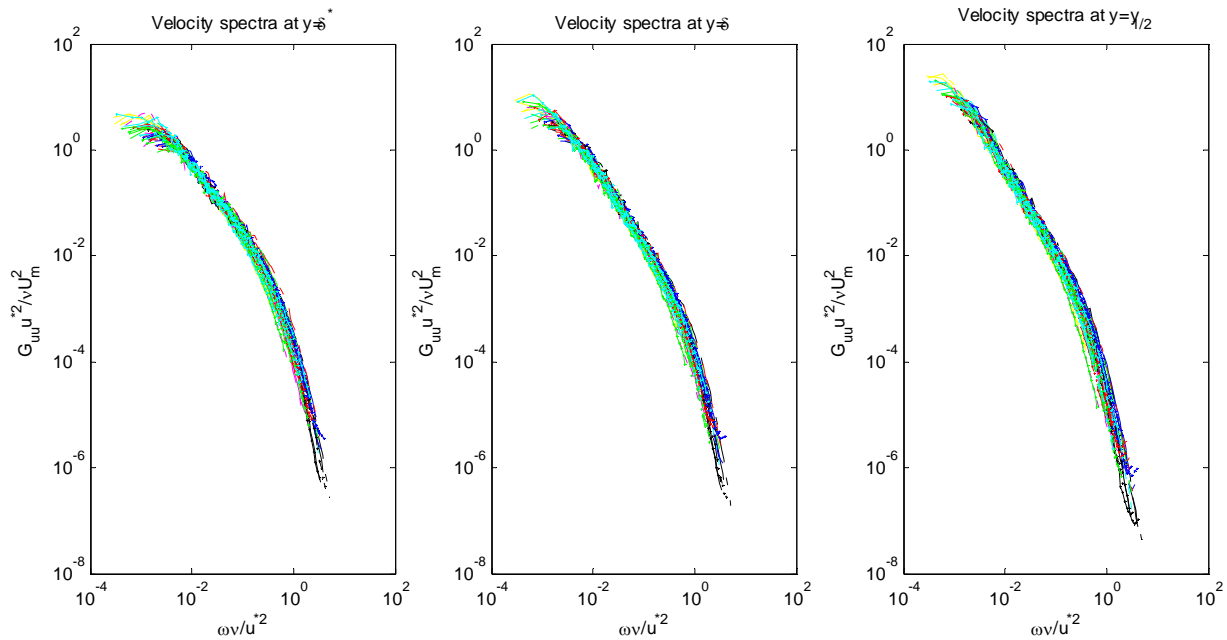


Figure 3.89 All measured rough wall jet velocity spectra taken at δ^* , δ , $y_{1/2}$ using the inner scaling presented in Ueda and Hinze (1975)

It is clear that the outer variable scaling seems to scale the velocity spectra better than the inner scaling even at high frequencies and closer to the wall. However, the spectra shown were taken at a variety of initial test conditions, and it was desired to investigate the effects of just a change in roughness size more closely.

In order to see the effects of the roughness size alone, the rough wall velocity spectra from test condition C were plotted dimensionally as in Figure 3.87 and are shown in Figure 3.90 below. The profiles from which the spectra were taken were measured behind 305 mm patches of roughness where the probe was located 1562 mm aft of the nozzle exit. The roughness patches were constructed of sand paper ranging from the 20 grit to 220 grit varieties which correspond to roughness heights of 0.069 mm to 0.95 mm (k^+ ranging from approximately 2 - 158).

In Figure 3.90 below, the dimensional velocity spectra taken at δ^* , δ , and $y_{1/2}$ are presented for the profiles taken at test condition C noted in Table 3.2 above. The collapse of the profiles is very good for the spectra taken at the boundary layer thickness and at $y_{1/2}$ indicating that the roughness has no noticeable effect on the spectra taken at these heights off of the surface. It is important to remember that the initial flow conditions are held constant for the plots in this figure. The profile collapse is not as good for the spectra taken at the displacement thickness height. This would suggest that the presence of the roughness has a noticeable effect on the velocity spectra near the wall but is relatively unimportant in the outer regions of the rough wall jet flows. In other words, the turbulent motions near the wall are being augmented by the presence of the rough surface, but those away from the wall appear to be undisturbed by the rough surface. This observation lends credence to the discussion in section 3.2.2 above.

In Figure 3.91 the same spectra are shown scaled on the outer variables that scaled the smooth wall jet spectra so well. Other length scales were investigated for these spectra, but none of the boundary layer length scales did a better job scaling the spectra when the scaling velocity was U_m . Any improvement in the collapse of the spectra is completely imperceptible in this figure which would be expected for the spectra taken at δ and $y_{1/2}$ because the Figure 3.90 showed that the spectra were almost entirely unaffected by the presence of roughness and because the initial flow conditions for all of these spectra are the same. However, the fact that the spectra taken at the displacement thickness do not collapse better when scaled on $y_{1/2}$ and U_m would lead one to believe that other scaling variables might be better suited for spectra taken near the wall.

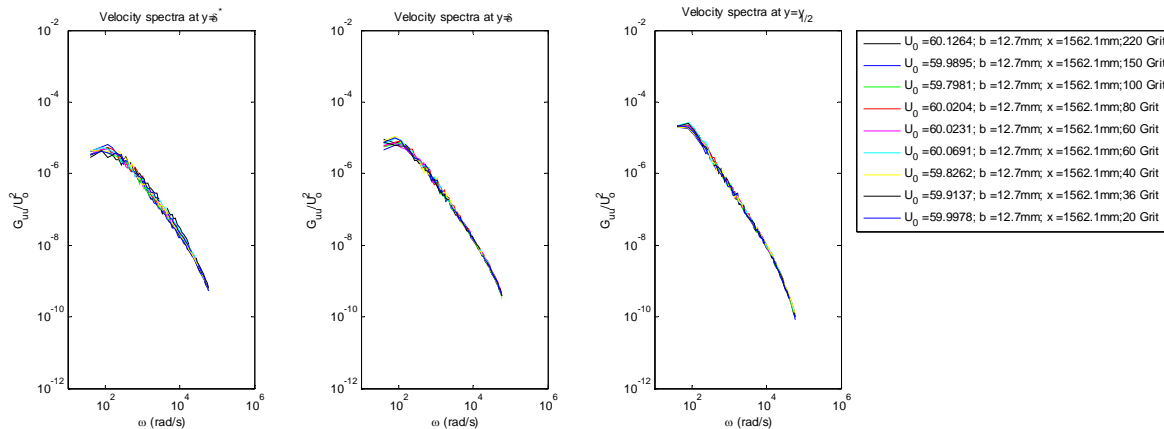


Figure 3.90 Dimensional rough wall jet velocity spectra of varying k_g at δ^* , δ , and $y_{1/2}$ (left to right)

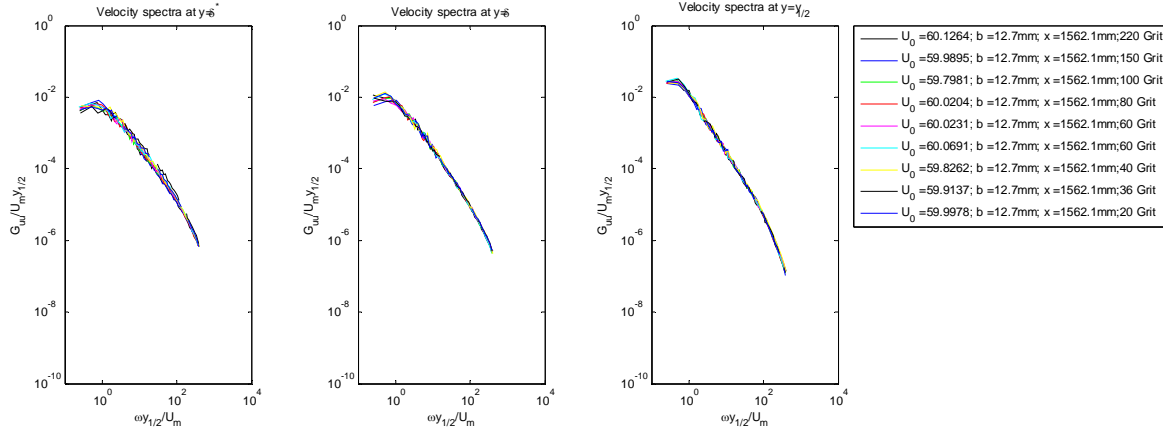


Figure 3.91 Rough wall jet velocity spectra scaled on U_m and $y_{1/2}$ at δ^* , δ , and $y_{1/2}$ (left to right)

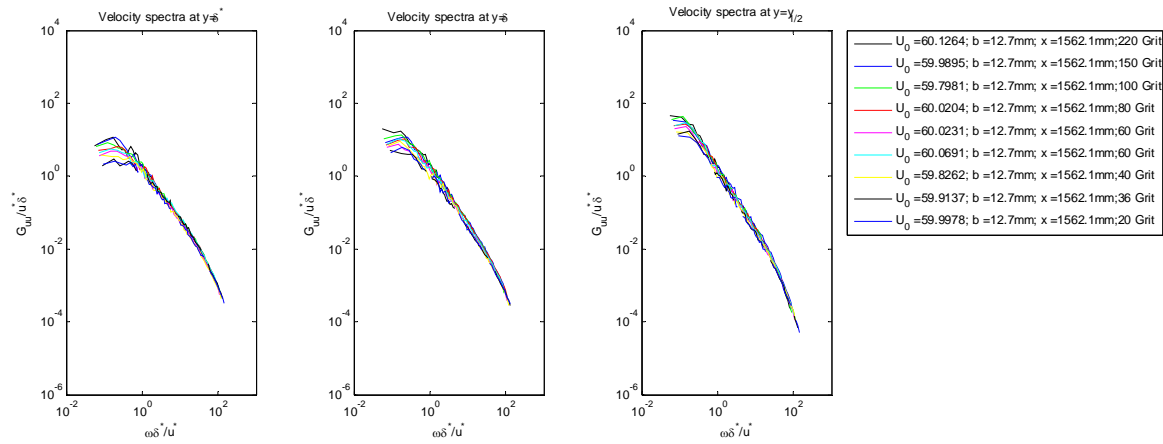


Figure 3.92 Rough wall jet spectra scaled on u^* and δ^* at δ^* , δ , and $y_{1/2}$ (left to right)

In Figure 3.92 the same spectra are scaled on the skin friction velocity and δ^* as follows:

$$\frac{G_{uu}}{u^* \delta^*} \nu S. \frac{\omega \delta^*}{u^*} \quad (3.26)$$

The displacement thickness was chosen as a length scale because it was shown to vary distinctly with the change in roughness size. It was also hypothesized that the skin friction velocity would be a more appropriate velocity scale in the flow region affected by the roughness. The spectra taken at the displacement thickness height that are scaled on the displacement thickness show a much tighter collapse from a nondimensional frequency of about 1 (about 200 Hz) onward than the spectra scaled on the outer variables. Note that the low frequency region of the spectra do not scale well on the skin friction velocity and the displacement thickness showing that the low frequency turbulent motions are determined by the outer flow. These length scales were also investigated for spectra taken at the boundary layer thickness and at $y_{1/2}$, but these at these probe positions, the outer variables scaled the spectra much better. This result indicates that very near the wall, the presence of the roughness is important to the behavior of the velocity spectra, and that a more suitable length scale than the outer $y_{1/2}$ scaling length may be available. This also supports the observations above showing that the mean velocity and turbulent flow properties are only very slightly affected by the presence of roughness away from the wall but significantly

affected near the wall. However, if all of the rough wall velocity profiles are scaled on the skin friction velocity and the displacement thickness as seen in Figure 3.93 below, the choice of the displacement thickness as a scaling length is brought into question. The scaling used in Figure 3.92 above and Figure 3.93 below shows an inability to deal with changes in the initial flow conditions. It is clear that this scaling is not optimal for rough wall velocity spectra, but it does draw attention to the fact that an outer scaling length like that used in the smooth wall scaling also has difficulty dealing with the velocity spectra taken near a roughened flow surface

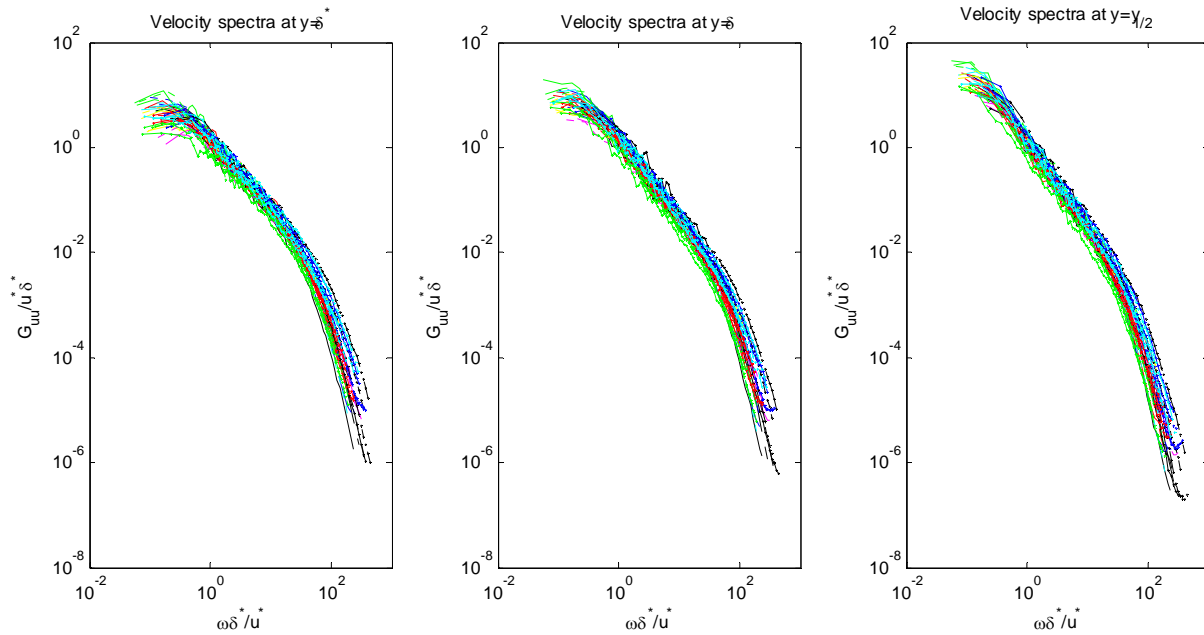


Figure 3.93 All measured rough wall jet velocity spectra taken at δ^* , δ , $y_{1/2}$ scaled on u^* and δ^*

In addition to checking the ability of the boundary layer length scales to scale the velocity spectra, an investigation was conducted into the ability of the nominal roughness height, k_g , to scale the velocity spectra. In Figure 3.94 below, the same spectra shown in the figures above taken at the displacement thickness height, boundary layer height, and mixing layer half height were scaled as follows:

$$\frac{G_{uu} u^{*2}}{U_m^2 k_g} \text{ vs. } \frac{\omega k_g}{u^*} \quad (3.27)$$

The clear result is that the roughness size does not scale the velocity spectra well at all, and that the roughness size does not appear to be the appropriate length scale for the velocity spectra even close to the wall.

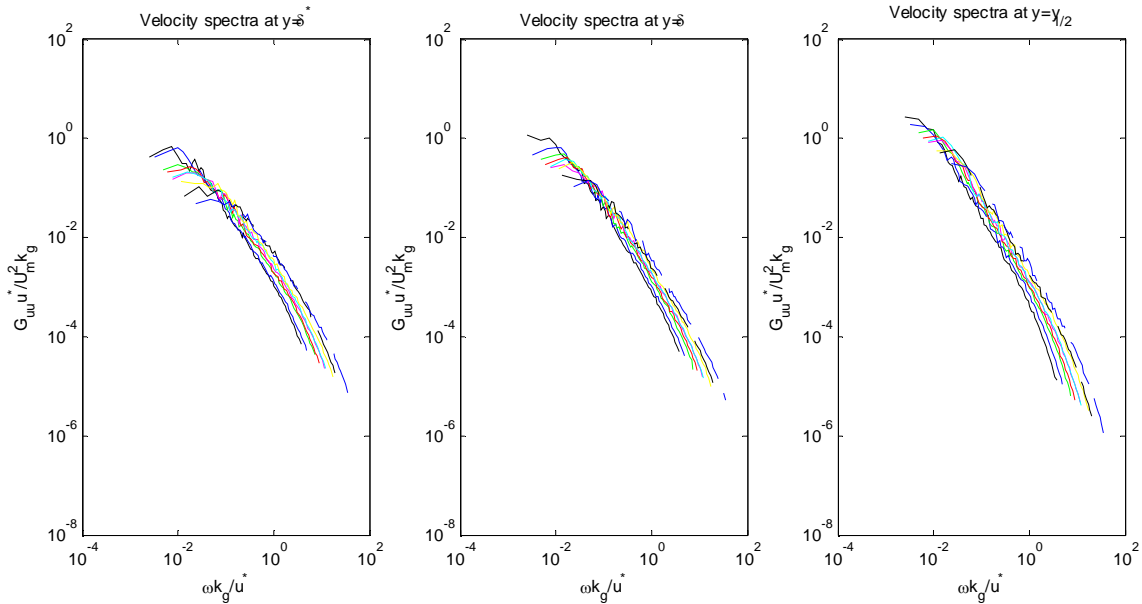


Figure 3.94 Rough wall velocity spectra scaled on U_m , u^* , and k_g

In the investigation of the effects of the nozzle exit velocity, the nozzle height, and the roughness patch length the scaled profiles that were observed did not add anything to the scaling discussions for rough wall jet spectra above, and therefore, will not be presented. However, the dimensional spectra do provide some interesting points of discussion. Figures Figure 3.95 (showing measurements from test condition A), Figure 3.96 (showing measurements from test conditions A and E), and Figure 3.97 (showing measurements from test condition A) below show the dimensional spectra taken at δ^* , δ , and $y_{1/2}$.

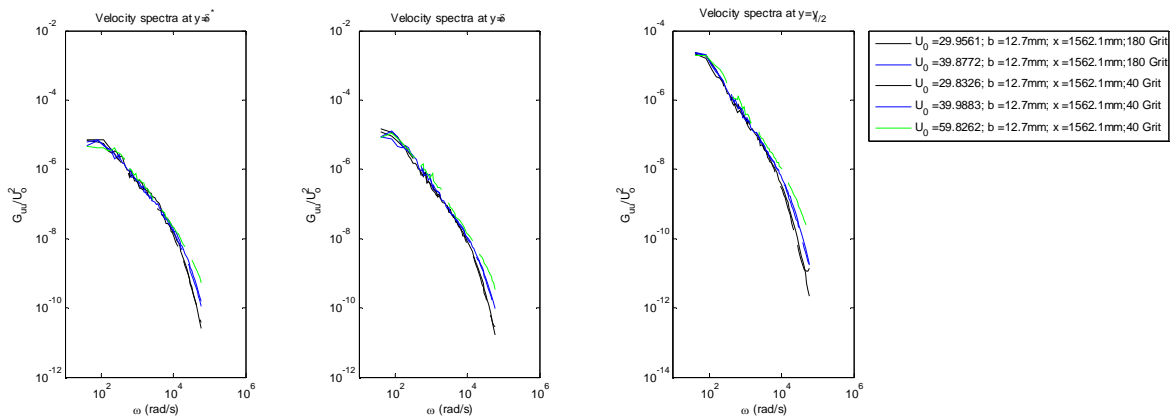


Figure 3.95 Dimensional rough wall velocity spectra at δ^* , δ and $y_{1/2}$ (left to right) showing effects of variations in U_0

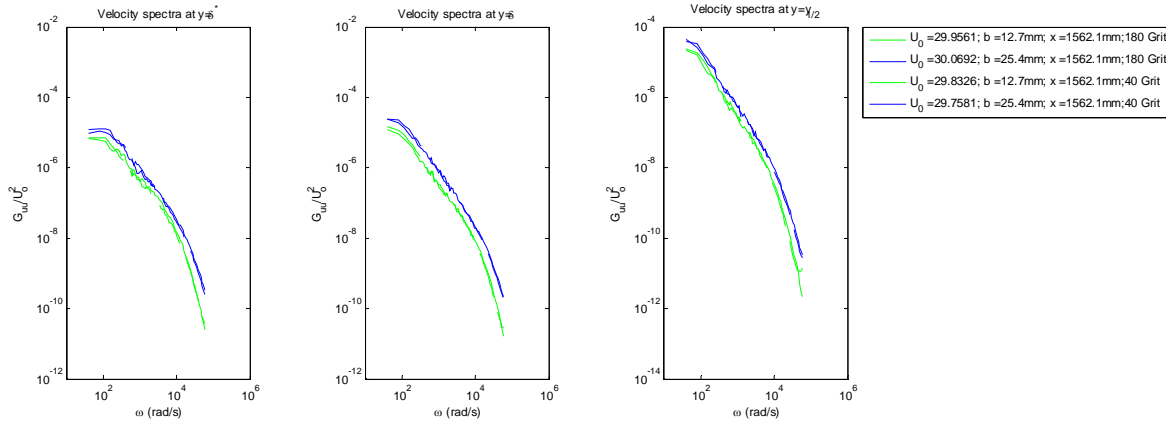


Figure 3.96 Dimensional rough wall velocity spectra at δ^* , δ and $y_{1/2}$ (left to right) showing effects of variations in b

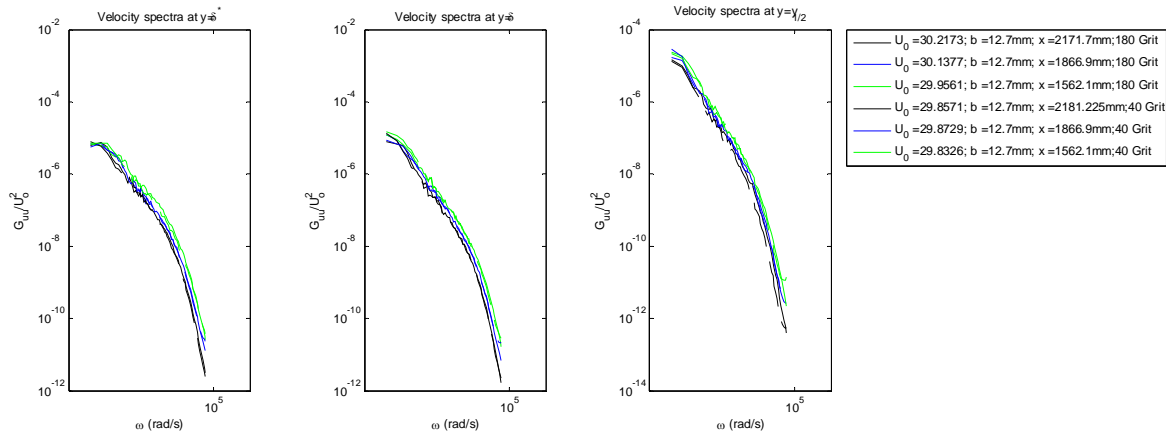


Figure 3.97 Dimensional rough wall velocity spectra at δ^* , δ and $y_{1/2}$ (left to right) showing effects of variations in roughness patch length

In Figure 3.95 above, the spectra shown were taken from profiles measured behind 305 mm patches of 40 and 180 grit roughness with the probe positioned 1562 mm aft of the nozzle exit. The nozzle height was set at 12.7 mm, and the nozzle exit speed was varied from approximately 30 to 60 m/s. It can be seen that the nozzle exit velocity affects the velocity spectra significantly at frequencies above 1600 Hz (10000 rad/s) where the spectra begin to spread out showing an increase in the high frequency turbulent motions with an increase in Reynolds number. One also notices that the spectra that are taken from profiles with the same nozzle exit speed tend to be grouped together even for the spectra taken at the displacement thickness height.

In Figure 3.96 above, the spectra shown were taken from profiles measured behind 305 mm patches of 40 and 180 grit roughness with the probe positioned 1562 mm aft of the nozzle exit. The nozzle exit velocity for these profiles was fixed at approximately 30 m/s. The nozzle height was varied from 12.7 mm to 25.4 mm. One can see in this figure that the profiles taken at common nozzle heights are grouped together for the spectra taken at the displacement thickness as well as the other probe positions.

Finally, in Figure 3.97 above, the spectra shown were taken from profiles measured behind 305 mm, 610 mm and 914 mm patches of 40 and 180 grit roughness with the probe positioned 1562 mm, 1867 mm, and 2172 mm aft of the nozzle exit. The nozzle exit speed for these profiles was set at approximately 30 m/s, and the nozzle height was set at 12.7 mm. The spectra taken behind the same roughness patch length tend to be grouped together, although this feature is a little less clear in the spectra taken at $y_{1/2}$. The same type of effect was seen in the variation of the smooth wall jet velocity spectra for streamwise variations in x , and it is difficult to determine how the effects of the roughness patch length affect the velocity spectra. This is also consistent with investigation of the normal stress profiles with variations in patch length that showed little or no consistent variation.

3.2.11 Smooth and Rough Wall Jet Velocity Spectra Viewed Together

Velocity spectra were taken for every profile measured with a single hotwire measurement system. In particular, spectra were taken at $y=\delta^*$, δ , and $y_{1/2}$ for the entire range of initial flow conditions, streamwise locations, and roughness sizes given in Table 3.1 and Table 3.2 above. In Figure 3.98 below, spectra taken at $y=\delta$ for all test conditions for both smooth and rough wall jet flows are presented together. It can be seen that the spectra occupy a band and that all of the spectra seem to behave in a similar manner out to about 10,000 rad/s (~ 1600 Hz). Then the spectra tend to fan out.

In Figure 3.99 below, the velocity spectra at δ^* , δ , and $y_{1/2}$ scaled on the outer variables discussed above (U_m and $y_{1/2}$) are shown. In this figure, one can see that spectra seem to collapse regardless of the probe position indicating that even the spectra taken at δ^* (which is over 13 times closer to the wall δ) scale well on U_m and $y_{1/2}$. The profiles show a $-5/3$ region that increases in its frequency extent as the probe position is moved from the wall. As the probe position is raised, the profiles also show a slope at the high frequencies approaching -7 . Other possible length scales were attempted, but even for the profiles taken at δ^* the best scaling length scale for the smooth and rough wall jet velocity spectra when viewed collectively appears to be $y_{1/2}$. However, as seen above for the rough wall velocity spectra, when the rough wall profiles are viewed separately, the need for a more representative length scale is indicated by the fact that u^* and δ^* seem to account for changes in the roughness size alone. However, the scaling on u^* and δ^* does not seem to account for changes in initial flow conditions.

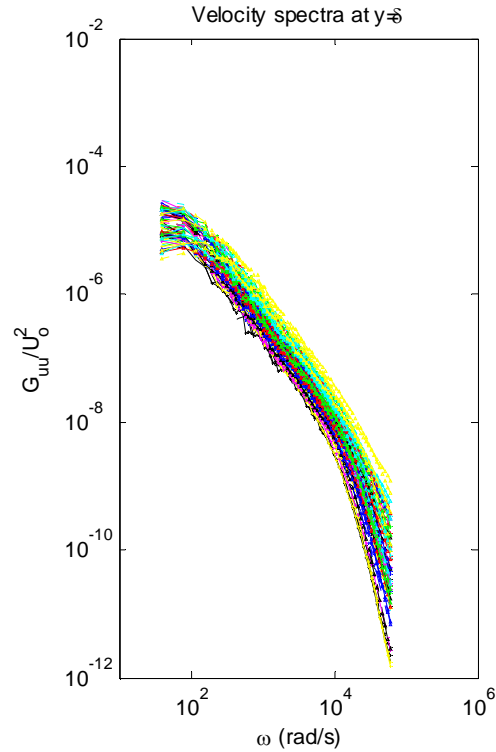


Figure 3.98 Smooth and rough wall jet velocity spectra

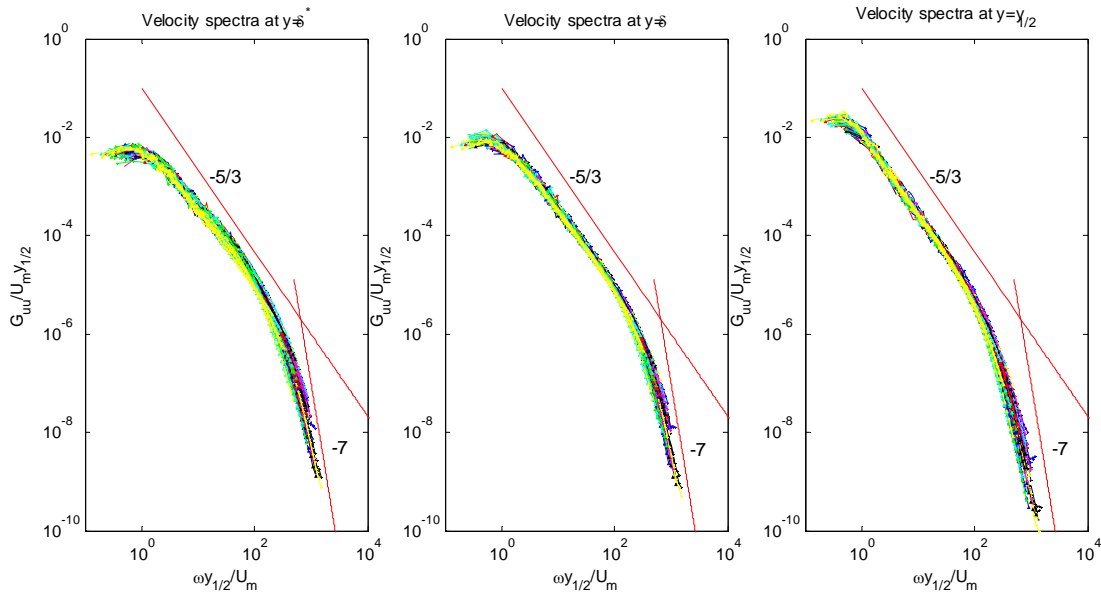


Figure 3.99 Velocity spectra scaled on U_m and $y_{1/2}$ at δ^* , δ and $y_{1/2}$ (left to right)

Figure 3.100 below shows the velocity spectra taken at δ^* scaled on various possible length scales. It is evident that when the velocity scale, U_m , is used, the best scaling length is $y_{1/2}$. The differences in the scaled spectra with the different length scales might seem unexpected since, for the smooth wall profiles, the profile scaling length scale, $y_{1/2}$, was found to be a

constant multiple of all other boundary layer length scales. However, this is not true for the rough wall profiles, so it should not be a surprise to see some dependence of the scaling length on the spectra in this figure because both rough and smooth wall profiles are seen together.

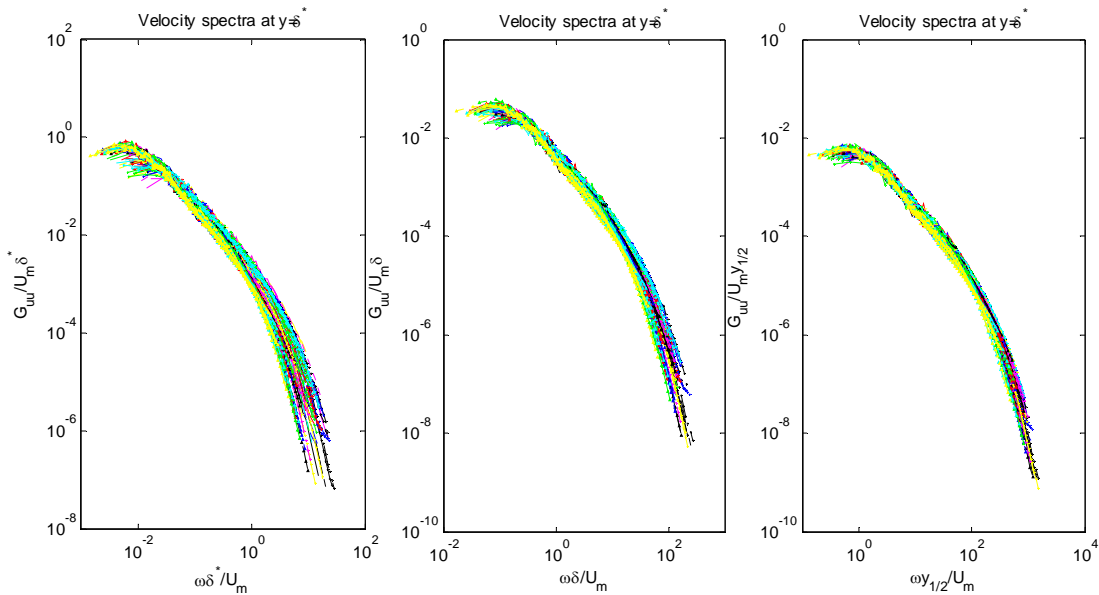


Figure 3.100 Velocity spectra taken at δ^* scaled on U_m and δ^* , δ and $y_{1/2}$ (left to right)

The velocity spectra shown above were scaled on the skin friction velocity and on the length scales δ^* and $y_{1/2}$. It was found that even when the probe position was near the wall at δ^* the smooth and rough wall spectra (viewed collectively) did not scale as well as when they were scaled on U_m and $y_{1/2}$. This can be seen in Figure 3.101 below. What can also be seen is that when the scaling velocity is taken to be the skin friction velocity, the length scale δ^* seems to collapse the spectra better in the mid frequency range, but $y_{1/2}$ does a better job at higher frequencies.

The dependence of the normalized spectra on different length scales depending on the probe position or chosen velocity scale indicate that there may not be a single set of scaling variables that deal with both the smooth and rough wall jet spectra.

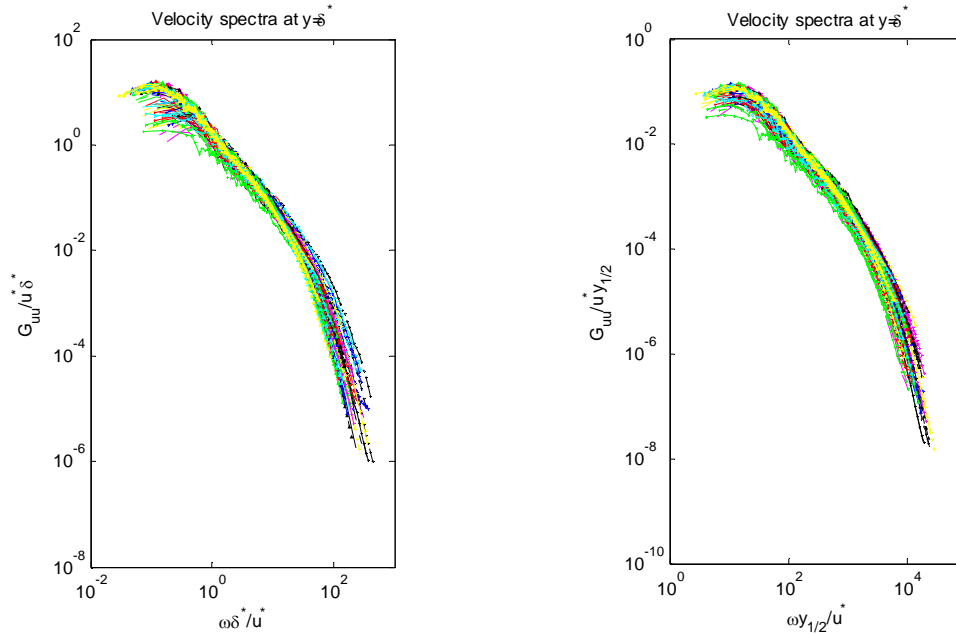


Figure 3.101 Velocity spectra scaled on u^* and δ^* and $y_{1/2}$ (left to right)

3.2.12 Relation of the Rough Wall Mean Velocity, Turbulence, and Spectral Data

When the rough wall mean velocity, turbulence, and spectral data are viewed collectively, some insight into the nature of the wall jet flow over rough surfaces can be obtained. As for the smooth wall flow, the mean velocity and turbulence measurements scale on outer variables away from the wall. However, this scaling deteriorates as the wall is approached much sooner than was seen in the smooth wall data. The mean velocity profiles seem to show variations with the roughness size that extend to nearly the boundary layer thickness. The normal stress profiles seem to show a breakdown of the outer scaling at a height off of the flow surface of 0.5 times the boundary layer thickness. The mean velocity profiles and normal stress profiles do not scale well on wall variables, even near the wall as the surface roughness condition is altered. If one considers the notion that there is a region of the flow where the effects of the roughness are evident that grows with downstream distance from the origin of the rough surface as discussed in Smits and Wood (1985) and Simpson (1971), one could argue that the mean velocity and turbulent flow character are unaffected and lie in undisturbed flow above the boundary layer thickness at the trailing edge of the roughness patches. However, it does appear that the boundary layer thickness is increased by the presence of roughness, but not dependent on the size of the roughness.

The rough wall jet velocity spectra presented scale well on outer variables (U_m , and $y_{1/2}$) when the spectra were taken at the boundary layer thickness height or the mixing layer half height indicating the dominance of large high energy structures away from the wall. However, when the velocity spectra were taken at the displacement thickness height, velocity spectra taken for varying surface roughness were shown to scale well on the skin friction velocity and the displacement thickness if only the roughness size was varied. However, when the initial flow

conditions were varied, these scaling variables were not as successful. When the rough wall jet velocity spectra and smooth wall velocity spectra are viewed together, they are seen to scale best on outer variables even when the spectra are taken at the displacement thickness as is evidenced by the comparison of Figure 3.99 and Figure 3.101. This would indicate that the scaling variables u^* and δ^* , while capable of accounting for changes in surface roughness as shown in Figure 3.92, they are not capable of accounting for differences in the initial flow condition as well as the outer variables and that the larger turbulent structures are dominating the wall jet flow over the rough surfaces.

3.2.13 Rough Wall Jet Flow Summary

The rough wall jet outer flow continues to scale well on U_m and $y_{1/2}$ as for the smooth wall jet flows. Both of these scales show no discernable variation with the roughness height. The height of the maximum velocity, δ , was shown to increase slightly in the presence of roughness, but its variation with roughness height did not show a clear trend. The outer portion of the normal stress profiles tend to scale well on these outer scaling variables, and these nondimensional normal stress profiles do not show any real variation with the variation of the initial flow parameters, b or U_o . The normal stress profiles normalized on outer variables show no discernable effect of the roughness size in the outer region of the flow.

The scaling method proposed by Hogg *et al.* (1997) seems to scale the length scales δ^* and θ for any given roughness. From these observations, and by using a procedure similar to that used in the development of the estimations for the smooth wall jet parameters, rough wall estimations were obtained for δ^* and θ while the smooth wall estimations for U_m , $y_{1/2}$, and δ (note that the smooth wall variation was adopted for estimations of the rough wall boundary layer thickness, but the apparent increase of 29.5% in the boundary layer thickness due to the presence of the roughness patch was accounted for with a simple scale factor) were determined to be adequate for the rough wall jet flows in the current study.

The skin friction coefficient was determined using a momentum balance over the rough patch length. The results show reasonable estimates for the rough wall jet flow skin friction coefficient and allow for the determination of the skin friction velocity which was chosen as the velocity scale for the inner region rough wall jet flow profiles.

The rough wall jet profiles presented in inner coordinates do not scale well on the skin friction velocity alone. They do show that the slope of the log region remains the same regardless of the roughness size. Also, the normal stress profiles presented in inner coordinates do not seem to scale well on the skin friction velocity for rough wall jet flows, and show larger separations amongst the profiles than for the smooth wall normal stress profiles as a rule. The normal stress profiles did seem to begin to converge as the roughness size got large. It would be interesting to see if this trend continued if larger roughnesses were tested. Unfortunately, these types of tests were not possible for the current study.

For a rough wall jet, the outer variables were found to scale the spectra effectively for probe positions away from the wall. When only the surface roughness was varied, the spectra taken at the displacement thickness height were shown to scale on the skin friction velocity and the displacement thickness. However, when the initial flow conditions were altered, the appropriate scaling spectral scaling variables were found to be the outer variables indicating that the rough wall jet velocity spectra are dominated by large, high energy motions associated with

the outer region, even for spectra taken at the displacement height even though these spectra show an increased dependence on u^* and δ^* .

The behavior of the smooth and rough wall jet flow has been discussed in detail above. In the following chapter, the surface pressure fluctuations of the smooth and rough wall jet flows tested in the current study will be investigated in detail. This will provide yet another way to view the wall jet flow over smooth and rough surfaces, and will provide understanding complimentary to that gained from the discussion of the results in this chapter.

4 Smooth and Rough Wall Jet Surface Pressure

4.1 Surface Pressure Measurement Setup

In this chapter, surface pressure measurements of smooth and rough wall jet flows will be presented for a variety of flow conditions and rough surfaces. The measurement system used to obtain these measurements was described in Chapter 2 above. Sennheiser KE 4-211-2 microphones were used with an in-house fabricated $\frac{1}{4}$ mm pinhole. In this section the author discuss the effects of surface microphone height, pinhole size and calibration method.

4.1.1 Surface Pressure Microphone Calibrations

The calibration setup is shown in Figure 4.1 below and consists of the anechoic enclosure covering the plate that forms the flow surface of the wall jet flow described above, a University Sound ID60C8 speaker, a B & K 4138 microphone with Nexus 7749 type 2690 conditioning amplifier, and Sennheiser KE 4-211-2 microphones with amplification circuits. In the setup shown in Figure 4.1 the speaker face was always located in the same position in the anechoic enclosure as were the B & K and Sennheiser microphones. The speaker face and B & K or Sennheiser microphones were located 464 mm above the aluminum plate and 229 mm off of the centerline of the flow facility as shown in Figure 4.1 below. The speaker face was always located 990 mm aft of the nozzle exit, and the B & K or Sennheiser microphones were always placed 2946 mm aft of the nozzle exit during all microphone calibrations.

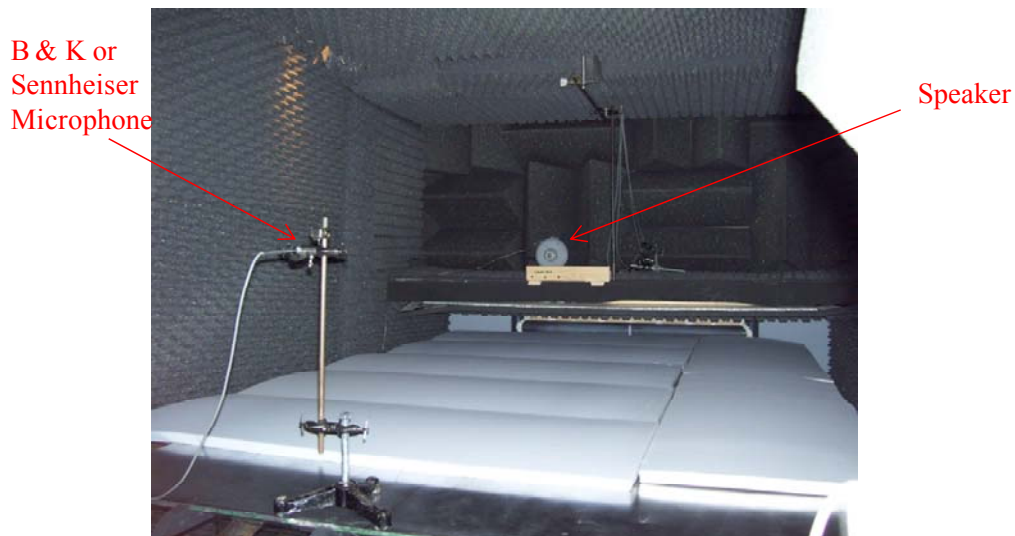


Figure 4.1 Picture of microphone calibration setup

The current calibration method can be described as follows. A known signal (in this case a white noise signal) was generated by the Agilent VXI data acquisition system used in the current study and sent to a speaker. Then a speaker calibration was obtained by taking the cross spectrum of the input to the speaker and the output from the speaker (measured by the B & K 4138 1/8th inch microphone) and dividing that by the auto-spectrum of the input signal and the sensitivity of the B & K 4138 1/8th inch microphone. The B & K microphone has a known flat response within ± 1 dB out to over 25.6 kHz (which is the frequency limit of any useful data that can be obtained imposed by the data acquisition system). Once the speaker calibration is obtained, the speaker output is measured with the measurement microphones (in the current study they are Sennheiser KE 4-211-2 microphones). The measurement microphone calibration is obtained by taking the cross spectrum of the input signal to the speaker and the output signal from the speaker as measured by the Sennheiser microphones and dividing this by the auto-spectrum of the speaker input signal and the speaker calibration.

The measurement setup in the current study was determined to be comprised of Sennheiser KE 4-211-2 microphones fitted with 1/4 mm pinholes. An investigation into the effect of pinhole size will be presented in more detail below, but for the time being, it will suffice to say that the pinhole size was reduced from that provided by the factory in order to increase the frequency range of the collected data not affected by spatial averaging. The setup described above was used to calibrate the Sennheiser microphones fitted with the 1/4 mm pinholes which were used in the surface pressure measurements. In Figure 4.2 below, one can see a plot of a typical magnitude calibration for the measurement microphones. One should notice the low frequency oscillations. These are believed to be due to near field effects of the University Sound ID60C8 speaker used in the calibration. One should also note that the calibration is relatively flat from about 200 Hz to about 1000 Hz where it begins to rise until it reaches a peak at about 5 kHz and then falls off sharply. The factory information on the Sennheiser microphones used suggests that the microphone frequency response is flat from 100 Hz out to 20 kHz. The peak and roll off behavior of the calibration shown are due to the presence of the pinhole, and in a later section calibrations for a microphone with the factory pinhole will be compared with those of microphones with 1/2 mm and 1/4 mm pinholes.

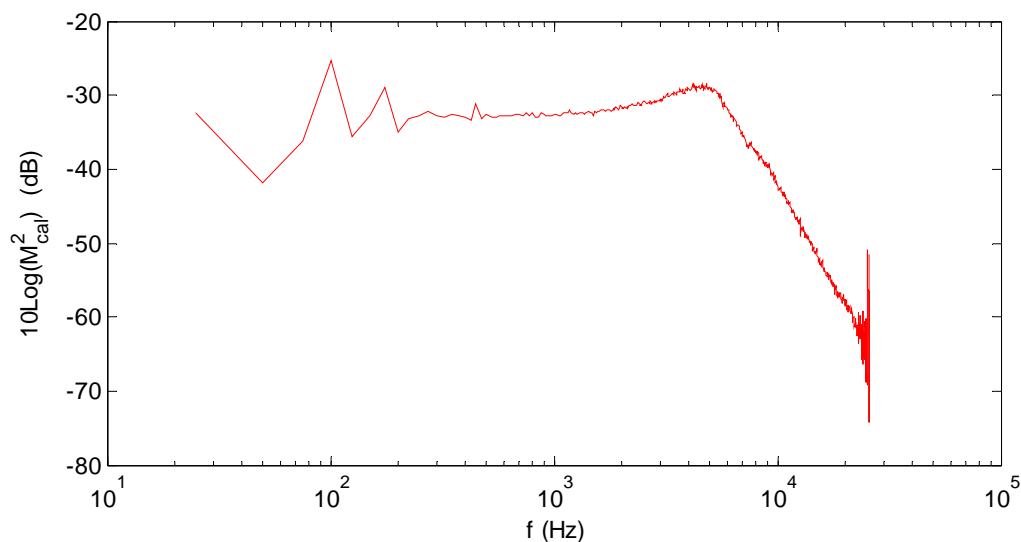


Figure 4.2 *Magnitude calibration for a typical measurement microphone; M_{cat} is the magnitude of the calibration for microphone fitted with a 0.25 mm pinhole*

The calibration is applied to the Fourier transform of the voltage obtained by the data acquisition unit in order to convert the voltage measured to pressure, and the single sided power spectrum is computed as:

$$G_{pp} = \frac{2}{S_R R_L N} \sum_1^N FFT^*(p(t)) FFT(p(t)) \quad (4.2)$$

where S_R is the sampling rate of the data acquisition system, R_L is the record length, and N is the number of records acquired. Note that a Hanning window was applied to the FFT of the signal.

The magnitudes of the calibrations of the measurement microphones are presented below in Figure 4.3. It can be seen that the levels vary by as much as 3 dB between measurement microphones. The microphones are differentiated by an S designation. In preliminary tests, there were 14 measurement microphones, and each was given an S designation. The microphones whose calibrations are shown below were considered to be the most reliable of the available microphones, and were used for the majority of the measurements discussed below.

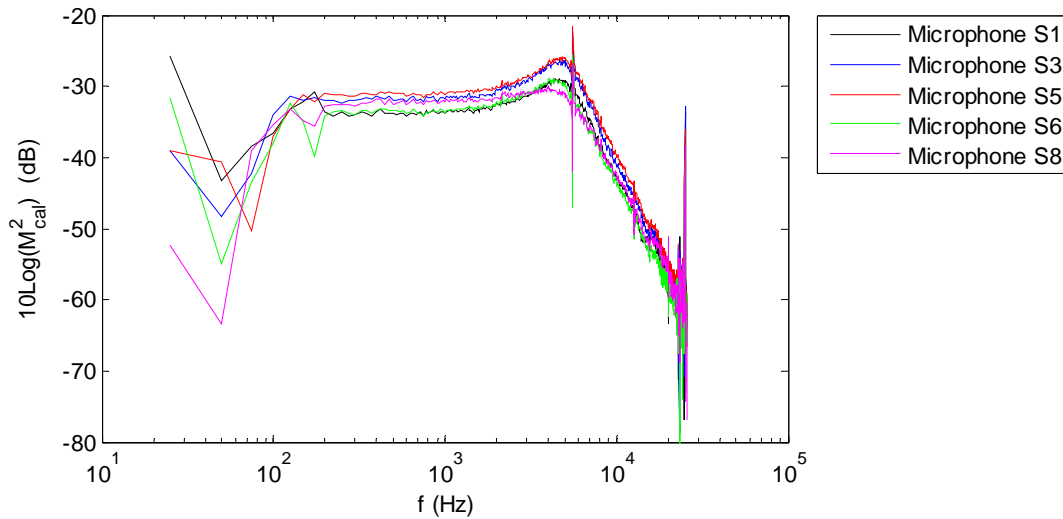


Figure 4.3 *Magnitude calibrations for measurement microphones used in the current study*

After applying the calibrations to surface pressure measurements from test cases, it was noticed that small anomalies in the calibration such as noise spikes or undulations in the calibration manifested themselves in the corrected surface pressure spectra. It was, therefore, desired to smooth the calibrations to reduce the error. It is thought that if more averages were taken for the calibrations then the uncertainty in the calibrations would be reduced. In Figure 4.4 below, the magnitude of the S1 microphone calibration above in Figure 4.3 is presented along with a smoothed fit to this calibration.

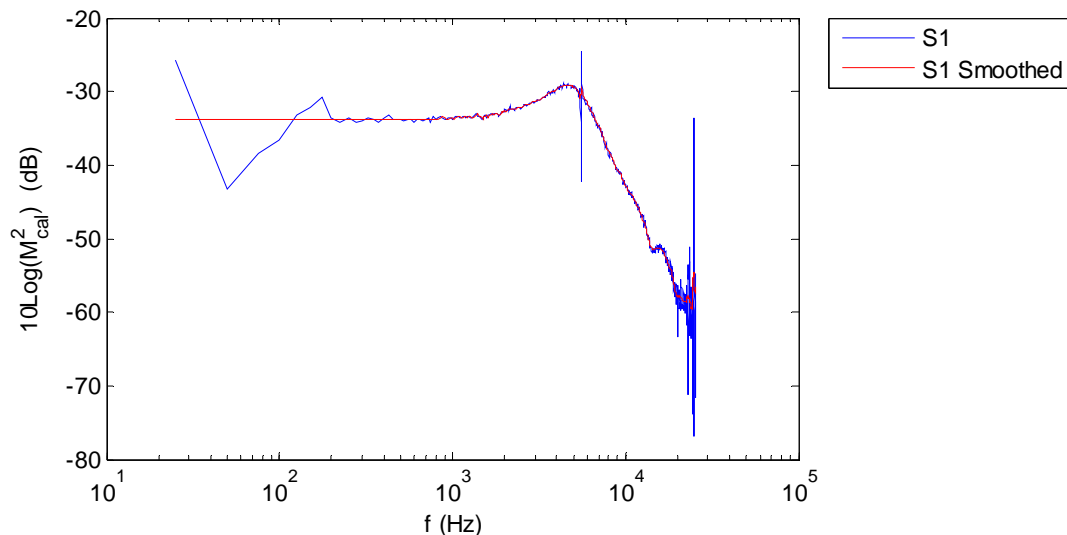


Figure 4.4 Smoothed and original calibration comparison

The portion of the calibration above 2 kHz was smoothed by taking the average of all of the calibration values in the 1/12th octave band surrounding each 25 Hz frequency interval in the original calibration. The same type of averaging was done for the portion of the calibration between 800 and 2000 Hz using a 1/24th octave band width. Below 800 Hz, the smoothed calibration was taken to be equal to the average value of the original calibration between 500 and 800 Hz. It was assumed that the calibration was constant in this region because the original calibration appeared to approach a constant region below 1000 Hz, and because the technical information provided by Sennheiser suggests that the frequency response is flat to within ± 1 dB between 100 and 1000 Hz. It is believed that this smoothed calibration is representative of the actual calibration over the entire frequency range. Not that there is a feature in this calibration at around 14kHz that appears to be suspect. For the calibration shown in Figure 4.2 above, this feature is not present. The calibration shown in Figure 4.2 is an older calibration for the microphone shown in Figure 4.4. If the old and current calibrations are compared, the results can be seen in Figure 4.5 below. The two calibrations agree at all frequencies to within 1.25 dB except around 14 kHz where this odd calibration feature is observed. During an extensive preliminary test for the measurement of the surface pressure fluctuations, this calibration feature was not observed for this or any other measurement microphones, and it is only in this latest calibration that this feature has been observed. This feature was observed to a lesser degree in other microphones calibrated at the same time as the one shown in Figure 4.4 above and Figure 4.5 below indicating that it is a feature that is specific to the calibration setup and is not believed to be indicative of the microphone's true calibration.

The old calibration seems to agree with the current calibration at frequencies bounding this high frequency feature and varies smoothly with frequency through the region where this feature is seen. If one uses the old calibration magnitude to replace the current calibration in the region where this high frequency feature exists, an updated smoothed calibration can be obtained that is believed to be more representative of the actual calibration. This smoothed magnitude calibration is shown in Figure 4.6 below. The uncertainty in the fluctuating pressure measurements was determined, in part by looking at the repeated calibrations of measurement microphones used in this experiment. Old and new calibrations were compared in the same way

as that shown in Figure 4.5 below and the variation was always seen to be less than 1.25 dB for every measurement microphone investigated, so the estimated uncertainty in the spectral densities associated with the microphone measurement system was taken to be ± 1.25 dB.

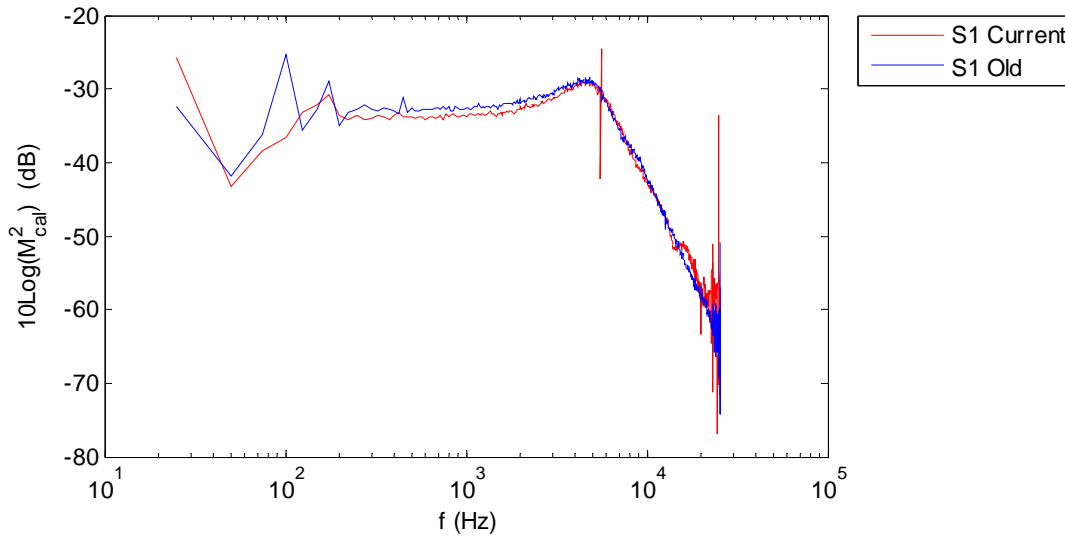


Figure 4.5 Original and current microphone pinhole calibrations

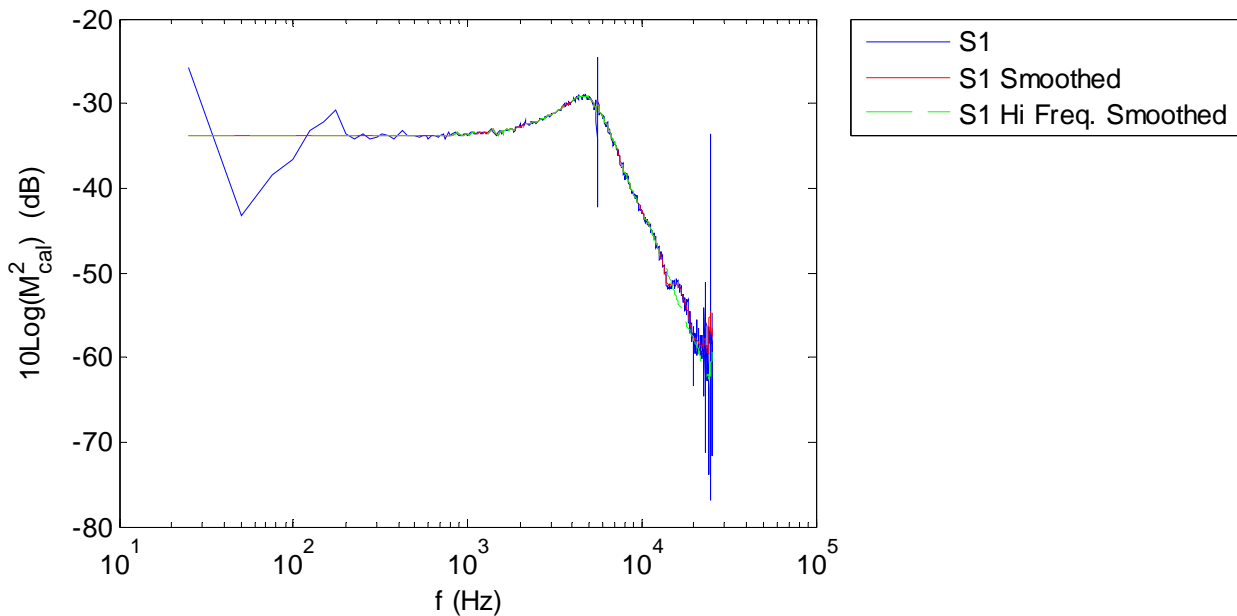


Figure 4.6 Original and high frequency smoothed calibrations for current measurement microphone calibration

In order to eliminate the effects of the drift in the calibration, surface pressure fluctuations measurements were taken with a series of measurement microphones regularly for the smooth wall jet flow with a nozzle height of 12.7 mm and a nozzle exit velocity of, nominally, 60 m/s (test condition C from Chapter 3 above). The microphone calibrations were

then adjusted to account for differences in the measured spectra and a trusted reference measurement set taken at the same test conditions with a single microphone. These differences were rarely more than 0.5 dB throughout the experiments conducted.

These reference measurements were taken at test condition C with one microphone whose smoothed calibration is shown in Figure 4.6 above. The microphone was moved to each of the 5 measurement locations used in the current study, and the surface pressure fluctuations were measured. The measured surface pressure spectra taken in this test case are shown in Figure 4.7 below. The spectra occupy a band that is only about 2 to 2.5 dB wide. If one looks closer, it can be seen that the spectra show a consistent progression downward in level as the distance downstream of the nozzle exit is increased. This progression was expected, and from the 2 – 2.5 dB band across the frequency range measured one can determine that the power is reduced by 37 – 44 % as the measurement location is moved from $x = 1303$ to 1505 mm. The maximum local velocity reduces by 8% across this interval, and the boundary layer thickness increases by 14% across this interval.

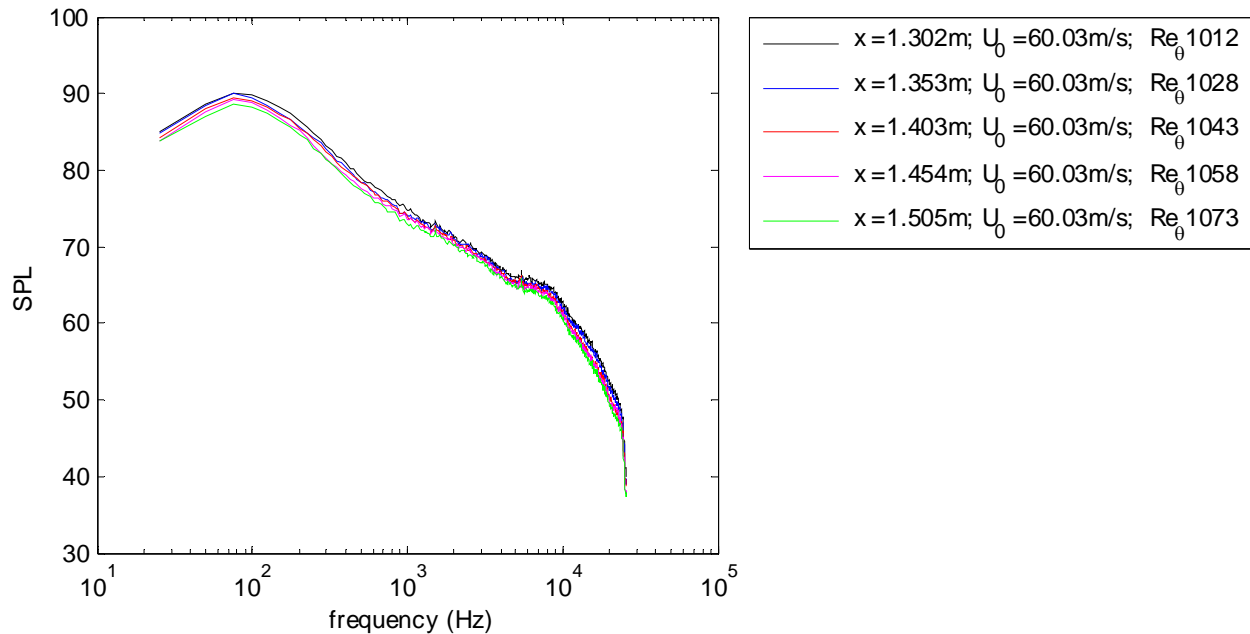


Figure 4.7 Clean plate surface pressure trusted reference test case

4.1.2 Microphone Height and Placement Effects

Before the trusted reference set above could be measured, the consistency of the smooth wall surface pressure measurements had to be established. The effects of the microphone height on rough wall surface pressure are discussed in detail below. In Figure 4.8 below, the effects of the microphone height relative the Nylon bushing are seen for one case where the microphone was inadvertently recessed $0.25 \text{ mm} \pm 0.15 \text{ mm}$ into the bushing while the bushing was mounted flush with the plate. The nozzle exit flow velocity for both spectra shown was approximately 60 m/s, the nozzle height for both cases was 12.7 mm (test condition C), and the x location of the measured spectra was 1302 mm aft of the nozzle exit (the forward most measurement location for all surface pressure measurements). The difference between the spectra is substantial at

about 8 dB at maximum and underlines the importance of accurate microphone positioning. All other microphones were examined to ensure that they were flush with their housing bushings at the beginning and throughout the smooth and rough wall tests.

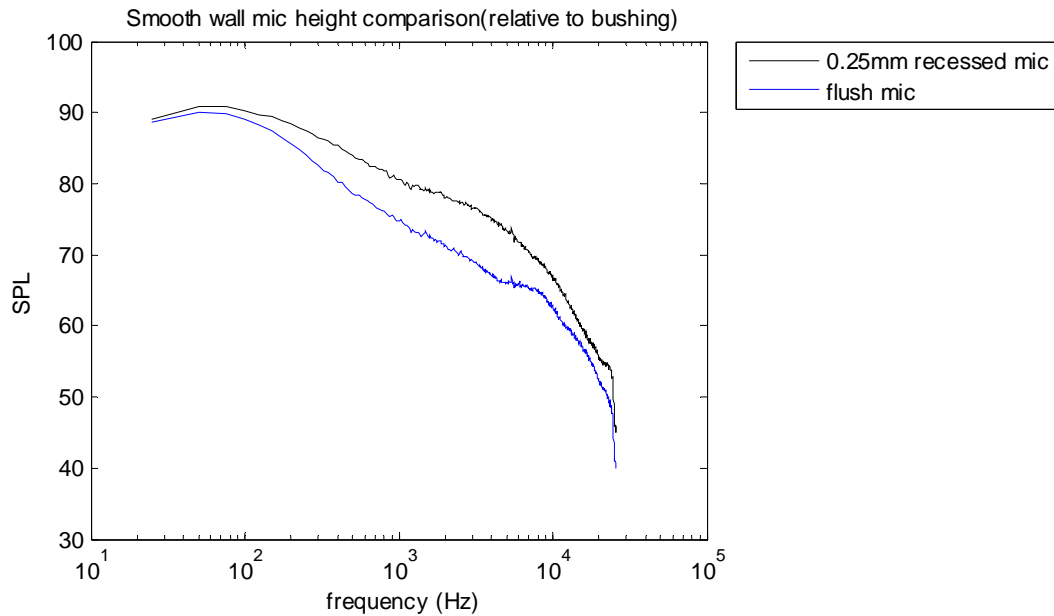


Figure 4.8 Effects of microphone height relative to Nylon bushing.

The effect of the height of the microphone and bushing assembly relative to the plate on smooth wall surface pressure measurements was also investigated. In Figure 4.9 below, the effects of recessing or protruding the microphone bushing assembly can be seen. Each of these spectra were taken with the same microphone used to measure the spectra shown in Figure 4.8 above at the same initial flow conditions and microphone measurement location.

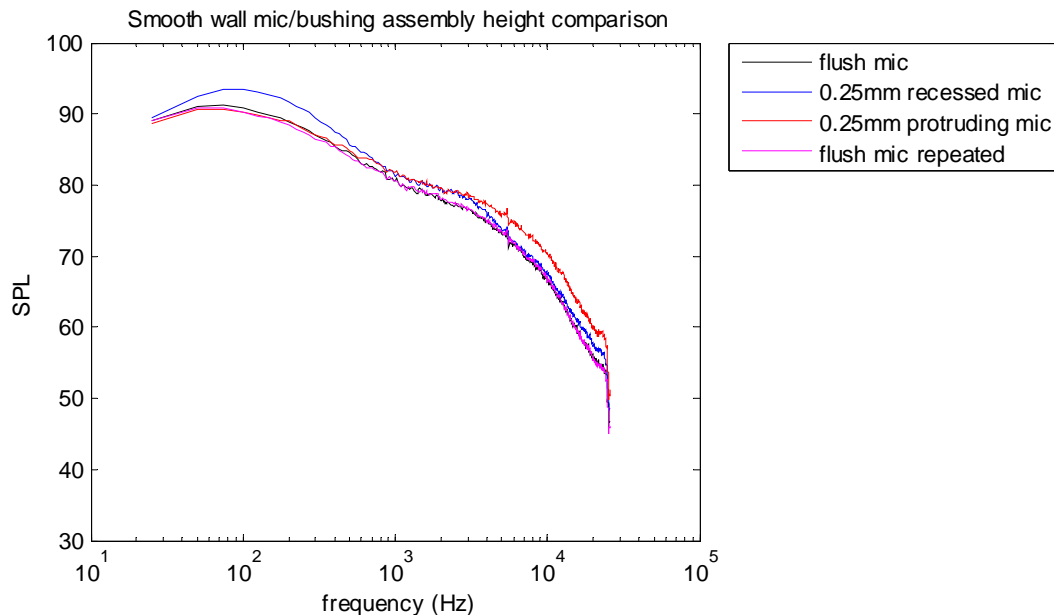


Figure 4.9 Effects of microphone bushing assembly height relative to aluminum plate.

Again, changing the microphone height relative to the flow surface causes spectral level and character changes and differences between spectra are as large as 4dB. The spectra in Figure 4.9 above were taken for test cases where the microphone bushing assembly was flush and recessed or protruded by $0.25 \text{ mm} \pm 0.1 \text{ mm}$ relative to the plate. When the microphone bushing assembly was set to be flush with plate, the results were repeatable.

The variations in the measured spectra with a change in microphone height might seem surprising considering that the magnitude of the change in microphone height is only about 0.25 mm. However, similar behavior was observed by Farabee and Casarella (1984) who measured the surface pressure fluctuations downstream of a backward facing step, and showed that the spectral character is affected most about 6-8 times the step height downstream of the step change in the surface which corresponded roughly to the reattachment region in their study. In 1986, they presented measurements that indicated that the effects of a backward facing step on the surface pressure spectra can be seen as far downstream as 72 times the step height aft of the step. These studies were made with step sizes that were as small as 20% of the boundary layer thickness and as large as 220% of the boundary layer thickness. The step size of 0.25 mm in the current study is at most 1.5% of the boundary layer thickness so no direct comparisons can be made between these studies. However, for the microphone recessed with respect to the bushing, the pinhole opening is approximately 8 times the step height of 0.25 mm downstream of the step. For a microphone bushing assembly that is recessed 0.25 mm, the pinhole opening is about 19 times the step height downstream of the step.

4.1.3 Effects of Pinhole Size

$\frac{1}{4}$ mm pinholes were fabricated and applied to the Sennheiser KE 4-211-2 measurement microphones. This was done because the factory 1 mm pinhole was incapable of resolving the finer scales in the turbulent wall jet flow. The microphone system is only able to resolve turbulent scales that are larger than the pinhole diameter. If the wave speed near the wall is estimated to be 12 times the skin friction velocity (this is a reasonable assumption for turbulent boundary layers), then the 1 mm pinhole is only able to resolve turbulent motions associated with frequencies of less than 12000 Hz for the highest speed flow cases. If the pinhole is reduced in size to 0.25 mm, the measurement microphone will be able to resolve turbulent scales associated with a frequency of more than 25.6 kHz which is limit of the data acquisition system used in the current study.

A test to define the effect of the pinhole size was conducted. In this test three pinhole sizes were investigated. Calibrations and smooth wall surface pressure spectra were acquired with three microphones having the factory, $\frac{1}{2}$ mm, and $\frac{1}{4}$ mm pinholes. In Figure 4.10 below, the calibrations for each of the three microphones can be seen.

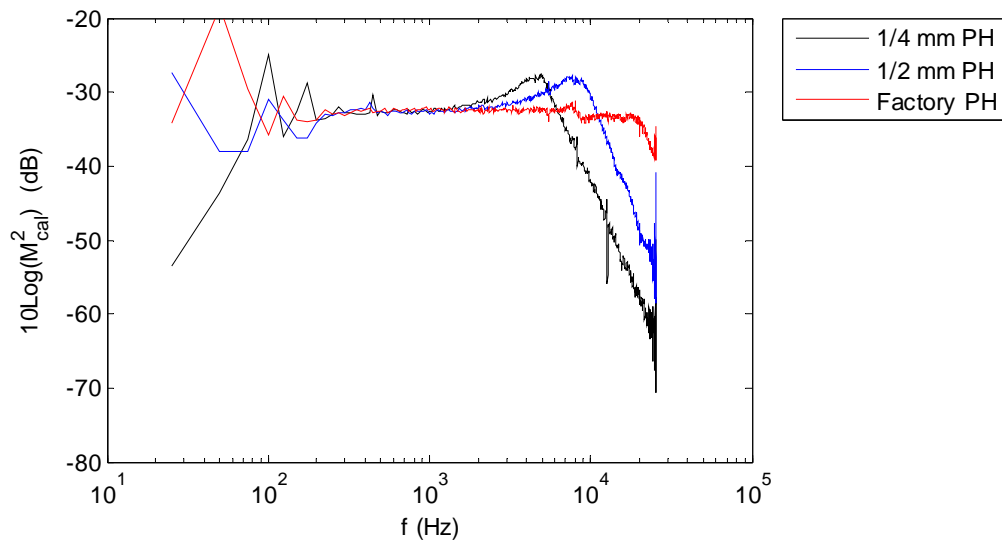


Figure 4.10 *Calibrations for microphones with varying pinhole diameter*

The microphone with the factory pinhole shows a nearly constant frequency response with the exception of the 1 – 2 dB drop off at around 8 kHz. The other two microphone calibrations begin to rise at around 1 kHz and peak before they roll off at higher frequencies clearly showing the loss in microphone sensitivity. It should be noted that the peak values in these two calibrations are about the same, but the frequency at which the peak occurs varies from 5 kHz for the microphone with the $\frac{1}{4}$ mm pinhole to about 7500 Hz for the microphone with the $\frac{1}{2}$ mm pinhole.

Smooth wall surface pressure spectra were also collected with each of the three microphones mentioned above and corrected with the associated calibrations. They were taken for flows with a nozzle height of 12.7 mm, and nozzle exit speeds ranging from 20 – 60 m/s. The 40 and 60 m/s test cases shown below correspond to test conditions B and C in Table 3.1 above. All spectra collected were taken 1422 mm (112 times nozzle height) downstream of the nozzle exit and are shown in Figure 4.11 below.

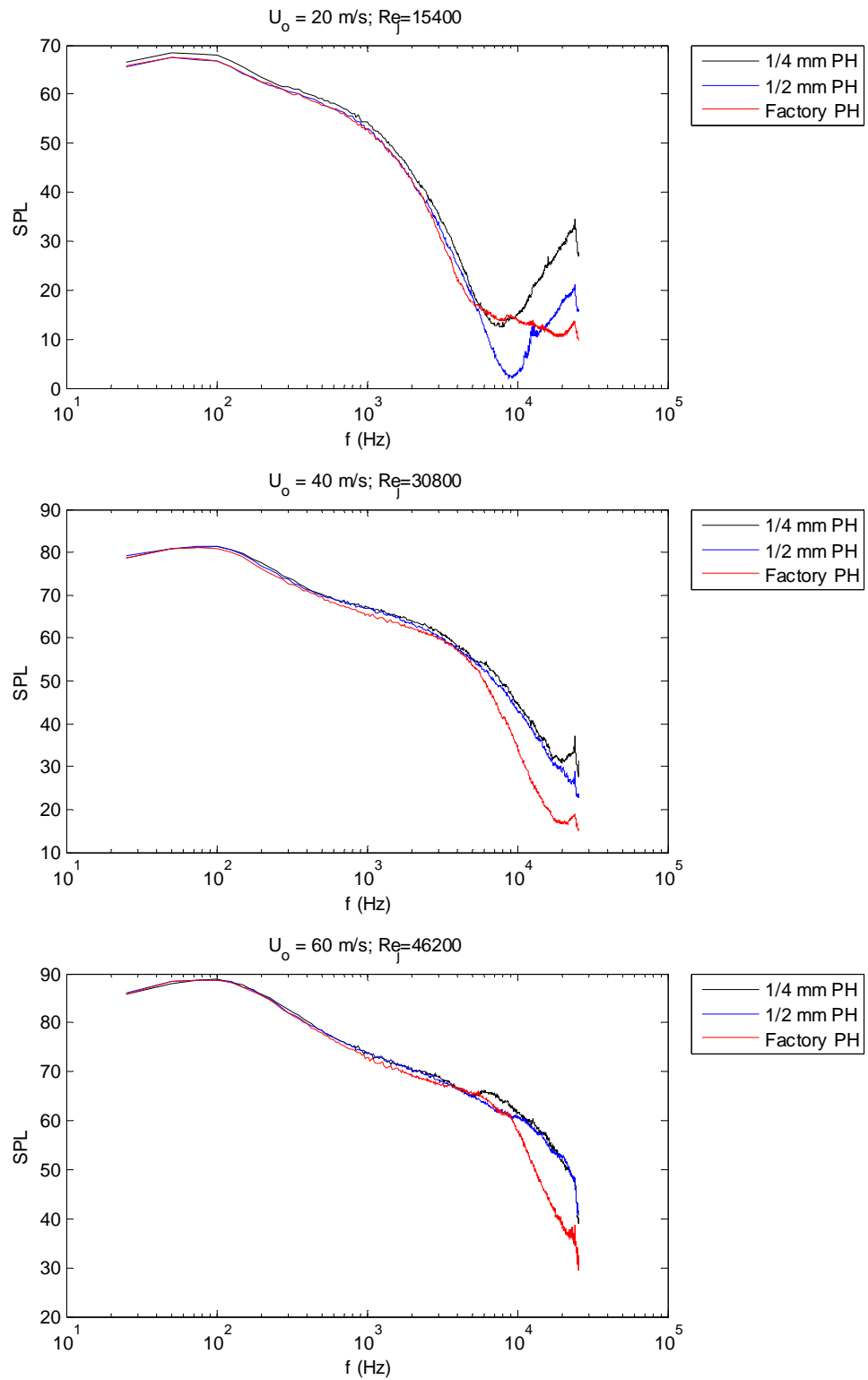


Figure 4.11 Smooth wall surface pressure spectra at nozzle exit speeds of 20, 40 and 60 m/s

The figure above shows the corrected surface pressure spectra for three different microphones that have three different pinhole configurations. For the spectra taken at a nozzle exit speed of

20 m/s one can see that the microphone with the factory pinhole does not adequately resolve the higher frequency pressure fluctuations while the noise floor of the other two measurement microphones is reached at a frequency of about 7500 Hz and 9000 Hz for the $\frac{1}{4}$ mm and $\frac{1}{2}$ mm pinholes, respectively. For the surface pressure spectra taken at U_o equal to 40 m/s, the microphone with the factory pinhole continues to do a poor job of resolving the higher frequency pressure fluctuations, and the other two measurement microphones yield virtually identical results out to 20 kHz where the microphone with the $\frac{1}{4}$ mm pinhole reaches its noise floor and the two spectra depart. For the pressure spectra taken at U_o equal to 60 m/s, the $\frac{1}{4}$ and $\frac{1}{2}$ mm pinhole spectra follow one another very well except in the frequency range between 5 and 10 kHz where there is a bulge in the $\frac{1}{4}$ mm pinhole microphone spectra. This minor anomaly is rather perplexing because it is not readily apparent in the U_o equal to 20 or 40 m/s spectra. It is likely that this feature is due to the effects of measurement sensor installation, and if one looks closely, the $\frac{1}{4}$ mm spectra shows a slight increase in level for the U_o equal to 40 m/s case at the same frequencies as the spectral bulge in the test case for a nozzle exit speed of 60 m/s. It has already been shown that the clean plate surface pressure spectra are very sensitive to small differences in the installation of the microphones.

4.1.4 Effects of Microphone Height and Placement on Surface Pressure

For rough wall surface pressure measurements, the height at which the microphone was placed was seen to be important. The 5.1 mm diameter microphones were placed through 9.5 mm diameter Nylon bushings that were described in Chapter 2 above so that the pinhole was flush with the top of the bushing. The bushing and microphone were then placed in 11 mm diameter holes that were punched in the roughness patches. In Figure 4.12 below, a schematic of the microphone installation is given. The microphone was not always centered in the punched hole of the roughness patch, and the eccentricity varied between 0 and 0.75 mm.

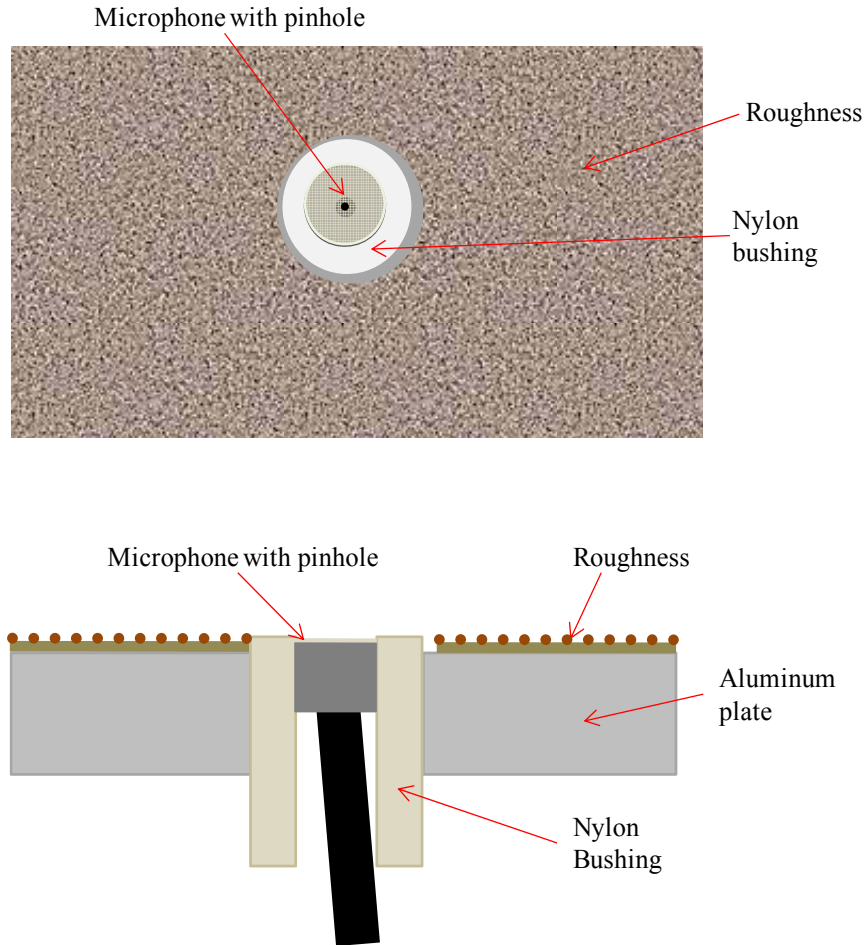


Figure 4.12 *Microphone installation schematic showing microphone positioning relative to the pre-punched holes in the roughness patches*

In order to investigate the effects of varying the microphone height and varying the installation of the microphone on the measured surface pressure spectra, a simple series of tests was conducted. First, a 203 mm x 279 mm piece of 40 grit sand paper with a pre-punched microphone hole was placed on the aluminum plate. Then one of the measurement microphones fitted with a $\frac{1}{4}$ mm pinhole was placed so that it was flush with the underlying aluminum plate. Then the surface pressure spectrum was measured. The flow conditions for this measurement and all others in this simple test were as follows. The nozzle exit velocity was set to be 60 m/s, and nozzle height was set to be 12.7 mm (test condition C mentioned in Chapter 3), and the microphone was placed 1302 mm aft of the nozzle exit and 45 mm aft of the leading edge of the roughness patch. After this measurement was complete, the microphone and bushing were removed and replaced, setting the microphone height to $2.62k_g$, $1.62k_g$, $1.07k_g$, $0.5k_g$, and $0.0k_g$ below the tops of the roughness grains on the rough surface, where k_g is the nominal grain size. The measured pressure spectra are shown in Figure 4.13 below. The surface pressure spectra are affected across the entire frequency range by changing the microphone height relative to the tops of the roughness. However, the surface pressure spectra taken with the microphone height above the roughness bottoms appear to be much less susceptible to variations in microphone height. In fact, there is only a difference of 0.5 to 0.75 dB at most between the spectrum taken with the

microphone at the roughness tops and the spectrum taken with the microphone at 0.5 times the nominal roughness height below the tops of the sand grains. The results seen in Figure 4.13 below show that all spectra that were taken with the microphone above the bottoms of the roughness grains agreed well, and those spectra taken below the bottoms of the roughness grains were significantly different. The spectra taken with the microphone set above the roughness bottoms also showed lower levels at low frequencies and higher levels at high frequencies than the spectra taken when the microphone height was below the roughness bottoms.

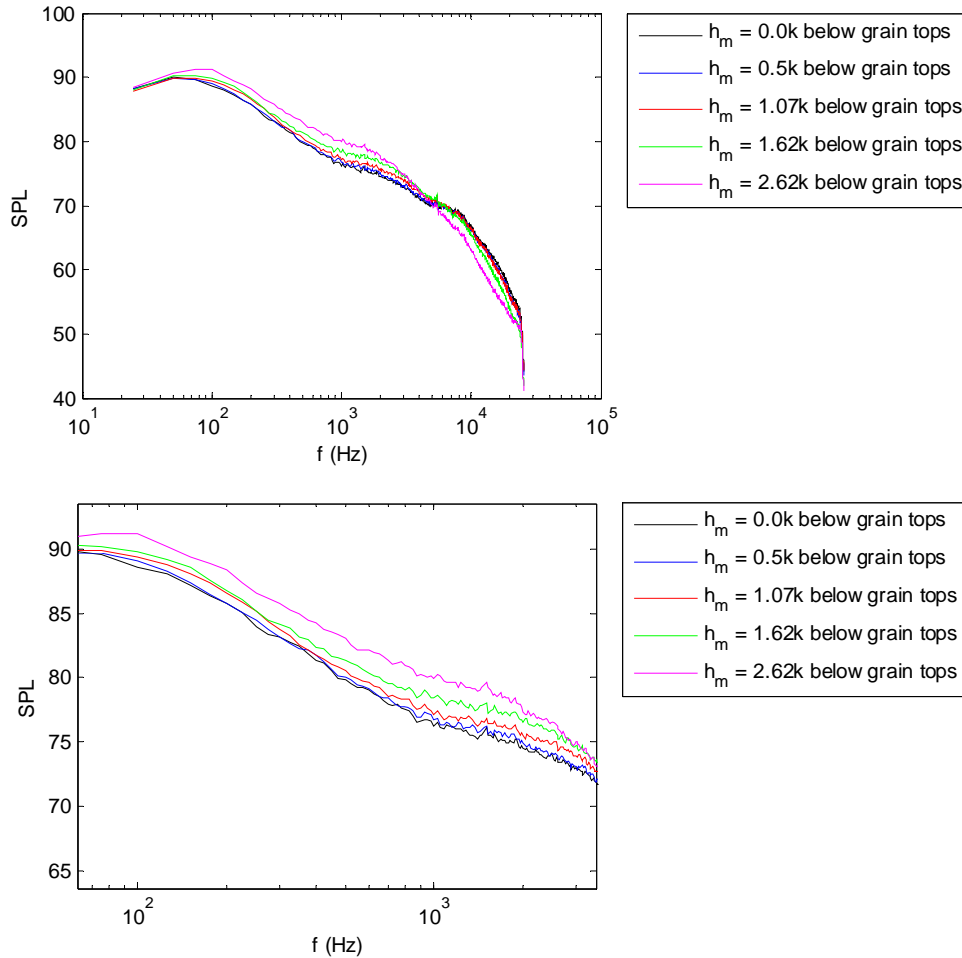


Figure 4.13 Microphone height variation test; clean plate surface pressure spectra

The effects of the microphone installation were investigated further in a different test by taking surface pressure spectra with a microphone set at a height of $0.85k_g$ below the tops of the roughness for three separate installations of the same rough surface. The nozzle exit velocity was 40 m/s and the nozzle exit height was 12.7 mm. To accomplish this test a 203 mm x 203 mm patch of 40 grit roughness with a pre punched hole for the microphone was applied to the plate. The microphone was then inserted from underneath the plate and set to a height that was $0.85k_g$ below the tops of the roughness sand grains. The surface pressure spectrum was measured (noted as Test #1), and then the rough patch was removed leaving the microphone in the plate. Then the rough patch was replaced as closely to the original installation condition as was possible, and the surface pressure spectrum was measured again (Test #2). Then the rough patch was removed and a new hole was punched in the rough patch. The roughness patch was

then placed over the microphone in such a way as to allow the microphone to protrude through the newly punched hole, and the surface pressure spectrum was measured (Test #3). This set of three tests was repeated for a microphone height of $2.05k_g$ below the roughness tops. The results are shown in Figure 4.14 below show that for the spectra taken with the microphone below the bottoms of the roughness grains, there is agreement at low frequencies, but as the frequency increases, the spectra diverge differing by as much as 4-5 dB at 10 kHz. However, the spectra taken above the bottoms of the roughness grains show agreement throughout all frequencies and only show variations of up to 1.5 - 2 dB at 10 kHz. This would suggest that even though changes in microphone installation do affect the measured surface pressure spectra, these changes are less evident when the microphone is at a higher position. From the results seen in Figure 4.14 below, one can conclude that there is some uncertainty in the absolute spectral level to be expected for rough wall surface pressure measurements on the order of ± 1 dB in addition to that already expected from the repeatability of the calibration measurement.

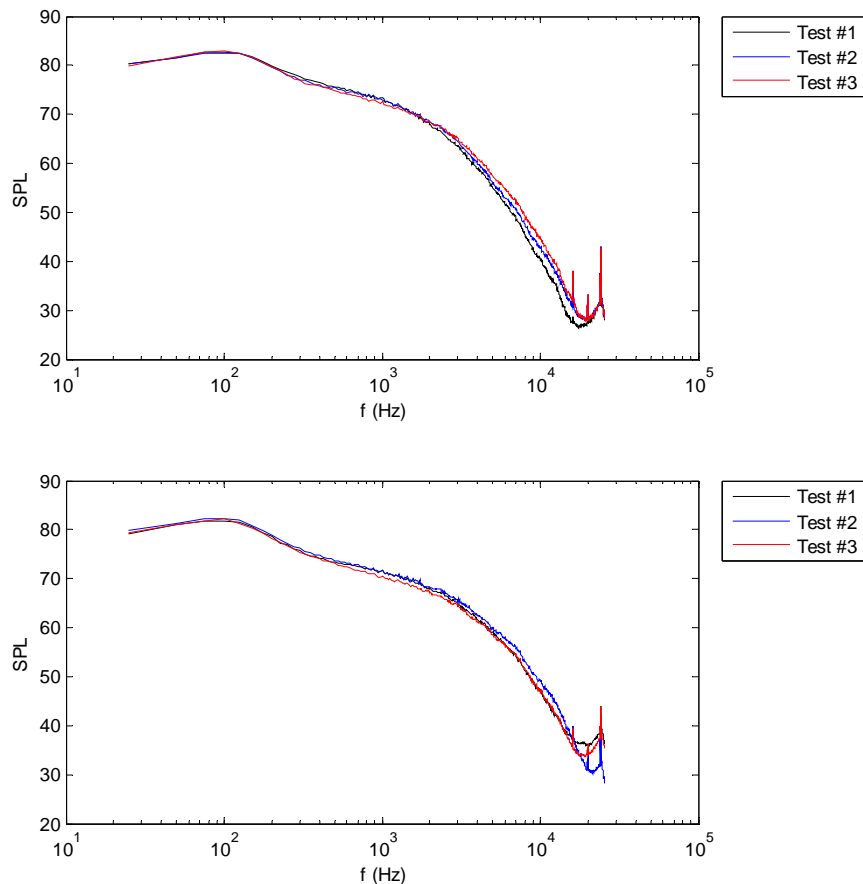


Figure 4.14 Installation variation at constant microphone height surface pressure spectra; microphone heights were $2.05k_g$ below the tops of the roughness (top plot) and $0.85 k_g$ below the tops of the roughness (bottom plot)

In order to measure the surface pressure fluctuations of rough wall jet flows, a standard microphone height relative to the roughness size had to be set for all measurement cases. It was

decided to place the microphone at the roughness tops. This decision was made because the surface pressure spectra seemed to be only very slightly affected by the microphone height when the microphone is placed in this location, and at this height, the effects of the microphone installation seem to influence the surface pressure spectra less than at lower heights.

Placing the microphone at the roughness tops is also a less uncertain process than placing it elsewhere because all that was required was a piece of flat material to be placed on the rough surface. Then the measurement microphones and Nylon Bushings were raised up through the plate through pre-punched holes in the rough surface until the bushing came into contact with the flat material that was placed on top of the rough surface. Then the microphone was glued into the plate from underneath and fixed in place.

4.2 Smooth Wall Surface Pressure Fluctuations

4.2.1 Smooth Wall Test Cases

Surface pressure measurements were taken with 5 measurement microphones at 5 measurement positions for a range of nozzle exit speeds from 20 to 60 m/s at every 5 m/s. The nozzle height was held constant at 12.7 mm. Table 4.1 below shows the flow properties over a range of nozzle exit speeds at the first microphone measurement location x equal to 1302 mm aft of the nozzle exit for the smooth wall test configuration.

U_o (m/s)	x (mm)	b (m/s)	Re_θ	U_m (m/s)	u^* (m/s)	δ (mm)	δ^+ (mm)
20	1302	12.7	419	7.29	0.38	17.3	1.3
25	1302	12.7	501	9.06	0.47	16.6	1.2
30	1302	12.7	580	10.82	0.55	16.1	1.2
35	1302	12.7	656	12.58	0.64	15.7	1.2
40	1302	12.7	731	14.34	0.72	15.3	1.1
45	1302	12.7	803	16.08	0.80	15.0	1.1
50	1302	12.7	874	17.83	0.88	14.8	1.1
55	1302	12.7	944	19.57	0.96	14.5	1.1
60	1302	12.7	1012	21.29	1.04	14.3	1.1

Table 4.1 Range of flow conditions for the smooth wall surface pressure measurements at microphone measurement position #1 ($x = 1302$ mm)

In Table 4.2 below, the flow properties over a range of nozzle exit speeds at the fifth microphone measurement location ($x = 1505$ mm) for the smooth wall test configuration are shown. The x location of the microphones relative to the nozzle exit is given below in Table 4.3. The 30, 40 and 60 m/s test cases shown in the table above and below correspond to the A – C test conditions given in Table 3.1 above

U_o (m/s)	x (mm)	b (m/s)	Re_θ	U_m (m/s)	u^* (m/s)	δ (mm)	δ^* (mm)
20	1505	12.7	444	6.77	0.36	19.7	1.5
25	1505	12.7	531	8.41	0.43	19.0	1.4
30	1505	12.7	614	10.05	0.51	18.4	1.4
35	1505	12.7	695	11.68	0.59	17.9	1.3
40	1505	12.7	775	13.32	0.66	17.5	1.3
45	1505	12.7	851	14.93	0.74	17.2	1.3
50	1505	12.7	927	16.55	0.81	16.9	1.3
55	1505	12.7	1001	18.17	0.88	16.6	1.2
60	1505	12.7	1073	19.77	0.96	16.3	1.2

Table 4.2 Range of flow conditions for the smooth wall surface pressure measurements at microphone measurement position #5 ($x = 1505$ mm)

Mic Position #	1	2	3	4	5
x (mm)	1302	1353	1403	1454	1505

Table 4.3 Microphone position numbers and corresponding locations for smooth wall tests

4.2.2 Smooth Wall Jet Surface Pressure Measurements

There is very little, if any, literature available on the surface pressure character of wall jet flows over smooth surfaces, so when investigating the surface pressure measurements of the current study work done describing the surface pressure character of turbulent boundary layers provided some guidance into what the expected results from this wall jet study should be. Remember, there are similarities and differences between the wall jet flow and the standard turbulent boundary layer flow. This is important to bear in mind when interpreting the surface pressure measurements from the smooth and rough wall jet flows.

The smooth wall surface pressure spectra from the middle microphone location at $x=1.403$ m are presented in Figure 4.15 as a function of nozzle exit velocity in terms of 1Hz-bandwidth SPL vs. frequency in Hz and encompass test conditions A – C defined in Chapter 3 above. The spectra plotted from this point will not include data from below 100 Hz because this was the determined to be the lower useful limit of the microphone calibrations.

$$SPL = 10 \text{Log} \left(\frac{\Phi}{p_{ref}^2} \right) \quad (4.3)$$

where p_{ref}^2 is the reference pressure and is equal to 20 μ Pa, and Φ is the power spectrum of the surface pressure fluctuations such that

$$\bar{p}^2 = \int_0^\infty \Phi(f) df \quad (4.4)$$

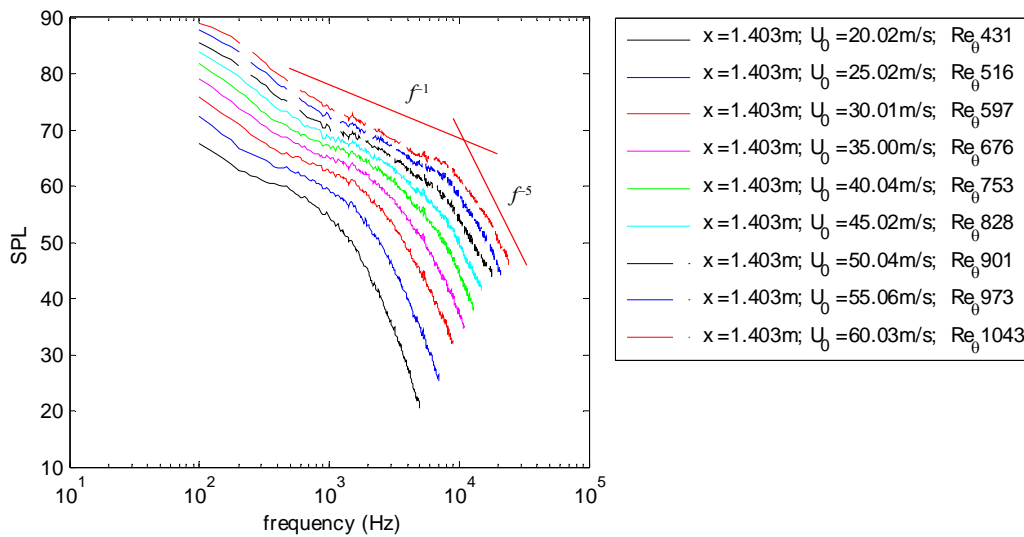


Figure 4.15 Smooth wall surface pressure spectra taken at $x = 1302$ mm over a range of nozzle exit speeds

The x location and Reynolds number based on the momentum thickness are given for each spectrum shown above in the figure. The figure above shows spectra taken over a range of nozzle exit velocities that range from 20.1 m/s to 60.1 m/s. The spectra above are typical for those at all the measurement locations, but this particular measurement location was presented because when roughness is applied to the aluminum plate, the streamwise center of the roughness patch corresponds with the measurement location presented in Figure 4.15 above.

There are some important features that are apparent in the spectra above. The spectral levels show a region that varies as f^{-1} , or at least nearly so. At higher frequencies the spectra decay and approach a f^{-5} variation. The f^{-1} and f^{-5} regions have been predicted by Blake (1986) among others for conventional turbulent boundary layers. In conventional turbulent boundary layers, the predicted f^{-1} region is due to turbulent motions in the log layer where the convection velocity approaches the mean velocity.

The spectral scaling of the surface pressure is important because it provides insight into the turbulent motions in the wall jet flow in particular frequency ranges. Because of the scarcity of studies of wall jet surface pressure, the scaling attempts shown here will largely echo some of the scaling attempts presented in previous studies of turbulent boundary layers.

The surface pressure spectra shown in Figure 4.15 above were scaled using the inner variables ν/u^* , u^* , and τ_w representing the length, velocity, and pressure scaling variables. These scaling variables have been used frequently in the literature and are regarded as being the most appropriate scales for surface pressure spectra at high frequencies for conventional turbulent boundary layers. This scaling is very similar to the velocity spectral scaling of Ueda and Hinze (1975) used above to scale the high frequency regions of the velocity spectra. These scaled surface pressure spectra are plotted in Figure 4.16, and the flow conditions are indicated in the legend.

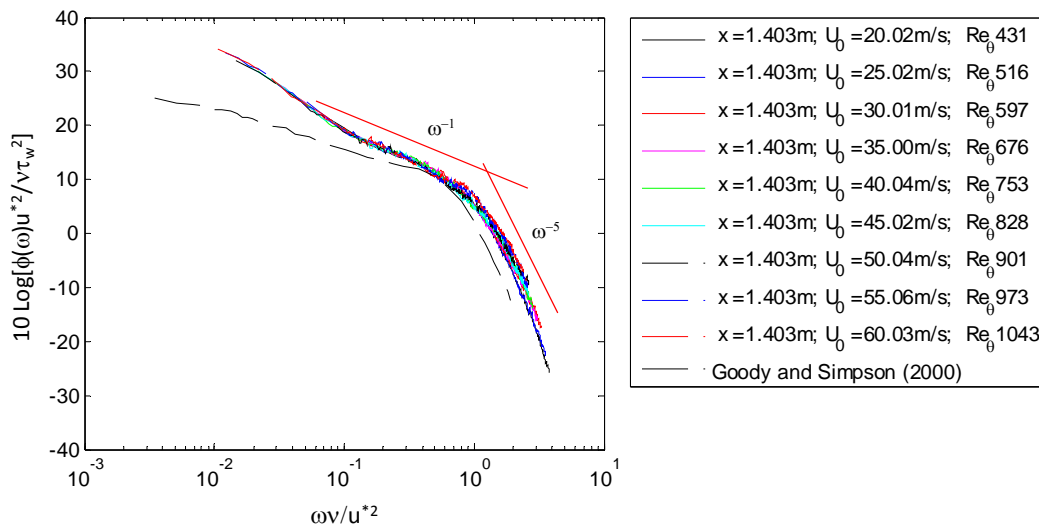


Figure 4.16 Surface pressure spectra scaled on inner variables (v/u^* , u^* , and τ_w)

The surface pressure spectra are seen to scale on the inner variables from nondimensional frequency values of 0.01 up through the rest of the frequency range. The inner scaling variables collapse the spectra to within 5 dB of one another from a spread of over 50 dB. From nondimensional frequencies of 0.01 to 0.8, the collapse is very good indeed (the collapse is within 1.5 dB in this region). This scaling is meant to account for the fine scale turbulent motions associated with the buffer layer, but also scales the spectra in the mid to low frequency range where the corresponding turbulent motions are those found in the semilog region.

Also shown is in the figure one of the conventional turbulent boundary layer spectra taken by Goody and Simpson (2000) normalized on inner variables. This spectrum was taken at a much higher momentum thickness Reynolds number than the current measurements. Even so, this spectrum is indicative of other spectra from other workers presented by Goody and Simpson (2000) that cover a wide range of local Reynolds numbers. The normalized wall jet surface pressure spectra shown begin to roll off at non-dimensional frequencies of 0.8 while those from the spectra presented in Goody and Simpson (2000) begin to roll off at around 0.5. Both the turbulent boundary layer and wall jet spectra approach a ω^{-5} variation at high frequency.

In the nondimensional frequency range from 0.01 to 0.8, the inner scaling variables collapse the wall jet spectra very well, but there is a marked difference between the scaled surface pressure spectra from the regular turbulent boundary layer measured by Goody and Simpson (2000) whose data show a variation with frequency much different than the current wall jet data.

This frequency region is alluded to as the overlap region where both inner and outer variables will scale the spectra by Goody (2004) who credits this notion Blake (1986) and others. It will be shown later that this thought seems to be applicable to wall jet surface pressure spectra because there is a sizable frequency region before the roll off where the wall jet surface pressure spectra scale on outer variables. The size of the overlap region has been shown to grow with increases in Reynolds number. This is indeed what is seen in Figure 4.16 above; as the Reynolds number increases, the ω^{-1} region of the spectra that is scaled by the inner variables is extended to lower and lower nondimensional frequencies. Interestingly, the actual measured spectra variations with frequency in the overlap region for turbulent boundary layers have been shown to

vary from $\omega^{-0.7}$ by McGrath and Simpson(1987) to $\omega^{-0.8}$ by Goody and Simpson(2000), and many others. The current study shows some agreement with the theoretical frequency variation suggested by Blake (1986). However, the actual frequency variation is observed to be closer to $\omega^{-1.1}$.

The spectrum from Goody and Simpson (2000) showed a spectral decay in the overlap region with $\omega^{-0.8}$ while that seen in the wall jet spectra varies with $\omega^{-1.1}$. The differences between the wall jet spectra and the regular turbulent boundary layer spectra in the overlap region are not really surprising considering the aerodynamic results presented in the previous chapter. Even though the wall jet mean velocity profiles showed similarities between canonical turbulent boundary layers, there were differences, and the turbulent character of the wall jet was shown to be markedly different from the turbulent boundary layer especially as the measurement position moved away from the wall. One possible explanation for the spectral differences could be the presence of the shear layer in the wall jet flow. It is likely that turbulent structures from the shear layer alter the turbulent character of the wall jet flow below the velocity maximum in the log layer, thus affecting the spectral overlap region mentioned above. One would expect that these turbulent structures would be quite a bit larger and more slowly moving than those below the velocity maximum, and thus, would have more of an impact on the lower frequency portions of the spectra.

The higher frequency region shows a spectral variation with ω^{-5} . This variation was experimentally observed by McGrath and Simpson (1987) and again later by Goody and Simpson (2000). The current data also shows good agreement with these observed frequency variations for conventional turbulent boundary layers in the high frequency regime.

The consensus on the inner scaling variables is broad. However, there is very little agreement concerning the appropriate outer scaling variables for conventional turbulent boundary layers in the literature. Goody and Simpson (2000) provide a review of the scaling variables used by various workers, and they present 2 length scales, 2 velocity scales, and 2 pressure scales that have been used in past studies. The length scales presented were δ and δ^* (boundary layer and displacement thicknesses), the velocity scales were U_e and u^* (edge and friction velocities), and the pressure scales were τ_w and Q_e (wall shear and dynamic pressure at the boundary layer edge). These scaling parameters were applied to the surface pressure spectra in the current study, but the edge parameters U_e and Q_e were replaced with the wall jet velocity maximum parameters, U_m and Q_m . These possible scaling parameters yielded 8 possible combinations of spectral scalings. However, it has been argued previously that the boundary layer length scales proposed as spectral scaling lengths are proportional to one another, at least for the smooth wall jet flow. Therefore, the question becomes which scaling velocity and pressure scale are the best choices for scaling the wall jet surface pressure spectra? These scalings were investigated and applied to the spectra shown in Figure 4.15 above. In Figure 4.17 below, the spectra are shown scaled on outer variables δ , U_m and τ_w . These variables were chosen based on the investigation of the possible scaling parameters mentioned above. There was no discernable difference in the scaled spectral behavior between the surface pressure spectra scaled with the maximum local velocity and those scaled with the skin friction velocity. However, spectra scaled using the wall shear as a pressure scale seemed to collapse more consistently in the overlap region than those spectra scaled using the dynamic pressure at the velocity maximum. The surface pressure spectra shown in Figure 4.18 below are scaled using the dynamic pressure. There are portions of the overlap region where the spectra collapse better than those shown in Figure 4.17, but there are also portions that do not show as good of a

collapse. Therefore, it was decided that for the smooth wall surface pressure spectra, that the scaling variables used in Figure 4.17 were the most successful outer scaling variables for smooth wall jet flows. It should also be noted that the length scale, $y_{1/2}$, was investigated as a possible scaling variable for the surface pressure outer spectral scaling because it scaled the outer mean velocity and turbulence profiles of the wall jet flow. However, no improvement in the scaling was seen when $y_{1/2}$ was used over that seen when the boundary layer thickness was used. This is not a surprise because the boundary layer thickness was found to be proportional to $y_{1/2}$.

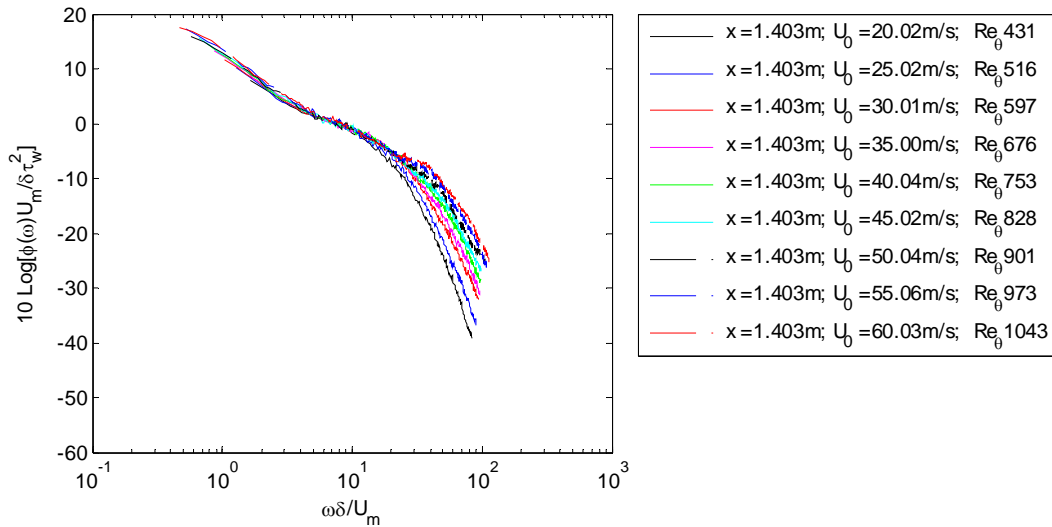


Figure 4.17 Smooth wall surface pressure spectra scaled on outer variables (δ , U_m , and τ_w)

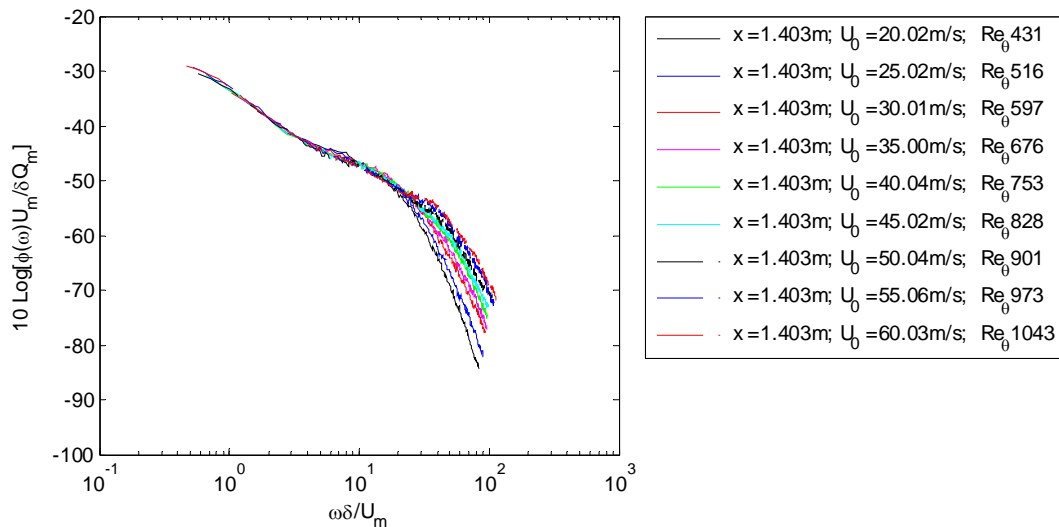


Figure 4.18 Smooth wall surface pressure spectra scaled on outer variables (δ , U_m , and Q_m)

After observing all possible scaling variable combinations, it was determined that the most appropriate outer-region length scale for the wall jet surface pressure spectra in the outer region was δ . The velocity scale chosen was the maximum velocity, U_m . The appropriate

pressure scale was determined to be the wall shear, τ_w . Blake (1970) presents spectra scaled on δ^* , U_m , and τ_w , Simpson and Goody (2000) present their measurements scaled on δ , u^* , and τ_w , and Goody (2004) presents his empirical model scaled on δ , U_m , and τ_w . Farabee and Casarella (1991) use Q_e as their pressure scale and use δ^* and U_e as their length and velocity scales. The wide range of scaling parameters used in the literature and the difficulty in determining an optimum set of outer scaling variables encountered in the current study indicates just how difficult it is to obtain definitive scaling variables for the outer, low frequency region of surface pressure spectra of wall bounded flows. It is important to note the differences between all of the scaling parameter permutations observed in this study were very small, and all of the possible scaling parameters scaled the spectra in the overlap regions well. Indeed, a legitimate case could be made for using any set of the scaling parameters investigated as there is very little discernable improvement between the scaling that were investigated.

There have been attempts, both theoretical and empirical, to model the surface pressure spectra of canonical turbulent boundary layer flows. Goody (2004) develops and presents an empirical model. He also presents what he calls the Chase-Howe model below.

$$\frac{\Phi(\omega)U_e}{\tau_w^2\delta^*} = \frac{2\left(\frac{\omega\delta^*}{U_e}\right)}{\left[\left(\frac{\omega\delta^*}{U_e}\right)^2 + 0.0144\right]^{\frac{3}{2}}} \quad (4.5)$$

This model was presented by Howe (1998) who gives credit for its inception to Chase (1980). At low frequencies the model predicts spectral level variations with ω^2 while at higher frequencies it predicts variations with ω^{-1} . The model does not predict the high frequency variation with ω^{-5} that is seen in the experimental data for both wall jet flows and turbulent boundary layer flows. In Figure 4.19 below, the spectra shown in Figure 4.15 above are presented and compared with the Chase-Howe model.

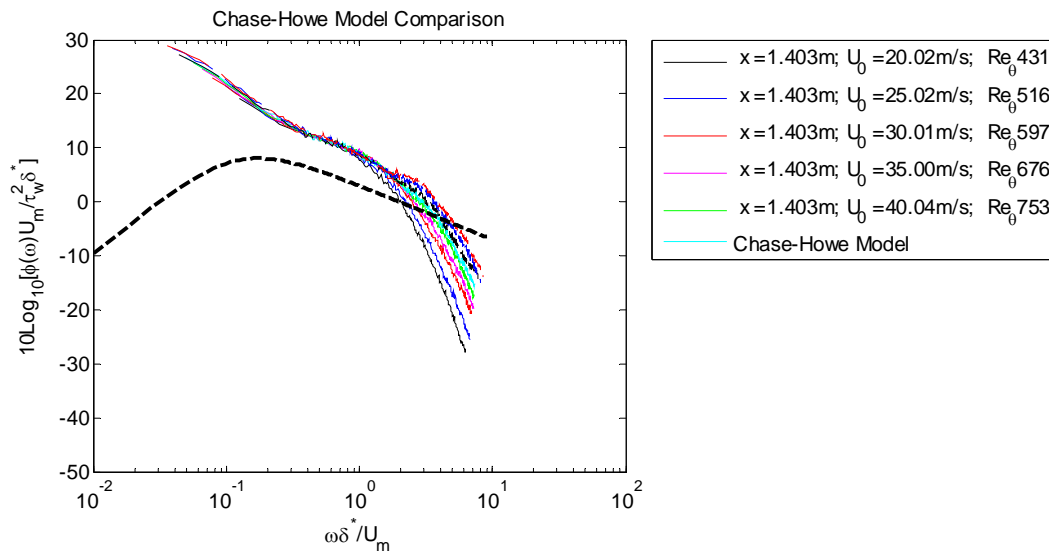


Figure 4.19 Smooth wall jet surface pressure spectra compared with Chase-Howe model for turbulent boundary layer surface pressure spectra

The low frequency behavior of the experimental data for the smooth wall jet flow presented above does not agree well with that predicted by the Chase-Howe model. This discrepancy has also been seen in the comparison of wall jet measurements with turbulent boundary layer measurements seen in Figure 4.16 above. The frequency region where the spectra begin to vary closely with ω^{-1} begins roughly at a nondimensional frequency of 0.3 for both the model and experimental wall jet data presented. The Chase-Howe model was not designed to predict the ω^{-5} drop off at high frequencies at nondimensional frequencies above 0.7 or 0.8. The spectral levels of the model in the overlap region are lower than those of the experimental wall jet data. One should recall that the measured wall jet spectra did not agree with the turbulent boundary layer spectra measured by Goody and Simpson (2000) in this overlap region either.

Goody (2004) presents an empirical model for the surface pressure spectra of turbulent boundary layer flows which was discussed in Chapter 1, and it is given below.

$$\frac{\Phi(\omega)U_e}{\tau_w^2\delta} = \frac{3.0\left(\frac{\omega\delta}{U_e}\right)^2}{\left[\left(\frac{\omega\delta}{U_e}\right)^{0.75} + 0.5\right]^{3.7} \left[(1.1R_T^{-0.57})\left(\frac{\omega\delta}{U_e}\right)\right]^7} \quad (4.6)$$

The constant, 3.0, in the numerator, and the constant, 0.5, in the denominator are experimentally determined constants. The R_T term in the denominator is also experimentally determined by Goody (2004) and is a ratio of the outer to inner timescales that are used to normalize the frequency in the inner and outer spectra scaling attempts.

$$\frac{\left(\frac{\delta}{U_e}\right)}{\left(\frac{\nu}{u^*2}\right)} = \frac{\left(\frac{u^*\delta}{\nu}\right)}{\sqrt{\frac{c_f}{2}}} = R_T \quad (4.7)$$

The fanning out of the spectra at high frequencies in figures Figure 4.17 and Figure 4.19 above is commonly thought of as a Reynolds number effect. Goody (2004) suggests that this effect is actually driven by the parameter R_T instead of the Reynolds number. In Figure 4.20 below, the previously discussed wall jet surface pressure spectra are compared with the empirical model of Goody (2004).

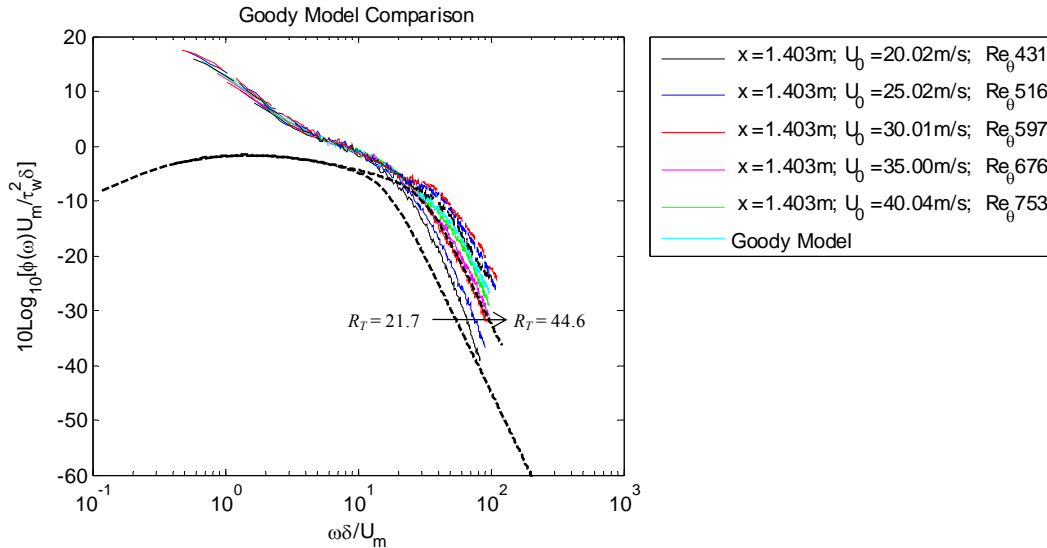


Figure 4.20 Smooth wall jet surface pressure spectra compared with Goody (2004) empirical model for turbulent boundary layer surface pressure spectra

In the figure above, smooth wall jet surface pressure spectra are compared with the empirical model of Goody (2004). The value of R_T for each of the spectra shown was calculated, and applied to the model. The effect of the R_T on the model can be clearly seen. Again, the experimental wall jet spectra and empirical model for turbulent boundary layers do not agree well in the overlap and low frequency regions. This has been a consistent theme throughout the investigation of wall jet surface pressure spectra. The levels in the high frequency range of the model are 3 – 4 dB lower than those of the wall jet spectra at a nondimensional frequency of 10. The measured spectra begin to roll off at higher frequencies than that predicted by the Goody (2004) model, but the spectral levels at the onset of the high frequency roll off are within 2 – 3 dB of the levels predicted by the model. The spectra of the wall jet surface pressure also fan out more at high frequencies than the model predicts. It is important to remember that one must be careful in making direct comparisons between the wall jet surface pressure spectra and the Goody (2004) prediction because the model was designed to predict the smooth wall surface pressure spectra for turbulent boundary layers, and the purpose of comparing the two is to highlight the differences in the surface pressure spectra of wall jet flows and turbulent boundary layer flows.

The results presented and discussed above were all taken with the same microphone in the same x location over a range of momentum thickness Reynolds numbers. The same scaling and model prediction analysis was applied to all of the 4 other microphones and locations. In the figures below, surface pressure spectra from a few of the other measurement microphones will be presented. The dimensional spectra will be shown along with the nondimensional spectra normalized on inner and outer variables. The spectra normalized on outer variables will be compared with the Goody (2004) empirical model because the choice of appropriate scaling variables is consistent with that employed by the Goody (2004) model.

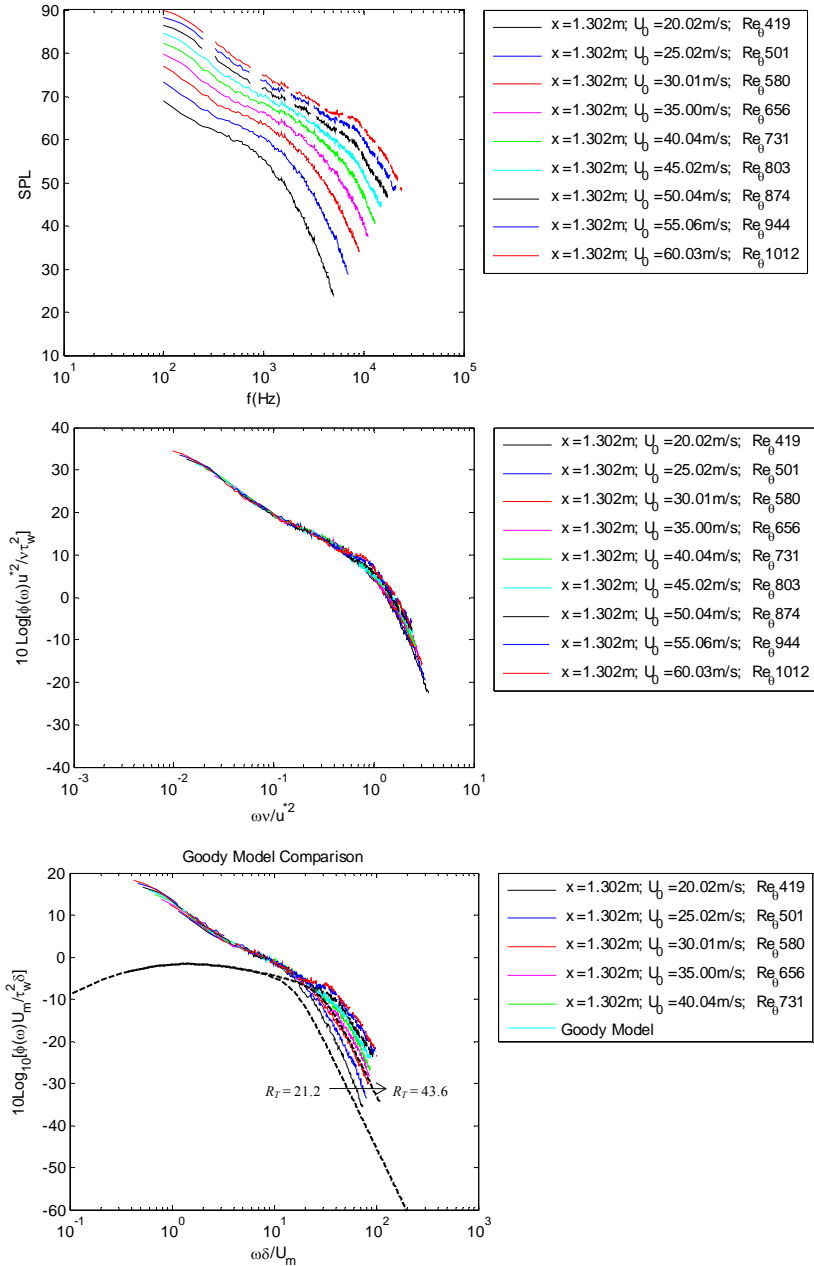


Figure 4.21 Smooth wall surface pressure spectra taken at $x = 1302$ mm (foremost microphone measurement position)

The spectra shown above were taken at an x location of 1302 mm aft of the nozzle exit for a range of momentum thickness Reynolds numbers from 420 to 1010. The spectra scale very well at high frequencies on inner variables as was shown before for the spectra taken at x equal to 1403 mm. The scaling of these spectra on outer variables is consistent with that seen for the spectra taken at x equal to 1403 mm as well, and the agreement with the Goody (2004) model is also comparable.

The spectra in Figure 4.22 below were taken at an x location of 1505 mm over a momentum thickness Reynolds number range of 444 to 1073. Again, the spectra scale very well

at high frequencies on inner scaling variables. The scaling of these spectra on outer variables is consistent with that seen for the spectra taken at x equal to 1302 mm and 1403 mm, and the agreement with the Goody (2004) model comparable yet again.

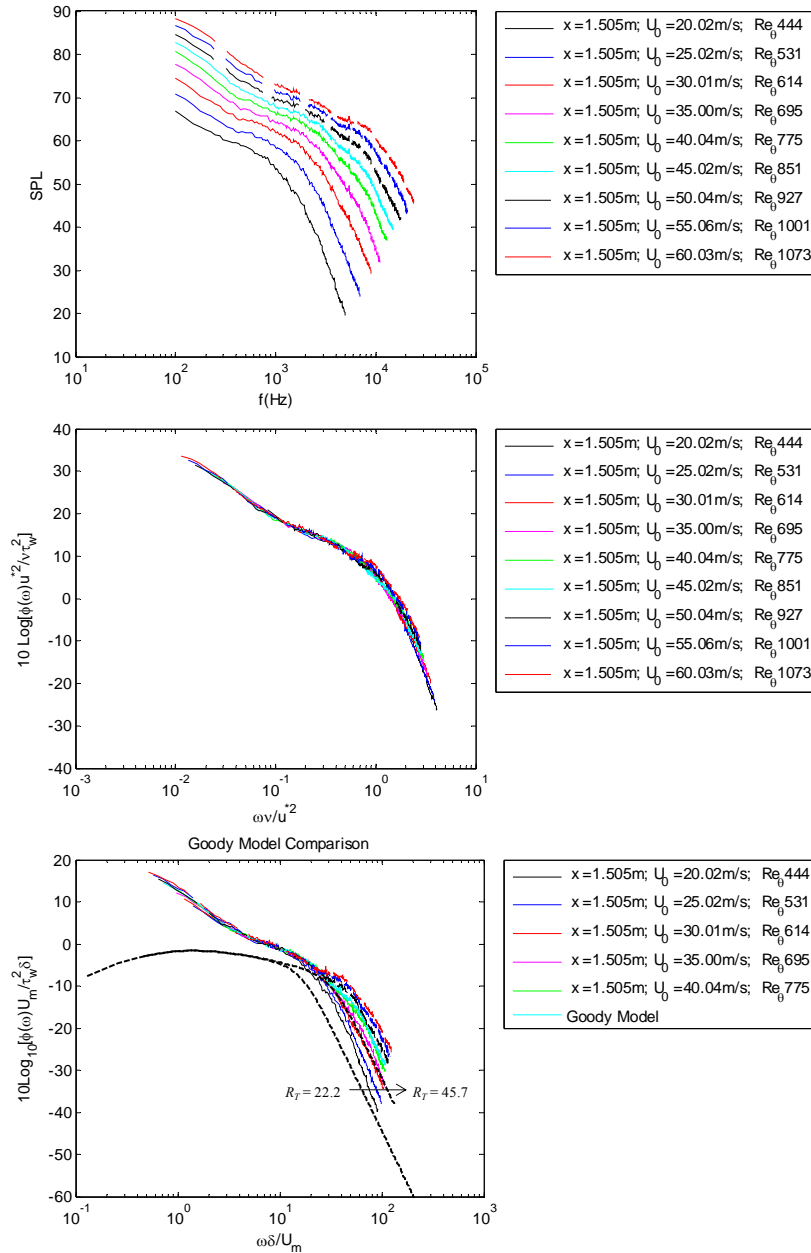


Figure 4.22 Smooth wall surface pressure spectra taken at $x = 1505$ mm (aft most microphone measurement position)

In the smooth wall surface pressure spectra shown above, the momentum thickness Reynolds number was varied by increasing the nozzle exit speed, and the spectra were analyzed over this range of flow conditions for each individual microphone. The momentum thickness Reynolds number can also be varied by changing the measurement location. The spectra presented below were all taken at a nearly constant nozzle exit speed of approximately 60 m/s

(test condition C mentioned in Chapter 3 above) over a range of x locations resulting in a variation in the momentum thickness Reynolds number.

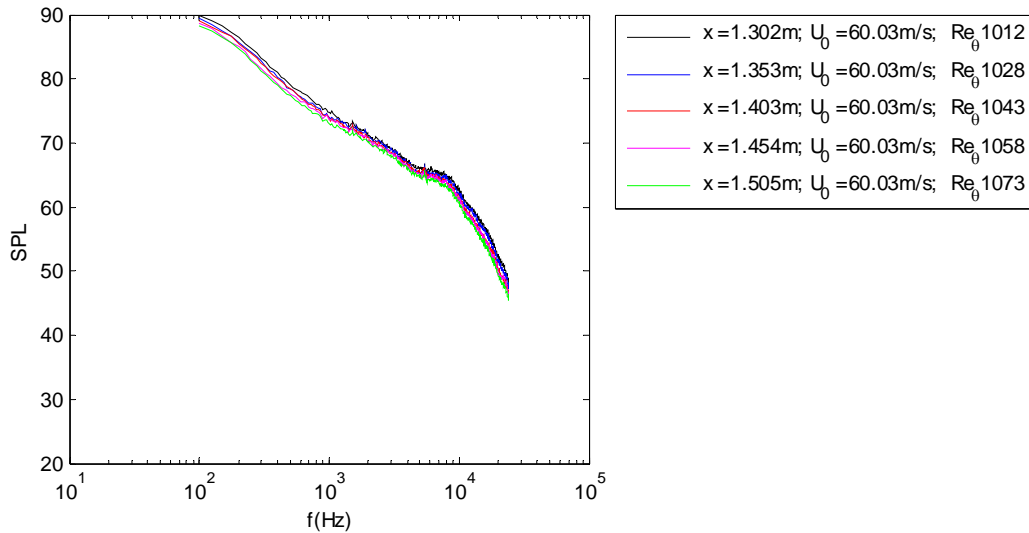


Figure 4.23 Smooth wall surface pressure spectra taken at varying x locations

The spectra above occupy a band that is about 2 to 2.5 dB wide over the entire frequency range. The maximum velocity for the flow at each one of the measurement locations shown in the figure above ranged from 21.3 m/s at the first microphone measurement location down to about 19.8 m/s at the aft most microphone location. If one looks more closely at these spectra, a definite progression of the spectral levels with the downstream distance of the microphone measurement location can be seen and is shown in Figure 4.24 below.

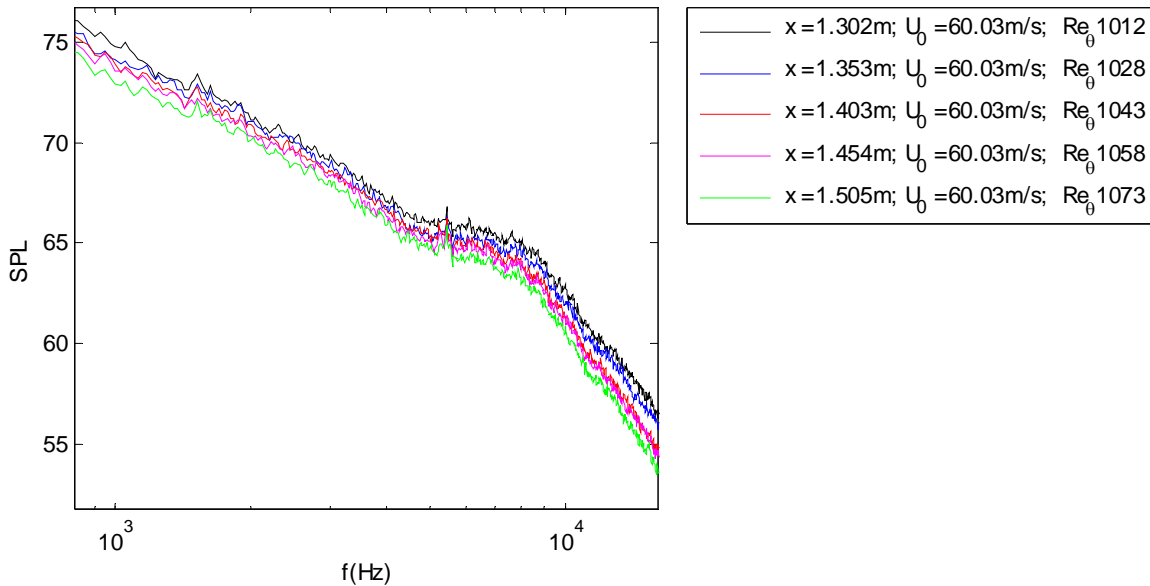


Figure 4.24 Smooth wall surface pressure spectra taken at varying x locations

This progressive behavior was observed to be present in the smooth wall surface pressure spectra over the entire range of nozzle exit speeds tested. In Figure 4.25 below, the surface pressure spectra for the 20 m/s nozzle exit speed test case are shown and can be seen to exhibit the same progressive behavior.

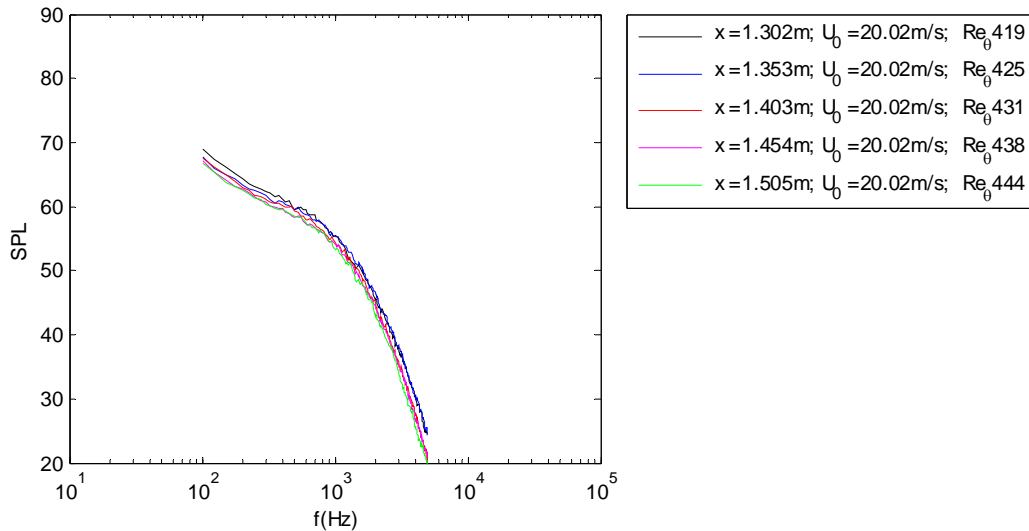


Figure 4.25 Smooth wall surface pressure spectra taken at varying x locations

The spectra in Figure 4.25 above occupy a band 2 to 3 dB wide throughout the entire frequency range. The maximum velocities varied from 7.29 m/s at $x = 1302$ mm to 6.77 m/s at $x = 1505$ mm. In Figure 4.26 below, the inner and outer scaling variables are applied to the surface pressure spectra in Figure 4.23 above. When this is done all of the scaled spectra collapse down to within 1 to 2 dB over the entire frequency range. The collapse of the spectra scaled on outer variables at high frequencies is not a surprise here because the local flow conditions are not significantly different between the foremost and aft most microphone measurement locations.

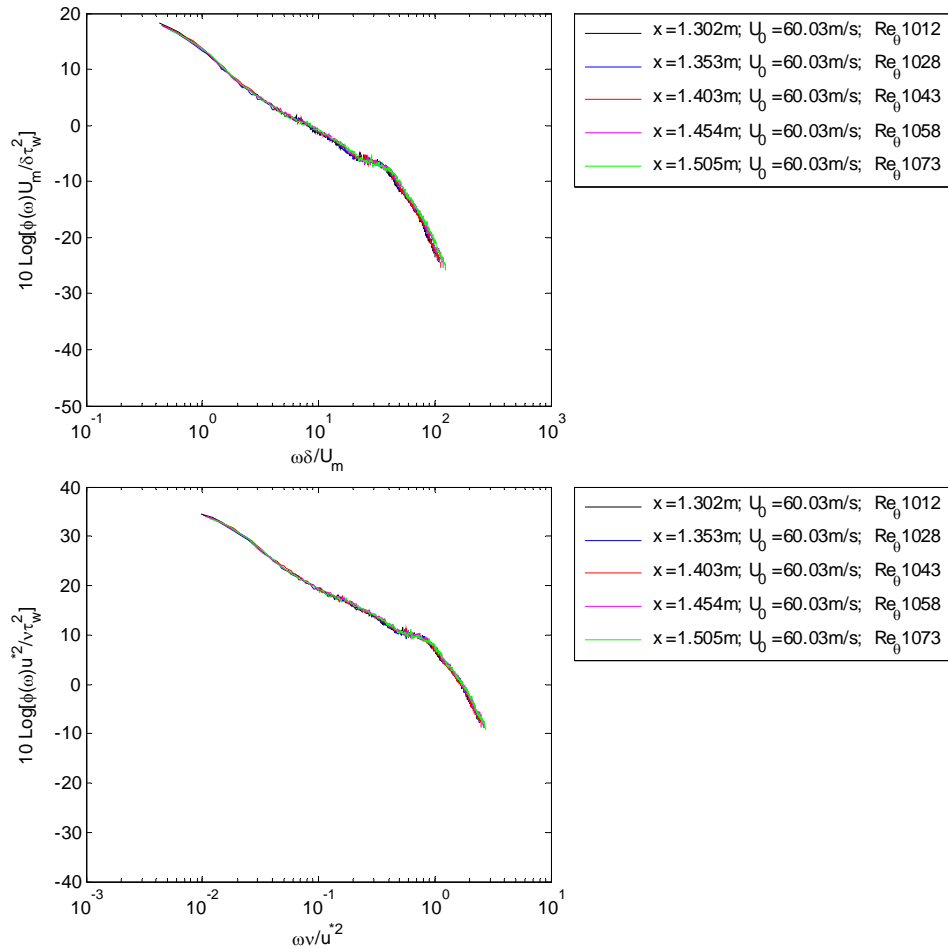


Figure 4.26 Smooth wall surface pressure spectra taken at varying x locations scaled on outer and inner variables (top and bottom, respectively)

4.2.3 Smooth Wall Surface Pressure Summary

The smooth wall jet surface pressure spectra were found to scale well on the inner and outer scaling variables that are commonly used to scale turbulent boundary layer surface pressure spectra in the overlap region. This scaling in the overlap region is due to the overlap region in the wall jet flow where both the maximum and skin friction velocities scale the flow yielding the semilog region seen in the velocity profiles seen in Chapter 3 above. The inner scaling variables scale the wall jet surface pressure spectra well at high frequencies as well. The scaled smooth wall jet surface pressure spectra were found to vary both in character and in level from both the measured and predicted surface pressure spectra of turbulent boundary layers, particularly in the overlap region, but to a lesser degree at high frequencies. This variation is thought to be due to the presence of the shear layer in wall jet flows and the interaction of turbulent structures associated with it. In particular, the shear layer is thought to affect the turbulent structures in the log layer significantly explaining why the overlap region of the scaled wall jet surface pressure spectra differ so starkly from the that of conventional turbulent boundary layers. The smooth wall surface pressure spectra were found to vary in a consistent and progressive way with the

downstream distance from the nozzle exit. Over the entire streamwise measurement range, the surface pressure spectra were found to vary by less than 2.5 dB for nozzle exit speeds of approximately 60 m/s and by less than 3 dB for nozzle exit speeds of approximately 20 m/s.

4.3 Rough Wall Surface Pressure Fluctuations

As mentioned above in Chapter 1, the available literature regarding rough wall boundary layer surface pressure fluctuations is limited. When one considers that the current flow is a wall jet flow and not a canonical turbulent boundary layer, the available literature dealing with rough wall surface pressure is very rare indeed, if any exists at all. Thus, the surface pressure spectral character of wall jet flows over rough surfaces is of interest because, heretofore, it has remained somewhat of a mystery. The current work will shed light on this spectral behavior, and should also provide some added insight into the spectral behavior of the surface pressure of wall bounded flows in general.

In the current study, surface pressure measurements were taken with 5 microphones placed along the centerline of the aluminum plate in the same positions as those for the smooth wall surface pressure measurements. Some 400 surface pressure spectra measurements were taken over the same range of initial flow conditions as for the smooth wall test cases (encompassing the A – C test conditions mentioned in Chapter 3). For each roughness tested, a roughness patch with a streamwise length of 305 mm and a spanwise width of 610 mm was placed such that its leading edge was located at 1257 mm aft of the nozzle exit. The patch length is on the order of 10 to 20 times the boundary layer thickness at the leading edge of the patch. The measurement microphones were placed up through the roughness patch such that the pinhole opening was at the level of the roughness grain tops as discussed earlier. A schematic of the roughness patch setup and the microphone placement is given in Figure 4.27 below.

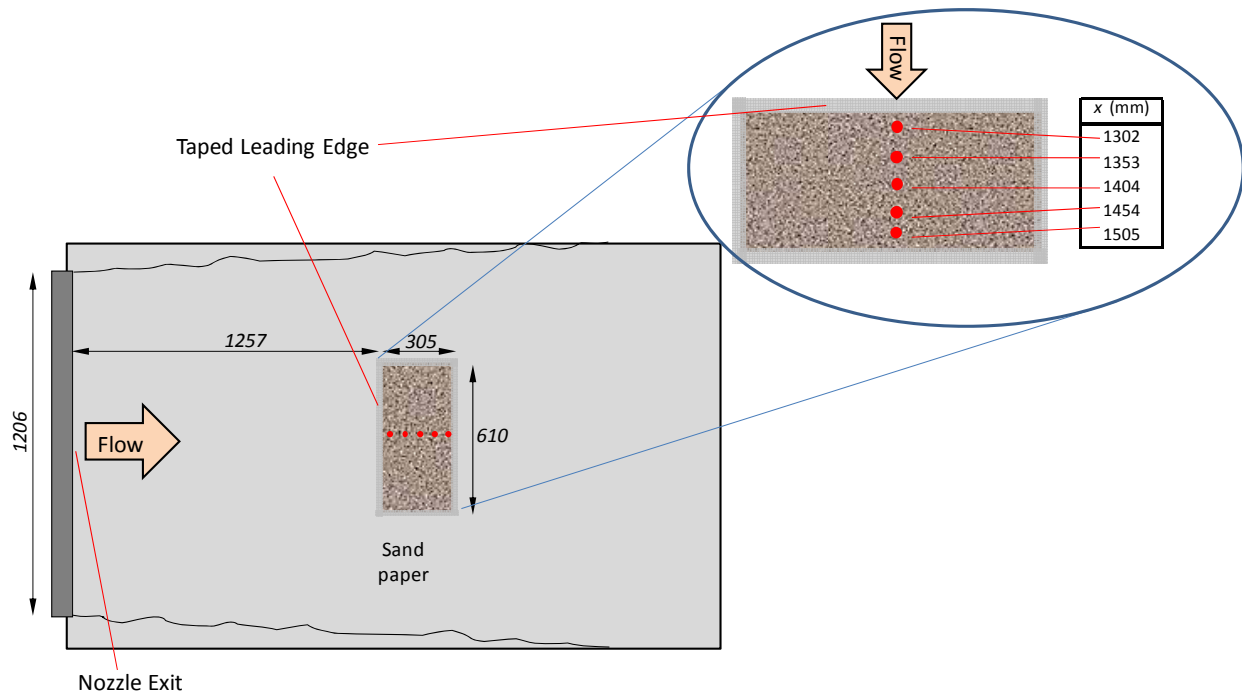


Figure 4.27 *Surface pressure microphone setup (dimensions in mm)*

The geometric roughness characteristics for each surface tested are given in more detail above in Chapter 2. Surface pressure measurements will be presented for wall jet flows over 9 different roughnesses of varying sand grain sizes. All roughnesses used were of a sand grain type, and the roughness elements were not deterministically distributed. The roughnesses used will be referred to in terms of a grit number, and these grit numbers and corresponding geometric characteristics are given in Chapter 2.

4.3.1 40 Grit Surface Pressure Measurements

Surface pressure measurements for both the 40 and 180 grit cases were taken over the same range of initial flow conditions and microphone placement locations as the smooth wall surface pressure measurements presented above with the only differences due to atmospheric changes on the different testing days. In Figure 4.28 below, the dimensional spectra are shown for the 40 grit measurements over a range of nozzle exit speeds from approximately 20 m/s to 60 m/s. Initial and local flow conditions are presented in the legends. The local Reynolds number was obtained using local flow parameters estimated as discussed earlier in Chapter 3, and k^+ was determined using the equivalent sand grain roughness height along with the skin friction velocity which was calculated using the momentum balance method described in Chapter 3 above in conjunction with the estimated local flow parameters. The three plots below each show the surface pressure spectra at a different microphone location. As for the smooth wall surface pressure spectra, the spectral levels do not decrease substantially over the length of the roughness patch. The variation of the surface pressure spectra with the downstream distance will be discussed in more detail later. In the mid frequency ranges, the surface pressure spectra show a closer variation with f^1 than the smooth wall cases showed, and the spectra approach a f^5 variation as they roll off at high frequencies. The downstream measurement locations shown in Figure 4.28 below correspond to the foremost, mid and aft most microphone locations (top to

bottom). The middle microphone measurement location corresponds to the streamwise center of the roughness patch.

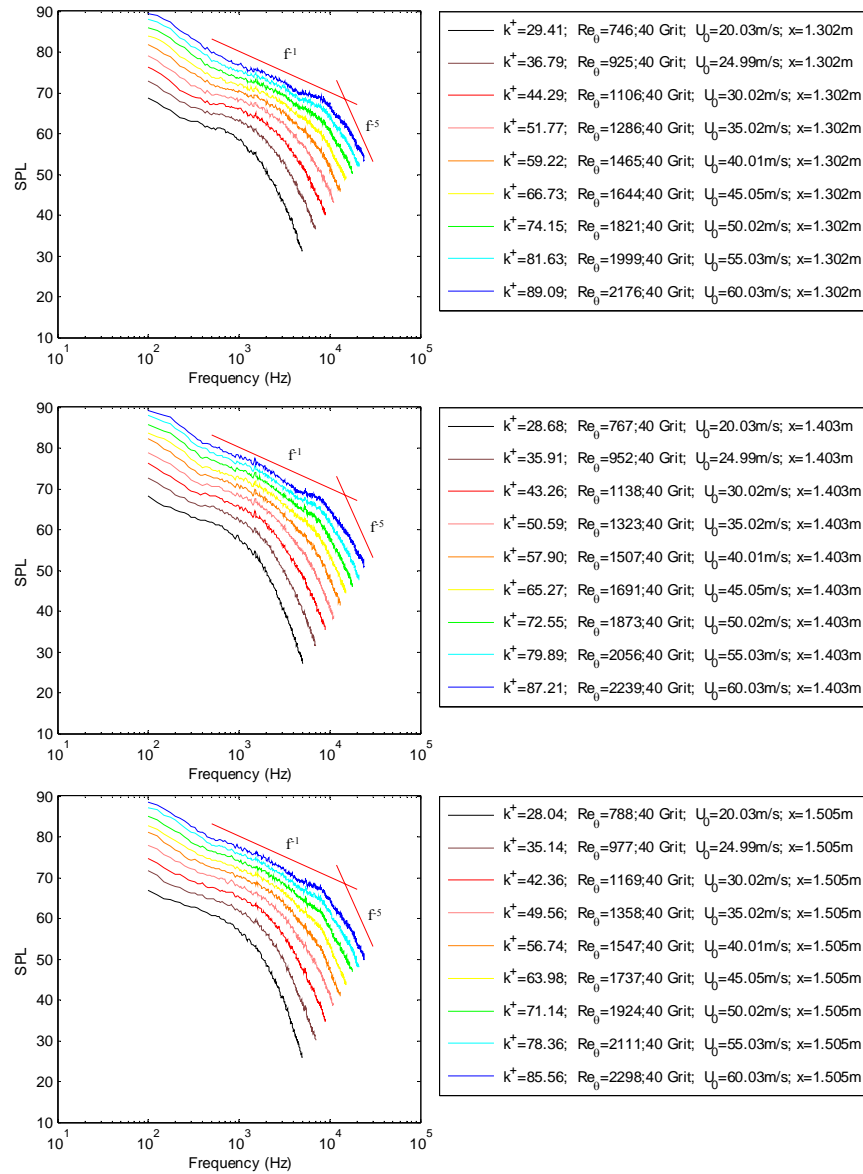


Figure 4.28 Dimensional surface pressure spectra at $x = 1302, 1403, \text{ and } 1505 \text{ mm}$ (top to bottom, respectively)

The surface pressure spectra from the 40 grit tests were scaled on the same outer and inner variables discussed above for the smooth wall surface pressure spectra. The scaled spectra shown in Figure 4.29 through Figure 4.32 below were taken at the streamwise center of the roughness patch. In Figure 4.29 below, the 40 grit spectra are shown normalized on inner variables in the same way that Goody and Simpson (2000) normalized their conventional turbulent boundary layer spectra. The spectra shown were taken at $x = 1403\text{mm}$ aft of the nozzle exit and 146 mm aft of the leading edge of the roughness patch. The inner scaling scales the spectra well in the high frequency ranges as for the smooth wall surface pressure spectra. In the overlap region between nondimensional frequencies of 0.01 and 1 these inner scaling variables

do not scale the spectra as well (varying by as much as 3 dB) as the smooth wall surface pressure spectra scaled on inner variables, and there is a consistent spectral progression seen in this region indicating that the inner scaling variables are not entirely capable of scaling the overlap region when a rough flow surface is present. This observation would also indicate that the roughness affects the spectra in the overlap region (which corresponds to the low to mid frequency range) more than at the high frequency range. This seems a little counterintuitive at first because one might expect the presence of roughness to affect the high frequency spectral character most and that these effects would become less apparent as the frequency is reduced. However, it is important to note that the spectra shown below were taken for a single rough surface, and it will be shown below that as the surface roughness condition is changed, the smooth wall scalings shown below in Figure 4.29 and Figure 4.31 do not account for changes in surface condition.

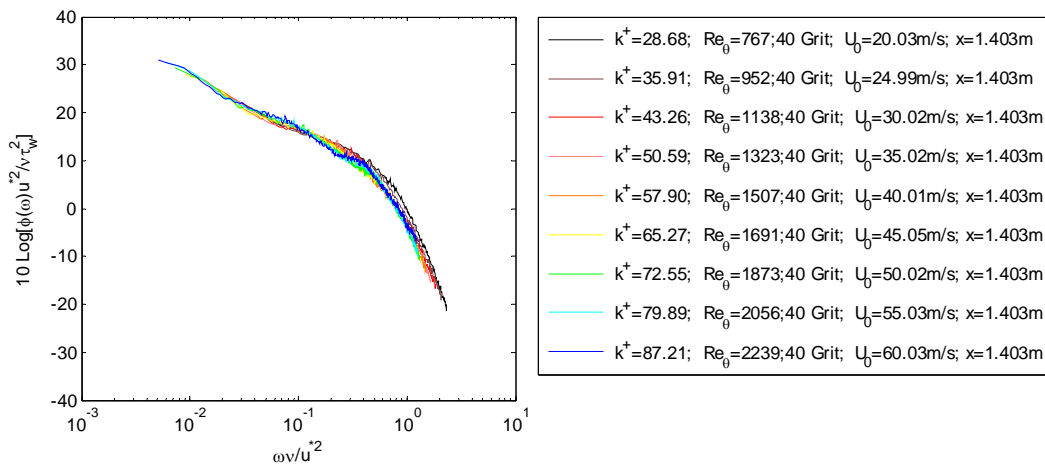


Figure 4.29 40 grit surface pressure spectra normalized on inner variables (v/u^* , u^* , and τ_w) at $x = 1403$ mm

The roughness size is constant for the spectra shown above, and would be desirable to see what the effects of a change in roughness might be for this scaling. In Figure 4.30 below, the 40 grit surface pressure spectra shown in Figure 4.29 and smooth wall surface pressure spectra taken at the same x location and initial flow conditions are shown together. The spectra for each surface condition shown cover a range of initial nozzle exit speeds from approximately 20 m/s to 60 m/s.

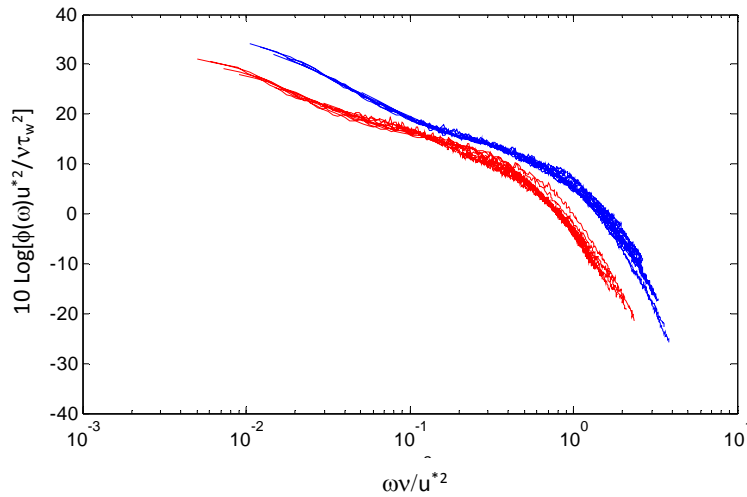


Figure 4.30 Smooth (blue) and 40 grit (red) surface pressure spectra normalized on inner variables ($\sqrt{u^*}$, u^* , and τ_w) taken at the same range of initial flow conditions and x microphone locations (1403 mm)

The difference in surface roughness has a definite impact on the surface pressure spectra especially at high frequencies. The inner variable scaling used for the smooth wall surface pressure spectra is not equipped to deal with the change in surface roughness as is evidenced by the spectral level and frequency shift.

The 40 grit surface pressure spectra were also normalized on outer variables in the same way that the smooth wall surface pressure spectra were normalized earlier in this chapter. In Figure 4.31 below, the 40 grit surface pressure spectra are taken over a range of initial nozzle exit speeds and are presented and normalized on outer variables in the same way as proposed by Goody (2004). These spectra were taken at $x = 1403$ mm aft of the nozzle exit and 146 mm aft of the rough patch leading edge.

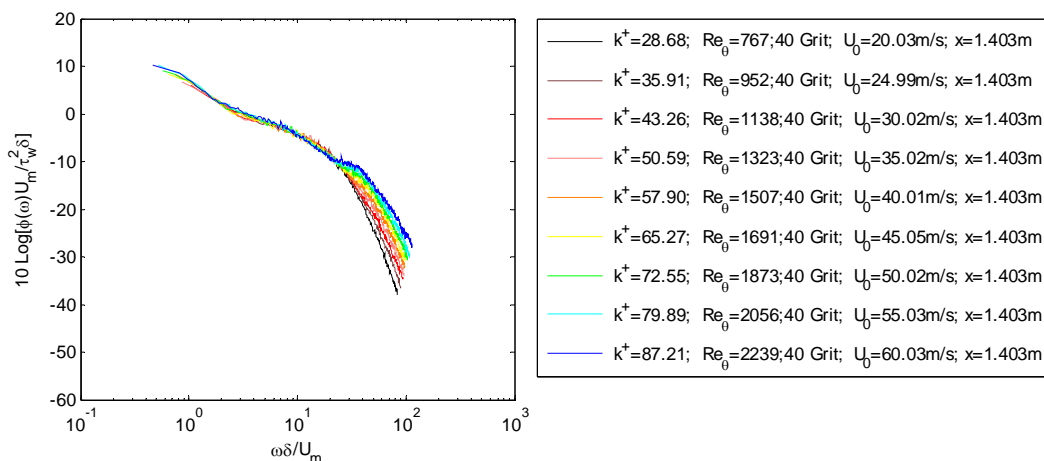


Figure 4.31 40 grit surface pressure spectra normalized on outer variables (δ , U_m , and τ_w) at $x = 1403$ mm

As in the case of the smooth wall data taken over a range of speeds, the normalization on outer variables scales the spectra well in the overlap region from nondimensional frequencies of about 2 to 20, but at higher frequencies, the spectra begin to fan out. The scaling on outer variables seems to scale the spectra in the overlap region marginally better than the inner variable scaling collapsing the spectra to within 2 dB from nondimensional frequencies of 11 to over 23. Also, the spectra shown here are of constant surface roughness.

The 40 grit spectra normalized on outer variables are compared with the normalized spectra for the smooth wall test cases taken at the same microphone locations and initial flow conditions. This comparison is shown in Figure 4.32 below.

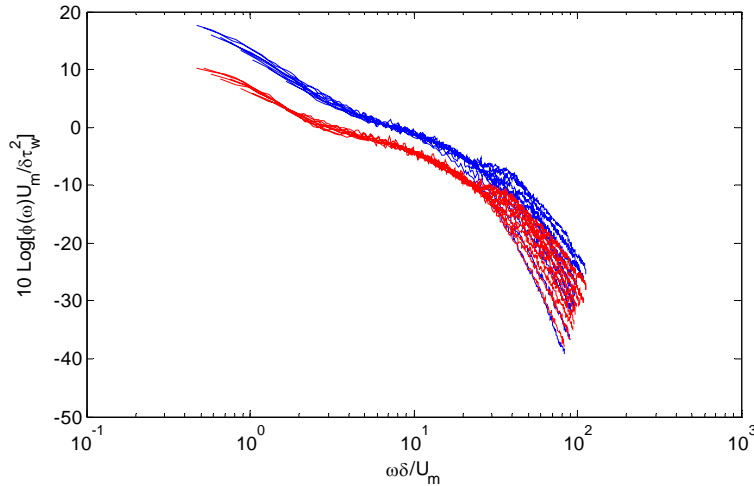


Figure 4.32 Smooth (blue) and 40 grit (red) surface pressure spectra normalized on outer variables (δ , U_m , and τ_w) taken at the same initial flow conditions and x microphone locations (1403 mm)

This outer scaling does not scale the overlap regions of the spectra well when a change in surface roughness is introduced. The difference in scaled spectral levels increases as the frequency is reduced in the overlap region. The scaled spectra show a marked difference at high frequencies as well. As was seen for the inner scaling variables, the outer scaling variables shown in Figure 4.32 above fail to account for the change in roughness size compared in this figure.

It is clear from the investigation of the 40 grit surface pressure spectra and from the comparison of these spectra with those of the smooth wall tests that the smooth wall normalizations on inner and outer variables do not account well for the presence of a rough surface. A scaling that deals with the change of the surface roughness and collapses the surface pressure spectra is desirable, and there have been a few attempts at scaling rough wall surface pressure spectra for ordinary turbulent boundary layers. Blake (1970) proposed the use of $\overline{k_g}$, u^* , and τ_w for the length, velocity, and pressure scales, respectively, where $\overline{k_g}$ is the mean roughness height. He showed some agreement at higher frequencies. The range of momentum thickness Reynolds numbers in the test cases of Blake (1970) was about 8000 to 28000. Even his lowest Reynolds number cases are at significantly higher momentum thickness Reynolds number than those of the current study. The roughness sizes used by Blake (1970) are also significantly higher than all but the largest of the rough surfaces used in this study. Blake (1970) uses roughnesses whose average height is 1.27 mm or larger (the roughness Reynolds numbers,

k^+ , ranged from 236 – 670). The largest of the roughness grain sizes of the current study are less than 1mm (the maximum k^+ value in the current study was seen to be roughly 155).

In Figure 4.33 below, the 40 grit surface pressure spectra shown in Figure 4.31 above are plotted normalized on the scaling variables proposed by Blake (1970) with the exception that the length scale used below is the r.m.s. roughness height, k_{rms} . These spectra were taken at the streamwise center of the patch. In the absence of the mean roughness height measurements, this length scale was chosen over the available nominal roughness heights because it is believed that this is a more accurate representation of the geometric character of the roughness than the nominal grain sizes that were determined from standardized tables. A list of the r.m.s. roughness heights for all rough surfaces used in the current study can be found in Chapter 2 above. The spectra below cover a range of initial nozzle exit velocities from approximately 20 m/s to 60 m/s.

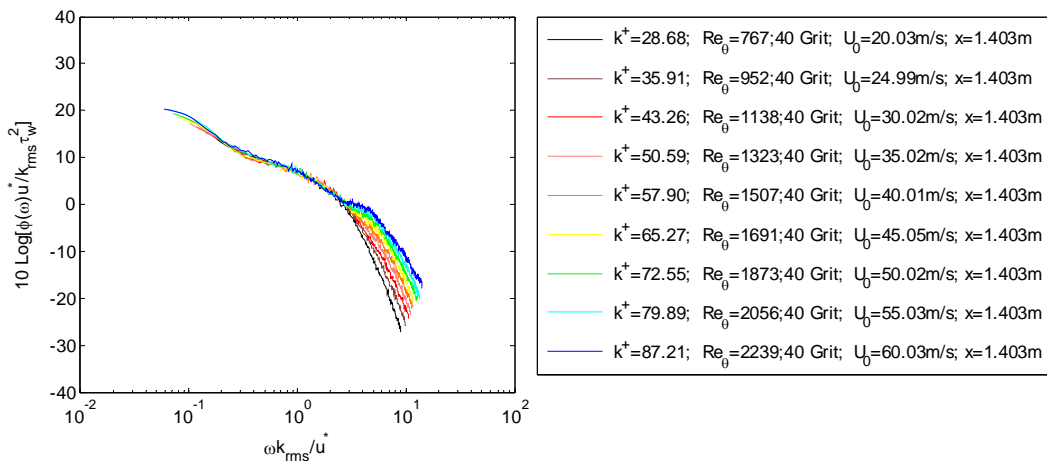


Figure 4.33 40 grit surface pressure scaled on $(k_{rms}, u^*$, and $\tau_w)$ as suggested by Blake (1970)

The normalized spectra shown above seem to be similar in character to those seen in Figure 4.31 above. The scaling variables proposed by Blake (1970) seem to scale the overlap region well. However, at high frequencies, the scaling variables do not collapse the spectra, and the spectra show a clear variation with speed. Blake (1970) shows some variation at high frequencies between his scaled rough wall surface pressure spectra, but not to the extent that is seen above. It is possible that the differences seen from the figure above to those presented by Blake (1970) are due to the fact that the flow of the current study is a wall jet. However, the qualitative agreement in the spectral character of the wall jet flow and that of Goody and Simpson (2000) and Goody (2004) at higher frequencies would suggest that this is not the case. Another possible reason for the lack of agreement between the current study and that of Blake (1970) might be the fact that the test cases used in the Blake (1970) study were in the fully rough regime while those of the current study range from transitionally rough to fully rough. The spectra seen above show tighter agreement as k^+ approaches and surpasses the fully rough threshold of 70.

Another attempt at scaling rough wall surface pressure spectra was proposed by Aupperle and Lambert (1970). They proposed using the scaling variables k_s , u^* , and τ_w where k_s is the equivalent sand grain height as defined by Nikuradse (1950). They also proposed dividing the spectral level by the skin friction. The test cases of Aupperle and Lambert (1970) were well into the fully rough regime as well. The actual roughness grain sizes used in their study were between 5 and 36 mm (corresponding to k^+ ranging from 500 – 3300). The spectra that were

presented by Aupperle and Lambert (1970) were taken at a constant free stream velocity, but the roughness size was varied substantially. The scaled surface pressure spectra of Aupperle and Lambert (1970) collapse well in the overlap region. In the high frequency portions of their presented normalized spectra the spread in the spectra is about 3 – 5 dB.

The spectra shown in Figure 4.31 above are normalized on the scaling variables proposed by Aupperle and Lambert (1970) and presented below in Figure 4.34. The spectra were taken at the streamwise center of the roughness patch. Again, the proposed normalizations scale the overlap region, but in the higher frequency regions the spectra diverge. The spectral scaling proposed by Aupperle and Lambert (1970) really is not much different in form than that proposed by Blake (1970), so it is really not a surprise that the results of this applied scaling is essentially the same as that seen above in Figure 4.33. Also, the same possible reasons for the lack of agreement in the scaled spectra behavior of the current study and that of Blake (1970) are applicable to the comparison of the current study and that of Aupperle and Lambert (1970).

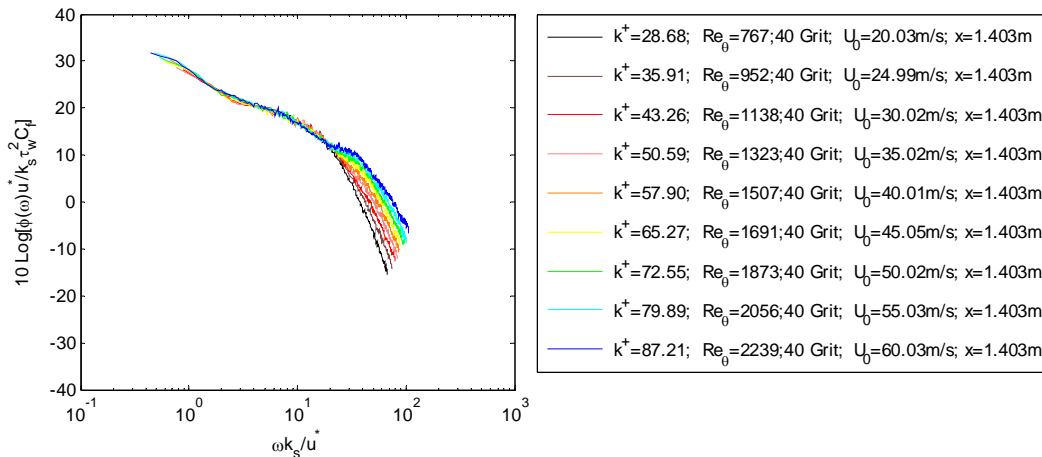


Figure 4.34 40 grit surface pressure spectra scaled on $(k_s, u^*, \text{ and } \tau_w)$ and divided by the skin friction coefficient, C_f , as suggested by Aupperle and Lambert (1970)

The spectra from the other microphone measurement locations were analyzed in the same way and the spectral behavior associated with these microphone locations is consistent with what has been presented above, and presenting these data would not add anything new to the discussion presented above.

The dimensional surface pressure spectra for a wall jet flow over a 40 grit roughness patch with initial nozzle exit flow velocity of approximately 60 m/s are shown in Figure 4.35 below for microphone measurement locations along the roughness patch. The spectra fall into a tight band at low to mid frequencies, and at frequencies higher than 3 kHz there is a definite spectral level progression downward with downstream distance. There is a general decrease in spectral level as the microphone position is moved aft.

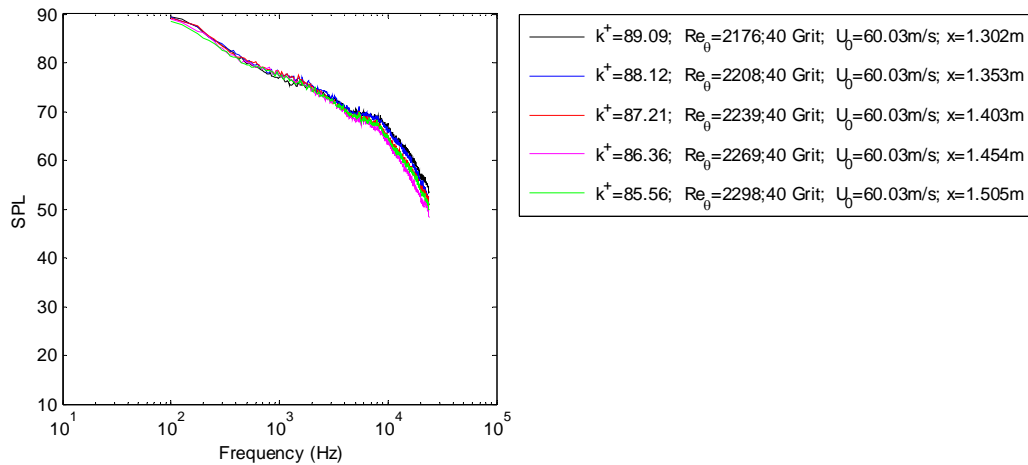


Figure 4.35 40 grit surface pressure spectra at constant initial flow conditions and varying microphone location

At high frequencies the spectra occupy a band that is 4.5 – 5 dB wide. In the mid frequency range, the spectra occupy a band that is no more than 2 dB wide. Great care was taken to position the measurement microphones in a consistent way for the rough wall surface pressure measurement. However, as indicated above in the discussion regarding microphone installation, there is some uncertainty in the measured spectra due to the microphone placement, and it is estimated that this uncertainty is on the order of ± 1 dB for rough wall measurements. The surface pressure spectra that are seen in Figure 4.35 fall within this uncertainty range at the mid frequencies. It is thought that perhaps the increased spread at high frequencies is due to the leading edge of the roughness patch, and that by the time the middle microphone position is reached, the flow near the wall associated with the small high frequency turbulent motions has reached some sort of equilibrium.

If the smooth wall inner and outer scalings for conventional turbulent boundary layers given above are applied to these spectra, the high frequency region is collapsed to within 3 dB. This can be seen in Figure 4.36 below. The spectra in the overlap region are not collapsed and even show some small spread in levels. However, this spread is due mostly to the difference between the measured surface pressure at microphone location 1 ($x = 1302$ mm) and the rest of the measurement spectra. One possible explanation for this is that the wall jet flow is still experiencing the effects of the leading edge of the roughness patch and the surface pressure spectrum at this foremost measurement location is affected.

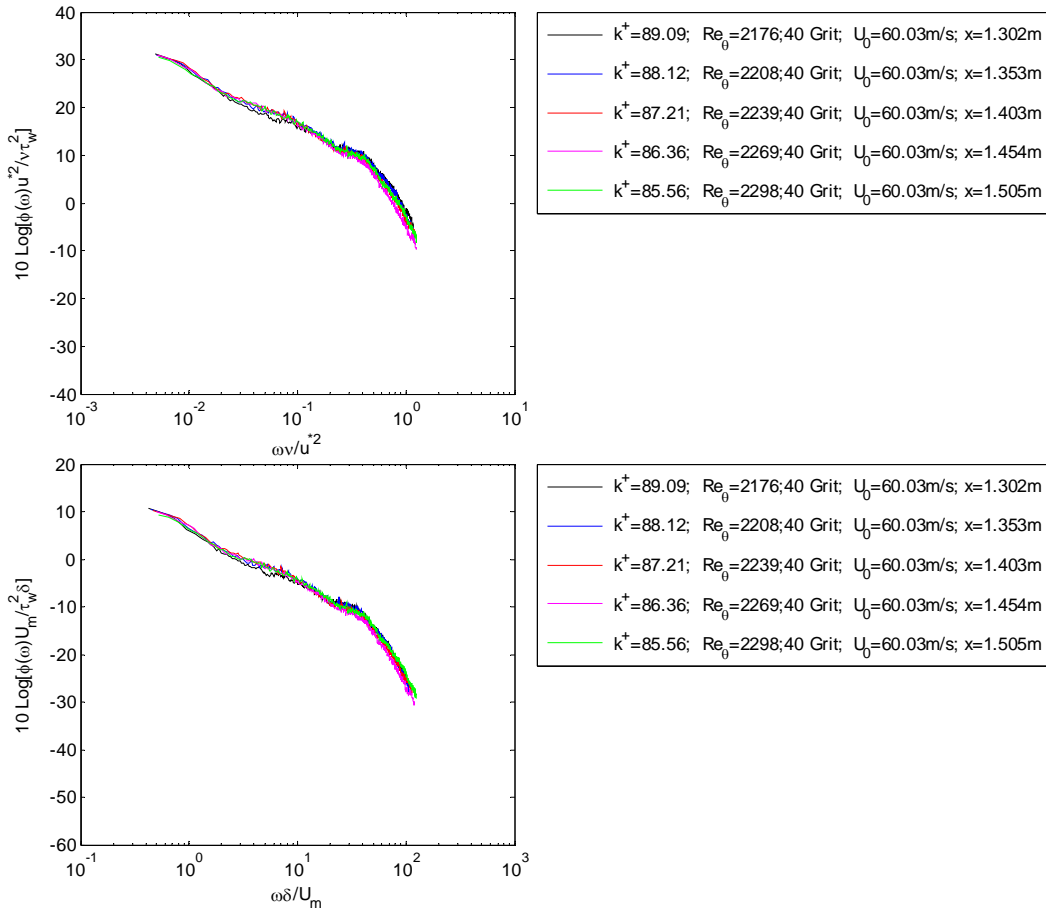


Figure 4.36 40 grit surface pressure spectra at constant initial flow conditions and varying microphone location scaled on inner (ν/u^* , u^* , and τ_w) and outer (δ , U_m , and τ_w) variables (top and bottom, respectively)

When these spectra are scaled as suggested by Blake (1970) and Aupperle and Lambert (1970) the spectra collapse at high frequencies (Figure 4.37), but not as well as when the smooth wall scalings seen above were used as seen in Figure 4.36 above. Again, the spectrum from the foremost measurement microphone is showing slight disagreement with the other measured spectra in the overlap region, and as before, it is believed that this may be due to the proximity of this microphone to the leading edge of the roughness patch.

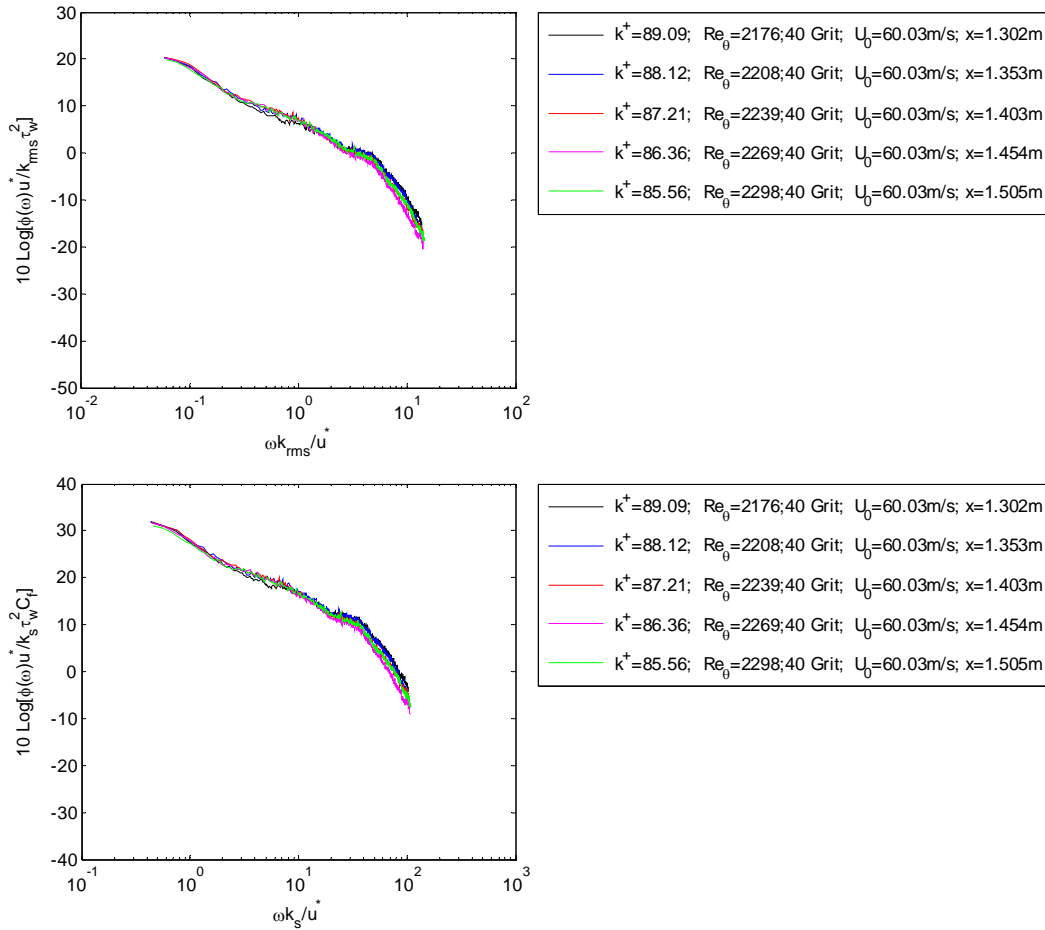


Figure 4.37 40 grit surface pressure spectra at constant initial flow conditions and varying microphone location scaled on roughness variables (k_{rms} , u^* , and τ_w) and (k_s , u^* , and τ_w) variables proposed by Blake (1970) and Aupperle and Lambert (1970) (top and bottom, respectively)

The surface pressure spectra presented above showing the effects of downstream distance were shown for a nozzle exit speed of approximately 60 m/s. Other nozzle exit speeds were examined and are shown in Figure 4.38 below. The spectra show a consistent progression with downstream distance like the spectra taken for a nozzle exit speed of 60 m/s showed. If the scaling attempts shown in Figure 4.36 and Figure 4.37 above are applied to the spectra shown in Figure 4.38 below, similar results are seen as for the $U_o = 60$ m/s cases. The scaled spectra collapse in the high frequency region, and the scaled spectra do not show any reduction in the spread of the data in the overlap region.

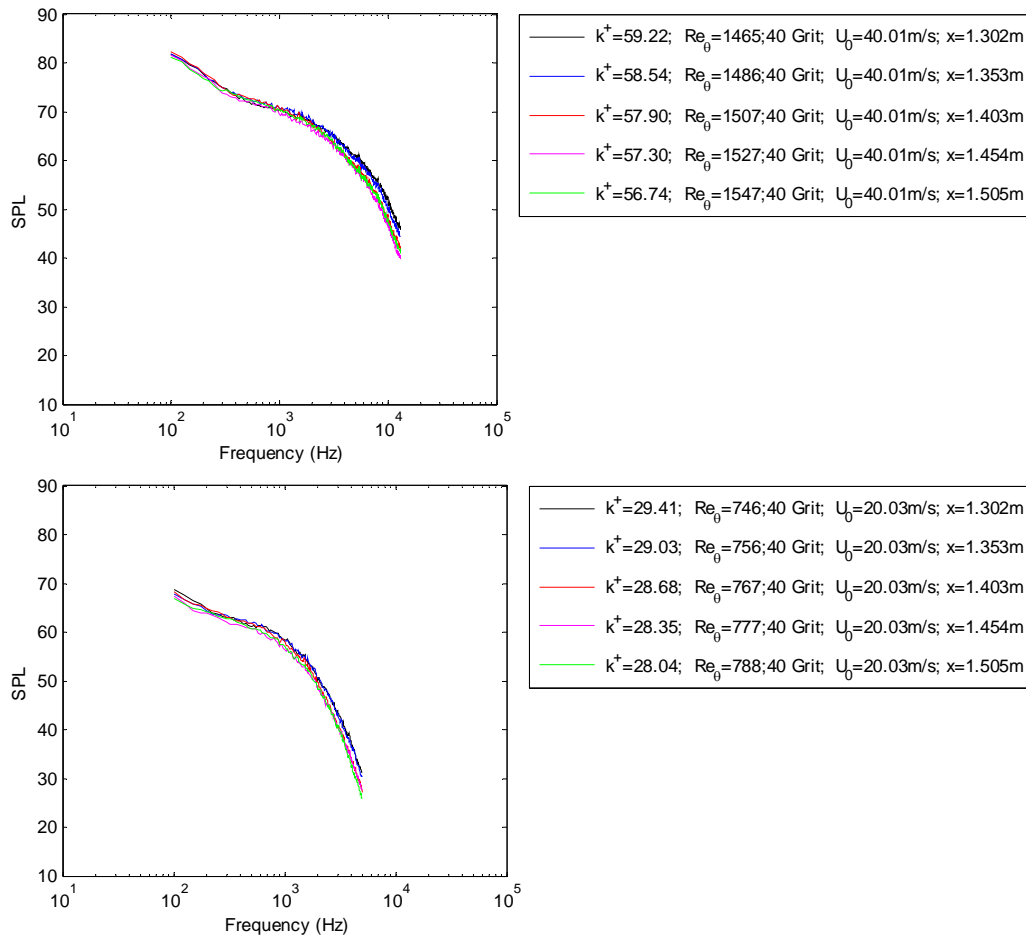


Figure 4.38 40 grit surface pressure spectra at constant initial flow conditions and varying microphone location

4.3.2 180 Grit Surface Pressure Measurements

Surface pressure measurements were taken for the current wall jet flow over a 305 mm patch of 180 grit roughness. These surface pressure measurements were taken for the same range of initial flow conditions as the smooth wall and 40 grit test cases, and the microphone measurement locations were consistent between all three of these surface conditions. In Figure 4.39 below, the dimensional spectra are shown over a range of nozzle exit speeds from approximately 20 m/s to 60 m/s (encompassing test conditions A – C described in Chapter 3 above). Each plot shows the spectra taken at a different microphone location. As for the 40 grit dimensional spectra shown in Figure 4.28 the microphone measurement locations are at $x = 1302, 1403, \text{ and } 1505 \text{ mm}$. In the mid frequency regions the spectra show a nearly f^1 variation followed by a roll off at higher frequencies that approaches a f^5 variation. The surface pressure spectra variation with the downstream distance will be presented below.

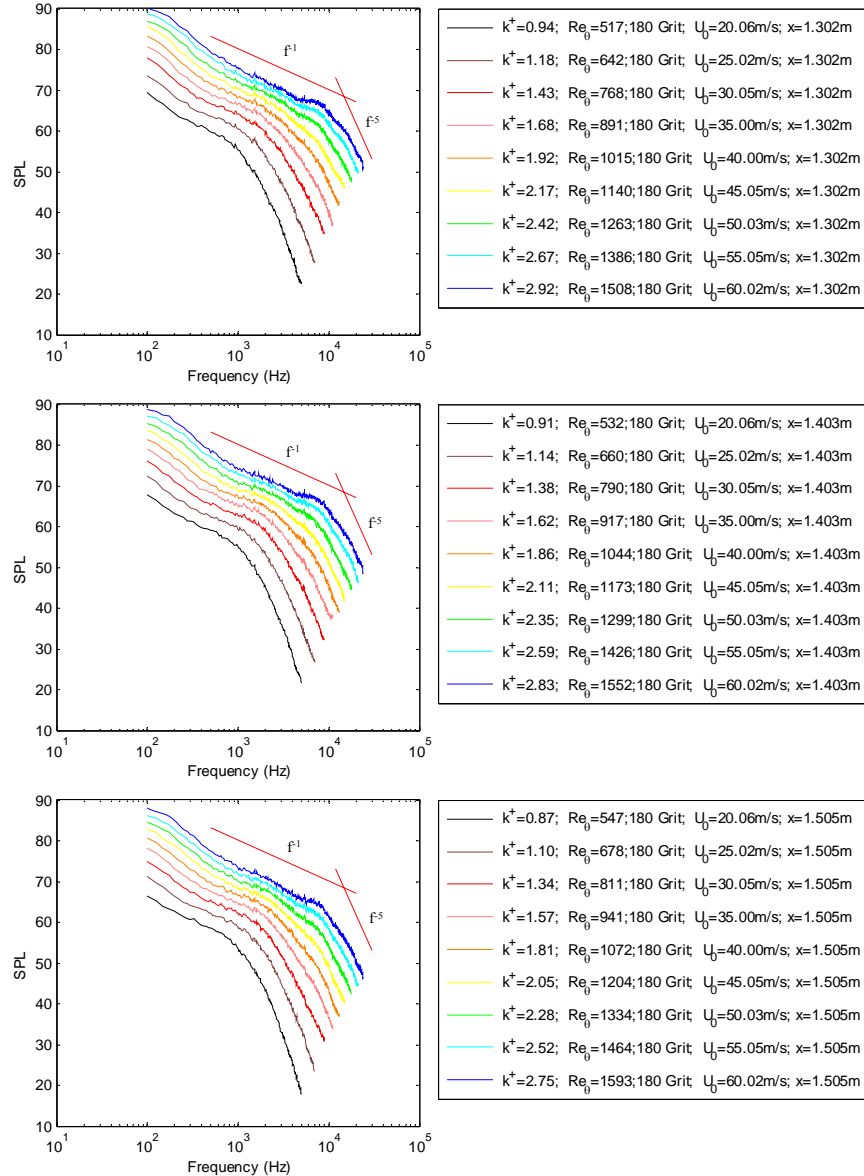


Figure 4.39 Dimensional surface pressure spectra at $x = 1302, 1403, \text{ and } 1505$ mm (top to bottom, respectively)

The surface pressure spectra from the 180 grit tests were scaled on the same outer and inner variables discussed above for the smooth wall and 40 grit surface pressure spectra. In Figure 4.40 below, the 180 grit spectra taken at $x = 1403$ mm (streamwise center of the roughness patch) are shown normalized on inner variables in the same way that Goody and Simpson (2000) normalized their spectra. The spectra shown were taken at $x = 1403$ mm aft of the nozzle exit and 146 mm aft of the leading edge of the roughness patch. The inner scaling again scales the spectra in the overlap and high frequency ranges as was the case for the smooth wall and 40 grit test cases.

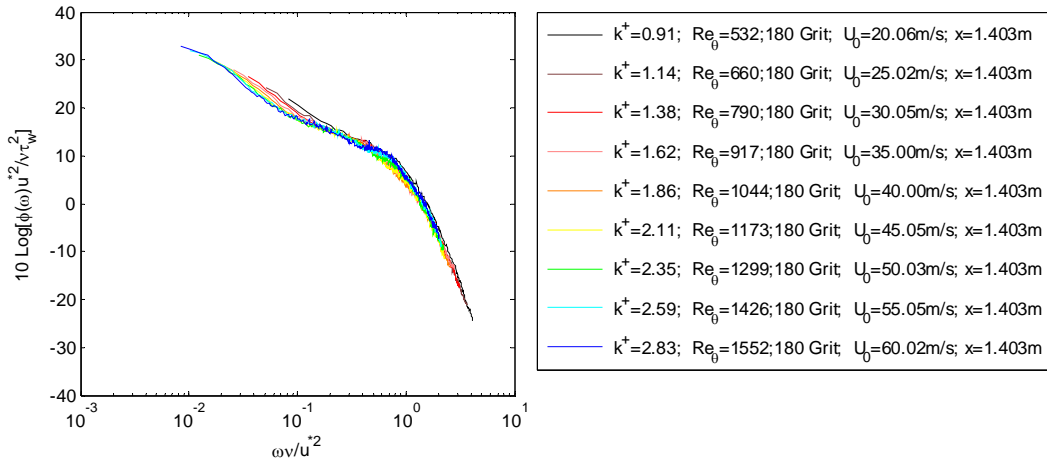


Figure 4.40 180 grit surface pressure spectra normalized on inner variables (v/u^* , u^* , and τ_w) at $x = 1403$ mm

The 180 grit surface pressure spectra seen Figure 4.40 above are plotted with the smooth wall surface pressure spectra taken at the same measurement location and at the same initial flow conditions in Figure 4.41 below. The 180 grit scaled spectra fall nearly exactly on top of the smooth wall spectra as expected. This figure would indicate that the surface pressure spectra that are being measured for the rough wall test cases are behaving in a way that is consistent with what is expected as the 180 grit test cases have k^+ values that indicate hydrodynamically smooth flow and should be nearly identical to those of the smooth wall.

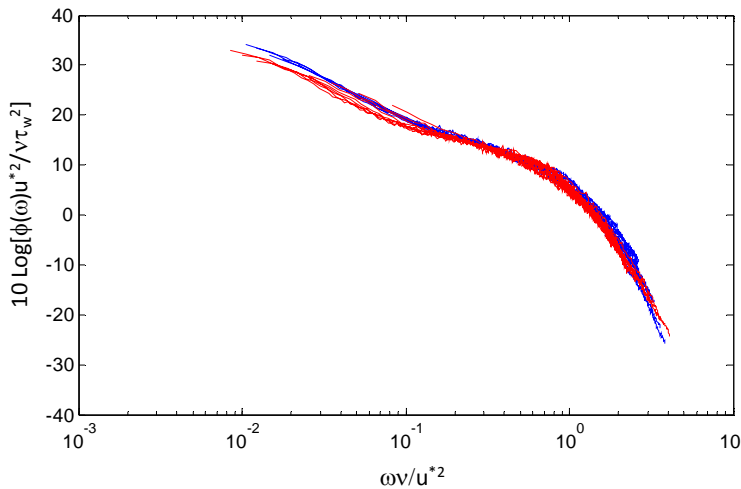


Figure 4.41 Smooth (blue) and 180 grit (red) surface pressure spectra normalized on inner variables (v/u^* , u^* , and τ_w) taken at the same initial flow conditions and x microphone locations (1403mm)

The 180 grit surface pressure spectra were also normalized on outer variables in the same way that the smooth wall and 40 grit surface pressure spectra were normalized earlier in this chapter. In Figure 4.42 below, the 180 grit surface pressure spectra taken over a range of initial nozzle

exit speeds are presented and normalized on outer variables in the same way as proposed by Goody (2004). These spectra were taken at $x = 1403$ mm aft of the nozzle exit and 146 mm aft of the rough patch leading edge.

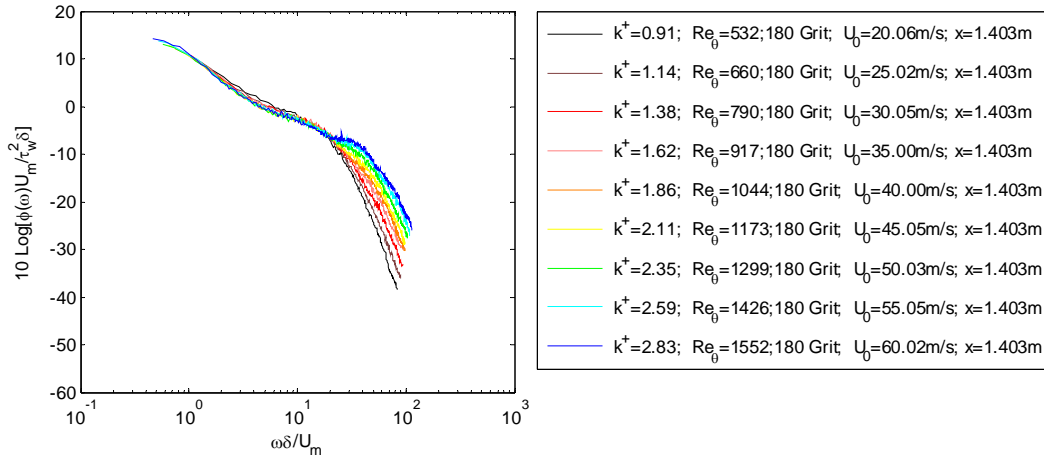


Figure 4.42 180 grit surface pressure spectra normalized on outer variables (δU_m , and τ_w) at $x = 1403$ mm

As with the smooth wall and 40 grit scaling attempts, the outer variables used in the figure above scale the spectra well in the overlap region, but do not scale the high frequencies well. The surface roughness condition has been held constant for the spectra shown in Figure 4.42 above. The surface pressure spectra for the 180 grit test cases are plotted with the surface pressure spectra from the smooth wall test cases normalized on outer variables in Figure 4.43 below. The spectra for the 180 grit test cases scaled on the outer variables shown agree more closely with the smooth wall scaled spectra than was the case for the 40 grit scaled spectra seen in Figure 4.32. The scaled spectra agree very well at high frequencies, although closer agreement was expected in the overlap region and low frequency region. After all, the 180 grit test cases were determined to have k^+ values that would indicate a hydrodynamically smooth flow for conventional turbulent boundary layers. The lack of agreement in the overlap region could also be due to microphone installation uncertainties. A study of the effects of the microphone height was conducted above and it indicated that as long as the microphone is placed between the tops and the bottoms of the roughness elements, the measured spectra are not greatly affected by small changes in microphone height. However, this test was conducted using a 40 grit roughness patch which was one of the largest of the roughnesses examined in this study. As the grain size becomes smaller and smaller, the microphone placement becomes more important because small changes in microphone position are not necessarily small when compared to a small grain size.

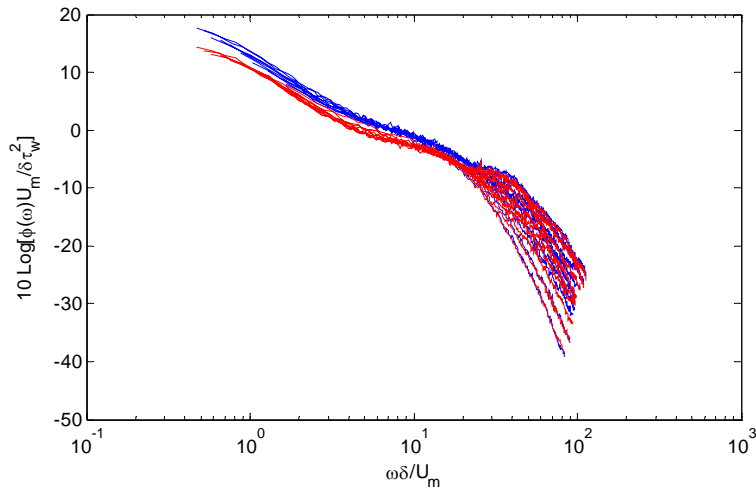


Figure 4.43 Smooth (blue) and 180 grit (red) surface pressure spectra normalized on outer variables (δ , U_m , and τ_w) taken at the same initial flow conditions and x microphone locations (1403 mm)

Again, the inability of the smooth wall inner and outer scaling variables to scale the surface pressure spectra as the surface roughness is changed is seen. Even though the smooth and rough wall pressure spectra in Figure 4.41 and Figure 4.43 above are very close, they are different and this difference is believed to be due to the change in surface roughness.

The proposed scaling of Blake (1970) and Aupperle and Lambert (1970) were also applied to the 180 grit spectra, and are shown in Figure 4.44 and Figure 4.45 below. The spectra shown in these figures were taken at the streamwise center of the roughness patch over a range of initial flow conditions that encompass test conditions A – C described in Chapter 3 above. Again, these normalizations appear to scale the overlap region well, but the rough surface condition is held constant for the test cases shown in the Figure 4.44 and Figure 4.45 so it is not readily apparent how well these scaling attempts do at scaling even the overlap regions when the surface roughness condition is altered. This will be investigated further below. These scaling attempts do not scale the high frequency regions well.

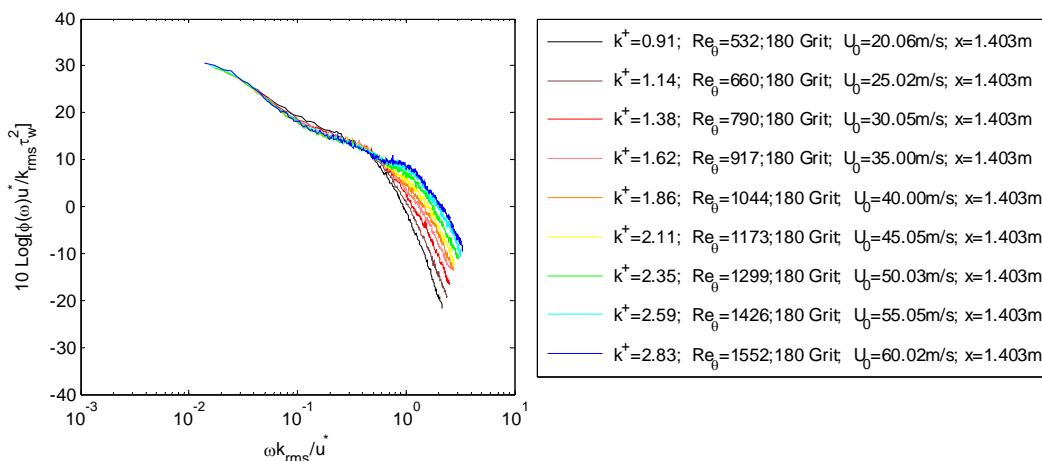


Figure 4.44 180 grit surface pressure scaled on (k_{rms} , u^* , and τ_w) as suggested by Blake (1970)

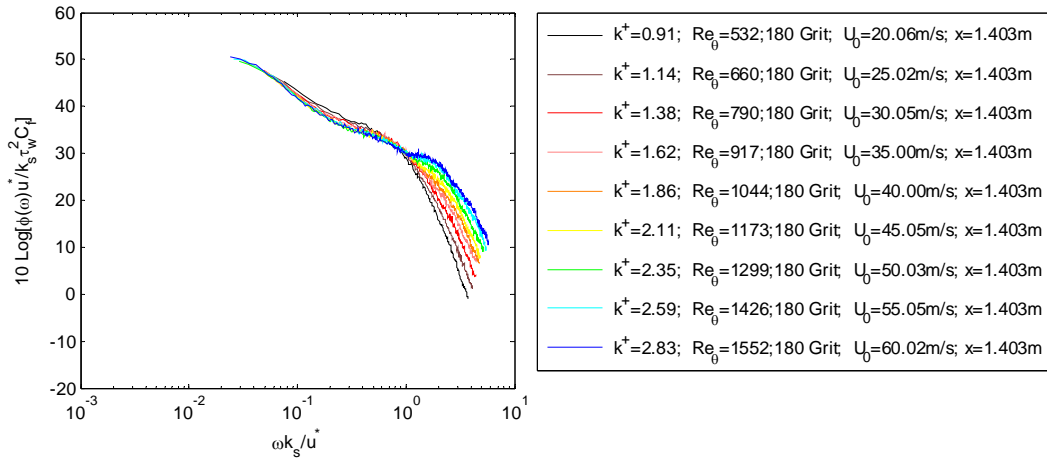


Figure 4.45 180 grit surface pressure spectra scaled on $(k_s, u^*, \text{ and } \tau_w)$ and divided by the skin friction coefficient, C_f , as suggested by Aupperle and Lambert (1970)

For the 180 grit test cases shown above, the initial flow conditions were varied while the microphone location was held constant. The surface pressure measurements for the other microphone measurement positions over the range of speeds shown above were analyzed and show behavior consistent with that seen above. In the test cases presented in Figure 4.46, Figure 4.47 and Figure 4.48 below, the microphone position is varied while the initial flow conditions are held constant. This is done in the same way as for the 40 grit test cases in Figure 4.35, Figure 4.36, and Figure 4.37. Again, the nozzle exit velocity is approximately 60 m/s for the 180 grit spectra shown below.

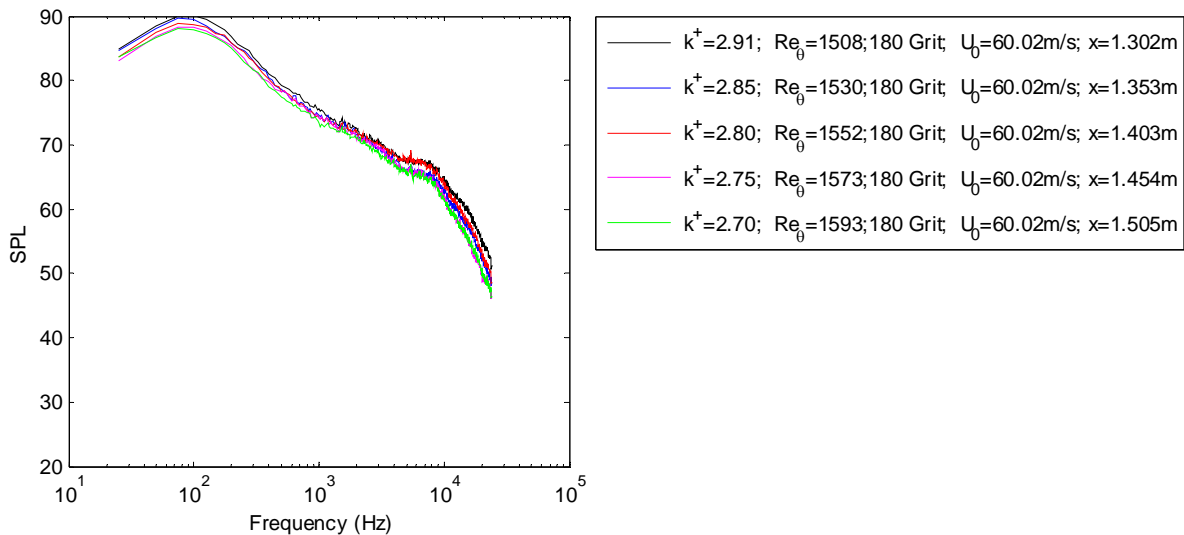


Figure 4.46 180 grit surface pressure spectra at constant initial flow conditions and varying microphone location

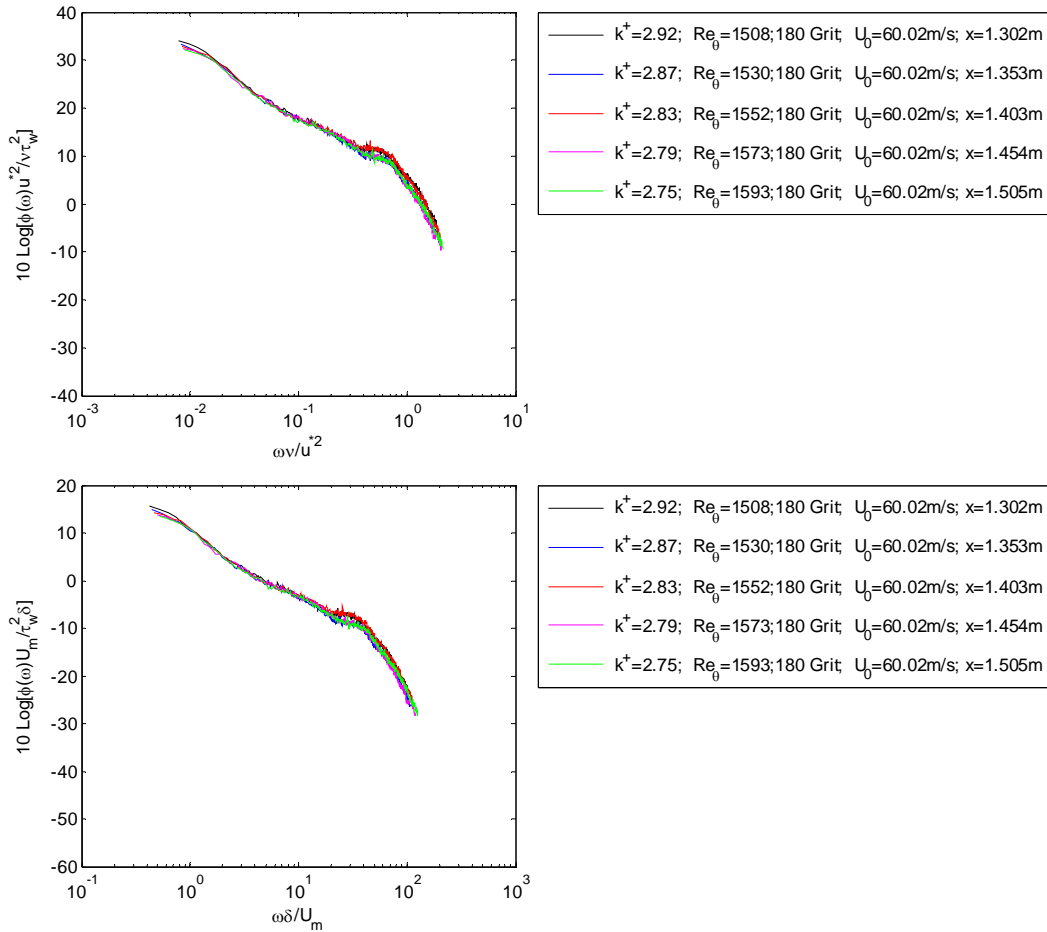


Figure 4.47 180 grit surface pressure spectra at constant initial flow conditions and varying microphone location scaled on inner (ν/u^* , u^* , and τ_w) and outer (δ , U_m , and τ_w) variables (top and bottom, respectively)

The dimensional spectra shown in Figure 4.46 above lie within a band that is 2.5 dB wide in the mid frequency range and between 5 and 6 dB wide at higher frequencies. A general progression is seen with downstream distance except that the spectrum from the third microphone measurement position ($x = 1403$ mm) shows levels that are higher than expected from about 3 kHz onward. This inconsistent behavior relative to the spectra measured at other microphone positions is believed to be due to uncertainties in the installation of the measurement microphones.

The spectra normalized as seen in Figure 4.47 above behave in much the same way as for the 40 grit test cases. The nondimensional spectra appear to be scaled well in the overlap regions and high frequency regions by the inner and outer scaling attempts. The spectra are collapsed in a band that is 2.5 dB wide at its widest point at around 2 – 3 kHz. Again, the surface conditions are held constant. The surface pressure spectra show little change with downstream distance because the local flow conditions do not appreciably change across the roughness patch of 203 mm.

The spectra scaled on roughness length scales seen in Figure 4.48 below behave in a similar way as those scaled the same way in Figure 4.37. The overlap and high frequency

regions appear to be well scaled, but this is due to the fact that the roughness condition is held constant, and the local flow conditions do not change enough to illustrate the inability of these scaling attempts scale the high frequency regions as the local flow conditions are significantly altered. This result is also seen in Figure 4.44 and Figure 4.45 above. The effects of changes in surface roughness on the surface pressure spectra and the inner, outer, and roughness scaling presented above will be investigated in more detail in section 4.3.3 below.

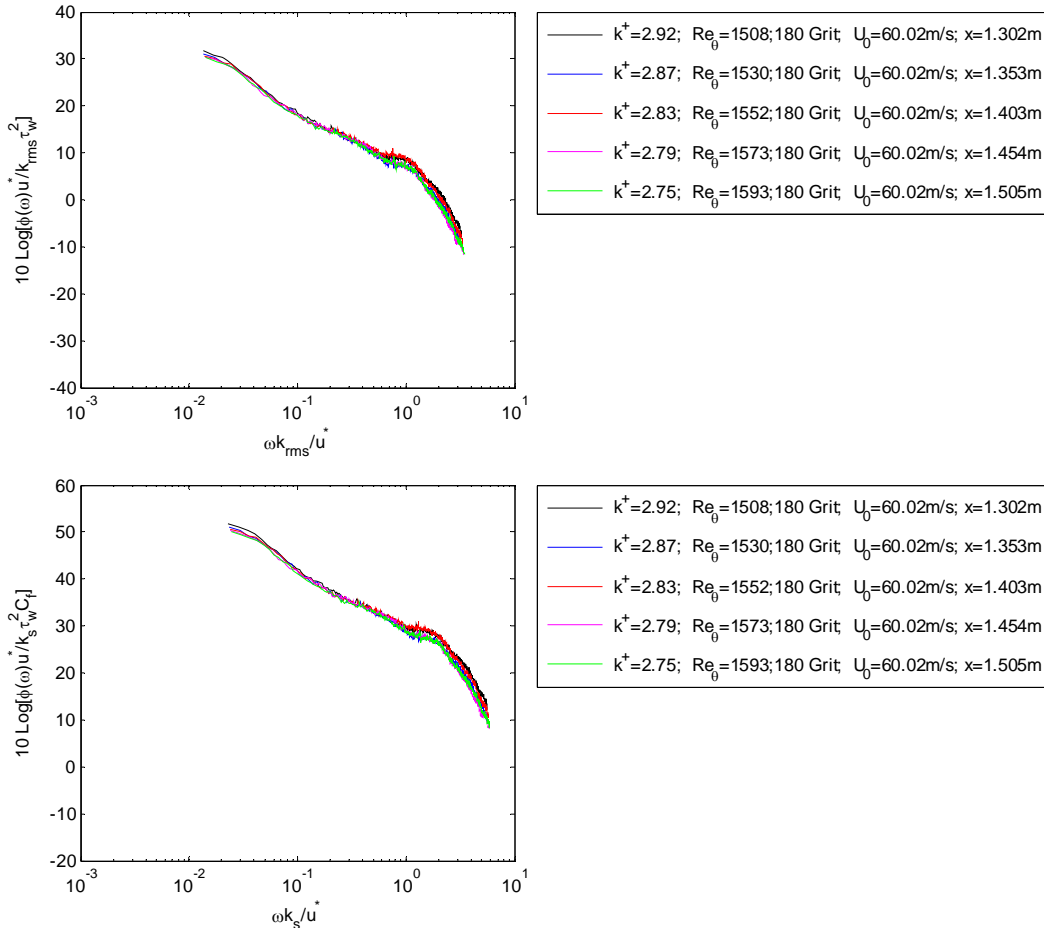


Figure 4.48 180 grit surface pressure spectra at constant initial flow conditions and varying microphone location scaled on roughness variables (k_{rms} , u^* , and τ_w) and (k_s , u^* , and τ_w) proposed by Blake (1970) and Aupperle and Lambert (1970) (top and bottom, respectively)

4.3.3 Surface Pressure Measurements for Varying Surface Roughness

In the results presented above, all surface pressure spectra were taken at constant roughness conditions while the initial flow conditions were varied. In the discussion below, the effects of varying roughness height on the spectral character will be investigated. The effectiveness of the inner and outer smooth wall turbulent boundary layer scalings will be investigated as well as the effectiveness of the Blake (1970) and Aupperle and Lambert (1970) scalings which were intended to deal with the effects of surface roughness on the surface pressure spectra.

In Figure 4.49 below, dimensional surface pressure spectra are presented for a constant nozzle height and exit velocity of 12.7 mm and 60 m/s respectively (test condition C noted above in Chapter 3). All spectra shown were taken at the streamwise center of the patch. The surface pressure spectra shown were taken for a range of rough surfaces that are described in detail in Chapter 2 above. The change in roughness has the most effect on the spectra in the frequency range between 200 Hz and 10000 Hz. There also seems to be an effect on the high frequency range of the spectra plotted below.

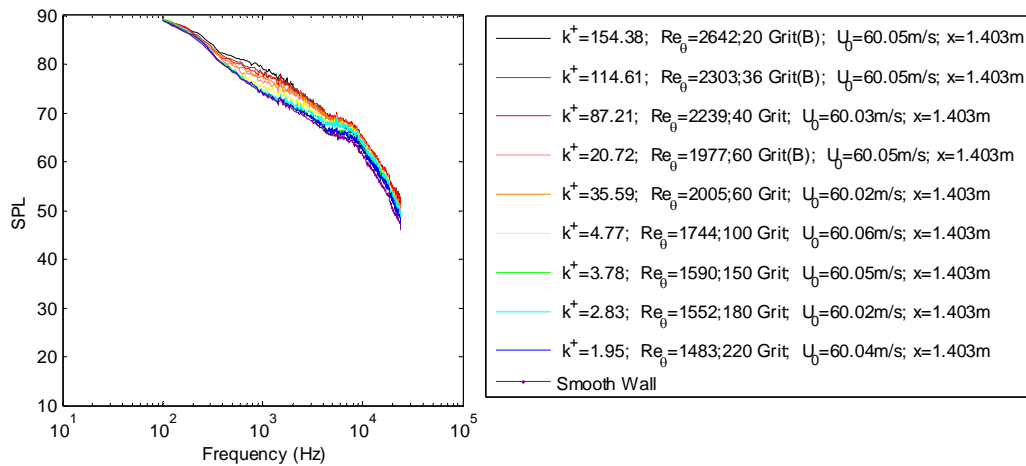


Figure 4.49 Surface pressure spectra for wall jet flow with constant initial flow conditions over rough patches 305 mm long of varying roughness heights

In Figure 4.50 below, the spectra in Figure 4.49 are viewed more closely. There is a consistent progression that can be seen as the grit size is increased with the exception of the spectra from the 180 grit test case. It was shown earlier that this particular microphone showed increased levels for the 180 grit test cases that are believed to be due to installation effects. Surface pressure spectra taken at different microphone locations for the 180 grit test cases that will be shown below are not inconsistent with the rest of the measured spectra for different roughnesses indicating that the microphone installation really is the cause of the 180 grit inconsistency seen in Figure 4.50 below. As the roughness size is increased, the spectral levels in the mid frequency region increase and shift to lower frequencies until the frequency reaches 300 – 400 Hz. At this point the spectra converge. It is believed that spectra in these frequencies are illustrating the flow effect discussed in section 3.2.2 above. The fact that the surface pressure spectra seem to be invariant with the change in roughness size indicates that the low frequency large turbulent motions associated with the mixing layer of the wall jet flow are not greatly affected by the presence of roughness and lie predominantly outside the region of flow affected by the roughness in the undisturbed flow region. In other words, at very low frequencies, the surface pressure spectra are dominated by the flow character upstream of the roughness patch.

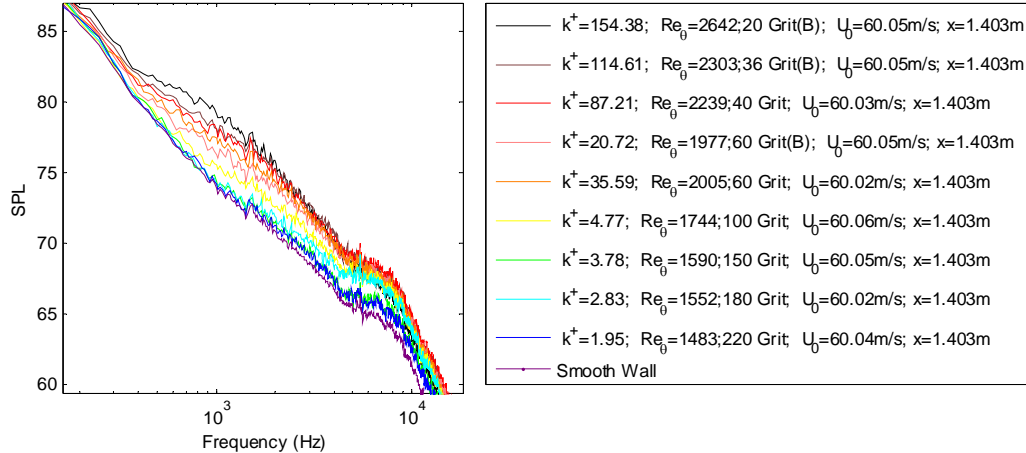


Figure 4.50 A closer look at the surface pressure spectra for wall jet flow with constant initial flow conditions over rough patches 305 mm long of varying roughness heights in the low to mid frequency range

At high frequencies, the variation becomes less consistent in its progression. The larger roughness sizes yield higher levels above 10 kHz in general, but the ordered progression seen in the mid frequency regions is not as apparent. The spectra in the high frequency region fall within a 3-4 dB band, but this is not necessarily unexpected. A non-monotonic variation in the spectral levels would be expected as the energy in the flow shifts to lower frequencies. What is more interesting is that while the high frequency spectral levels do vary with roughness size, it is the mid and low frequency regions that are most affected.

Surface pressure spectra measured at other microphone locations at the test conditions of the spectra in Figure 4.49 and Figure 4.50 above were analyzed, and surface pressure spectra from the foremost, mid, and aft most microphone measurement locations are presented in Figure 4.51 below. The spectral character at the mid and aft most measurement locations is quite similar, and both show variation between the spectra with changes in the surface roughness that is consistent, at least to within the uncertainty of the measurement due to the microphone installation. However, the spectra measured with the foremost microphone show a noticeable difference in spectral character. The high frequencies are more affected by the roughness height variations, and the spectral character in the mid frequency regions does not appear to be as highly impacted as that seen in the spectra from the microphone measurement locations further downstream. This would indicate that at the first microphone measurement location in the flow is still experiencing the effects of the leading edge of the roughness patch and/or the abrupt change in the surface roughness. Also, one would not expect to see mid to low frequencies affected very near the leading edge of the roughness patch because the region of the flow that is affected by the roughness has not had time to grow to a significant height off of the plate, and the large, low frequency turbulent structures away from the wall do not see the effects of the roughness patch close to the leading edge. However, by the time the flow reaches the microphone in the streamwise center of the roughness patch, the surface pressure seems to be fully developed or at least nearly so.

The effects of variation in surface roughness for rough wall surface pressure spectra taken at different initial flow conditions were also investigated. In Figure 4.52 below, the

surface pressure spectra taken at the microphone measurement position in the center of the roughness patches are shown for 20 and 40 m/s to illustrate the effects of changing the initial flow conditions in the spectra character of the surface pressure at varying roughness heights. There is a clear progression in the spectral character with roughness height in the mid frequency and high frequency regions. Any inconsistencies in the spectral level with the evident trends associated with varying roughness height are well within the uncertainty of the measurement due to errors in installation (± 1 dB).

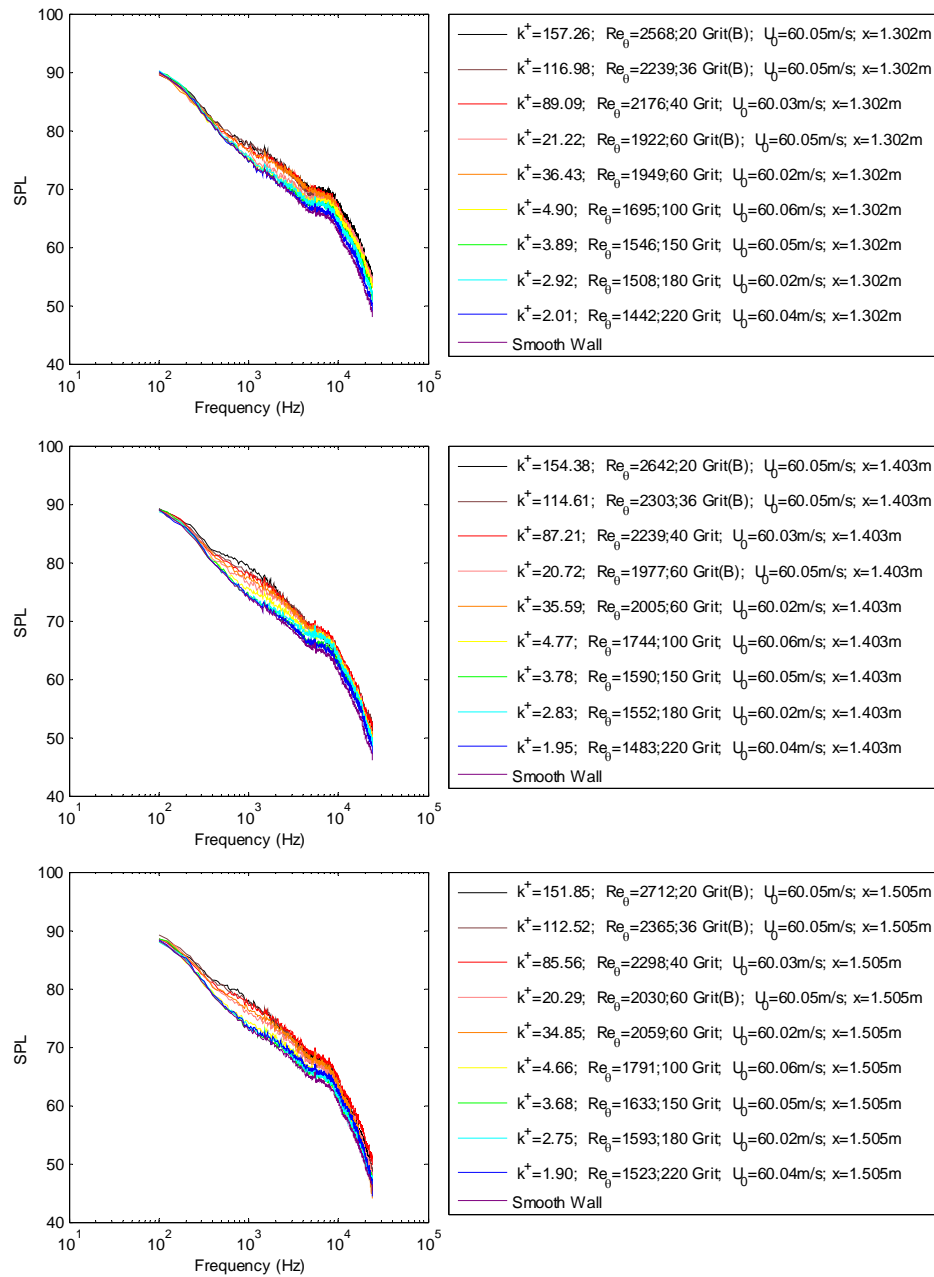


Figure 4.51 Surface pressure spectra for wall jet flow with constant initial flow conditions over rough patches 305 mm long of varying roughness heights at 3 streamwise microphone measurement locations.

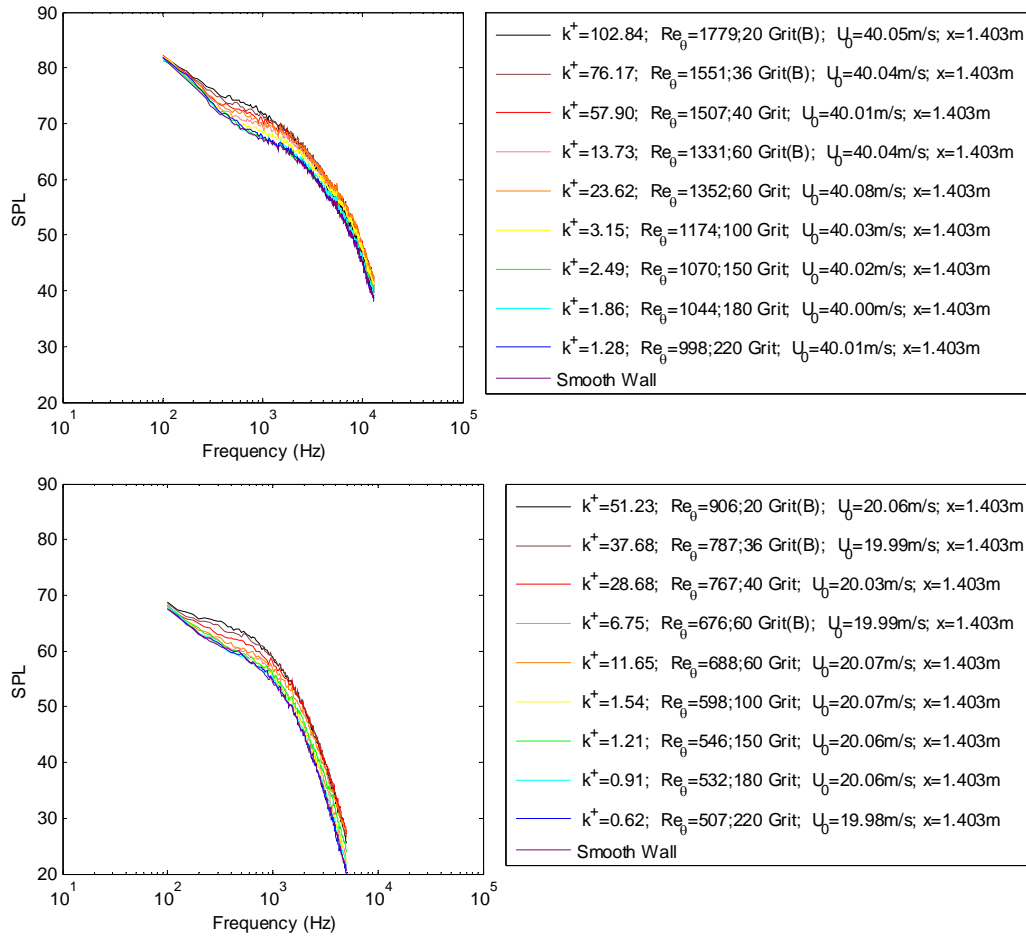


Figure 4.52 Surface pressure spectra for wall jet flow with varying nozzle exit velocity over rough patches of varying roughness heights at the center microphone measurement location ($x = 1403$ mm)

The outer scaling used by Goody (2004) was applied to the surface pressure seen above in Figure 4.50 in an attempt to show the effects of a change in roughness size on the ability of the proposed smooth wall turbulent boundary layer outer variables (δ , U_m , and τ_w) to scale rough wall jet surface pressure spectra. These results are shown in Figure 4.53 below.

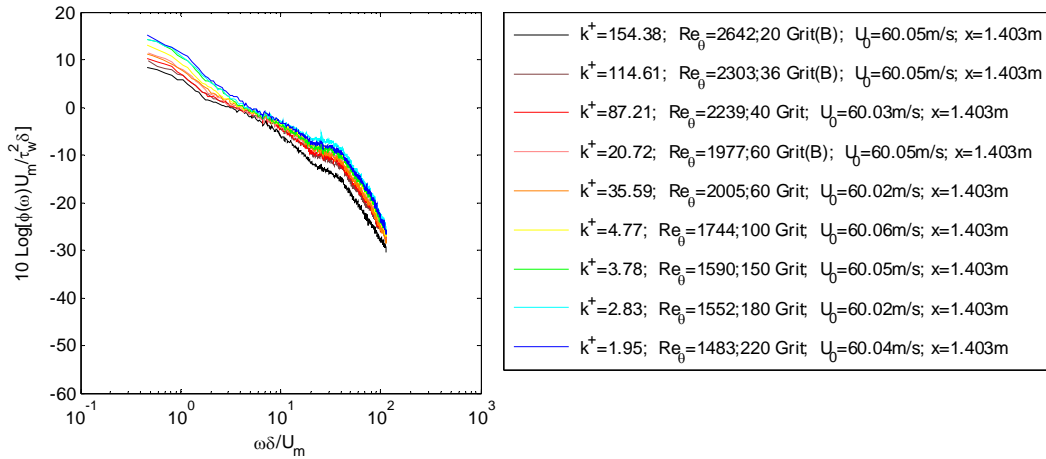


Figure 4.53 Surface pressure spectra of wall jet flows having constant initial flow conditions and varying rough surface sizes scaled on outer variables (δ , U_m , and τ_w)

The outer scaling collapses the surface pressure spectra in a localized nondimensional frequency of between 4 and 8 to within about 2 dB. However, at low and high frequencies, this outer scaling is incapable of accounting for changes in surface roughness as was indicated in Figure 4.32 above. It appears that the frequency is scaled well, but this should not be a surprise given that the variables used to scale the frequency were shown in chapter 1 above not to vary in any consistent way with the variation in roughness size. The spectral levels are not scaled well reflecting the increase in the wall shear due to the increase in roughness size.

The inner scaling used by Goody and Simpson (2000) for smooth wall turbulent boundary layers was applied to the rough wall jet surface pressure spectra shown above in Figure 4.49 in an attempt to show the effects of a change in roughness size on the ability of the proposed inner variables (ν/u^* , u^* , and τ_w) to scale rough wall jet surface pressure spectra in the high frequency spectral regions. These results are presented in Figure 4.54 below.

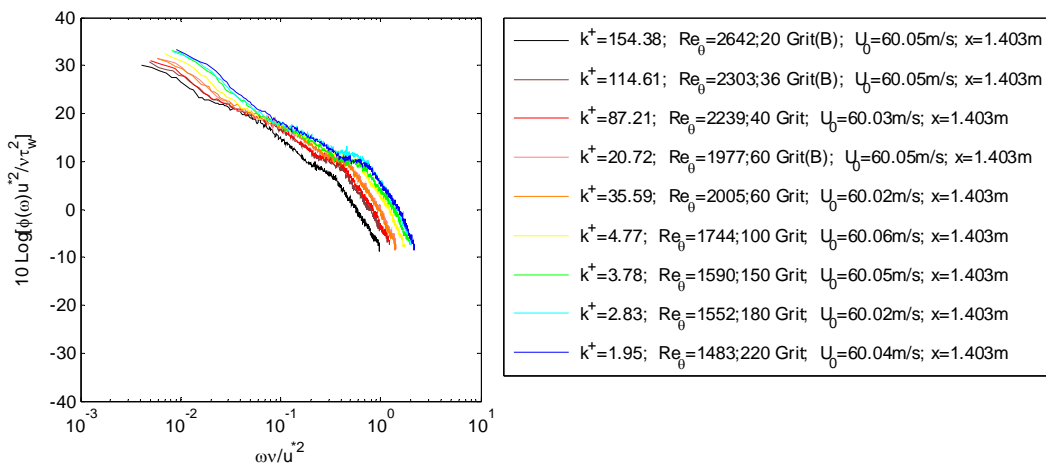


Figure 4.54 Surface pressure spectra of wall jet flows having constant initial flow conditions and varying rough surface sizes scaled on inner variables (ν/u^* , u^* , and τ_w)

The inner scaling used by Goody and Simpson (2000) to scale smooth wall surface pressure spectra in the high frequency region of smooth wall turbulent boundary layer flows does collapse the surface pressure spectra around a nondimensional frequency of 0.1 to within 3 dB, but the collapse in the rest of the overlap region and in the high frequency region is very poor. The inability of the smooth wall turbulent boundary layer spectral scalings to collapse the rough wall jet surface pressure should not be a surprise given the comparison of these scalings for the 40 grit rough wall jet flow and the clean plate flow given above in Figure 4.30 and Figure 4.32. Here, there appears to be a fair scaling in the spectral level, but the frequency is not scaled well reflecting the increase in the skin friction velocity with roughness size.

The idea that the roughness size must come into play as a scaling variable in some form or another has been implied by the spectral scaling attempts of Blake (1970) and Aupperle and Lambert (1970). Attempts to bring in a geometric roughness length scale have been presented for the 180 and 40 grit test cases where the initial conditions are varied and the roughness conditions are held constant. These scaling attempts using scaling variables suggested by Blake (1970) and Aupperle and Lambert (1970) and are shown below in Figure 4.55 and Figure 4.56 for cases where the roughness size is varied and the initial flow conditions are held constant. The nozzle exit speed for the spectra shown in these figures is approximately 60 m/s, and the nozzle height was 12.7 mm (test condition C discussed above in Chapter 3).

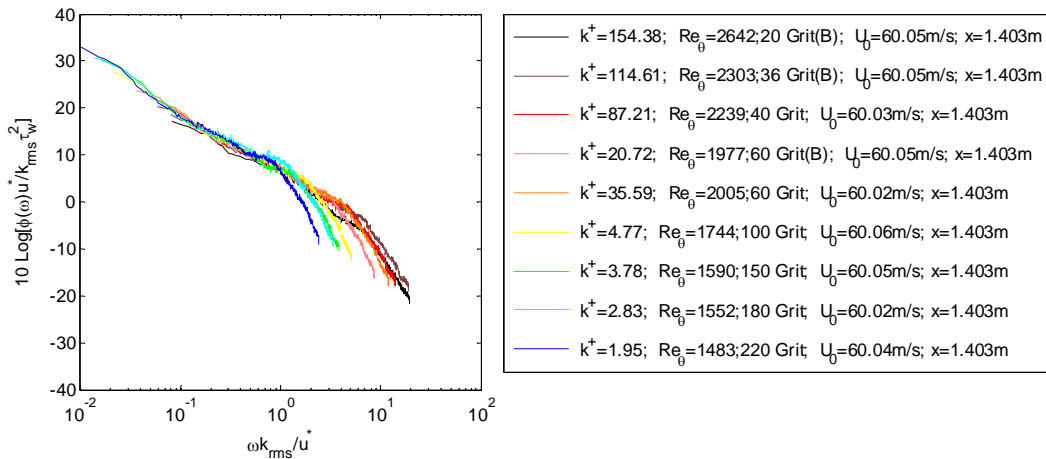


Figure 4.55 Surface pressure scaled on $(k_{rms}, u^*, \text{ and } \tau_w)$ as suggested by Blake (1970) for test cases with constant initial flow conditions and varying roughness size

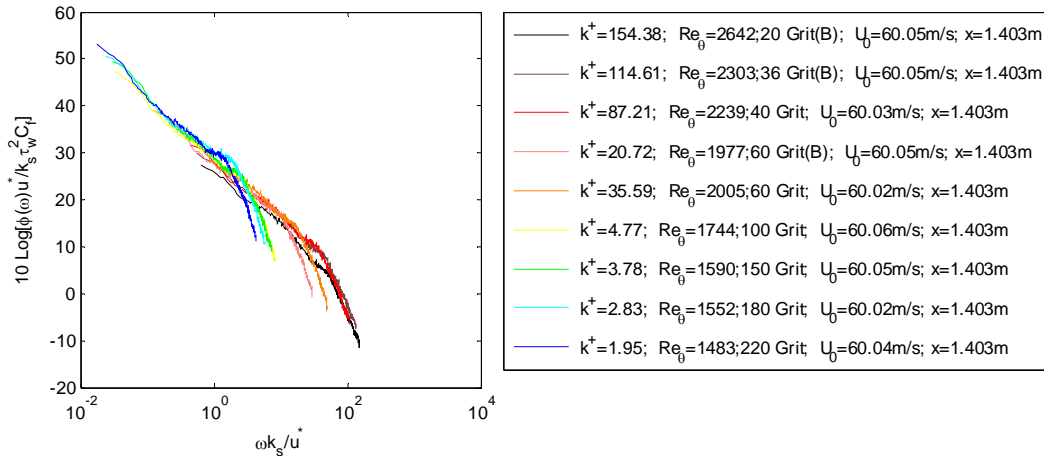


Figure 4.56 Surface pressure spectra scaled on $(k_s, u^*, \text{ and } \tau_w)$ and divided by the skin friction coefficient, C_f , as suggested by Aupperle and Lambert (1970) for test cases with constant initial flow conditions and varying roughness size

These scaling attempts do not scale the spectra in the high frequency region. This is not unexpected as the use of the scaling variables proposed by Blake (1970) and Aupperle and Lambert (1970) did not scale test cases where the roughness was held constant and the speed was varied as in Figure 4.44 or Figure 4.45 above. There is a definite progression in the behavior of the scaled spectra with the change in roughness size at high frequencies. The change in roughness size seems to spread out the scaled spectra across the nondimensional frequency range by shifting the surface pressure spectra with smaller roughness sizes towards lower frequencies and higher spectral levels. For the nondimensional spectra scaled on the variables proposed by Blake (1970) and those scaled on the variables proposed by Aupperle and Lambert (1970), the overlap regions seem to remain somewhat coincident in level but not in frequency. When the roughness size is held constant, the overlap regions scale in both level and frequency. It should also be noted that the scaled spectra for which the roughness Reynolds number indicates fully rough flow seem to approach one another. It is possible that the level of agreement seen in Blake (1970) and Aupperle and Lambert (1970) may be due to the fact that the flows tested were well into the fully rough regime. Indeed, this is hinted at by Aupperle and Lambert (1970) who note that, at least for fully rough flows, the surface pressure spectra scale as described in Figure 4.56 above.

The behavior of the surface pressure spectra scaled using the Blake (1970) and Aupperle and Lambert (1970) scaling variables at other nozzle exit speeds while the roughness size was varied was investigated by plotting the scaled surface pressure spectra taken at the roughness patch center microphone position at three nozzle exit velocities (20, 40, and 60 m/s) over the same range of roughness conditions. These spectra are shown in Figure 4.57 and Figure 4.58 below.

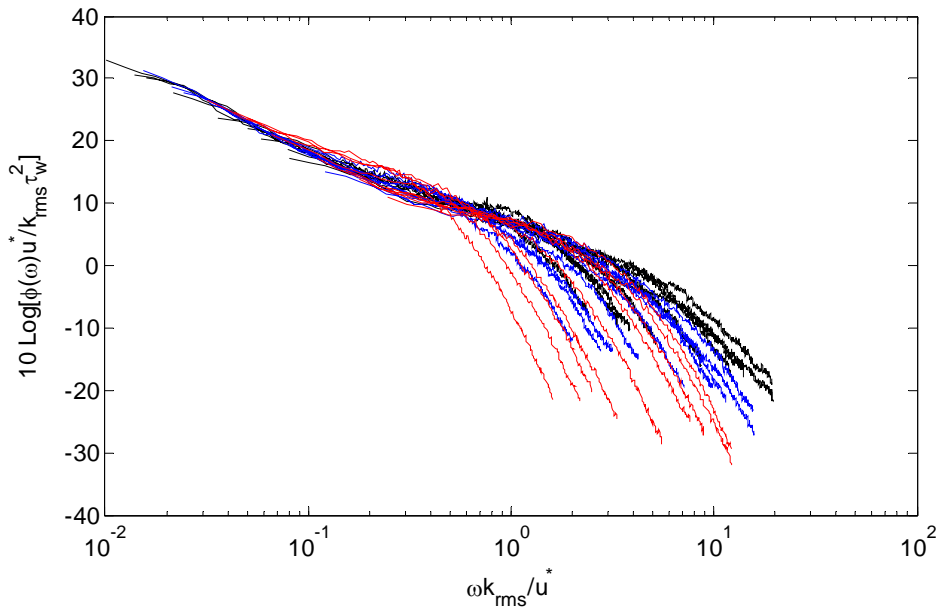


Figure 4.57 Surface pressure scaled on $(k_{rms}, u^*, \text{ and } \tau_w)$ as suggested by Blake (1970) for test cases with varying roughness size at $U_o = 20, 40, \text{ and } 60 \text{ m/s}$ (red, blue, and black, respectively)

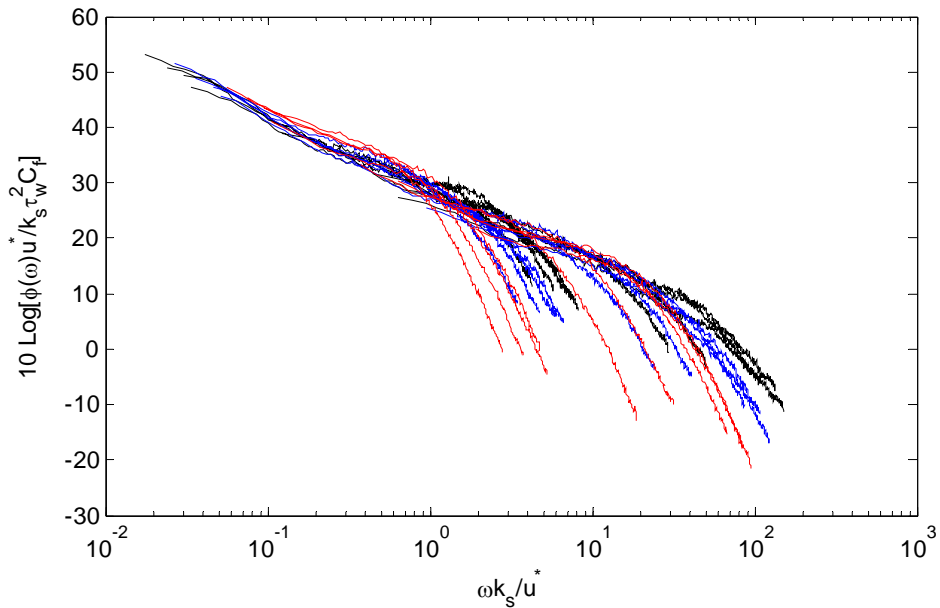


Figure 4.58 Surface pressure spectra scaled on $(k_s, u^*, \text{ and } \tau_w)$ and divided by the skin friction coefficient, C_f , as suggested by Aupperle and Lambert (1970) for test cases with varying roughness size at $U_o = 20, 40, \text{ and } 60 \text{ m/s}$ (red, blue, and black, respectively)

There are a couple of interesting features seen in these figures. First of all, the overlap region is seen to decrease in its frequency range as the nozzle exit speed is decreased. This is not surprising because the dimensional spectra show this quite clearly as seen in Figure 4.28 and Figure 4.39 above. Also, the high frequency regions tend to drop off faster for the lower nozzle

exit speeds. The momentum thickness Reynolds numbers at the trailing edge of the roughness patches range from 507 to 906, 998 to 1779, and 1483 to 2642 for the nozzle exit speeds of 20, 40, and 60 m/s. The scalings proposed by Blake (1970) and Aupperle and Lambert (1970) both show some agreement of the spectral levels in the overlap region of the spectra, but not the frequency. Again, it should not be a surprise that these two sets of scaling variables provide similar behavior of the normalized spectra because the two sets of scaling variables are very similar. In fact the only difference is the choice of roughness length scale which is chosen to be k_s for the Aupperle and Lambert (1970) scaling, and k_g (k_{rms} was used in the current study) for the Blake (1970) scaling.

The use of the roughness size as a length scale to scale the rough wall surface pressure spectra seems only natural, but given the results above, it does not appear that the roughness size can account for the spectral variation seen in the surface pressure spectra. The roughness size does appear to scale the spectra better providing that the flow is fully rough. However, when the roughness size is small, it appears the roughness length scales proposed by Blake (1970) and Aupperle and Lambert (1970) are not effective at scaling the surface pressure spectra. This is not a surprise for the roughnesses with k^+ values indicating hydrodynamically smooth flows because these roughnesses modify the turbulent flow structure only slightly or not at all outside of the sublayer.

Given the inability of the Blake (1970) and Aupperle and Lambert (1970) scaling variables to scale the nondimensionalized surface pressure profiles for wall jet flows over rough surfaces, any set of scaling variables or nondimensional parameters that scaled the rough wall jet surface pressure spectra would be a welcome addition to the study of rough wall surface pressure fluctuations and to any application where the spectral form of the surface pressure spectra is desired. The section below will describe an alternative scaling method for rough wall surface pressure spectra in wall jet flows, and will present results to support this scaling.

4.3.4 Alternative Scaling Methods

During the analysis of the surface pressure spectra shown above and the numerous others that were measured in the current study, various length, velocity, and pressure scales were investigated as possible scaling variables. The length scales investigated were δ , δ^* , $y_{1/2}$, k_{rms} , and k_s . The velocity scales that were investigated were U_m and u^* , and the pressure scales investigated were τ_w (the wall shear) and Q_m . These velocity and pressure scales have been proposed by various workers as possible scaling variables for the scaling of surface pressure spectra. An investigation was done into all possible permutations of these scaling variables for smooth and rough wall jet surface pressure spectra, and the scalings presented above used by Goody and Simpson (2000) and by Goody (2004) discussed above seem to be the best choice for inner and outer scaling of the surface pressure spectra in a smooth wall jet flow. There are most certainly other scaling variable possibilities that could be investigated. The most readily conceivable of these would be related to the roughness geometry, and could involve some measure of the characteristic length between sand grain elements in the roughness patch or some formulation of a length scale relating the sparseness of the roughness sand grains on the rough surface. These types of investigations have not been done in this study, but would be logical areas of investigation in future studies.

In addition to the investigation of the scaling variables mentioned above, some work has been done to create an empirical scaling method. This method is based off of the type of scaling

proposed by Blake (1970) and Aupperle and Lambert (1970) because of the fact that the roughness geometry information was introduced in these proposed scaling as an attempt to account for the change in the surface roughness condition. After observing the scaling behavior of these normalizations seen in Figure 4.55 and Figure 4.56 above and other surface pressure spectra scaled in this way, the normalized frequency and spectral levels were modified by multiplying by nondimensional parameters to some empirically determined powers:

$$\frac{\omega k_s}{u^*} \text{ was replaced with } \frac{\omega k_s}{(k^+)^{0.825} u^*} \quad (4.8)$$

and

$$\frac{\Phi(\omega)u^*}{k_s^2 \tau_w^2 C_f} \text{ was replaced with } \frac{\Phi(\omega)u^*}{(k^+)^{1.325} k_s^2 \tau_w^2 C_f Re_\delta^{0.5}} \quad (4.9)$$

The k^+ term in the denominator of the nondimensional frequency shifted the spectra in such a way as to align the surface pressure spectra relative to frequency. The k^+ term in the denominator of the nondimensional surface pressure spectral density serves to adjust the levels to provide better agreement between scaled spectra, and the boundary layer Reynolds number term in the denominator of the nondimensional surface pressure spectra acted as a fine tuning parameter to improve agreement in the transition between the overlap and high frequency regions. In the scaling attempts earlier in this chapter, it was found that many of the normalizing variables scaled the spectra well in either the overlap or high frequency regions depending on the initial flow conditions or the surface roughness conditions. It will be shown that the scaling method described in equations 4.8 and 4.9 above will scale the surface pressure spectra regardless of the initial flow conditions and will scale spectra of varying roughness height to some degree as well.

In Figure 4.59 below, surface pressure from 40 grit test cases of varying velocity are presented for a microphone location of 1403 mm aft of the nozzle exit and 146 mm aft of the leading edge of the roughness patch. These spectra are scaled using the method described above. The proposed scaling method scales the nondimensional spectra well in the overlap and high frequency ranges, and demonstrates its ability to handle changes in the initial flow conditions.

The same type of analysis was conducted for 180 grit test cases of varying initial flow conditions. The results of this analysis are presented in Figure 4.60 below. Again, the overlap and high frequency ranges are shown to scale well using the empirical method described above. The very low frequency ranges are not scale well by this proposed empirical scaling method. From these observations, the empirical scaling can be said to scale surface pressure spectra whose initial flow conditions are varied.

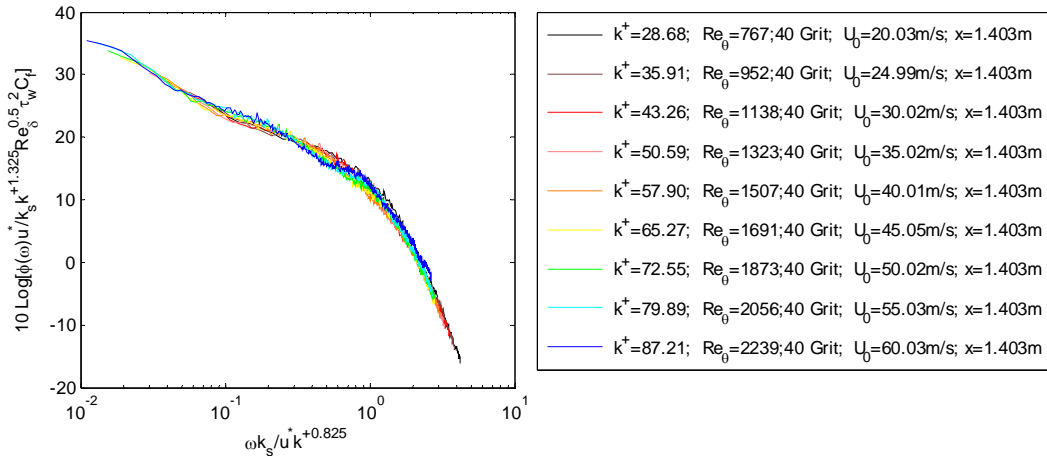


Figure 4.59 Empirical scaling of surface pressure spectra taken at 40 grit test cases of varying nozzle exit velocity.

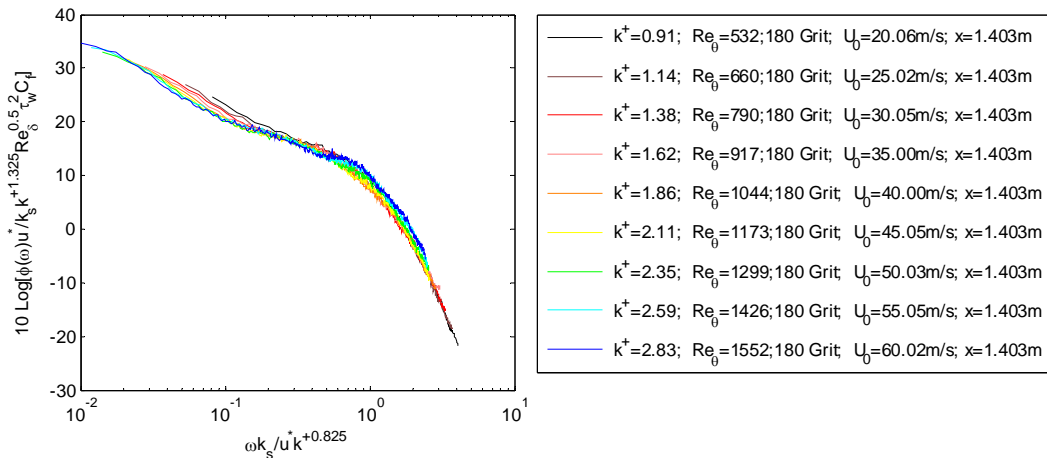


Figure 4.60 Empirical scaling of surface pressure spectra taken at 180 grit test cases of varying nozzle exit velocity.

The ability of the empirical method to scale surface pressure taken at varying microphone measurement locations is seen in Figure 4.61 below. In this figure, the surface pressure spectra are presented for 40 grit test cases having constant initial flow conditions and varying microphone measurement locations. The scaling method performs well in the test cases where the microphone measurement position is varied and collapses the spectra to within 2.5 dB in the overlap and high frequency regions.

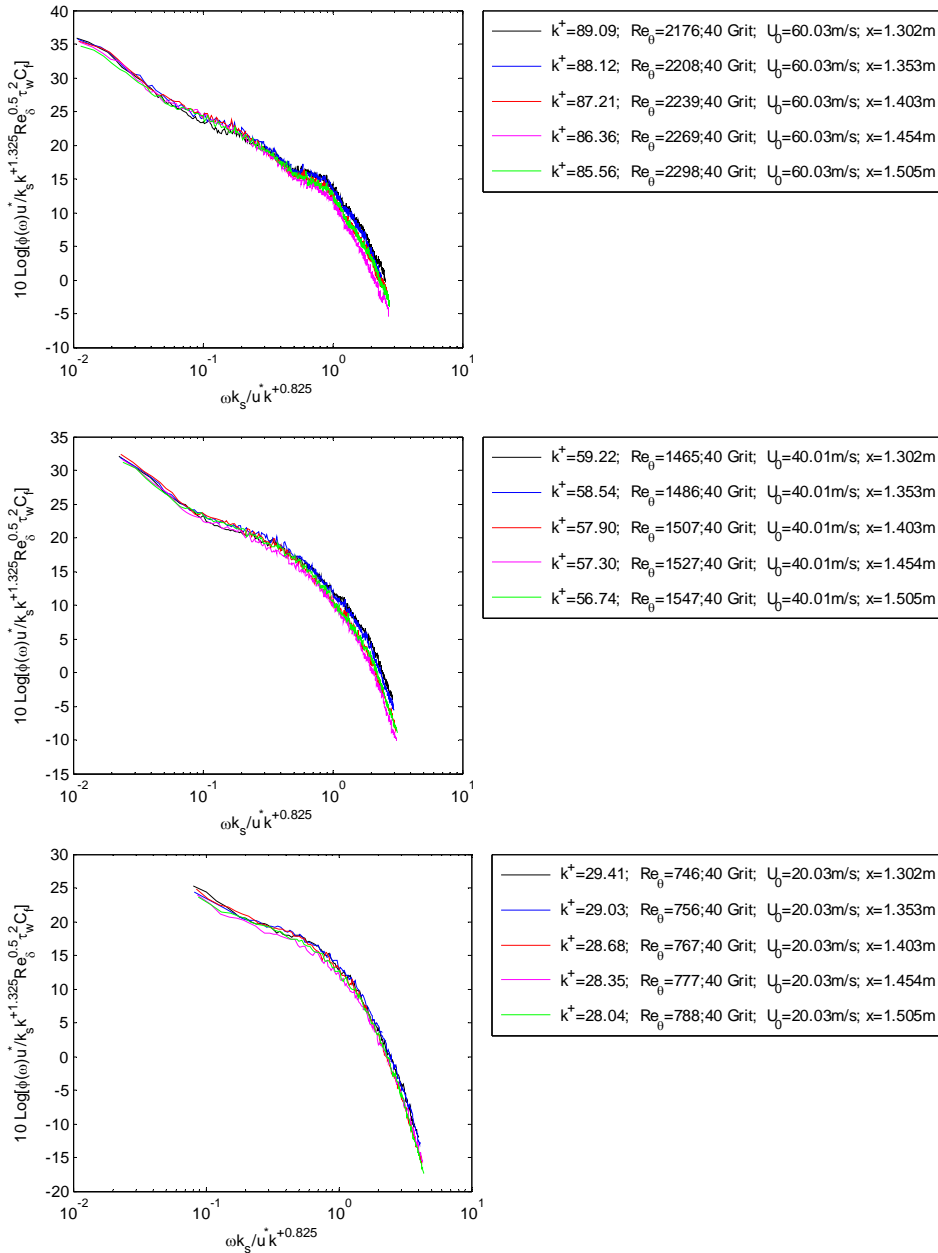


Figure 4.61 Empirical scaling of surface pressure spectra taken at 40 grit test cases of varying microphone measurement position and constant initial flow conditions of $U_o = 60, 40,$ and 20 m/s (top to bottom)

Finally, the ability of the empirical method to scale nondimensional spectra when the roughness surface condition is altered is shown in Figure 4.62 below. The empirical method shows only a comparable collapse of the spectra in the overlap and high frequency regions as compared to the dimensional spectra. It was not expected that proposed scaling would eliminate the spread of the data in the overlap region because the proposed empirical scaling multiplies the entire spectra by a nondimensional number altering the spectral level but not the spectral shape. Because the rough wall surface pressure spectra vary in shape with roughness, these spectra cannot be completely collapsed by any method similar to the proposed empirical scaling. The

proposed method does, however, seem to scale the surface pressure spectra taken at various initial conditions well, and brings the rough wall surface pressure spectra into agreement in frequency when the initial flow conditions are held constant.

This scaling is robust in the sense that it scales surface pressure spectra of varying initial flow conditions, roughness conditions, or microphone measurement locations. This scaling is empirical in nature and it should be noted that further investigation into possible surface pressure scaling variables or methods are needed, but it is believed that this scaling method could be a useful tool for dealing with the spectral character of surface pressure fluctuations in rough wall flows. It is believed that the discussions and analyses shown above will be useful in the study of rough wall flows in turbulent boundary layers even though the current study is focused on wall jet flows.

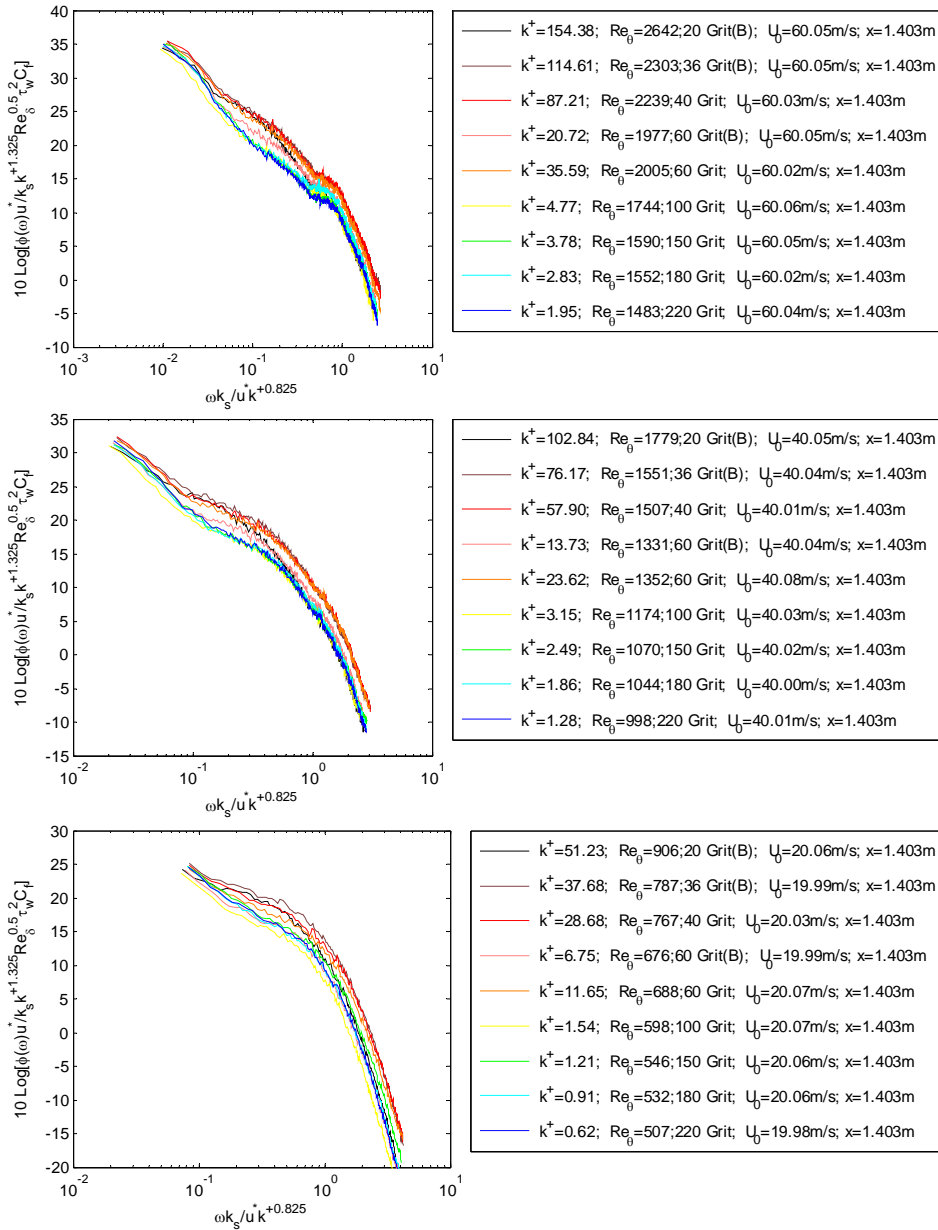


Figure 4.62 Empirical scaling of surface pressure spectra taken at constant initial flow conditions and varying surface roughness

4.4 Summary

The microphone height relative to the plate was determined to be of great importance for the smooth and rough wall flows. The microphones were placed in bushings, and it was observed that if the microphone was not flush with the upper surface of the bushing, then the differences in the measured surface pressure spectra could be as large as 8 dB depending on the frequency for a 0.25 mm recessed height difference between the microphone and the bushing (with the bushing flush with the plate) for smooth wall jet flows. If the bushing and microphone

assembly was raised or recessed relative to the plate by ± 0.25 mm, the differences in the measured spectra were as much as 4 dB depending on the frequency. The effects of the microphone height were not constant throughout all frequencies and affected some frequency regions more than others. However, even the very low frequencies were affected by a deviation in microphone measurement height from the plate level.

For rough wall flows the effects of microphone height were less stark, but nonetheless important. It was found that if the microphone was placed at a height such that the pinhole opening was positioned somewhere between the roughness grain bottoms and tops, then the measured spectra do not seem to be greatly dependent on the microphone height. This is especially true if the microphone is placed between the grain mid heights and the tops, and the difference between measured spectra was less than ± 1 dB. Because the uncertainty of placing the microphone at the roughness tops was far less than placing the microphone anywhere else, and given the fact that the measured spectra showed a minimal dependence on microphone height when the microphone was placed at the roughness tops, the microphone heights for all measurement microphones for all test cases was set to be at the roughness tops.

The placement of the microphone relative to the punched holes in the roughness patch was determined to affect the measured spectra by an amount around ± 1 dB. The experimental data used to assess this effect was collected for a 40 grit rough surface. It is possible that the effects of the microphone installation for roughnesses of smaller size are more important than for the larger grit sizes.

The smooth wall surface pressure spectra measured at constant initial flow conditions over a range of downstream axial locations from 1303 mm to 1505 mm aft of the nozzle exit showed a consistent, however small, progression with the downstream distance varying by less than 2.5 dB between the foremost and aft most microphone measurement locations. When the nozzle exit velocity is varied, the measured surface pressure spectra vary in a clearly progressive way. These surface pressure spectra can be scaled well in the overlap and high frequency regions by using the common inner scaling variables used to deal with surface pressure spectra underneath ordinary turbulent boundary layer flows. These surface pressure spectra are scaled well in the overlap region with the outer scaling variables used by Goody (2004) among others.

The smooth wall surface pressure spectra show a significant difference in character with the surface pressure spectra for ordinary turbulent boundary layer flows. The high frequency roll off occurs at a higher frequency for the wall jet flows, and the spectral character in the overlap region shows higher levels than for conventional turbulent boundary layer surface pressure spectra. The wall jet surface pressure spectra show a frequency variation with $f^{1.1}$ in the overlap region while the frequency variation in this region has been reported to be more on the order of $f^{0.7}$ to $f^{0.8}$ for turbulent boundary layer flows. The high frequency variation of the wall jet flow approaches f^5 and, in this regard, is similar to turbulent boundary layer flows. It is believed that the mixing layer present in the wall jet flow significantly alters the turbulent character even down in the semilog region of the flow, thus increasing the surface pressure spectra in the spectral overlap region relative to that of a turbulent boundary layer. This notion is supported by the comparison of the turbulence intensity profiles of smooth wall jet flows and turbulent boundary layer flows in Chapter 3 above.

The rough wall surface pressure spectra also show high frequency variation that approaches f^5 while the mid frequencies are more complicated. The rough wall surface pressure spectra for various rough surface test cases show the most affected frequency region lies between 200 and 10 kHz. While the high frequency region is much less affected showing differences in

spectral level of 3 – 4 dB, the mid frequency region shows spectral level differences of up to 7 or 8 dB. There is a consistent progression associated with the roughness size variation at these mid frequencies, and a more general variation at the high frequencies. The rough wall surface pressure spectra converge at frequencies below 400 Hz. This would indicate that the turbulent motions associated with these frequencies are in undisturbed flow and that the region of flow affected by the presence of the roughness patches (discussed in section 3.2.2 above) has not grown enough to alter the large low frequency turbulent motions. This notion could also explain why the surface pressure spectra taken at the foremost microphone measurement location vary less at low frequencies with roughness size than the surface pressure spectra taken at microphone measurement locations further aft of the leading edge of the roughness patch.

The rough wall surface pressure spectra scale well on the inner and outer variable scalings used for the smooth wall surface pressure spectra in the overlap region if the rough surface condition is held constant. However, these smooth wall scalings are not able to account for the variation in roughness size. The two suggested scalings for rough wall surface pressure spectra under turbulent boundary layers proposed by Blake (1970) and Aupperle and Lambert (1970) do not scale the wall jet surface pressure spectra as the roughness size is altered. However, as the roughness size is increased and the flow approaches a fully rough condition, the surface pressure spectra scaled according to Aupperle and Lambert (1970) and Blake (1970) appear to begin to converge. This could indicate that for fully rough flows, a measure of the roughness size can be used to scale the surface pressure spectra of rough wall flows. However, for smaller roughnesses, this does not appear to be the case.

An empirical scaling was developed from the current study and is shown to scale the rough wall surface pressure spectra with only limited success. This empirical scaling uses the nondimensional parameters k^+ and Re_δ to modify the Aupperle and Lambert (1970) roughness scaling scheme.

5 Conclusions

A facility has been developed that has been shown to generate a classical plane turbulent wall jet flow that is two dimensional over a large region of the flow surface. This facility was used to obtain smooth and rough wall jet measurements of the mean velocity, turbulent character, and velocity spectra. This facility was also used to obtain surface pressure fluctuation measurements of the wall jet flow over smooth and rough flow surfaces. The rough surfaces tested ranged in sand grain size from 0.07 mm to 0.95 mm, yielding k^+ values ranging from hydrodynamically smooth to fully rough. Conclusions are as follows:

The Smooth Wall Jet Flow:

- 1) The wall jet mean velocity profiles and normal stress profiles scale well on the outer variables, U_m and $y_{1/2}$, except very near the wall. This is in agreement with previous wall jet studies.
- 2) The momentum scaling proposed by Narasimha *et al.* (1973) was used to describe the variation of U_m , $y_{1/2}$, δ , δ^* , and θ with the nozzle exit Reynolds number and the Reynolds number based on the streamwise distance from the nozzle exit showing that the boundary layer length scales were proportional to one another. This allowed for the estimation of these flow parameters in the absence of experimental data.
- 3) The mean velocity profiles scale well on inner coordinates when the skin friction is estimated using the method of George *et al.* (2000).
- 4) These scaled profiles show a well defined semilog region that is different in slope than that of a conventional turbulent boundary layers. The differences between wall jet flows and turbulent boundary layer flows are believed to be due to the presence of the mixing layer in the wall jet flow.
- 5) Inner variables were shown to scale the normal stress profiles to only a limited extent even at y^+ values as small as 10. This is agreement with George *et al.* (2000) who only show good collapse of the normal stress scaled on inner variables for y^+ values less than around 7.
- 6) Turbulence intensity comparisons of wall jet and conventional turbulent boundary layer flows show a significant difference in the normalized profiles both very near the wall and also further away displaying the effect of the shear layer on the flow.
- 7) Smooth wall velocity spectra were shown to scale well on U_m and $y_{1/2}$ as the velocity and length scales, respectively even as close to the wall as the displacement thickness height where even the high frequency regions are scaled well. This suggests that the larger more energetic turbulent structures in the flow are the dominant turbulent motions in the wall jet flow.
- 8) The inner scaling suggested by Ueda and Hinze (1975) for conventional turbulent boundary layers scales the smooth wall surface velocity spectra at the highest frequencies very well, but does not scale the low to mid frequency spectral regions as well as the outer variables.
- 9) Smooth wall surface pressure spectra vary in a consistent progression in spectral level with the flow speed and streamwise position.

- 10) The smooth wall surface pressure spectra scale well in the overlap region on the conventional turbulent boundary layer surface pressure outer scaling employed by Goody (2004),
- 11) The smooth wall jet surface pressure spectra scaled well in the overlap and high frequency regions on the inner scaling employed by Goody and Simpson (2000) among others.
- 12) The scaled surface pressure spectral variation with frequency followed a $\omega^{-1.1}$ variation in the overlap region and a ω^{-5} variation at high frequencies. In ordinary turbulent wall jets, these variations have been theoretically proposed to be ω^{-1} and ω^{-5} in the overlap and high frequency regions, respectively, and have been experimentally shown to be $\omega^{-0.7}$ to $\omega^{-0.8}$ in the overlap region and ω^{-5} in the high frequency region. This would imply that the presence of the shear layer present in wall jet flows alters the spectral character in the overlap region while not greatly affecting the higher frequency regions of the surface pressure spectrum. This result is also supported by the differences shown between the turbulence intensity profiles for wall jet flows and turbulent boundary layer flows.
- 13) The smooth wall jet surface pressure spectra show higher levels in the low frequency and overlap regions when compared with the Goody (2004) empirical model for smooth wall turbulent boundary layer surface pressure spectra. Also, the high frequency roll off occurs at a higher frequency for the wall jet flow than predicted by the Goody (2004) empirical model. It is believed that the higher spectral levels in the overlap region for wall jet flows are due to the large, high energy turbulent structures associated with the mixing layer.

The Rough Wall Jet Flow

- 1) For flows that encounter sudden changes in surface roughness, an inner layer develops and grows with the distance downstream of the change in surface roughness. Flow outside of this region remains unaffected by the rough surface and is determined by the undisturbed flow proceeding from the flow conditions at the onset of the surface roughness. The affected region grows eventually reaching a fully developed state where the flow similarity is regained. Flow measurements indicate that at the aft edge of the roughness patches in the current study, the flow region affected by the roughness has grown to near the boundary layer thickness, but it is unclear if the boundary layer thickness is affected substantially by the roughness or not.
- 2) The mean velocity profiles behind rough patches of finite length continue to scale well on outer variables away from the wall. However, the effects of roughness size are quite noticeable below $y/y_{1/2}$ equal to 0.125.
- 3) The normal stress profiles behind rough surfaces scaled on outer variables away from the wall as well, but a lack of collapse below $y/y_{1/2}$ equal to 0.075 was observed
- 4) Both U_m and $y_{1/2}$ show no discernable variation with the roughness size for the roughness patch lengths studied.
- 5) The boundary layer thickness was shown to increase when the 305 mm long patches of roughness were applied to the flow surface, but this increase was not seen to be dependent on the roughness size. The displacement and momentum thicknesses, however, showed a consistent variation with the roughness size when measurements were taken behind the 305 mm long roughness patches.
- 6) The estimated skin friction values calculated for the rough wall jet flows using a momentum balance appear accurate.

- 7) Rough wall mean velocity profiles presented in inner variables show qualitative agreement in the semilog region with what is seen in ordinary turbulent boundary layers, in that the semilog region shifts downwards but maintains the same slope as the roughness size is increased.
- 8) The normal stress profiles scaled on inner variables do not collapse well, but as the roughness size is increased, the dependence on roughness size becomes less noticeable indicating that the flow is approaching a fully rough regime.
- 9) As with the smooth wall, the rough wall jet velocity spectra taken at $y = \delta$ and $y = y_{1/2}$ scale with U_m and $y_{1/2}$ for the full range of roughness conditions. However, the velocity spectra taken at $y = \delta^*$ were shown to scale better on the skin friction velocity, u^* and the displacement thickness, δ^* (except at frequencies below 200 Hz) when only the roughness size was varied. However, when the initial flow conditions were altered, these scaling variables were not seen to collapse the spectra well. If all of the rough wall jet velocity spectra taken at the displacement height are considered, the best scaling variables are the outer variables indicating that the effects of the initial flow conditions are more dominant than the effects of the roughness size.
- 10) The roughness size was also investigated as a scaling length showing no collapse of the spectra taken at any height off of the plate.
- 11) Again, the surface pressure spectral levels measured for the wall jet flow over rough surfaces varied in a consistent and progressive way with the flow speed. The surface pressure spectra varied only slightly with the microphone measurement location except at high frequencies where the spectral levels varied by as much as 5 – 6 dB.
- 12) The rough surface pressure spectra varied most in the overlap region and not the high frequency region. These variations are consistent and progressive with the change in roughness size. This would indicate that the turbulent structures in the semilog region are the most affected by the presence of the rough surfaces. The surface pressure spectra converged below 400 Hz indicating that this frequency region is dominated by turbulent structures associated with the flow outside of the inner region of altered flow that develops at the onset of a sudden change in roughness.
- 13) The smooth wall turbulent boundary layer inner scaling was applied to the rough wall jet flows. For constant roughness conditions, the surface pressure scaled well at both high frequencies and in the overlap region. This inner scaling was unable to collapse the surface pressure spectra in the overlap region or at high frequencies with a change in roughness size.
- 14) The smooth wall turbulent boundary layer outer scaling was applied to the rough wall jet surface pressure spectra. For constant roughness conditions, the surface pressure scaled well in the overlap region. If the roughness size is varied, the outer scaling does not scale the surface pressure spectra well.
- 15) The proposed turbulent boundary layer scalings of Blake (1970) and Aupperle and Lambert (1970) were applied to the surface pressure spectra taken in the current study, but unable to account for the change in roughness size. As the wall jet flows over the rough surfaces approached and surpassed a fully roughened state, the surface pressure spectra scaled according to Blake (1970) and Aupperle and Lambert (1970) approached one another indicating that the spread in the scaled surface pressure spectra could be due to the transition of the flow from smooth to rough, and that once

a fully rough state is achieved, the scalings of Blake (1970) and Aupperle and Lambert (1970) become more applicable.

- 16) An empirical scaling was presented that is able to account for changes in the initial flow conditions of surface pressure spectra taken for various surface roughness conditions, but does little to bring the spectral levels into coincidence. This empirical scaling does not account for the difference in the spectral shape associated with the variation in surface roughness.

References

- Abrahamsson, H., Johansson, B. and Löfdahl, L. 1994, "A turbulent plane two-dimensional wall-jet in a quiescent surrounding", *Eur. J. Mech. B/Fluids* 13, 533-556
- Alcaraz, E., "Contribution `a l`etude d`un jet plan turbulent evolouant le long d`une paroi convexe `a faible courbure", *C.R. Acad. Sci, Paris* 286B
- Aupperle, F. A., and Lambert, R. F., 1970, "Effects of Roughness on Measured Wall Pressure Fluctuations Beneath a Turbulent Boundary Layer", *J. Acoust. Soc. Am.* 47, 359 – 370
- Blake, W. K., 1970, "Turbulent Boundary-Layer Wall-Pressure Fluctuations on Smooth and Rough Walls", *Journal of Fluid Mechanics*, vol. 44, pt. 4, pp. 637 – 660
- Blake, W. K., 1986, *Mechanics of Flow-Induced Sound and Vibration*, Academic Press, New York, 1986
- Bradshaw, P., 1967, "Inactive motion and Pressure Fluctuations in Turbulent Boundary Layers", *Journal of Fluid Mechanics*, vol. 30, pp. 241 – 258
- Bradshaw, P. & Gee, M., 1960, "Turbulent wall jets with and without an external stream", *Aero. Res. Council R & M.*
- Bradshaw, P., Ferriss, D. H., and Atwell, N. P., 1967, "Calculation of boundary-layer development using the turbulent energy equation", *Journal of Fluid Mechanics*, vol. 28, part 2, pp. 593 – 616
- Chase, D. M., 1980, "Modeling the Wavevector-Frequency Spectrum of Turbulent Boundary Layer Wall Pressure", *Journal of Sound and Vibration*, vol. 70, no. 1, pp. 29 – 67
- Clauser, F. H., 1954, "The Turbulent Boundary Layer", *Advances in Applied Mechanics*, vol. IV, Academic Press, New York
- Craft, T. J., and Launder, B. E., 2001, "On the spreading mechanism of the three-dimensional turbulent wall jet", *J. Fluid Mech.*, vol. 435, pp. 305 – 326
- Dey, S. and Sarkar, A., 2006, "Response of velocity and turbulence in submerged wall jets to abrupt changes from smooth to rough beds and its application to scour downstream of an apron", *J. Fluid Mech.*, vol 556, pp. 387 – 419
- Ead, S. A. and Rajaratnam, F., 2004, "Plane Turbulent Wall Jets on Rough Boundaries with Limited Tailwater", *Journal of Engineering Mechanics*, vol. 130, n10, pp. 1245-1250.
- Eriksson, J., Karlsson, R., and Persson, J., 1998, "An experimental study of a two-dimensional plane turbulent wall jet", *Expts. Fluids*, vol. 25, pp. 50 – 60

Fang, Fuh-Min, Chen, J. C., Hong, Y. T., 2001, "Experimental and analytical evaluation of flow in a square-to-square wind tunnel contraction", *Journal of Wind Engineering and Industrial Aerodynamics*, vol. 89, pp. 247-262.

Farabee, T. M., and Cassarella, M. J., 1984, "Effects of Surface Irregularity on Turbulent Boundary Layer Wall Pressure Fluctuations", *Journal of Vibration, Acoustics, Stress, and Reliability in Design*, vol. 106, pp.343 - 349

Farabee, T. M., and Cassarella, M. J., 1986, "Measurements of Fluctuating Pressure for Separated/Reattached Boundary Layer Flows", *Journal of Vibration, Acoustics, Stress, and Reliability in Design*, vol. 108, pp.301 - 307

Farabee, T. M., and Cassarella, M. J., 1991, "Spectral Features of Wall Pressure Fluctuations Beneath Turbulent Boundary Layers", *Physics of Fluids A*, vol. 3, no. 10, pp. 2410 - 2420

Förthmann, E. 1934, "Über turbulente Strahlausbreitung", *Ing. Arch.*, 5, 42

George, W. K., and Castillo, L. 1997, "Zero pressure-gradient turbulent boundary layer", *Appl. Mech. Rev.*, vol. 50, pp 689 – 729

George, W. K., 1995, "Some new ideas for similarity of turbulent shear flows", In *Proc. ICHMT Symposium on Turbulence, Heat and Mass Transfer, Lisbon, Portugal (1994)* (ed. K. Hanjalic and J. Pereira). Begell House

George, W. K., Abrahamsson, J. E., Karlsson, R. I., Löfdahl, L. and Wosnik, M., 2000, "A similarity theory for the turbulent plane wall jet without external stream", *J. Fluid Mech.*, vol. 425, pp. 367-411.

Glauert, M. B., 1956, "The wall jet," *J. Fluid Mech.*, 1, p. 625

Goody, M., 2004, "Empirical Spectral Model of Surface Pressure Fluctuations", *AIAA Journal*, vol. 42, no. 9, pp. 1788 – 1794

Goody, M. and Simpson, R. L., 2000, "Surface Pressure Fluctuations Beneath Two-and Three-Dimensional Turbulent Boundary Layers", *AIAA Journal*, vol. 38, no. 10, pp. 1822 - 1831

Grissom, D. L., 2007, "A Study of Sound Generated by a Turbulent Wall Jet Flow Over Rough Surfaces", Ph.D. dissertation, Aerospace and Ocean Engineering Dept., Virginia Tech, Blacksburg, VA

Grissom, D. L., Smith, B. S., Devenport, W. J., and Glegg, S. A. L., 2007, "Rough Wall Boundary Layer Noise", 2006, 12th AIAA/CEAS Aeroacoustics Conference (27th AIAA Aeroacoustics Conference)8-10 May2006, Cambridge, MA, AIAA-2006-2409

Grissom, D. L., Smith, B. S., Devenport, W. J., and Glegg, S. A. L., 2007, "Rough Wall Boundary Layer Noise: An Experimental Investigation", 13th AIAA/CEAS Aeroacoustics

Conference (28th AIAA Aeroacoustics Conference)21-23 May 2007, Rome, Italy, AIAA-2007-3418

Hall, J. W., Ewing, D., 2005, “The Rectangular Wall Jet. Part 1: The Effect of Varying Aspect Ratio”, 43rd AIAA Aerospace Sciences Meeting and Exhibit,10-13 January, 2005, Reno, Nevada, AIAA-2005-115

Hama, F. R., 1954, “Boundary Layer Characteristics for Smooth and Rough Surfaces”, Trans. Soc. Nav. Arch. Mar. Eng., vol. 62, pp. 333 - 358

Hari, M. V., 1973, “A method to analyse the wall jet flow” Aeronautical Journal, October, pp. 512 – 515

Hama, F. R., 1954, “Boundary Layer Characteristics for Smooth and Rough Surfaces”, Trans. Soc. Nav. Arch. Mar. Eng., vol. 62, pp. 333 – 358

Hogg, A. J., Huppert, H. E., and Dade, W. B., 1996, “Erosion by planar turbulent wall jets”, J. Fluid Mech. Vol. 338, pp. 317-340

Howe, M. S., *Acoustics of Fluid-Structure Interactions*, Cambridge Univ. Press, Cambridge, England, U. K., 1998

Hwang, L. S., and Laursen, E. M., 1963, ”Shear Measurement Technique for Rough Surfaces”, Proc. ASCE, J. of the Hydr. Div., March, 1963

Irwin, H. P. A. H., 1973, “Measurements in a self-preserving plane wall jet in a positive pressure gradient”, J. Fluid Mech., 61, 33

Karlsson, R. I., Eriksson, J., and Persson, J., 1993b, “An experimental study of a two-dimensional plane wall jet”, Report VU-S 93:B36, Vattenfall Utveckling AB

Klebanoff, P. S., 1955, “Characteristics of Turbulence in a Boundary Layer with Zero Pressure Gradient”, NACA Rep. 1247 (1955)

Launder, B. E., and Rodi, W., 1981, “The Turbulent Wall Jet”, Prog. Aerospace Sci., vol. 19, pp. 81-128

McGrath, B. E., and Simpson, R. L., 1987, “Some Features of the Surface Pressure Fluctuations in Turbulent Boundary Layers with Zero and Favorable Pressure Gradients”, NASA CR-4051

Mish, P. F., 2003, “An Experimental Investigation of Unsteady Surface Pressure on Single and Multiple Airfoils”, Ph.D. dissertation, Aerospace and Ocean Engineering Dept., Virginia Tech, Blacksburg, VA

Naib, S. K. A., 1968, “Spreading and Development of the Parallel Wall Jet”, Aircraft Engineering, December, pp. 30 – 33

- Nikuradse, J., Natnl. Advisory Comm. Aeron. Tech. Mem., TM 1292 (1950)
- Narasimha, R., Yegna Narayan, K. & Parthasarathy, S., 1973, "Parametric analysis of turbulent wall jets in still air", *Aero. J.*, pp. 355-359.
- Rajaratnam, N. 1967, "Plane Turbulent Wall Jets on Rough Boundaries, Part One", *Water Power*, April, pp. 149 – 153
- Rajaratnam, N. 1967, "Plane Turbulent Wall Jets on Rough Boundaries, Part Two", *Water Power*, May, pp. 196 - 201
- Rajaratnam, N. 1967, "Plane Turbulent Wall Jets on Rough Boundaries, Part Three", *Water Power*, June, pp. 240 – 242
- Schultz-Grunow, F., 1940, "A New Resistance Law for Smooth Plates", *Luftfahrt-Forsch.*, vol. 17, pp. 239 – 246
- Schwarz, W. H., and Cosart, W. P., 1960, "The two-dimensional turbulent wall-jet", *Fluid Mech.*, 10, 481 – 495
- Sforza, M. P., and Herbst, G., 1970, "A study of three-dimensional, incompressible turbulent wall jets", *AIAA J.*, 8, 276
- Sigalla, A., 1958, "Measurements of a skin friction in a plane turbulent wall jet", *J. R. Aero. Soc.*, 62, 873
- Simpson, R. L., 1971, "The Effect of a Discontinuity in Wall Blowing on the Turbulent Incompressible Boundary Layer", *Int. J. Heat Mass Transfer*, vol. 14, pp. 2083 – 2097
- Smits, A. J., and Wood, D. H., 1985, "The Response of Turbulent Boundary Layers to Sudden Perturbations", *Ann. Rev. Fluid Mech.*, vol. 17, pp. 321 - 358
- Tachie, M. F., Balachander, R., and Bergstrom, D. J., 2002, "Scaling the inner region of turbulent plane wall jets", *Experiments in Fluids*, 33, pp. 351 – 354
- Tachie, M. F., Balachander, R., and Bergstrom, D. J., 2004, "Roughness effects on turbulent plane wall jets in an open channel", *Experiments in Fluids*, 37, pp. 281 - 292
- Tailland, A. and Mathieu, J., 1965, "Jet parietal", *Academie des Sciences -- Comptes Rendus*, vol. 261, n 12, pp. 2282-2285.
- Tailland, A., "Contribution `a l'etude d'un jet plan dirige tangentiellement `a une paroi", Doctoral Thesis, Universite de Lyon, 1970
- Ueda, H., and Hinze, J. O., 1975, "Fine-structure turbulence in the wall region of a turbulent boundary layer", *J. Fluid Mech.*, vol. 67, part 1, pp. 125 - 143

Wynanski, I., Katz, Y. & Horev, E. 1992, "On the applicability of various scaling laws to the turbulent wall jet", *J. Fluid Mech.*, vol. 234, pp. 669-690